# A Cambridge Structural Database Search for Entangled MOFs and the Synthesis and Analysis of the Non-Entangled Counterparts of a Set of Entangled MOFs

Lungelo Tervin Bambiso




Supervisor: Assoc. Prof. Clive L. Oliver

Co-Supervisor: Dr Wilson M. Mogodi

# Acknowledgements

I would like to express my gratitude to:

- Assoc. Prof. Clive Oliver, my supervisor, for his invaluable guidance, commitment, patience, and support throughout this process, and for everything he has taught me.
- Kedibone Muguru, PhD candidate, for her input, instrumental help, late hours analyzing of samples, and sharing of her knowledge.
- Vuyolwethu Mpetshwa (MSc student), Nonhlanhla Baloyi (MSc student) and Andisiwe Mafika (PhD candidate), for their friendship, support, and encouragement.
- The members of the Oliver research group and members of the Centre for Supramolecular Chemistry Research group for their advice and assistance.
- To my daughter, Lunathi Chai Mgolombane, for the days she always makes me smile and laugh even if I am not feeling up to it, the late-night play dates when I am writing and the love.
- The University of Cape Town for financial support.

# Abbreviations

MOF – metal-organic framework

SBU – secondary building unit

1D – 1-dimensional

2D – 2-dimensional

3D – 3-dimensional

DMF – *N,N'*-dimethylformamide

DEF – *N,N'*-diethylformamide

$Cu(NO_3)_2 \cdot 2.5H_2O$ – copper(II) nitrate trihydrate

BET – Brunauer-Emmet-Teller

SCSC – single-crystal-to-single-crystal

CCDC – Cambridge Crystallographic Data Centre

CSD – Cambridge Structural Database

SCXRD – single-crystal X-ray diffraction

PXRD – powder X-ray diffraction

VT-PXRD – variable-temperature powder X-ray diffraction

HSM – hot stage microscopy

TGA – thermogravimetric analysis

DSC – differential scanning calorimetry

$H_2$hfipbb – 4,4'-(hexafluoroisopropylidene)bis(benzoic acid)

# Compound codes.

The metal-organic compounds synthesized have been given names which has no relation to the numbering of MOFs published elsewhere and named accordingly.

MOFDMF(NIP) – $[Cu_2(hfipbb)_2(DMF)_2]_n \cdot n(DMF)_4$

MOFDEF(NIP) – $[Cu(hfipbb)(DEF)]_n \cdot n(DEF)_2$

MOF$H_2O$(NIP) – $[Cu_2(hfipbb)_2(H_2O)_2]_n$

MOFDMF(IP) – $[Cu(hfipbb)(DMF)]_n \cdot n(DMF)_{0.5}$

MOFDEF(IP) – $[Cu(hfipbb)(DEF)]_n$

MOF$H_2O$(NIP) – $[Cu(hfipbb)(H_2O)]_n.n(DMF)_{0.5}$

# Abstract

Metal-organic frameworks (MOFs) have become a fast-growing field of research in the areas of synthetic chemistry, crystal engineering, materials science and supramolecular chemistry in recent years. The synthesis and characterization of novel MOFs have been of particular interest to researchers around the world due to their potential in several applications, such as gas sorption and separation, drug delivery and catalysis. The focus and pursuit in the early stages of MOF research was to design materials with as large pore volumes as possible, which lead to the phenomenon called entanglement. Entanglement in MOFs, of which interpenetration is a subtype, refers to when networks within the same crystal structure cannot be hypothetically separated from one another without breaking chemical bonds. This has a significant impact on the porous nature, structure, and functional applications of MOFs. Thus, initially entanglement was viewed as undesirable, however, it has since been recognized that entanglement could be advantageous, since these MOFs may be more stable.

The primary objective of this work was (i) to data mine the Cambridge Structural Database (CSD) for entangled MOFs and (ii) to investigate the structural, thermal and sorption properties of a set of non-entangled MOFs with their previously published isoreticular and entangled counterparts. The first section of this thesis, the computer-based section, presents the MOFs (not discriminating between entangled and non-entangled MOFs) belonging to seven different families extracted (using the CSD version 5.37 - May 2016 update) according to the search criteria used by Moghadam and Fairen-Jimenez *et al.* In this thesis, these seven families were updated using the CSD version 5.43 - April 2021. These families formed the basis sets from which entangled MOF structures were searched using search criteria based on intermolecular, non-bonded contacts such as hydrogen bonding, π–π and C–H···π interactions. The average of the two success rate indicators, showed that the percentage of retrieved entangled MOF structures from the four MOF families that had entangled structures, ranged from 13.6 – 38.6%, 11.8 – 38% and 4.4 – 34%, respectively, for the three search criteria.

The second section of this thesis, the experimental section, describes two novel non-entangled two-dimensional (2D), 2-periodic isoreticular fluorinated MOFs of formulae $[Cu_2(hfipbb)_2(DMF)_2]_n \cdot n(DMF)_4$ (**1**), $[Cu(hfipbb)(DEF)]_n \cdot n(DEF)_2$ (**2**), where hfipbb = 4,4′-(hexafluoroisopropylidene)bis(benzoate), DMF = *N,N′*-dimethylformamide and, DEF = *N,N′*-diethylformamide. These structures are compared to their entangled, isoreticular counterparts published by Chatterjee *et al.* in terms of their syntheses, structures, thermal and sorption properties.

The entangled structures had decomposition temperatures of 310 °C and 400 °C for the MOFs obtained from DMF and for DEF, respectively whilst the non-entangled MOFs had decomposition temperatures of 350 °C and 370°C for **1** and **2**, respectively. The non-entangled MOFs had contact surface potential void space of 39% and 40.4% for **1** and **2**, respectively, significantly higher than those of entangled MOFs with contact surface potential void spaces of 8.2% and 12.5% for the entangled MOFs obtained from DMF and DEF, respectively. Despite the lack of entanglement in **1** and **2**, as compared to their entangled counterparts, their 195 K $CO_2$ sorption isotherms also display inflection points and significantly increased sorption, as well as large extents of hysteresis, of 35% and 39% obtained for **1** and **2**, respectively, whilst both entangled MOFs displayed extents of hysteresis of 44%. Interestingly, the activated phase of a third MOF, $[Cu_2(hfipbb)_2(H_2O)_2]_n$ (**3**), synthesized through DMF ligand exchange with water in 7 days, does not display an inflection point in its 195 K $CO_2$ isotherm and subsequent increased sorption, despite also being non-entangled. This confirms that subtle differences in

the desolvated phases can lead to marked differences in the sorption behaviour of isoreticular MOFs.

# Table of Contents

# CHAPTER 1

# INTRODUCTION

This chapter presents pertinent themes and terms associated with the field of metal-organic frameworks (MOFs) research, e.g., supramolecular chemistry, crystal engineering, and the important issue of classification. The entanglement of MOFs, the effect of this phenomenon on their chemical and physical properties, factors affecting the degrees of entanglement, and their presence in the Cambridge Structural Database (CSD) are also discussed. The materials utilized, the aims and the objectives of this research project are expressed at the end of **Chapter-1**.

## 1.1. Supramolecular Chemistry

Johannes Diderik van der Waals in 1873 demonstrated for the first time intermolecular forces.[1-3] It was two decades later in 1894 that Nobel laureate Hermann Emil Fischer proposed the philosophical roots of supramolecular chemistry, in his study on enzyme–substrate interactions.[3-5] Years later, as the research on intermolecular forces continued, in 1948 H.M. Powell described hydroquinone clathrates, which caused the interest in supramolecular structures to grow exponentially.[6] Currently, supramolecular chemistry is one of the major topics of research in chemical sciences.

Supramolecular chemistry is concerned with the non-covalent interaction between molecules and or ions. Jean-Marie Lehn in his Nobel prize lecture, coined it as “chemistry beyond the molecule”.[7,8] The most crucial interactions are intermolecular bonds such as van der Waals interactions, electrostatic (coulombic) interactions, hydrophobic forces, halogen bonds, hydrogen interactions and π–π interactions (cation−π, anion−π).[9,10] An important consideration in these interactions is the mutual recognition of molecules that leads to self-assembly.

## 1.2. Crystal Engineering

Crystal engineering was defined by Desiraju as “The understanding and controlling of supramolecular interactions in the context of crystal packing and the utilization of such understanding is essential for more prominent control of supramolecular synthesis through the design of new molecular solids with wanted chemical and physical properties”.[11]

R. Pepinsky was the first to present the term crystal engineering in the literature in 1955,[12,13] however it is generally associated with G. M. J. Schmidt and A. I. Kitaigorodskii.[14,15] Schmidt's

article brought about an advancement on the concept of crystal engineering, and it became clear that crystal engineering, on the basis of organic solids is derived from the ideas of supramolecular chemistry.

The main objective of crystal engineering is to produce crystals, constructed from one or more molecules with specific functions. Thus, to form crystals by design one must have an understanding of the supramolecular interactions that can be utilized to assemble molecular components into a desired design. Supramolecular interactions between molecules such as van der Waals forces and hydrogen bonds are important in assembling molecular components into a target network.

The required bonding energies associated with these interactions span a wide range with van der Waals forces being of the lowest energy. The conceptual principles of crystal engineering are used in the synthesis of crystalline coordination polymers, i.e., zeolites, mesoporous silica, and metal-organic frameworks.

### 1.3. Porous Material

Scientific research into porous (permeable) materials has witnessed remarkable development over the past few decades with the improvement of nanostructured materials.[16] It is vital to appreciate that permeable materials have been around for longer than may be apparent.[16] Much consideration has been given to the utilization of numerous diverse compounds to make nanostructured materials. Porous materials can be beneficially applied for gas separation,[17-22] gas sorption and liquid storage,[23,24] catalysis,[25-30] photocatalysis and photoluminescence,[31-41] and photoenergy conversion in solar cells (**Figure 1.1.**).[42-44] This originates from their ability to host-guest molecules or ions due to their large pore sizes.

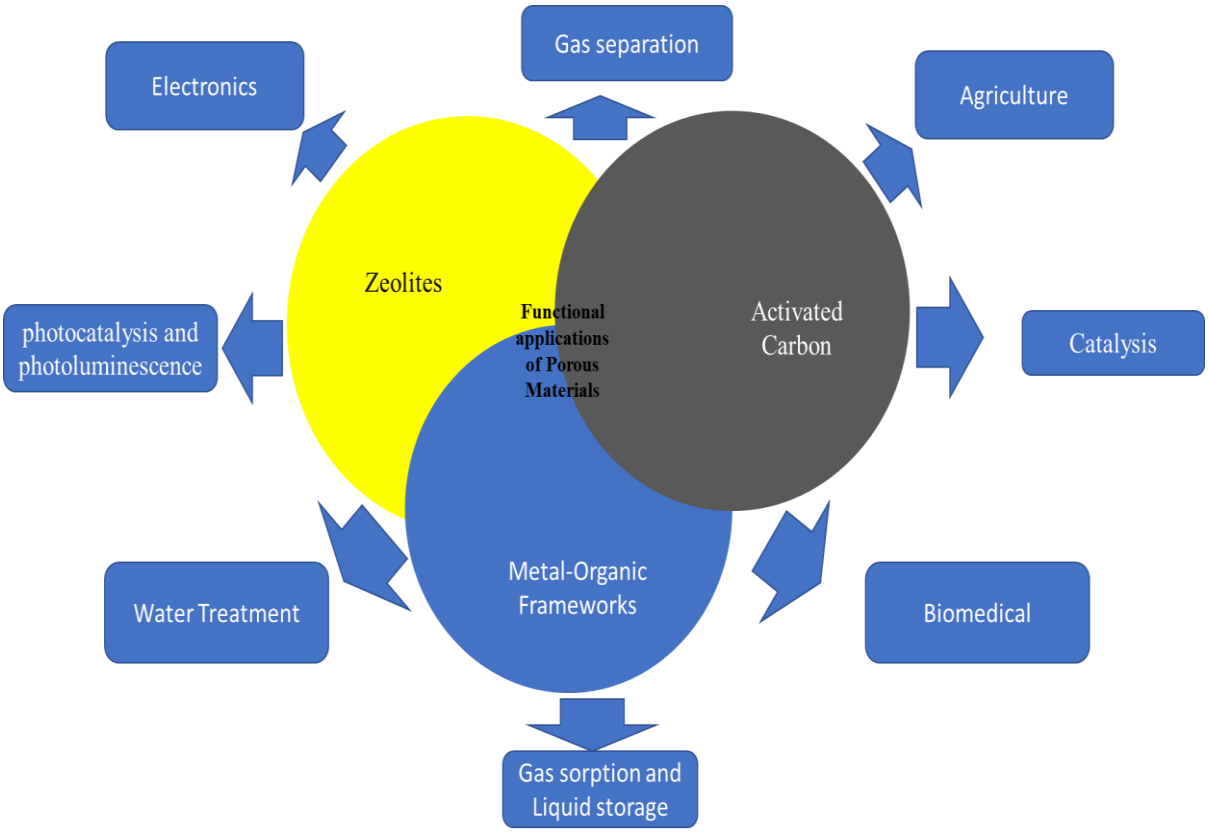


**Figure 1.1.** Functional applications of Porous Materials.

### 1.3.1. Zeolites

Mainly two types of porous materials were used up to the mid-1990s, namely activated carbon and inorganic based materials. Inorganic materials can be categorized into two classes, namely aluminosilicates and aluminophosphates.[45,46] Aluminosilicates are a class of microporous crystalline materials called zeolites. They are fundamentally made up of silica, alumina, and inorganic bases, in order to produce 3-dimensional, crystalline, hydrated alkaline structures with a general formula of $M^{n+}_{x/n}[(AlO_2)_x(SiO_2)_y]^{x-}\cdot_w H_2O$[24–26] (M = metal).[45] The framework of these structures is built from tetrahedra of corner-sharing $TO_4$ (T= Al, Si) (**Figure 1.2**), and have interconnected channels in which water and metal atoms are located.[45,47] Microporous crystalline aluminophosphates were first published in 1982 and many of them have crystal structures which are not observed in zeolites.[45]

Zeolites are highly stable with uniformity in the pore size even after activation and, as a consequence these structures have been deemed as good molecular sieves for sorption applications and other applications such as catalysis[48] and adsorption and separation.[48-50] Nevertheless, a few disadvantages have been noted. For instance, using zeolite 13X in the presence of moisture prevented VOCs from being absorbed.[51] Other limitations include, (i) they have a high susceptibility to be deactivated by steric obstruction of heavy secondary

products or irreversible adsorption, (ii) the impossibility of synthesizing large molecules using their microporosity.[52]

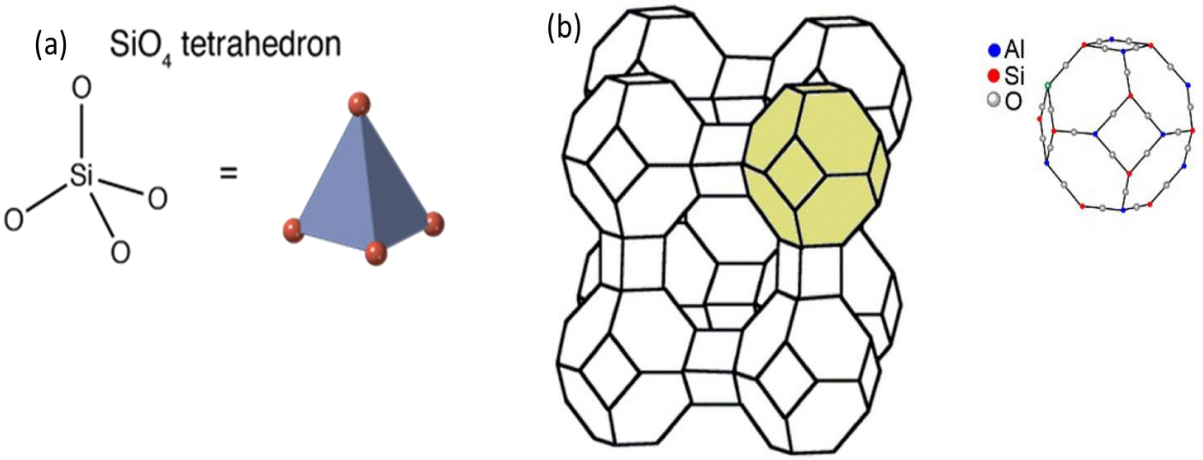


**Figure 1.2.** (a) Illustrated the building block of zeolites as tetrahedra corner-sharing $TO_4$ (T= Al, Si), (b) is a particular structure of a zeolite. *Figure reprinted (adapted) with permission from Verdoliva V, Saviano M, De Luca S. Zeolites as Acid/Basic Solid Catalysts: Recent Synthetic Developments. Catalysts. 2019; **9**(3):248. Copyright (2019) Catalyst.* [53]

### 1.3.2. Activated Carbon

Activated carbon is usually made from crude material such as wood, coal and other material by burning these materials with steam, $CO_2$ and acids at high temperatures in a process known as carbonisation.[54,55] It has strong adsorption cavities and high surface area for gases, unlike zeolites which have low affinity for guest molecules that allows for easy release of guests.[56,57] These materials have their own disadvantages. Activated carbons have variable cavity sizes, defective hexagonal carbon layers, twisted networks, require very high temperature reaction and lastly, their function is limited by moisture and non-homogeneity (**Figure 1.3**).[54,58,59]

Zeolites and activated carbons have strong Si-O and C-C bonds which makes them highly thermally stable. However, their synthesis remains challenging for the production of new structures with topologies which can surpass the existing ones.

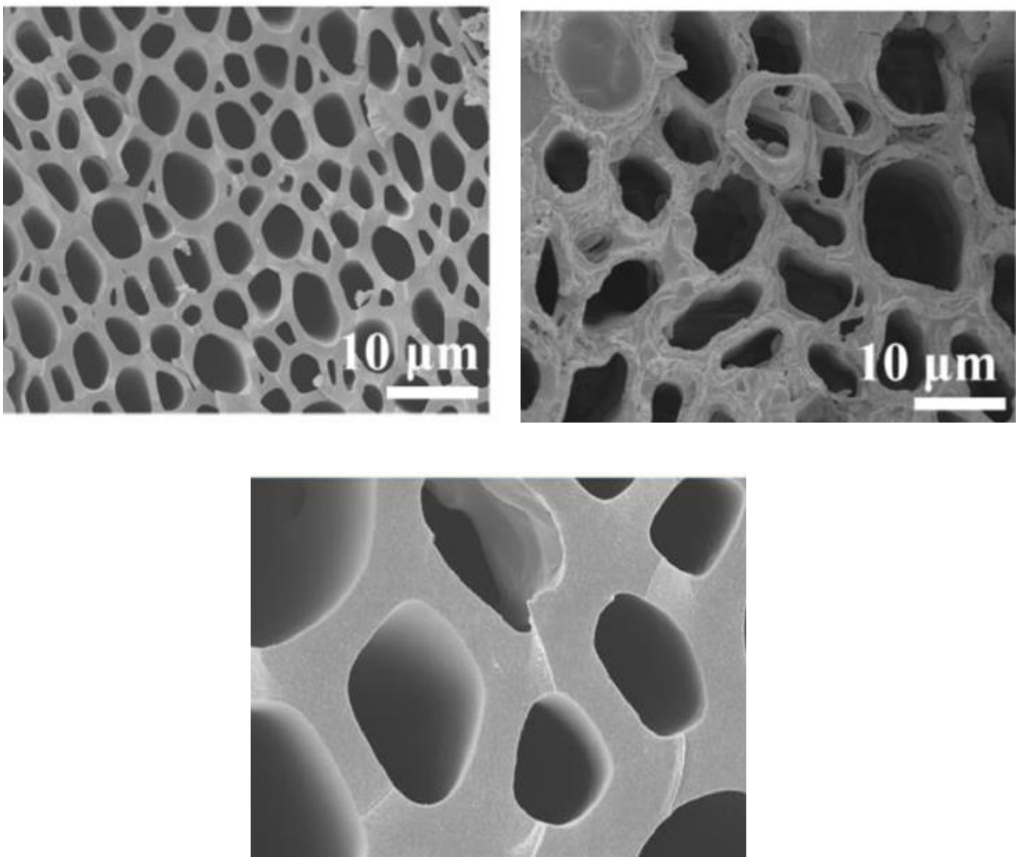


**Figure 1.3.** SEM and TEM images of activated carbon. *Figure reprinted (adapted) with permission from Tan Y, Li Y, Wang W, Ran F. High performance electrode of few-layer-carbon@ bulk-carbon synthesized via controlling diffusion depth from liquid phase to solid phase for supercapacitors. Journal of Energy Storage, 2020, 32, p.101672. Copyright (2020) Elsevier* [60]

As a result of these flaws in zeolites and activated carbons, i.e., (i) high susceptibility to be deactivated by steric obstruction, (ii) impossibility of synthesizing large molecules using their microporosity, (iii) variable cavity sizes and (iv) requirement of very high temperatures of reaction, considerable amount of attention has been given to new class of porous material, metal-organic frameworks.

### 1.3.3. Metal-Organic Frameworks (MOFs)

#### 1.3.3.1. Historical Background

One of the most fascinating advancements in porous materials science over the past 20 years has been the development of metal-organic frameworks (MOFs).[61,62] The versatility in synthesis,[63] their ability to host guest molecules or ions due to their enormous pore sizes is one of their primary, interesting qualities, and it results in one of their distinctive properties that offer a wide range of applications.

Hoskins and Robson in 1990, presented a new type of porous material comprising of a wide extension of infinite 3-dimensional scaffold-like systems that are easily tunable and accessible.[62,64] Unlike its counter-parts zeolites and activated carbons, the synthesis occurs under mild conditions, the framework can be made based on selected molecular units (cavities can be increased or decreased based on ligand spacer length), the surface areas are wider and accessible and most of all the frameworks are thermally stable and mostly of low density.[65-70]

Five years later, after Robson's initial report on this new type of porous material, Yaghi *et al*. demonstrated the synthesis of a 3D crystalline framework under hydrothermal/solvothermal synthesis containing a pyridine-based ligand with open cavities.[71] Later on, another 3D framework with the same method and ligand but a different counterion was constructed to store methane gas at room temperature.[72] Kitagawa also demonstrated the use of a 3D MOF for gas storage. He demonstrated that these frameworks can be constructed by combining different connectors such as clusters / metal nodes and organic linkers to produce a wide range of structures.[74]

Numerous uses are made possible by this characteristic, including gas and liquid storage.[23,24,74,75] They have also been employed in the sorption studies of solvents as well as the separation of gas mixtures.[76-80]

MOFs also have potential to be used as heterogeneous catalysts and have relatively recently become commercially available.[81] The tunable, percolative coordination crystals offer the precise nanospace for coordination, high surface areas, diversity in metal and functional groups that make them highly appropriate to be used as catalysts.[82-86] MOFs also serve as drug delivery systems for potential medicinal applications, which is another crucial role.[86] Following administration, medication concentration levels should guarantee optimal effectiveness without producing negative side-effects. MOFs have also demonstrated excellent potential for use in biological photoluminescence imaging and sensing.[88]

### 1.3.3.2. MOF Definitions, Terminology and Nomenclature

The construction of MOFs' interesting structures involves the self-assembly of organic ligands as "linkers" and metal ion or metal-ion clusters as "nodes" (**Figure 1.4a**). This creates a network of systematic structures of infinite coordination in one-, two-, or three- dimensions of very high pore volumes and surface areas (**Figure 1.4b**).[67] The distinction between a coordination polymer and a metal-organic framework has been hotly debated. In an article released in 2008 in the journal Dalton Transaction's, [89] Richard Robson wrote:

"The MOF terminology is unnecessarily restrictive: why should we set aside as a special category called MOFs, those coordination polymers that happen to make use of organic bridging ligands (or some even more narrowly defined sub-group thereof) and relegate networks formed from perfectly respectable "inorganic" bridging species to some limbo?"

The assertion that metal-organic frameworks are simply coordination polymers is evident from Robson's reasoning, and that this group of molecules does not require special classification. The International Union of Pure and Applied Chemistry (IUPAC) task group on Coordination Polymers and MOFs was established in 2009 due to the various terminology that was used to define this class of chemicals. In regular communication with experts in the field, this group has analysed, documented, and evaluated the strategies that are now in use. The Journal of Pure Applied Chemistry published the IUPAC nomenclature recommendations in 2013. [90-91]

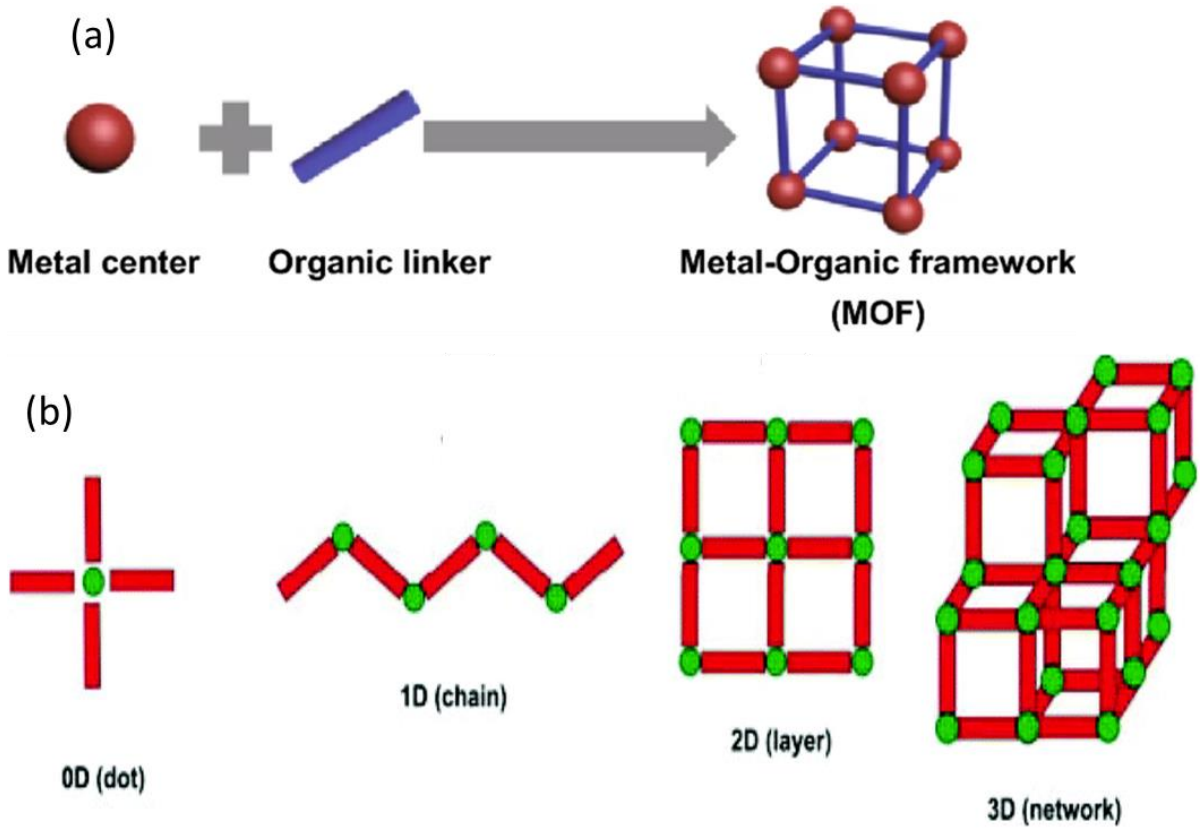


**Figure 1.4.** (a)Schematic illustration of a metal-organic framework consisting of a metal ion or clusters as ‘‘nodes’’ and organic ligands as bridging “linkers”.[95] (b) Schematic representation of MOFs/CPs with different dimensionalities (0D, 1D, 2D and 3D) from the same PBUs. *Figure reprinted (adapted) with permission from Mendes R.F, F. Paz A.A, Transforming metal–organic frameworks into functional materials, Inorg. Chem. Front., 2015, 2, 495-509. Copyright (2015) Royal Society of Chemistry.* [93]

The term "coordination polymer" (CP) refers to polymers constructed from extended connections or periodic architectures of metal and ligand linker coordinated via bonds.[93,94] It should be mentioned that these substances do not always have to be crystalline. This class of compounds has also been referred to as coordination networks which are compounds that extend through repeated coordination entities but cross link between two or more different chains. It is advised to use a hierarchical language, with coordination polymer serving as the most generic term and coordination networks serving as a subset of coordination polymers.[94]

In coordination polymers, the ligands are required to be polytopic, which means that they bridge many metal centres to form infinite arrays of coordinated units, as an infinite repeat of a specific atom group with a variety of tunable features.[96] This supports their inclusion in the field of crystal engineering.

Earlier definitions, which required that a MOF should only be applied to ligands with carboxylates.[90-91] Some earlier definitions of MOF are (i) described them as "a network with frames",[97] (ii) structures "which exhibit porosity",[98] this was problematic for those who only investigate magnetic or, luminescence properties or, sensing properties. As a result, a proper definition by IUPAC task group was made; A coordination network with organic ligands that may have voids is referred to as a metal organic framework, or MOF, in accordance with IUPAC recommendations.[93]

As a result, MOFs are a subclass of coordination polymers due to the additional condition that a MOF have a coordination network with possible voids. i.e., a coordination polymer it is not necessarily a MOF, but a MOF is always a coordination polymer.[93,99]

Unlike discrete inorganic complexes, which have a technical report from the IUPAC,[91] MOFs lack an IUPAC-endorsed nomenclature system, perhaps as a result of the complexity and rich diversity of MOF structures. The Coordination Polymers and Metal Organic Frameworks: Terminology and Nomenclature Guidelines task group, however, did concur that IUPAC-endorsed names in "flowing text will be cumbersome (although essential to include)"[93] and supported the currently accepted convention of naming MOFs using their country or the town of origin followed by a number. For instance, HKUST-1, MIL-101, and NOTT-112 were created at the University of Nottingham, the Matériaux de l'Institut Lavoisier, and the Hong Kong University of Science & Technology, respectively.[93] Probably, due to having the forerunners in MOF research, Omar Yaghi's team simply referred to their metal-organic frameworks as "MOF" or "IRMOF" followed by a number, for example, MOF-5.[100]

### 1.3.3.3. Network Topology

The study of three-dimensional relationships and shapes, or the placement of distinct components within a whole, is known as topology.[101] The description of MOF crystal structures is improved by topology. While analysing and creating MOFs, network topology is a key factor. This kind of research sheds light on a structure's underlying network. Crystal lattices that are complex can be reduced to equivalent sets of nodes and rods.[93,99] A node can take the place of a metal centre, a metal cluster centre, or the centroid of a ligand, such as the centre of the aromatic ring of the trimesic acid ligand.[102] Then, in accordance with the framework structure, rods, which are frequently aligned with the axis of a ligand, connect nodes to one another to form a motif. The MOF's general structure is then condensed to resemble a scaffolding, which more clearly displays the topology of the MOF and can be utilized to improve the framework's description.[93]

The main reason for the introduction of network topology or topology in metal-organic frameworks is to be able to differentiate between frameworks i.e., a development of the idea of stereoisomers like *E, Z*, or cis, trans and fac, mer.[93] For example (**Figure 1.5**), a 4-connected network has a number of topologies thus being the diamond (dia), quartz (qtz) or any other topology, this serves as evidence for the need of topology descriptors.[93]

To assist in the system of nomenclature using topology, a database designed to facilitate reticular chemistry called the Reticular Chemistry Structure Resource (RCSR) database was made.[103] This database hosts a number of designed topologies such as square lattice (**sql**), primitive cubic (**pcu**), twisted boracite (**tbo**), diamond (**dia**) and some nets were also contributed by the works of V. A. Blatov.[104] There is another database, that also focus on topologies of underlying nets called TOPOS Topological Databases (TTD).[105] In a 2014 survey of entangled, two-dimensional coordination networks, Carlucci, Proserpio, and Blatov found that the square lattice motif (**sql**) topology was the most frequent 2D motif among the 75 000 net topologies in the TOPOS TTD collection, with the honeycomb motif (**hcb**) topology appearing second most frequently.[106]

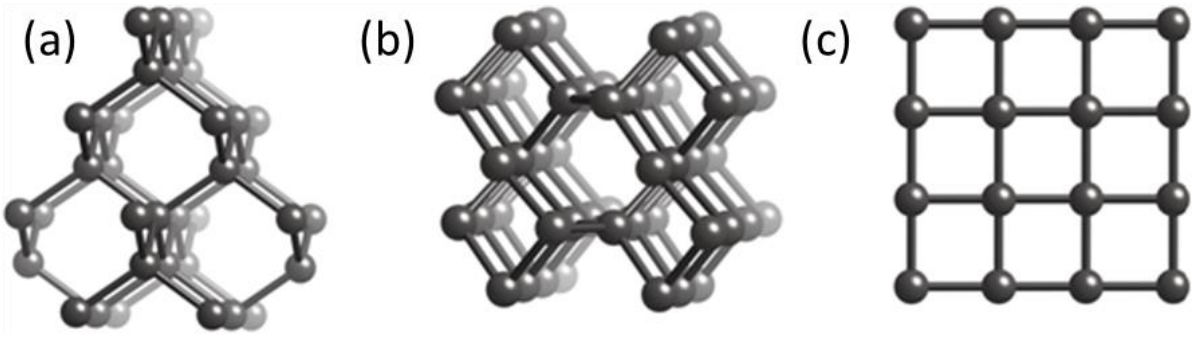


**Figure 1.5.** a-c illustrates the need to know the topologies of 4-connected network. (a) The **dia**-network based on the diamond structure; (b) The chiral **qtz**-network based on the quartz structure; (c) The **sql**-network 2D. *Figure reprinted (adapted) with permission from Batten S.R, Champness N.R, Chen X, Garcia-martinez J, S. Kitagawa, Ohrstrom L, Keeffe M.O, Suh M.P, and Reedijk J., Pure Appl. Chern., 2013, 85, 1715-1724. Copyright (2013) Pure and Applied Chemistry* [92]

### 1.3.3.4. Dimensionality and Periodicity

It is known that coordination polymers with different structural motifs in 1D, 2D, and 3D exist.[107] Out of all these simple chains make up one-dimensional (1D) coordination polymers, which are simple to self-assemble. This makes it relatively simple to incorporate various functional features at the metal centres or in the core of the organic linkers.[108,110] Depending on the conformations of the ligands and the coordination environment of the metal ions under particular circumstances, architectures like linear, ladder, ribbon, zigzag, and helical structures are feasible (**Figure 1.6**).[110]

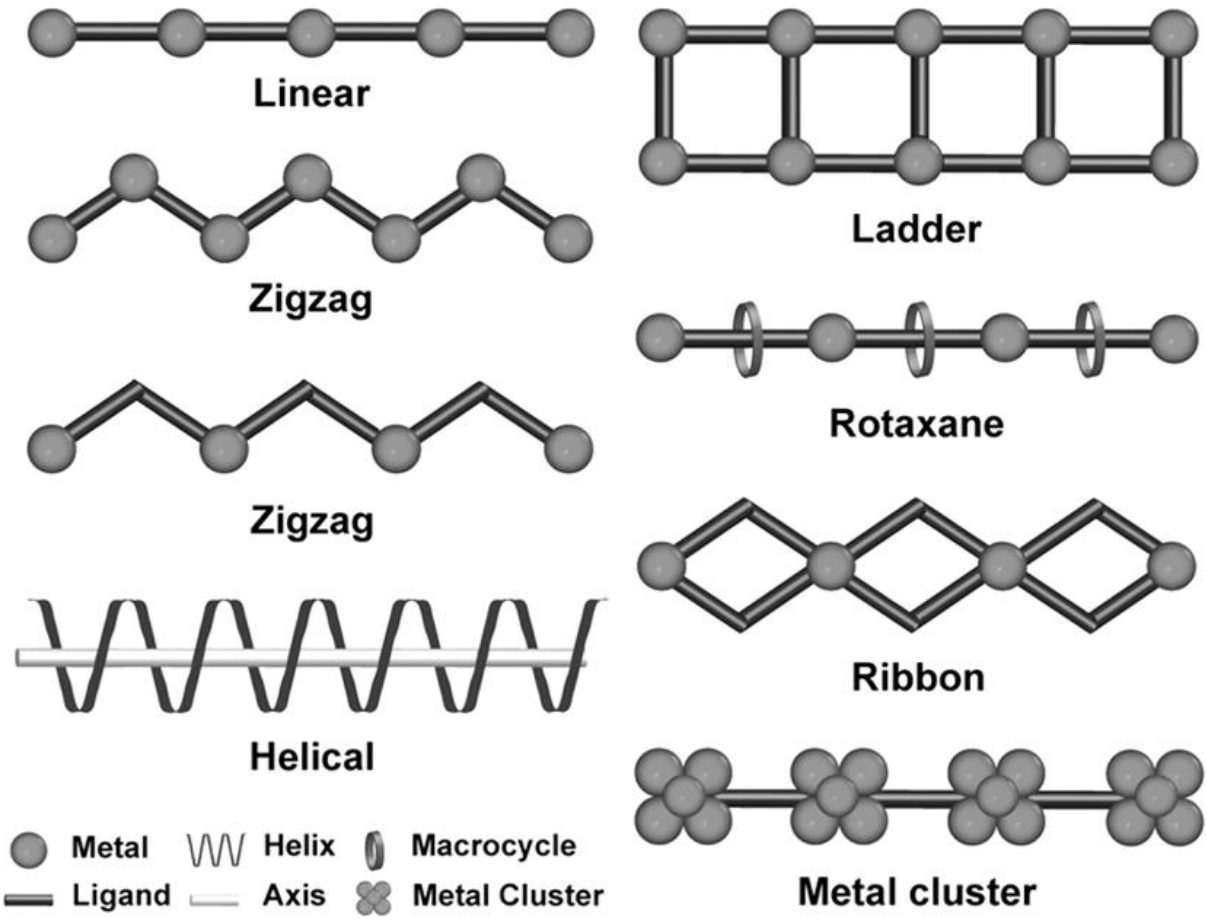


**Figure 1.6.** The diversity of 1D coordination polymers is demonstrated by a variety of geometrical conformations. *Figure reprinted (adapted) with permission from Leong W. L., Vittal J. J., Chem. Rev. 2011, 111, 688–764. Copyright (2011) American Chemical Society.* [110]

It is clear that a 2D framework's topology is influenced by a variety of variables, including the ligand to metal ion ratio, the preferred metal coordination geometries, and the chemical composition of the coordination ligands.[109] For instance, the 1:2 ratio of transition metal ions to linear bifunctional ligands has produced a large number of square grid 2D frameworks.[109] There have also been reports of rhombic, rectangular, herringbone, brick wall, honeycomb, and bilayer topologies (**Figure 1.7a**).

3D polymers are produced when ligand connectors are extended in all three dimensions (**Figure 1.7b**). A wide range of 3D MOFs are now possible thanks to various connector and linker configurations.[107] 3D polymers have a wide range of practical uses in gas sorption and separation because of their excellent stability and porosity. Anionic ligands are typically used in the syntheses of these polymers to account for the charge of the metal ions. The creation of more rigid 3D frameworks through the use of multidentate linkers, such as carboxylates, which are capable of gathering metal ions into M-O-C clusters, also known as secondary building units (SBUs).[65]

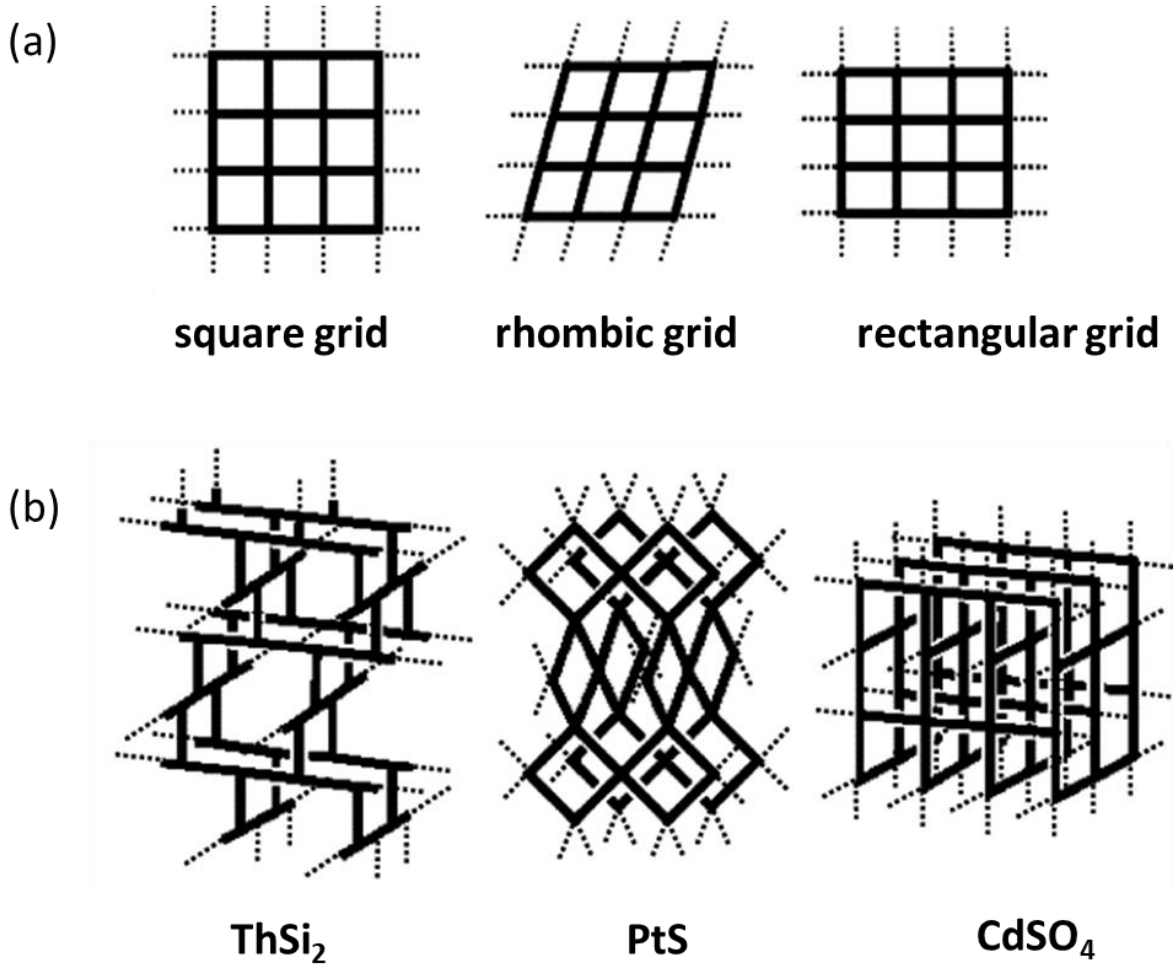


**Figure 1.7.** The diversity (a) 2D and (b) 3D coordination polymer. *Figure reprinted (adapted) with permission from Adeline Y. Robin,Katharina M. Fromm. Coordination Chemistry Reviews. 2006, 250, 2127-2157. Copyright (2006) Elsevier.* [109]

Delgado-Friedrichs *et al*., 2005 observed that there is a difference in periodicity and dimensionality in metal-organic frameworks.[111] When the edges in the repetition unit (basic cell) are specified, the topology of a periodic net is fully known.[112] Carlucci, Proserpio, and Blatov distinguished between dimensionality and periodicity in metal-organic frameworks in a review from 2014. [106] In this overview, two- and three-dimensional (2D and 3D) nets are distinguished from 2- and 3-periodic nets. While 2D nets are categorized as nets with no finite coordination in the third dimension and 3D nets are nets with a finite coordination in the third dimension that offer the layer a measure of "thickness," (**Figure 1.8**) Carlucci, Proserpio, and Blatov refer to 2- and 3-periodic nets as having infinite coordination in 2 and 3 dimensions, respectively.

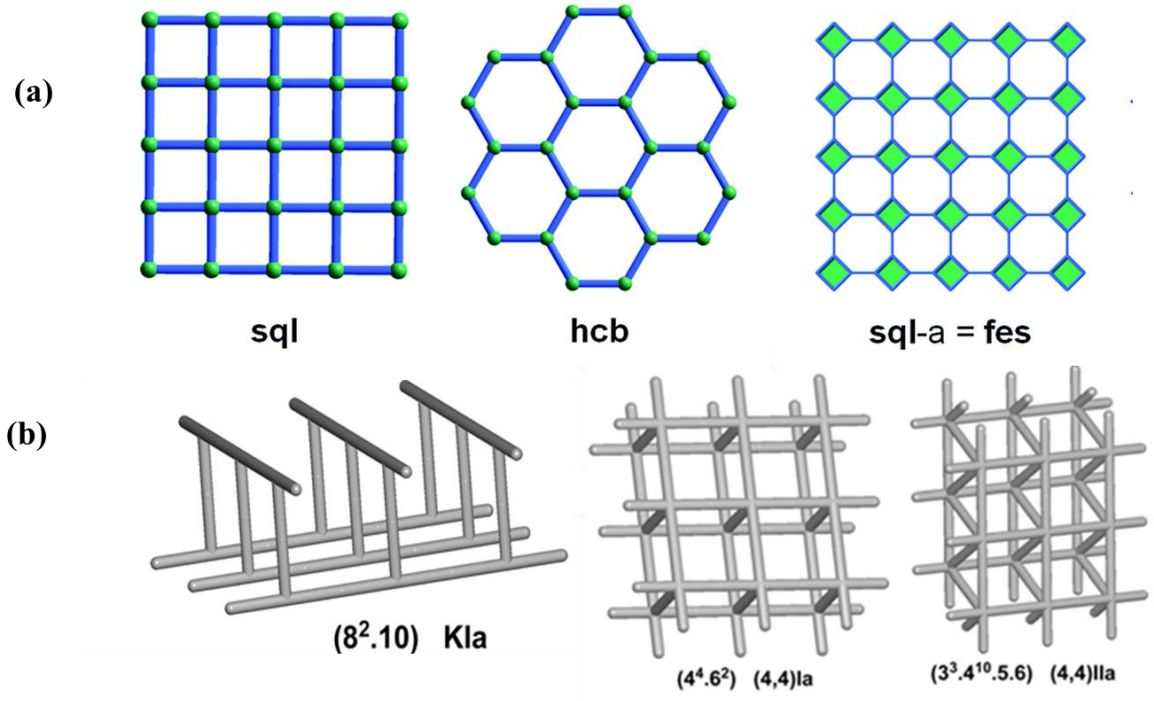


**Figure 1.8.** (a) Three illustrations of two-periodic, two-dimensional (2D) nets that represent unlimited extension in two dimensions and (b) two-periodic, three-dimensional (3D) nets that represent infinite extension in two dimensions and finite coordination in the third dimension, or "thickness of the layer," are shown. *Figure reprinted (adapted) with permission from Carlucci L, Ciani G, Proserpio D.M, Mitina T.G, Blatov V.A. Chem. Rev. 2014, 114(15), 7557–7580. Copyright (2014) American Chemical Society.* [106]

### 1.3.3.4. Synthesis of MOFs

Each year, new frameworks are produced as a result of the optimization of variables such the molar ratios of the reactants (starting materials), pH, solvent amounts/ratios, and types, as well as reaction duration, temperature, and pressure.[113] Evidently, varied circumstances and synthetic techniques can produce a range of intriguing structures utilizing the same ligands and metal ions.[114,115] The traditional solvothermal techniques of MOF synthesis, involve mixing the components at room temperature, heating for 12 to 48 hours, and then cooling to room temperature. Although the aforementioned methods often produce high-quality crystalline materials, they have lengthy reaction durations and can be challenging to scale up above 1 g, particularly when using costly high boiling point solvents like diethylformamide (DEF).[116]

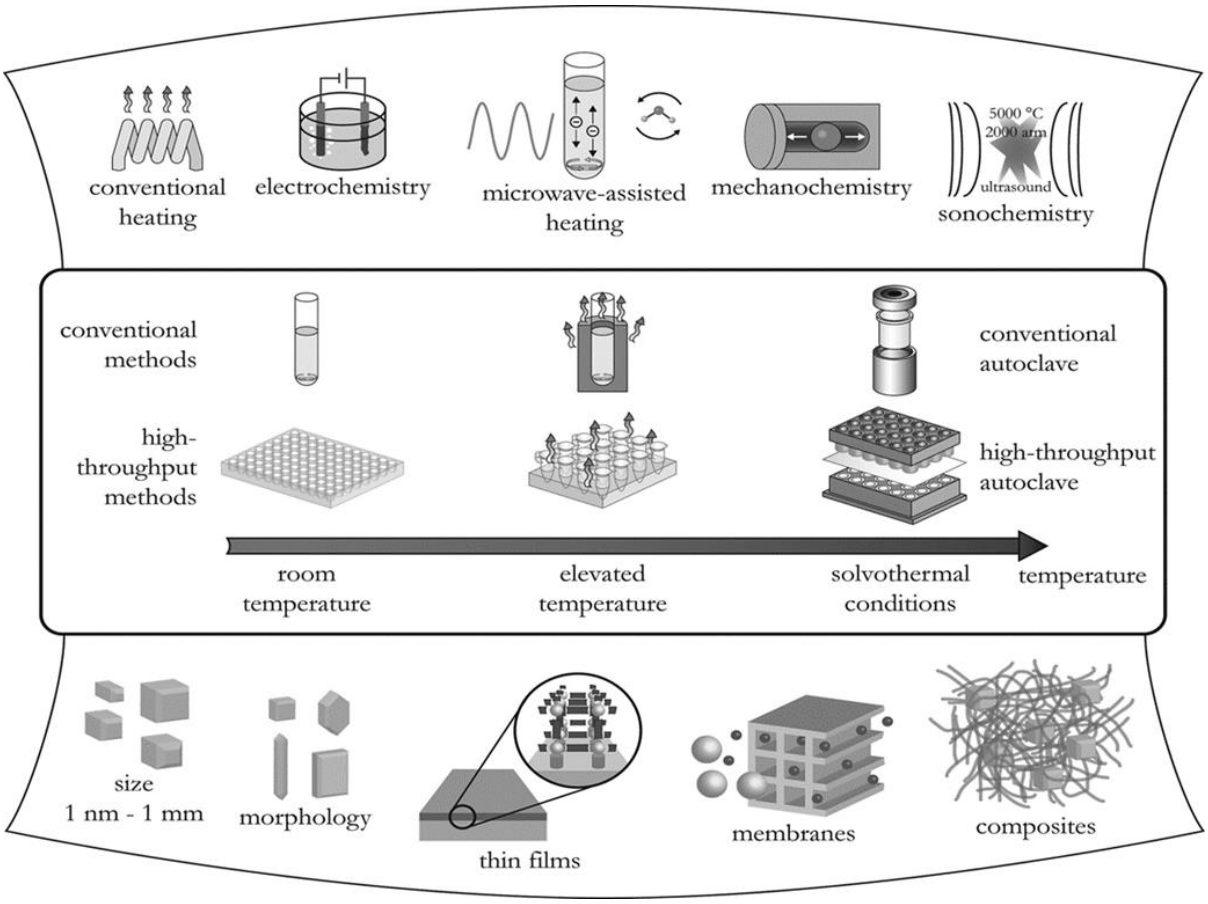


**Figure 1.9.** Overview of MOF synthesis procedures, potential reaction temperatures, and reaction outcomes. *Figure reprinted (adapted) with permission from Stock N, Biswas S. Chem. Rev. 2012, 112, 2, 933–969. Copyright (2012) American Chemical Society.* [115]

Alternative synthesis pathways, which require less solvent and have quick reaction times, have recently been reported (**Figure 1.9**). These include microwave, sonochemical, and mechanochemical approaches.[115,117] Solvents like *N*, *N*-dimethylformamide or water are used in solvothermal or hydrothermal synthesis, respectively. At high temperatures, these solvents can also function as reagents to deprotonate carboxylic acid groups of ligands. When the reactions occur in closed vessels under autogenous pressure the reaction temperatures of the solution may exceed the boiling point of the solutions at standard pressure.[118]

### 1.3.3.5. Secondary Building Units

The "secondary-building-unit" (SBU) concept was developed by Yaghi *et al.*[120] It allows MOF design to be justified by isolating directed metal-oxygen-carbon clusters and treating them as SBUs from which the structure is built. Given that the carbon and oxygen atoms are both defined as organic components and as a part of the SBU (**Figure 1.10**), the flexibility of the remaining organic ligand was the rational design feature of this approach. This results in

structures with the same network architecture but different SBU distances (which affect pore size). With MOF-2 and MOF-5 among the first examples, Yaghi *et al*. showed that this method works for a variety of structures.[119,120]

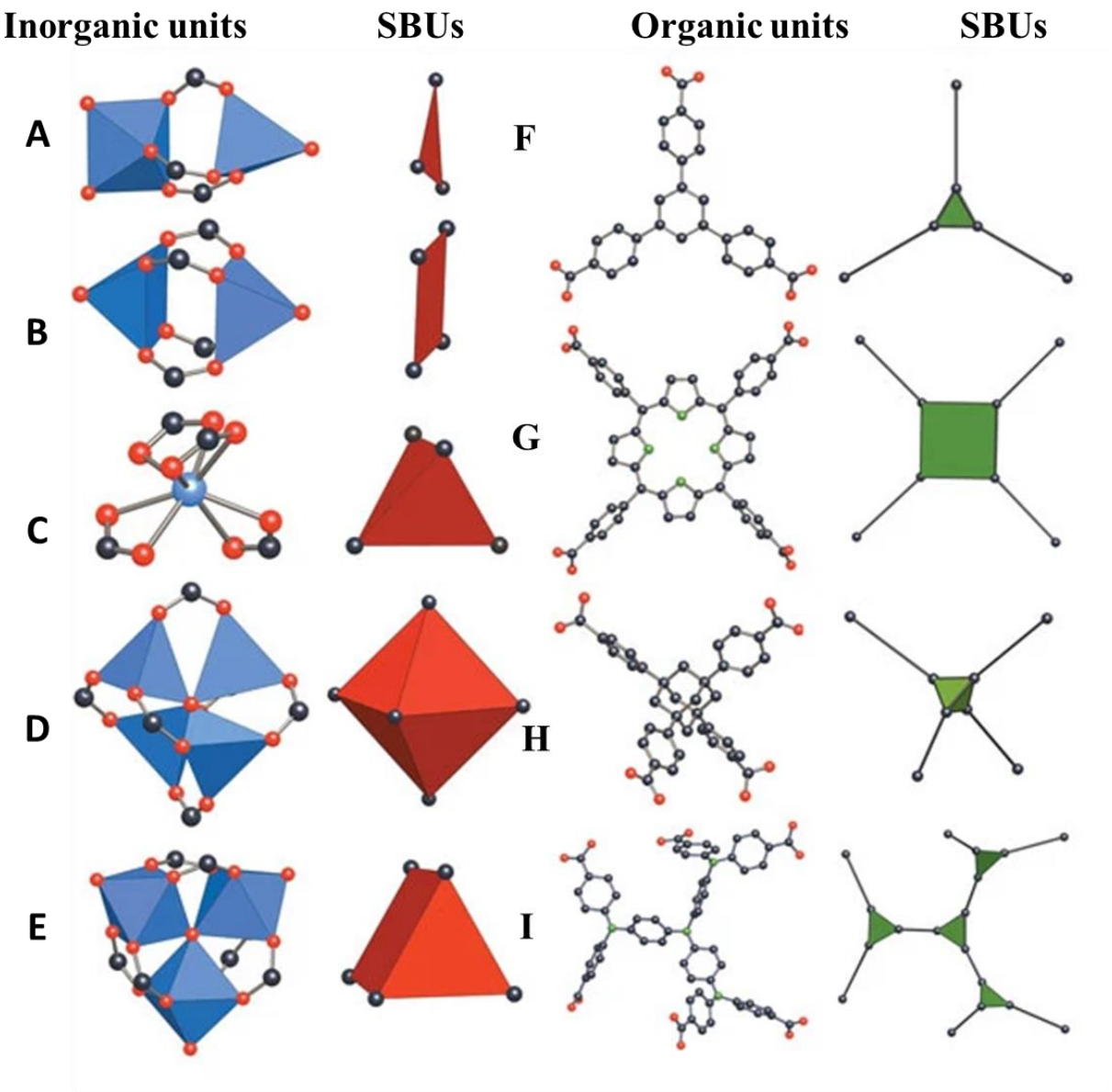


**Figure 1.10.** The polygon or polyhedron defined by carboxylate carbon atoms (SBUs) is red in inorganic units, while metal-oxygen polyhedra are blue. The polygons or polyhedrons in orgaic SBUs that linkers (all of the -C6H4- units in these cases) are linked to are depicted in green. *Figure reprinted (adapted) with permission from Yaghi M.O, O'Keeffe M, Ockwig N.W, Chae H.K, Eddaoudi M, and Kim J. Nature. 2003, 423, 705–714. Copyright (2003) Macmillan Magazines Ltd.*[120]

### 1.3.3.6. Reticular Synthesis

Developing methods to create MOFs with particular features is quite interesting. Reticular synthesis is a successful synthetic approach that entails the creation of materials with a certain geometry.[120,121] In order to create materials with specific architectures and properties, this approach leads to the synthesis of a desired network depending on the selection of secondary building units. Structures are isoreticular if they share the same topological net.[122] These MOFs are known as isoreticular MOFs or IRMOFs. IRMOFs allow systematic investigations to be done into structure property relationships of MOFs with respect to pore size and chemical functionality (**Figure 1.11**).[121]

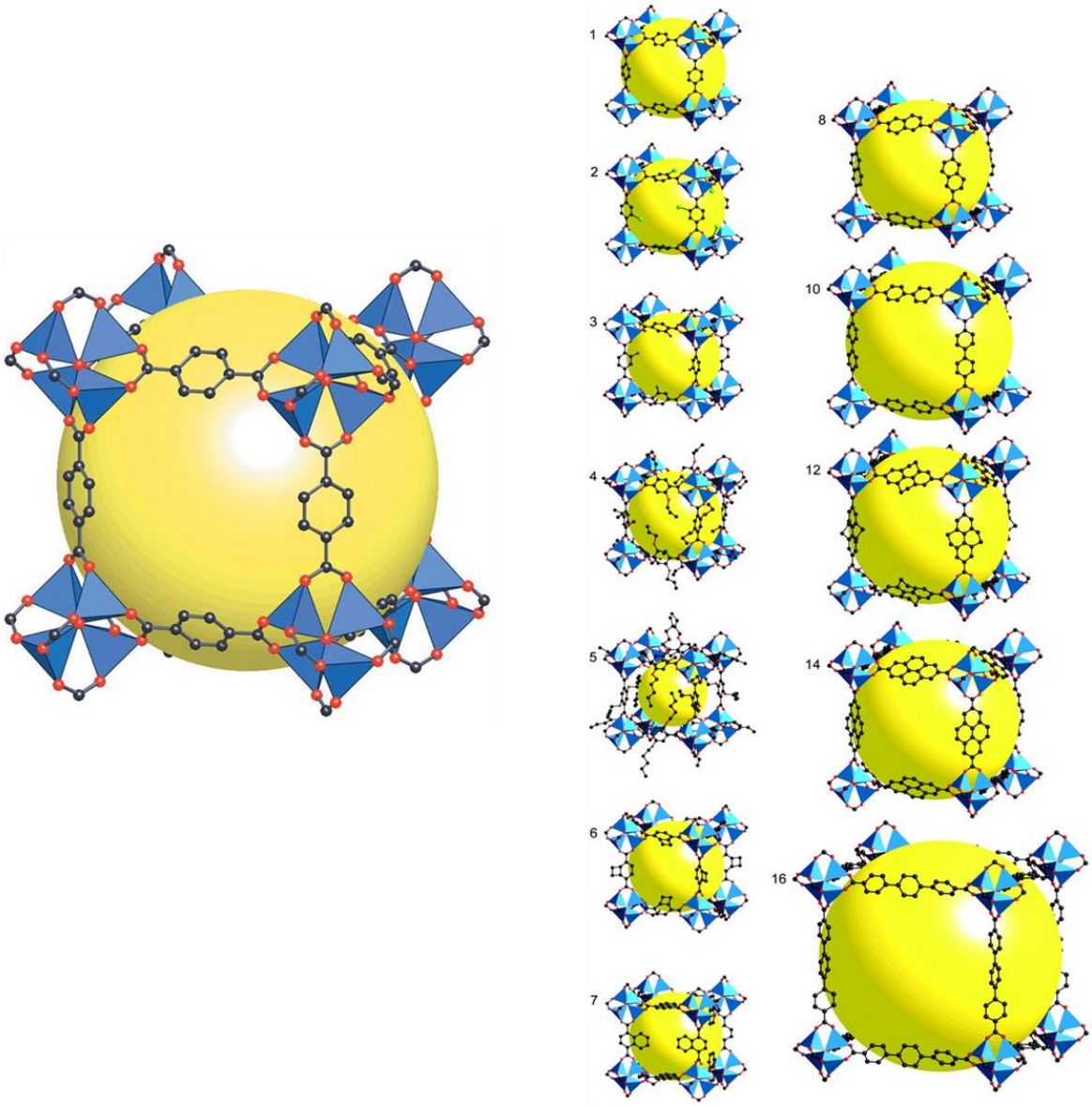


**Figure 1.11.** IRMOFs in an isoreticular series with different spacers. Each time, a sizable yellow sphere serves as a visual cue to the relative cavity size of MOF. *Figure reprinted (adapted) with permission from Eddaoudi M, Kim J, Rosi N, Vodak D, Wachter J, O'Keeffe M, Yaghi O.M, Science 2002, 295, 469-472. Copyright (2002) Science.*[121]

### 1.4. Entanglement of MOFs

Entanglement in MOFs refers to when numerous networks within the same crystal structure cannot be removed one from the other without breaking chemical bonds. This has a significant impact on the porous nature, structure, and functional applications of MOFs.[123] As it happens, the foremost regularly encountered sorts of entanglement ought to be interpenetration and polycatenation.

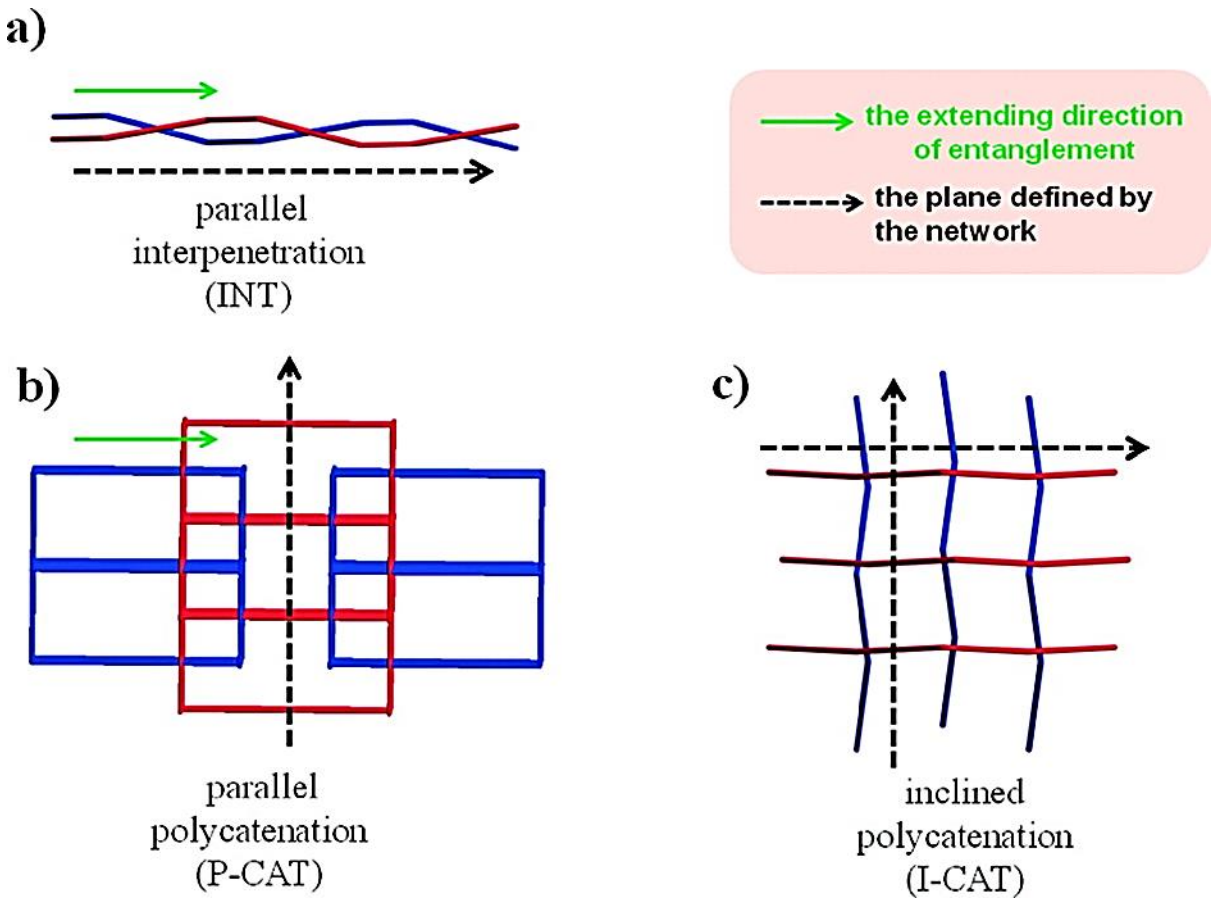


**Figure 1.12.** In terms of how distinct motifs are oriented and the direction in which entanglement extends, INT, P-CAT, and I-CAT differ from one other: Interpenetration (INT), Parallel Polycatenation (P-CAT), and Inclinated Polycatenation (I-CAT) are the three processes. *Figure reprinted (adapted) with permission from Mei L., Shi W.Q-, and Chai Z.F-, Bull. Chem. Soc. Jpn. 2018, 91, 554–562. Copyright (2018) The Chemical Society of Japan.*[124]

The focus within the early stages was to acquire materials with as large surface areas as possible. So, interpenetration was deemed as disadvantageous due to decreased pore volume and increase in surface areas per unit volume. But presently its significance has been appreciated.[99,125,126] In spite of the fact that they were thought to be disadvantageous, they more often than not have a few advantages, such as the stability of the framework due to supramolecular interactions, hydrogen bonding, π–π stacking interactions, van der Waals forces and the degree of flexibility of the overall systems.[123,127]

Interpenetration occurs between identical networks or of different networks; each network is completely entangled by all the other frameworks and the dimensionality of the resultant structure is the same as that of the individual network. The extent of interpenetration is measured by the number of nets that are linked to each other (**Figure 1.12.1**). In contrast, polycatenation does not require identical networks, each network is only entangled by the surrounding ones (i.e., not by all in the structure) and the dimensionality of the resulting structure is higher than that of the individual networks.[123]

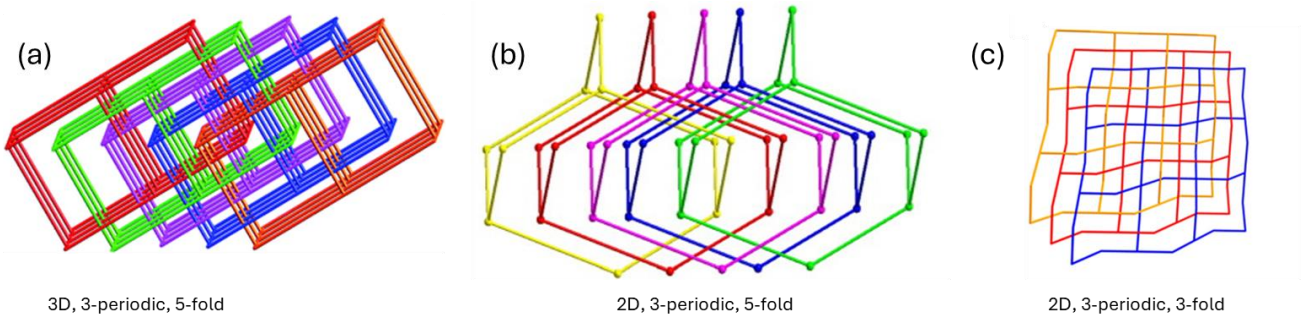


**Figure 1.12.1**: Examples of MOFs described in terms of dimensionality, periodicity and fold (extent of interpenetration).

There are several interpenetrated structures dimensions detailed so far, 0D- Polycatenanes, 1D- Parallel or inclined, 2D- Parallel or inclined and 3D- Different topologies are possible.[123,127] The conditions of interpenetration between 1D chains are that the discrete chains must contain rings. Also, different weak supramolecular forces (H-bonding, π–π aromatic stacking interactions, and van der Waals forces) are suspected to play imperative parts within the arrangement of interpenetrated structures. Interpenetration between 1D chains containing rings and rods for the most part very similar to that of catenanes or rotaxanes.[123,127]

Comparable to that of 1D chains, interpenetration between 2D layers also exhibits two types: parallel and inclined. The larger part of interpenetrated 2D systems is fundamentally based on either sql or hcb topological nets.[125] Compared to 1D and 2D MOFs with lower dimensionality, interpenetration in 3D MOFs is more prevalent. For the most part, MOFs built with longer ligands ordinarily have bigger voids, which make them unstable. Hence, interpenetration sensibly happens to minimize pore space to meet the efficient stability prerequisite in MOFs.[125]

## 1.5. Experimental Factors That Influence The Formation Of Interpenetration

### 1.5.1. Reaction Temperature and Concentration

Higher temperature generally appeared to favour increased degrees of interpenetration. This can be attributed to the increase in kinetics- when faster crystal development occurs, this

increases the possibility of interpenetrated MOFs.[128] For this reason, high concentration of reagent is additionally related with increased interpenetration. In **Figure 1.13** these two effects of temperature and concentration are shown clearly by Zhang *et al.* with the reaction of 4,4′-bipyridine (bipy), 1,4-benzenedicarboxylic acid (bdc), and $Cd(NO_3)_2 \cdot 4H_2O$.[128]

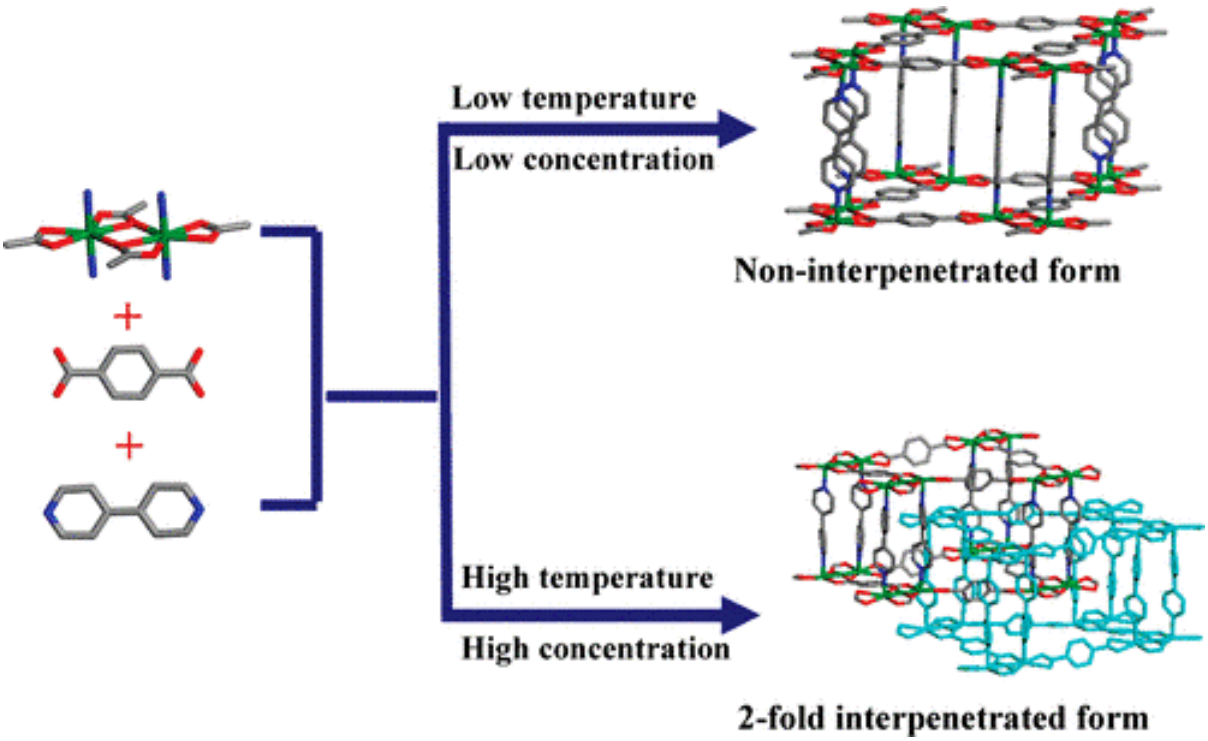


**Figure 1.13.** Control of degrees of interpenetration using [Cd(bipy)(bdc)], by examining the impact of temperature and concentration on the interpenetrated and non-interpenetrated form. *Figure reprinted (adapted) with permission from Zhang, J, Wojtas, L, Larsen, R. W, Eddaoudi, M.; Zaworotko, M. J. Temperature and Concentration Control over Interpenetration in a Metal–Organic Material. J. Am. Chem. Soc. 2009, 131, 17040– 17041. Copyright (2009) American Chemical Society.*[128]

A study that makes a contribution to this is by Aggarwal *et al.* (**Figure 1.14**) where a doubly interpenetrated framework and a triply interpenetrated isomeric form were formed by increasing the reaction temperature of crystallization when reacting 4,4′-bpy = 4,4′-bipyridine, ndc = 2,6-naphthalenedicarboxylate and Cd (salt).[129]

By adjusting the temperature and concentration, the authors were able to systematically adjust the level of interpenetration. They verified that high temperature and concentration influenced the formation of interpenetrated crystal, whereas low temperature and concentration favoured its non-interpenetrated form. The idea behind this was that higher temperatures would have a thermodynamic effect that would result in denser, more stable products.

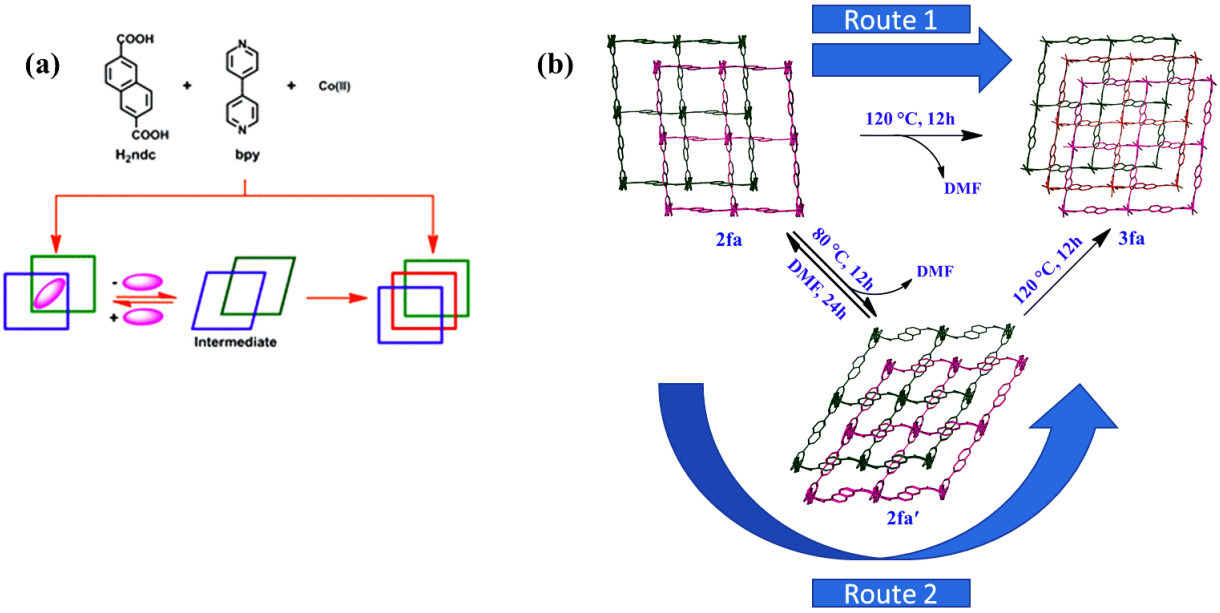


**Figure 1.14.** Diagram illustrating the $[Co_2(ndc)_2(bpy)]$ system's interpenetration bending and switching through increased the reaction temperature of crystallization. *Figure reprinted (adapted) with permission from Aggarwal H, Das RK, Bhatt PM, Barbour LJ. Isolation of a structural intermediate during switching of degree of interpenetration in a metal–organic framework. Chem Sci., 2015, 6:4986–4992. Copyright (2015) The Royal Society of Chemistry.*[129]

### 1.5.2. Solvent System

The size of the solvent molecules plays an imperative role in determining the degree of interpenetration. [131] While the smaller guests produce higher degree of interpenetration, the large template molecules typically result in a lesser degree of interpenetration or non-interpenetrated MOFs (**Figure 1.15**).[130]

The utilization of bulkier solvents such as tert-butylformamide causes channels to be wider and a lowers degree of interpenetration in the synthesized MOFs, this can be observed in the work of Elsaidi *et al.*[131] This is often likely due to intermolecular forces and steric hindrances between bulky solvents constituents and forming crystal lattices.[130] This impact is less apparent with less bulky solvents such as ethyl alcohol, which have shown smaller channels and higher degrees of interpenetration.[131]

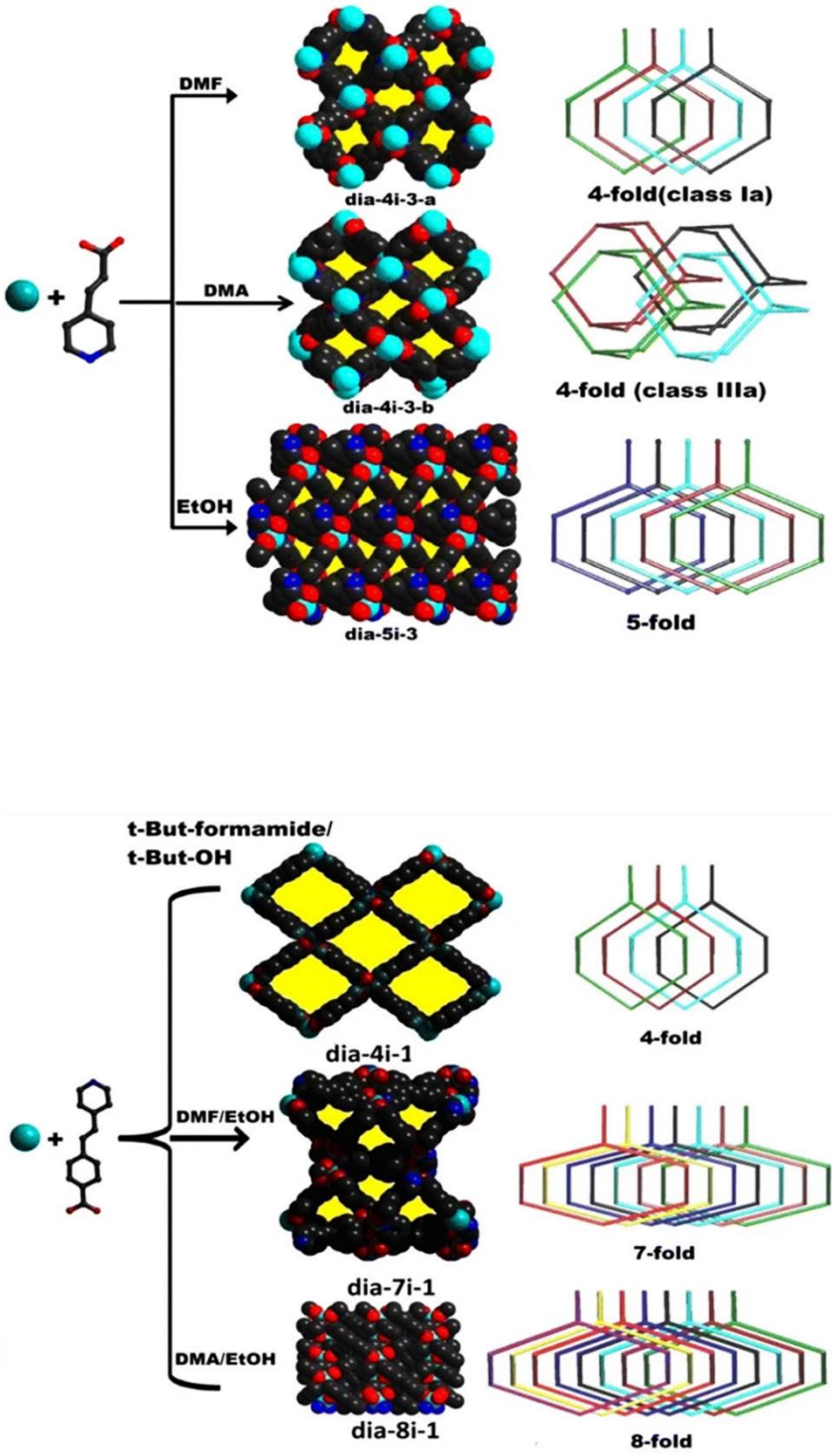


**Figure 1.15.** Solvent templating provides a picture of the control over the interpenetration level in dia nets. *Figure reprinted (adapted) with permission from S.K. Elsaidi, M.H. Mohamed, L. Wojtas, A. Chanthapally, T. Pham, B. Space, J.J. Vittal, M.J. Zaworotko, J Am Chem Soc, 2014, 136,5072–5077. Copyright (2014) American Chemical Society.*[131]

Additionally, Ferguson *et al*. thoroughly investigated how solvents affected the occurrence of partial interpenetration. They postulated that in order to construct a partially interpenetrated framework, the growth rate of the host-sublattice must be greater than that of the

interpenetrating sub-lattice.[132] The interpenetrating sub-lattice forms significantly more slowly in bulkier solvents, allowing for the accumulation of partially interpenetrated crystals.[132]

MUF-9 and MUF-10 partially interpenetrated forms were extracted from a solvent system consisting of *N*,*N*'-dibutylformamide (DBF) and N,N-dimethylformamide (DMF) during synthesis. These authors were able to systematically tweak and regulate the level of partial interpenetration by increasing the growth of the sub-lattice by mixing DMF to DBF.[132]

### 1.5.3. Time

Interpenetration can be significantly impacted by the reaction time of the MOF synthesis.[130] Decreased interpenetration results in larger pores, which are linked to shorter synthesis reaction times.[132] The likelihood of an interpenetrated net forming is directly constrained by decreased reaction time. Interpenetration is favourable thermodynamically since it reduces the energy of the system by reducing the number of open bonding sites in the nets. Therefore, given enough time, a framework will converge on the configuration that is most energetically stable.[130]

Using MUF-9 and MUF-10, Ferguson *et al*. confirmed this notion (**Figure 1.16**). They discovered a 52% largely interpenetrated isomer of MUF-9 after an 8-hour synthesis in DMF. The complete twofold interpenetrated isomer, -MUF-9, produced once the reaction time was prolonged. These scientists found that MUF-10, an enantiopure counterpart of MUF-9, displayed the same effect.[132]

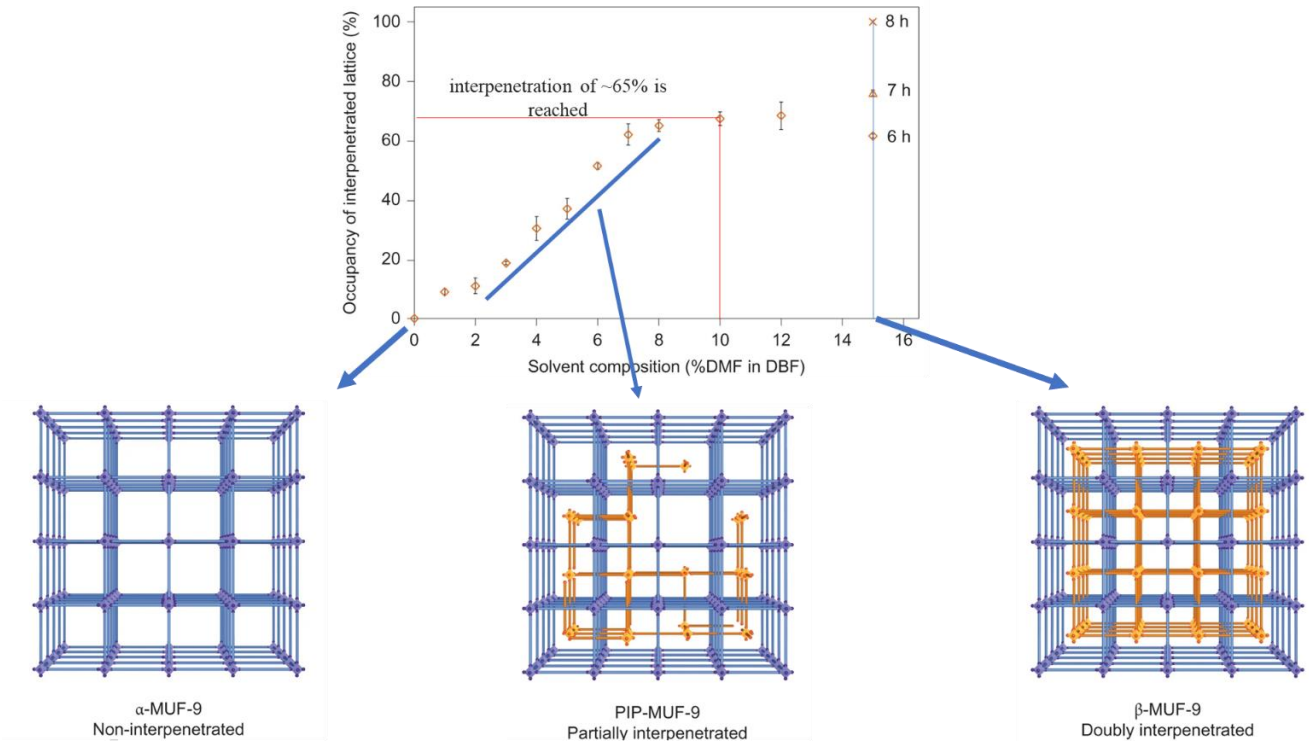

**Figure 1.16.** The level of partial interpenetration in MUF-9 is controlled by the reaction solvent's composition. From left to right, the structures of -MUF-9, PIP-MUF-9, and -MUF-9 were identified, showing the degree of interpenetration. The orange diamonds show the average interpenetration level as determined by a separate SCXRD. *Figure reprinted (adapted) with permission from Ferguson A, Liu L, Tapperwijn SJ, Perl D, Coudert F-X, Van Cleuvenbergen S, Verbiest T, van der Veen MA, Telfer SG. Controlled partial interpenetration in metal–organic frameworks. Nat Chem., 2016, 8:250. Copyright (2016) Springer Nature.*[132]

### 1.5.4. Ligand Design

Long organic linkers may easily lead to huge voids however are prone to and eventually give rise to interpenetrated frameworks.[134] Bulkier and longer organic linkers expected to have a greater tendency to create higher degrees of entanglement. The design of the ligand may also contribute to the degree of interpenetration based on the sterically bulky groups on ligand and elongated linkers.[133,134]

For instance, Prasad *et al.*'s syntheses of SNU-70 (non-interpenetrated) and SNU-71 (two-fold interpenetrated) differ in the starting material. The SNU-70's ligand has a double bond, because of this slight variation in the organic linker, the structure generates interpenetration and significant variation in pore size and gas uptake (**Figure 1.17**).[135]

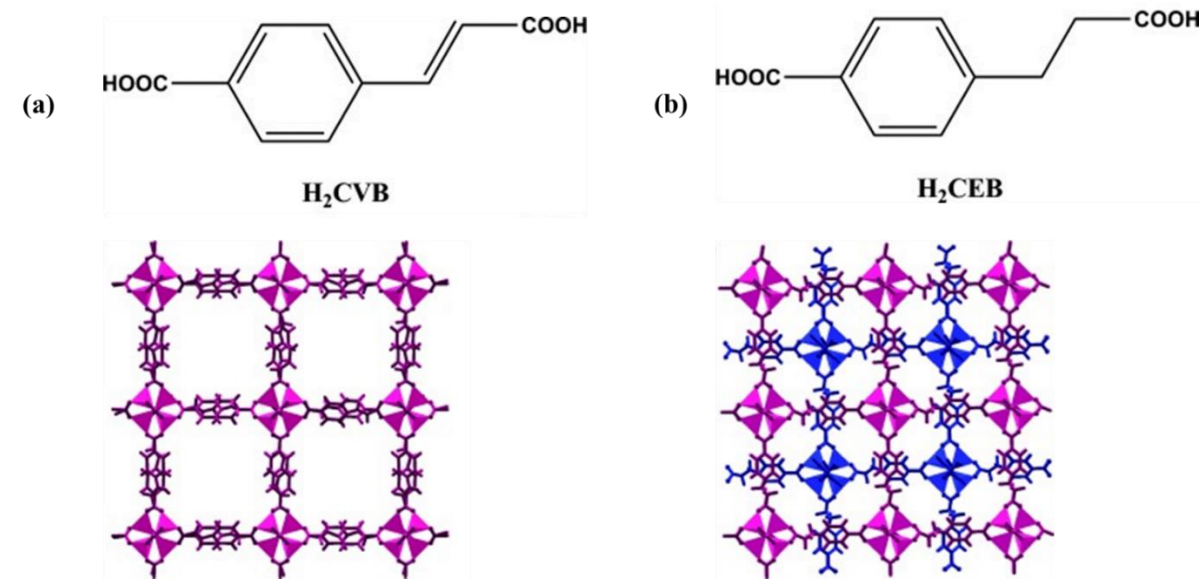


**Figure 1.17.** X-ray crystal structures and organic ligands for a) non-interpenetrated SNU-70 and b) doubly interpenetrated SNU-71. Red and blue are used to depict the two distinct frameworks that were interconnected. *Figure reprinted (adapted) with permission from Prasad TK, Suh MP. Control of interpenetration and gas-sorption properties of metal–organic frameworks by a simple change in ligand design. Chem A Eur J. 2012, 18,8673–8680. Copyright (2012) WILEY-VCH Verlag GmbH & Co. KGaA, Weinheim.*[135]

Sterically bulky groups on the organic ligand may prevent framework interpenetration, similar to the template effect. If the groups on the ligands begin to interact with one another, it may

increase the likelihood of interpenetration if the engaging groups move in closer proximity to one another. Therefore, the objective could be accomplished by carefully adding protecting groups to a ligand.[130]

Another tactic for preventing framework interpenetration is the deployment of large protective groups, followed by deprotection once the framework is formed.[130] Bulky thermolabile tert-butoxycarbonyl (Boc), used by Lun *et al.* (**Figure 1.18**) as a proline moiety, was removed post-synthesis to create open MOF with larger pores. Therefore, using the bulky protection group to create open frameworks is a good way to prevent framework interpenetration.[136]

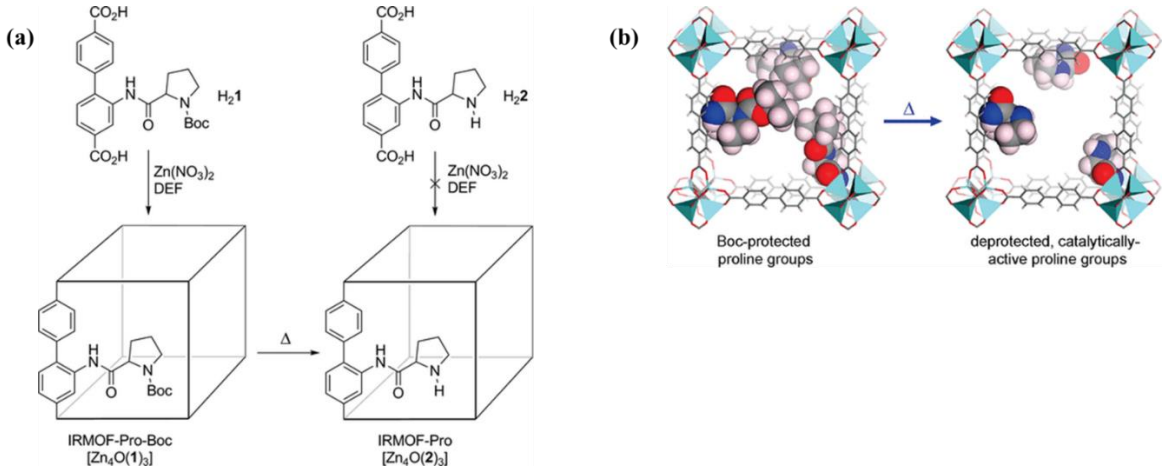


**Figure 1.18. (a)** Thermolytic expulsion of the Boc moiety creates IRMOF-Pro ($[Zn_4O(2)_3]$), which is produced as a product after the conversion of the ligand $H_2$1 to a cubic metal-organic framework, IRMOF-Pro-Boc ($[Zn_4O(1)_3]$). It also illustrates that the direct production of $[Zn_4O(2)_3]$) was not observed. (b) How the framework looks after the removal of Boc. *Figure reprinted (adapted) with permission from Lun DJ, Waterhouse GIN, Telfer SG, A general thermolabile protecting group strategy for organocatalytic metal–organic frameworks. J Am Chem Soc.,2011, 133, 5806–5809. Copyright (2011) American Chemical Society.*[136]

## 1.6. Porosity in MOFs

MOFs are appealing because they feature pores in their network architecture that can be functionalized and inhabited by guest molecules. Yet, permeability of the host phase should be established in order to show that a MOF is actually porous.[133] By measuring the surface areas of the material using BET (Brunauer-Emmet-Teller) analysis of a nitrogen sorption experiment at 77 K, porosity is often verifiable experimentally.[137] It is important to keep in mind that the aforementioned experimental technique has its own limitations because the MOF might only be permeable to nitrogen and not to other guests or vice versa. Therefore, MOF materials can contain voids without becoming inherently porous.[133,138]

Typically, a MOF's porosity is classified according to the dimension of the voids (**Figure 1.19**).[73] Zero-, one-, two-, or three-dimensional pores could make up these voids. Within the host framework, zero-dimensional pores are segregated. One-dimensional porosity is used to define non-intersecting channels, while two-dimensional porosity refers to assembly of distinct layers of free space. A series of crossing channels makes up three-dimensional porosity.[73]

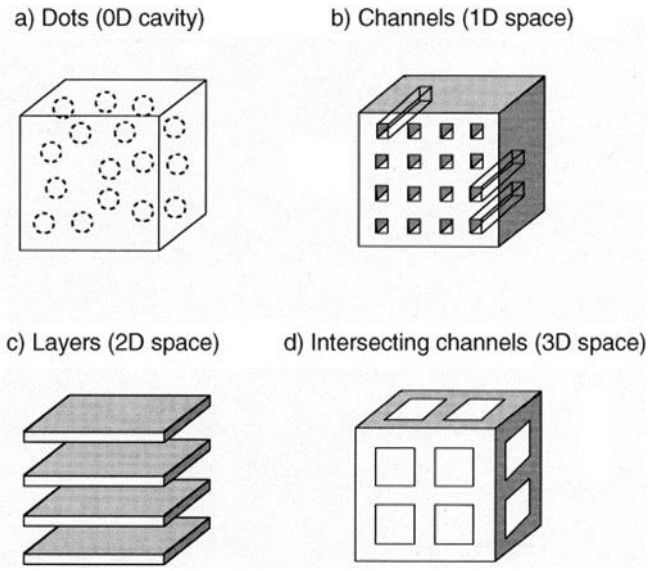


**Figure 1.19.** 0D, 1D, 2D, and 3D porosity are the four categories for the dimensionality of porosity in MOFs. *Figure reprinted (adapted) with permission S. Kitagawa, R. Kitaura, S. Noro, S. Angew. Chem. Int. Ed. 2004, 43, 2334-2375. Copyright (2004) WILEY-VCH Verlag GmbH & Co. KGaA, Weinheim.*[73]

## 1.7. Solid State Transformations

It is critical to understand the mechanisms underlying solid state transformations in the field of crystal engineering. Designing reactive substances and carrying out reactions in the solid state are made simple with such expertise.[71] The systematic study of solid-state transformations is made possible by the use of single crystal X-ray diffraction to monitor single crystal to single crystal transformations. This makes it possible to see how the structure changes throughout the transformation process.[71] Unfortunately, monitoring such reactions is challenging since crystallinity is not always preserved due to atom mobility.[140,141]

Typically, external stimuli like heat, pressure, and guest molecules cause structural changes in MOFs. Flexible MOFs can go through a variety of dynamic structural rearrangements that can result in behaviours including guest-opening absorption, stepwise sorption, and excellent selectivity for inclusion of guests. Pore expansion is a dynamic phenomenon that is triggered by one of the three mechanical variables listed below: (i) movement of interpenetrated motifs,[142] (ii) coordination bond reorientation or cleavage,[143,144] (iii) the bridging ligand's capability to freely rotate,[145,146] The latter entails rotating a restricted part of the bridging

ligand, which could cause slight changes in the ligand's structure as well as significant changes in the volume and geometry of the pores, improving guest inclusion.

### 1.8. Single-Crystal-To-Single-Crystal Transformations

When exposed to external stimuli like heat, light or when molecules enter or leave the host structure, single crystals of MOFs can survive and remain monocrystalline, a phenomenon known as single-crystal-to-single-crystal (SCSC) transitions of MOFs.[147,148] In order to analyze whether any structural changes have taken place that would assist in explaining features of the activated MOF, the structure of the MOF can be determined both before and after the external stimulus was applied. Yet, crystals that don't stay monocrystalline may still be polycrystalline rather than changing into an amorphous state.

### 1.9. Crystal Structure Stabilities of MOFs

The crystallinity, or periodicity, of MOFs' structures may be useful for their study in terms of revealing their structures, as well as for the reproducibility of their structure-related features. As an example, MOFs with uniform pore sizes can be more efficient in storage and separation applications due to the physical dimensions and chemical characteristics of their pores as opposed to other porous materials (such as activated carbons), where variations in these pore properties are common throughout the material and cause variation in storage capacities and separation efficiencies.[146,149]

The great majority of MOFs are synthesized with solvent molecules already present, which must be removed (referred to as "activation"), frequently by heating, before the MOF may be utilized in various applications that take advantage of the internal space. The discovery made by Yaghi et al., that's what sparked an increase in MOF research because these scientists were able to create stable, activated phases that could be utilized for molecule sorption.[61]

Unfortunately, many MOFs lose their crystallinity when attempts are made to remove the solvent molecules, resulting in the absence of internal space, despite having originally promising crystal structures, due to the collapse of their frameworks. Even though pore diameters are smaller in this case, entanglement in MOFs may be advantageous in generating stable phases via network-to-network interactions.[150]

### 1.10. Flexibility and Breathing Phenomena in MOFs.

Porous coordination compounds were first categorised according on how they responded to the removal of guests, and were initially divided into the first, second, and third generation

classifications in 1998, [150] and recently, Kitagawa suggested that fourth-generation MOFs should also comprise MOFs with material anisotropy and any other kind of defect, such as solid solutions and multivariate (MTV) MOFs.[151]

As guests are removed, or even after solubilization, the first-generation collapses and loses its structural integrity and porosity. Second-generation MOFs after guests are removed, the framework stays intact unlike its predecessor and sorption occurs however they are often rigid.[150] Third-generation MOFs are soft, flexible, and dynamic frameworks which collapse when a guest is removed and regenerate when a guest is taken in. Characteristically, third-generation MOFs exhibit structural flexibility with often reversible reactions to external stimuli, such as variation in temperature or gas pressure, even in the absence of a guest.[152,153]

Fourth-generation materials that mix a stiff framework with self-switching pores that can adjust to a specific guest through extra framework counterions that are free to move within the pore space or flexible ligand substituents would be another type.[154] Thus, these fourth-generation "hard-soft" materials could, at least in theory, combine the benefits of second- and third-generation MOFs while removing the following disadvantages: (a) retention of topology and structural integrity during gas or vapor adsorption; (b) soft pore surfaces that respond to external stimuli, leading to diverse sorption profiles; and (c) most importantly, the capability of self-adapt pore size and pore chemistry to accommodate different guests.[154]

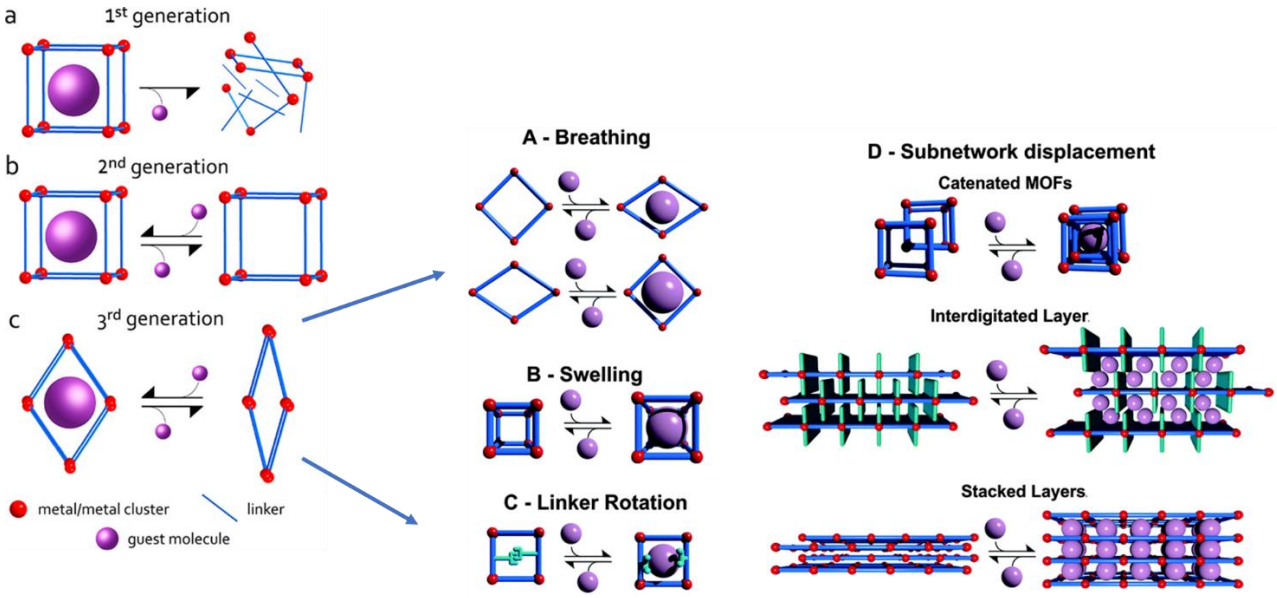


**Figure 1.20.** First, second, and third generation microporous coordination polymers shown schematically. Three classifications of Third Generation compounds (=flexible microporous coordination polymers) are used to describe them: "recoverable collapsing," "guest-induced transformation," and "guest-induced reformation." These three classifications are all achieved using flexible mechanisms in coordination networks. *Figure reprinted (adapted) with permission Zhang, S.-Y.; Jensen, S.; Tan, K.; Wojtas, L.; Roveto, M.; Cure, J.; Thonhauser, T.; Chabal, Y. J.; Zaworotko, M. J. Modulation of water vapor sorption by a 4th generation metal-organic material with a rigid framework and self-switching pores. J. Am. Chem. Soc. 2018, 140, 12545– 12552. Copyright (2004) American Chemical Society.*[154]

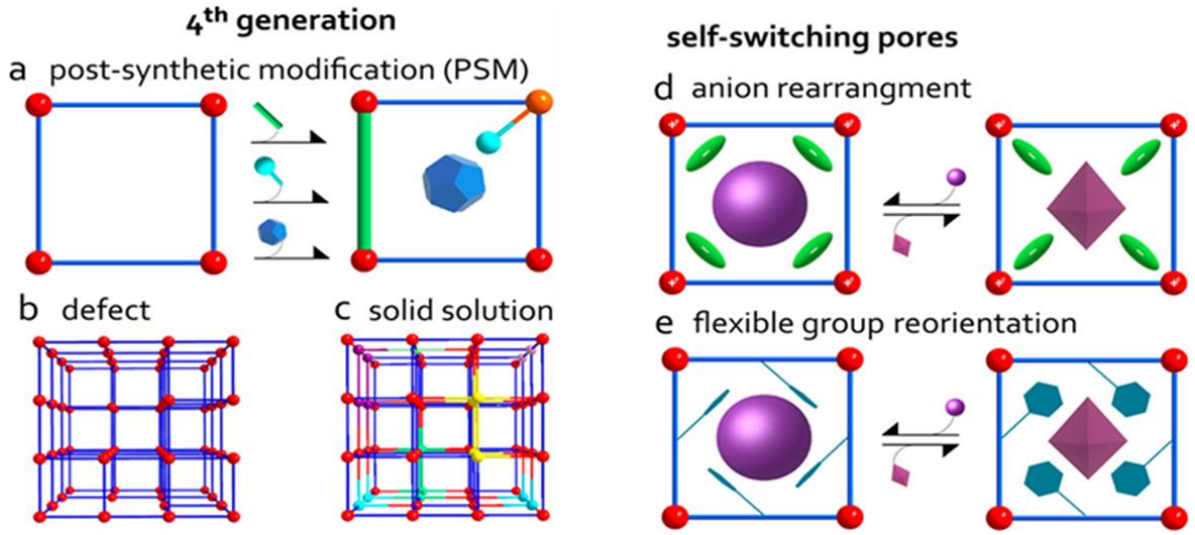


**Figure 1.21.** Fourth-Generation Porous Materials Can Be Modified Using (a) Postsynthetic Methods That Chemically Change Their Pore Structure, (b) Complex Systems That (c) Contain Defects, (d) Are Nonstoichiometric (Solid Solution), or (e) They Are Complex Systems; Rigid Frameworks with Self-Switching Pores that Adapt to a Specific Guest via (d) Rearrangement of Extraframework Counterions or (e) Reorientation of Flexible Ligand Substituents are two examples of a different type of fourth-generation porous materials. *Figure reprinted (adapted) with permission from Zhang, S.-Y.; Jensen, S.; Tan, K.; Wojtas, L.; Roveto, M.; Cure, J.; Thonhauser, T.; Chabal, Y. J.; Zaworotko, M. J. Modulation of water vapor sorption by a 4th generation metal-organic material with a rigid framework and self-switching pores. J. Am. Chem. Soc. 2018, 140, 12545– 12552. Copyright (2004) American Chemical Society.*[154]

Flexible MOFs are MOFs that can respond to the environment and change structure making them the focus of contemporary research. When they undergo these structural phase changes, they demonstrate a sharp increase or "step" in sorption.[153,155-157] This significant shift in sorption behaviour can be seen as a step in the sorption isotherm, which may also show hysteresis. Hysteresis improves selectivity, produces high working capacities, and lowers the need for heat control. A number of mechanisms, such as breathing (ligand stretching or flexing), swelling, linker rotation, subnetwork displacement, and sliding of interdigitated and stacked layers, can cause the structural phase shift behaviour of these materials.[158,159]

## 1.11. The Cambridge Structural Database (CSD)

### 1.11.1. The Cambridge Structural Database's History

Following the Braggs' work, X-ray crystal structure analysis was quickly acknowledged as a very unique analytical technique. In 1929, only 16 years after the structure solution of the first crystal structure, Strukturberichte (Structure Reports) was already compiling the practitioners' output from their varied original sources in order to offer easily accessible descriptions of recently discovered crystal structures on a regular publication schedule.[160] Up until the 1990s,

the Structure Reports, formerly known as the Strukturberichte, served as the International Union of Crystallography's (IUCr) official magazine.[161]

When it came to collecting crystal structure data, 1929 was a very significant year.[161] Since Linus Pauling released his five principles for figuring out the structures of complicated inorganic ionic crystals in 1929,[162] it was also unique in announcing the huge scientific significance of that curated information. Philosophically speaking, 1929 marks the beginning of the contemporary era of computerized databases for crystal structure, which started operating over four decades later: The Cambridge Structural Database (CSD: Cambridge, UK) was established in 1965,[161,165] it was then followed by The Inorganic Crystal Structure Database (ICSD: Karlsruhe, Germany), created in the early 1970s.[163]

The amount of scientific literature increased throughout this time, which made scientists concerned about keeping up with the publication of new crystal structures. These factors led to the establishment of the first "Crystallographic Data Centre," which Olga Kennard led in 1964.[161] The Cambridge Crystallographic Data Centre (CCDC), Cambridge Structural Database (CSD) a computer-based database, was founded in 1965 at the University of Cambridge's Department of Organic Chemistry.[164] The CSD currently has more than one million curated crystal structures as a result of the tremendous expansion in information and technological advancements.[164]

The demonstrated porosity of MOFs' by the research group of Professor Omar Yaghi in the late 1990s expedited the study of MOFs. Millions of distinct metal-organic frameworks can theoretically be created by mixing various metal nodes and organic linkers because of their modular structure. As of 2024, more than 100,000 MOF (actual number is 125 383) structures are currently listed in the most recent version of the CSD (in version 5.45 November 2023 + March update), as a result of exponential growth in the number of MOFs over the last 20 years.[165,166]

### 1.11.2. The Cambridge Structural Database Search Methods

In this project, the CCDC programs were used to visually inspect and extract interpenetrated structures. A number of different weak supramolecular forces (hydrogen bonding, π–π aromatic stacking interactions, and van der Waals forces), M···M (metallophilic) interactions were used to identify unique network···network interactions which may occur to differentiate entangled structures from their non-entangled counterparts.

The online, interactive CSD MOF subset explorer can be used to filter identified MOFs based on pore geometric parameters such as pore volume, void fraction, large cavity diameter, pore-limiting dimension, and accessible surface area. ConQuest is an interface that may be used to look up and retrieve structures from the CSD using specific search parameters.[161] Searching can be done using a variety of criteria, such as compound name, elemental composition,

formula, literature reference, unit cell characteristics, space groups, experimental data, and a few additional structural information specifics (**Figure 1.22**). Using a chemical substructure motif with or without chemical restrictions is one of the most popular search strategies. It also enables searches for nonbonded contacts, which may be intramolecular or intermolecular, as well as 3D geometric searching (e.g., bond distances or angles).[161,164]

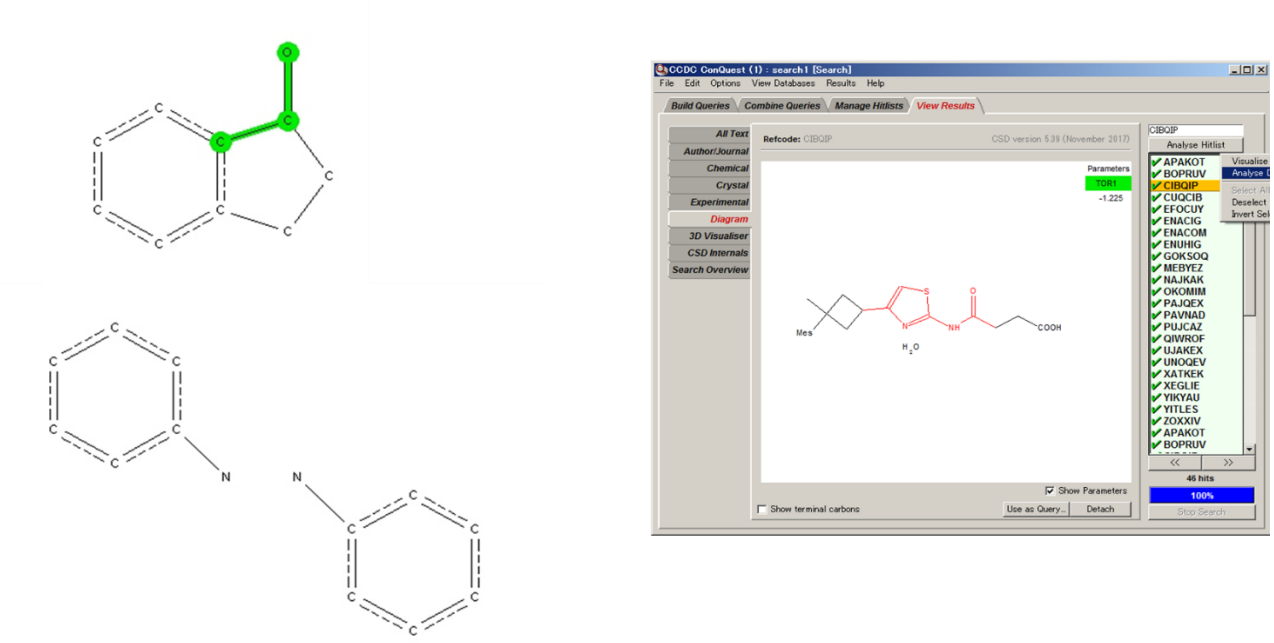


**Figure 1.22.** The ConQuest draw window is used for sketching chemical substructures and defining each query to be searched. *Figure reprinted (adapted) with permission from I. J. Bruno, J. C. Cole, P. R. Edgington, M. Kessler, C. F. Macrae, P. McCabe, J. Pearson and R. Taylor. Acta Cryst. B, 2002. B58, 389-397. Copyright (2002) the International Union of Crystallography.*[161]

The CCDC suite of programs also includes Mercury, a program that offers a wide array of features for the investigation of a single structure, such as powder diffraction patterns, visualization of void space, measure of distances and angles. The functions are not limited to these only, Mercury has the ability to allow the user to build and visualize a network of intermolecular contacts, invert crystal structures, reduce the symmetry of a structure from the current space group to one of the available subgroups (**Figure 1.23**).[164]

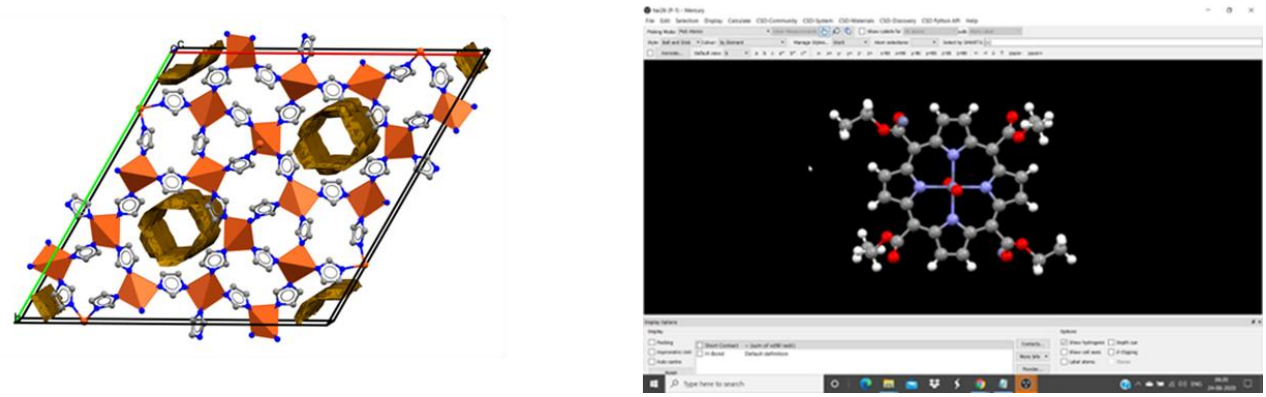

**Figure 1.23.** The ConQuest draw window is used for sketching chemical substructures and defining. *Figure reprinted (adapted) with I. J. Bruno, J. C. Cole, P. R. Edgington, M. Kessler, C. F. Macrae, P. McCabe, J. Pearson and R. Taylor. Acta Cryst. B, 2002. B58, 389-397. Copyright (2002) the International Union of Crystallography.*[161]

Another program that is offered by CSD is the CSD Python API which is presently part of the CSD-Enterprise, and it comes as a package when downloading CSD via the CCDC. This permits one to run pre-written or user-written Python search scripts to a set of structures or loaded structures. The CCDC Python-Built-In scripts include: (i) Analysis-generation, of conformers and calculation of their RMSD or of all torsion points for the stacked structures. External -one can upload the most recent or current structures into the sketch window provided for ConQuest. (ii) Reports- One can make reports in the form of *.html format. This will contain crystallographic details, the geometry, Mogul geometry analysis, and intermolecular bonding for halogen and hydrogen. It also provides chemical and crystallographic and publication information about the structures. Other functions include void calculation in a crystal, find covalently bonded clusters within a structure.[164]

Due to the large number of MOFs, it is challenging to identify particular types of MOFs from the database and analyse trends in their attributes. In fact, it was not possible to just extract MOF structures exclusively without including discrete, coordination molecules in the results lists until quite recently. Searches on distinct families of MOFs were not practical since these "mixed" lists would unavoidably be selective only to the local coordination environment of the structures and would not filter MOFs based on their extended structures. This issue is made worse by the fact that, as was already indicated, MOFs lack systematic names that may be used to search for only MOFs or a particular family of MOFs. [120,121,167] Researchers began using computer algorithms to develop a “language” for analysing similarities and evaluating differences between these structures in order to overcome this problem.

### 1.11.3. Successful MOF Databases and CSD MOF Subset

Attempts of creating MOF databases, such as the zeolitic imidazolate framework (ZIF) or porous polymer networks (PPN) databases, has been attempted and successfully completed by

a number of research teams.[170] With the help of available crystallographic data from known MOFs, Wilmer *et al.*[168] produced a theoretical MOF database with 137,953 structures at the time made from the recombination of a library of 102 building blocks containing SBUs and organic linkers.[168] Based on pre-existing experimental structures directly derived from the CSD, other research teams developed databases. As an illustrative example, Watanabe *et al.*[169] produced a database in 2012 that explicitly extracted 30 000 extended metal–organic compounds from the CSD, narrowing this list to 1167 3D MOF structures for the assessments of their $CO_2/N_2$ separation capabilities.[169]

Goldsmith *et al.* extracted 38 800 metal-organic frameworks from the CSD at the time 550 000 structures and created 22,700 "computation-ready" 3D MOFs in 2013.[170] These MOF structures have been changed by removing obstructive solvent molecules or do not contain any disorder. The "Computation-Ready, Experimental MOFs" (CoRE MOF) database, which Chung *et al.* created in 2014, is the first database that is accessible to the general public. A pore-limiting diameter (PLD) of 2.4 Å was present in 4,700 3D MOFs.[171]

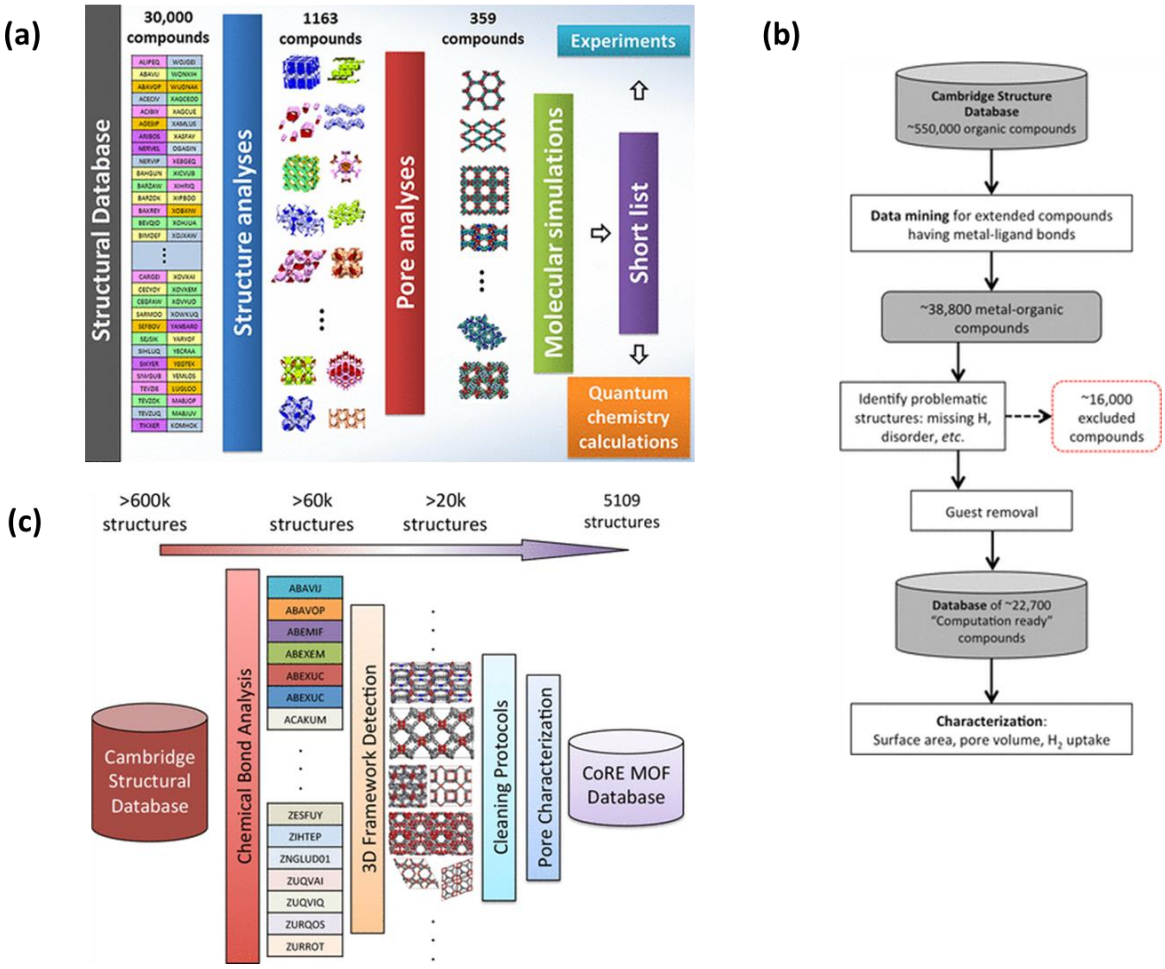


**Figure 1.24.** (a) Utilizing a multiscale computational method for $CO_2/N_2$ separations.[169] (b) Diagram showing the processing and analysis of the CSD's crystal structure database.[170] (c) Design of the CoRE MOF database is shown schematically. Utilizing the CCDC Conquest program, 3D framework detection, and pore characterization, chemical bond analysis was carried out. *Figure reprinted (adapted) with Chung Y.G, Camp J, Haranczyk M, Sikora B.J, Bury W, Krungleviciute V, Yildirim T, Farha O.K, Sholl D.S and Snurr R.Q, Chem. Mater., 2014, 26, 6185 —6192. Copyright (2014) American Chemical Society.*[171]

These many databases, however, deal with a number of issues. The system created by Wilmer *et al.*[168] has to deal with the challenge of creating an experimental synthesis pathway for the top structure chosen by the database, which is typically either challenging or impractical. Since the structures contained in the databases developed by Watanabe *et al.*[169], Goldsmith *et al.*[170], and Chung *et al.*[171] were hand-selected for adsorption applications, they need to be manually updated every time the CSD is updated (four times per year). As a result, MOFs with threshold pore dimensions based on gas adsorbate kinetic diameters were chosen and also restricted to 3D MOFs.

The databases above that were derived from CSD have shown to be highly helpful.[166] However, because they are not integrated into the CSD, they need to be updated manually whenever the CSD is updated, so later additions of MOF structures are not taken into consideration. Additionally, because the aforementioned databases contained designs that were intended for adsorption applications, only 3D structures with the proper pore and window sizes were included according to the desired adsorbate's kinetic diameter. Additionally, there are problems with using too broad or too narrow search criteria for MOFs. Since there are known examples of alkali-based MOFs, excluding MOFs with alkali metal ions from the Goldsmith *et al.* paper would be excessively restrictive.[170]

In an article that was published in 2017 by Moghadam, Fairen-Jimenez, *et al*.[140] in association with the CCDC, they demonstrated how search techniques in the CSD that are accessible to end users were utilized to produce the CSD MOF subset. For instance, the search term "catena," which the CSD employs to identify polymeric structures, was paired with one of the common search techniques involving a chemical diagram motif (i.e., a substructure search). The CSD MOF subset was created using seven search criteria.

The CSD 5.37 version served as the foundation for this (May 2016 update). It has been established that these criteria are not mutually exclusive, therefore other criteria may produce the same structures. This version of the CSD had 69 666 MOF structures that were discovered using the union of these seven criteria and the inclusion of the word "catena" in the compound name.

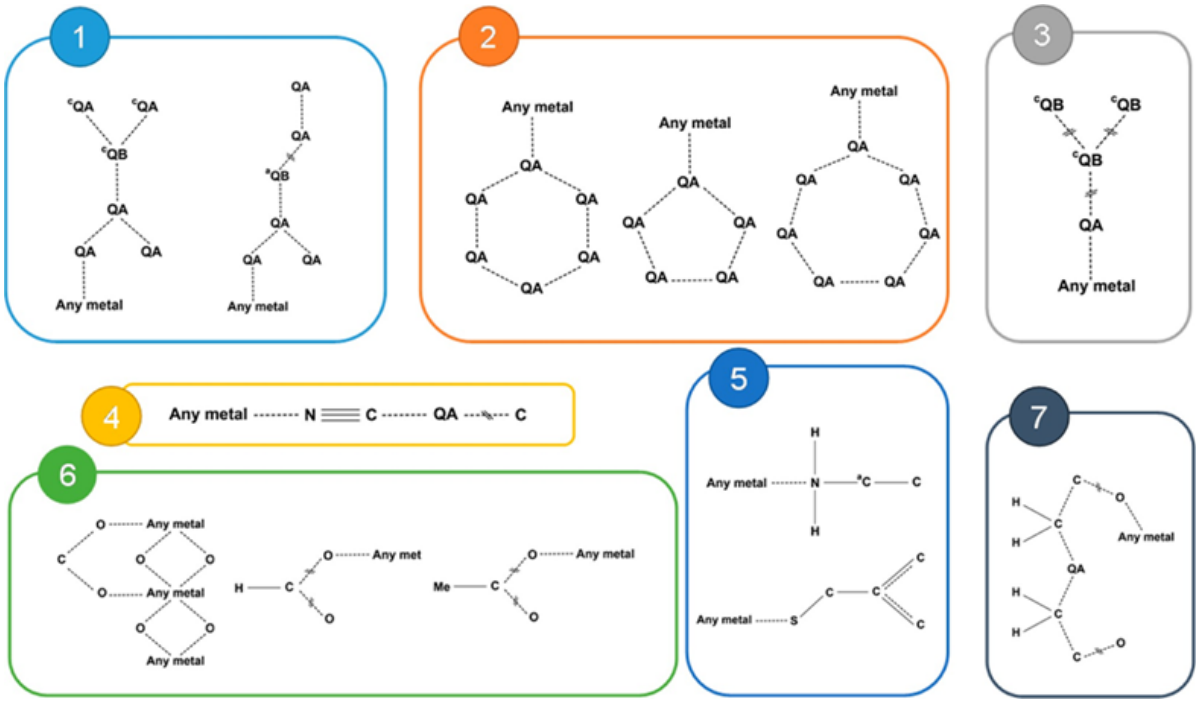


**Figure 1.25.** A list of the seven requirements used to create the CSD MOF subset. *Figure reprinted (adapted) with P. Z. Moghadam, A. Li, S. B. Wiggin, A. Tao, A. G. P. Maloney, P. A. Wood, S. C. Ward and D. Fairen-Jimenez, Chem. Mater., 2017, 29, 2618 —2625. Copyright (2017) American Chemical Society.*[172]

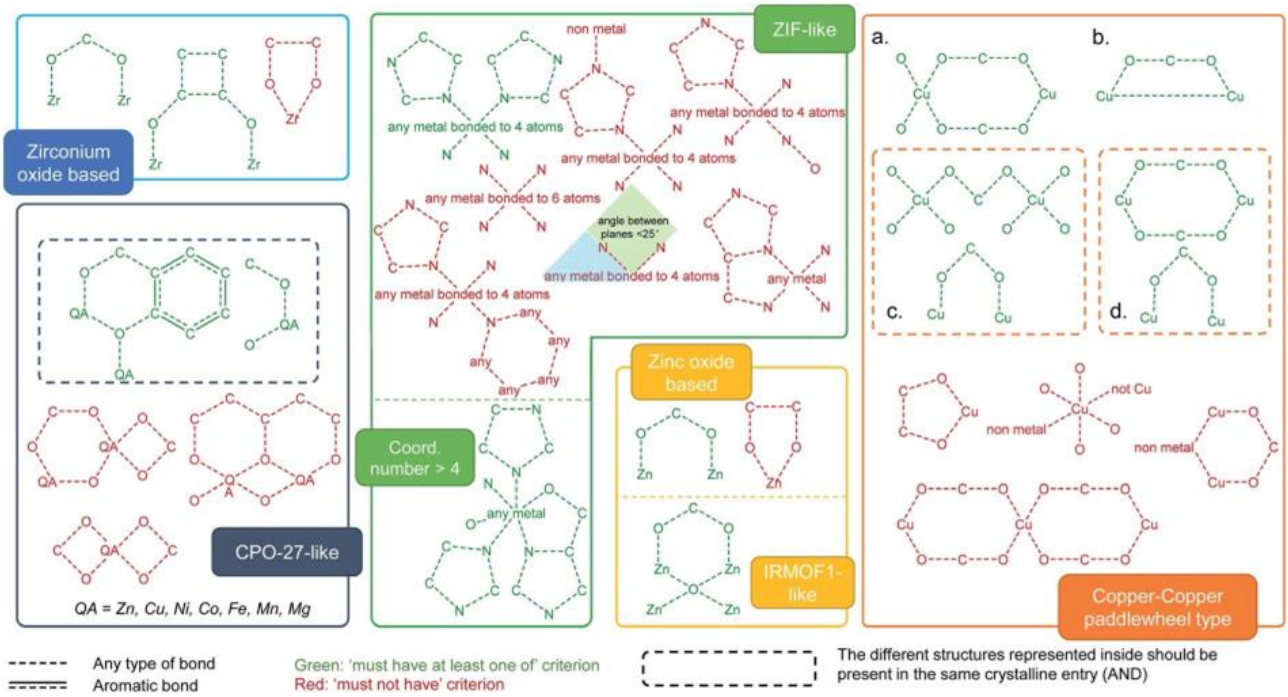


**Figure 1.26.** The CSD MOF subgroup of MOFs was identified using criteria based on certain secondary building components and their relationship to the organic linkers. *Figure reprinted (adapted) with P. Z. Moghadam, A. Li, X-W. Liu, R. Bueno-Perez, S.-D Wang, S.B. Wiggin, P.A. Wood, D. Fairen-Jimenez, Chem. Sci., 2020,11, 8373-8387. Copyright (2020) Royal Society of Chemistry.*[166]

The field has been growing exponentially, with MOFs having their own MOF subset in the CSD, setting them apart from other coordination polymers. MOFs have another property that can be exploited such as either the structure is entangled or non-entangled. This is imperative to distinguish one from the other as they have different properties to each other.

## 1.12. MOTIVATION AND OBJECTIVES

### 1.12.1. Rationale

This project is divided into two parts a computer-based component and laboratory experiment component.

### 1.12.2. Computer-based Section:

Currently, the CSD does not have search methods that can automatically extract entangled MOFs from the database. The development of such search method to mine and identify entangled MOF structures can be beneficial for (i) improved MOF type search, (ii) data management and (iii) discovery of structure–property relationships. The goal is to offer the broadest subset feasible to enable study in a wide range of applications, allowing users of this resource to further fine-tune criteria to specifically target their desired specifications.

### 1.12.3. Experimental Section:

Entanglement is a phenomenon that was thought to occur serendipitously in MOF structures. The effect of entanglement in 2D or 3D MOFs on polycrystalline or monocrystalline stability, involving the synthesis of a subset of entangled MOFs and their non-entangled counterparts. There will be characterized using single crystal X-ray diffraction (SCXRD) and powder X-ray diffraction (PXRD).

A series of other experiments such as hot stage microscopy (HSM), thermogravimetric analysis (TGA) and, differential scanning calorimetry (DSC) as thermal analyses for testing the stability of the crystals. Further stabilities of the crystal structures will involve *in situ* desolvation followed by PXRD analysis. Gas sorption properties of the synthesized MOFs will also be studied, and also perform solvent exchange.

## 1.13. Aims

The two main aims of this project are:

### 1.13.1. Computer-based Section:

(a) To establish search methods using the CSD end-user tools to extract entangled structures in the database belonging to several well-known MOF families.

(b) To create a subset of entangled MOFs from well-known families of MOFs and their non-entangled counter parts.

### 1.13.2. Experimental Section:

(a) To synthesize a subset of non-entangled MOFs for comparison with their entangled counterparts.

(b) To establish the effect of entanglement on the thermal stabilities, as well as liquid and gas sorption properties of the synthesized MOFs.

## 1.14. Objectives

### 1.14.1. Computer-based Section:

(a) Search for families of MOFs using the CSD search methods within the MOF subset.

(b) Identify intermolecular and non-bonded contacts in the respective families of MOF which occur only between networks of the MOFs and thus could be used to specifically extract entangled MOFs.

(c) Identify various physical properties in the respective families of MOF which could be used to specifically extract entangled MOFs.

### 1.14.2. Experimental Section:

(a) Follow published methods (e.g., the solvothermal method) for producing MOFs and change experimental conditions to produce entangled and non-entangled pairs.

(b) Use X-ray diffraction to elucidate MOF crystal structures and thermal analysis (hot stage microscopy, thermogravimetric analysis and differential scanning calorimetry) to assess their thermal properties.

(c) Use hot stage microscopy and powder X-ray diffraction as qualitative measures of determining retention of mono- and polycrystallinities of the MOFs.

(d) Evaluate the ability of synthesized MOFs for liquid and gas sorption.

## 1.15. References


1. Encyclopedia Britannica. *Van Der Waals Forces | Chemistry and Physics*. Encyclopedia Britannica., https://www.britannica.com/science/van-der-Waals-forces. Accessed 5 June 2023.
2. Tang, K.-T.; Toennies, J. P. Johannes Diderik van Der Waals: A Pioneer in the Molecular Sciences and Nobel Prize Winner in 1910. *Angewandte Chemie International Edition* **2010**, *49* (50), 9574–9579.
   Available: https://onlinelibrary.wiley.com/doi/10.1002/anie.201002332
3. Manna, A.K.; Supramolecular chemistry-concepts and applications. *Int. J. Sci. Res*, **2015**, 4 (4), .2319-7064. Available: https://www.ijsr.net/archive/v4i4/29031502.pdf
4. Fruton, J.S.; Contrasts in Scientific Style. Emil Fischer and Franz Hofmeister: Their Research Groups and Their Theory of Protein Structure,*Proc. Am. Phil. Soc.* **1985**, 129, 313-370.
5. Fischer, E. Einfluss Der Configuration Auf Die Wirkung Der Enzyme. *Berichte der deutschen chemischen Gesellschaft.* **1894**, *27* (3), 2985–2993. Available: https://chemistry-europe.onlinelibrary.wiley.com/doi/10.1002/cber.18940270364
6. Powell, H. M. 15. The Structure of Molecular Compounds. Part IV. Clathrate Compounds. *Journal of the Chemical Society (Resumed)* **1948**, No. 0, 61–73. Available: https://doi.org/10.1039/JR9480000061.
7. Lehn, J.-M. Supramolecular Chemistry. *Science* **1993**, *260* (5115), 1762–1763. Available: https://www.science.org/doi/10.1126/science.8511582
8. Desiraju, G. R. Chemistry beyond the Molecule. *Nature* **2001**, *412* (6845), 397–400. Available: https://www.nature.com/articles/35086640
9. Schneider, H.-J. Binding Mechanisms in Supramolecular Complexes. *Angewandte Chemie International Edition* **2009**, *48* (22), 3924–3977.
   Available: https://pubmed.ncbi.nlm.nih.gov/19415701/
10. Biedermann, F.; Schneider, H.-J. Experimental Binding Energies in Supramolecular Complexes. *Chemical Reviews* **2016**, *116* (9), 5216–5300.
    Available: https://doi.org/10.1021/acs.chemrev.5b00583.
11. Desiraju, G. R. Crystal Engineering in IUCrJ 2021: Interactions, Structures, Properties. IUCrJ 2022, 9 (3), 329–330. Available: https://doi.org/10.1107/s2052252522004274.
12. Pepinsky, R. Crystal Engineering: New Concepts in Crystallography. *Phys. Rev*, **1955**, 100, 20740-3844.
13. Tupe, S. A.; Khandagale, S. P.; Jadhav, A. B. Pharmaceutical Cocrystals: An Emerging Approach to Modulate Physicochemical Properties of Active Pharmaceutical Ingredients. *Journal of Drug Delivery and Therapeutics* **2023**, *13* (4), 101–112.
    Available: https://doi.org/10.22270/jddt.v13i4.6016.
14. Cohen, M. D.; Schmidt, G. M. J. 383. Topochemistry. Part I. A Survey. *Journal of the Chemical Society (Resumed)* **1964**, 1996.
    Available: https://doi.org/10.1039/jr9640001996.
15. Kitaigorodsky, A. *Molecular Crystals and Molecules*; Elsevier, 2012. Available: https://books.google.co.za/books?id=L8Qv0vvvP80C&printsec=frontcover&source=gbs_ge_summary_r&cad=0#v=onepage&q&f=false

16. Jeevanandam, J.; Barhoum, A.; Chan, Y. S.; Dufresne, A.; Danquah, M. K. Review on Nanoparticles and Nanostructured Materials: History, Sources, Toxicity and Regulations. *Beilstein Journal of Nanotechnology* **2018**, *9* (1), 1050–1074. Available: https://doi.org/10.3762/bjnano.9.98.Y. Zhao, K. X. Yao, B. Teng, Y. Han, *Energy Environ. Sci*. 2013, **6**, 3684– 3692.
17. Li, B.; Zhang, Y.; Krishna, R.; Yao, K.; Han, Y.; Wu, Z.; Ma, D.; Shi, Z.; Pham, T.; Space, B.; Liu, J.; Thallapally, P. K.; Liu, J.; Chrzanowski, M.; Ma, S. Introduction of π-Complexation into Porous Aromatic Framework for Highly Selective Adsorption of Ethylene over Ethane. *Journal of the American Chemical Society* **2014**, *136* (24), 8654–8660. Available: https://doi.org/10.1021/ja502119z.
18. Hasell, T.; Miklitz, M.; Stephenson, A.; Little, M. A.; Chong, S. Y.; Clowes, R.; Chen, L.; Holden, D.; Tribello, G. A.; Jelfs, K. E.; Cooper, A. I. Porous Organic Cages for Sulfur Hexafluoride Separation. *Journal of the American Chemical Society* **2016**, *138* (5), 1653–1659. Available: https://doi.org/10.1021/jacs.5b11797.
19. Fu, J.; Das, S.; Xing, G.; Ben, T.; Valtchev, V.; Qiu, S. Fabrication of COF-MOF Composite Membranes and Their Highly Selective Separation of $H_2/CO_2$. **2016**, *138* (24), 7673–7680. Available: https://doi.org/10.1021/jacs.6b03348.
20. Budd, P.; Msayib, K.; Tattershall, C.; Ghanem, B.; Reynolds, K.; McKeown, N.; Fritsch, D. Gas Separation Membranes from Polymers of Intrinsic Microporosity. *Journal of Membrane Science* **2005**, *251* (1-2), 263–269.
Available: https://doi.org/10.1016/j.memsci.2005.01.009.
21. Qiao, Z.-A.; Chai, S.-H.; Nelson, K.; Bi, Z.; Chen, J.; Mahurin, S. M.; Zhu, X.; Dai, S. Polymeric Molecular Sieve Membranes via in Situ Cross-Linking of Non-Porous Polymer Membrane Templates. *Nature Communications* **2014**, *5* (1).
Available: https://doi.org/10.1038/ncomms4705.
22. Husain, A.; Ellwart, M.; Bourne, S. A.; Lars Öhrström; Oliver, C. L. Single-Crystal-To-Single-Crystal Transformation of a Novel 2-Fold Interpenetrated Cadmium-Organic Framework with Trimesate and 1,2-Bis(4-Pyridyl)Ethane into the Thermally Desolvated Form Which Exhibits Liquid and Gas Sorption Properties. *Crystal Growth & Design* **2013**, *13* (4), 1526–1534. Available: https://doi.org/10.1021/cg301760a.
23. Mason, J. A.; Oktawiec, J.; Taylor, M. K.; Hudson, M. R.; Rodriguez, J.; Bachman, J. E.; Gonzalez, M. I.; Cervellino, A.; Guagliardi, A.; Brown, C. M.; Llewellyn, P. L.; Masciocchi, N.; Long, J. R. Methane Storage in Flexible Metal–Organic Frameworks with Intrinsic Thermal Management. *Nature* **2015**, *527* (7578), 357–361. Available: https://doi.org/10.1038/nature15732.
24. Yu, H.; Xiang, Q.; Fang, M.; Yang, Q.; Feron, P. Promoted CO2 Absorption in Aqueous Ammonia. *Greenhouse Gases: Science and Technology* **2012**, *2* (3), 200–208.
Available: https://doi.org/10.1002/ghg.1280.
25. Ding, S.-Y.; Gao, J.; Wang, Q.; Zhang, Y.; Song, W.-G.; Su, C.-Y.; Wang, W. Construction of Covalent Organic Framework for Catalysis: Pd/COF-LZU1 in Suzuki–Miyaura Coupling Reaction. *Journal of the American Chemical Society* **2011**, *133* (49), 19816–19822. Available: https://doi.org/10.1021/ja206846p.
26. Fang, Q.; Gu, S.; Zheng, J.; Zhuang, Z.; Qiu, S.; Yan, Y. 3D Microporous Base-Functionalized Covalent Organic Frameworks for Size-Selective Catalysis. *Angewandte Chemie* **2014**, *53* (11), 2878–2882. Available: https://doi.org/10.1002/anie.201310500.

27. Yang, D.; Gates, B. C. Catalysis by Metal Organic Frameworks: Perspective and Suggestions for Future Research. *ACS Catalysis* **2019**, *9* (3), 1779–1798. Available: https://doi.org/10.1021/acscatal.8b04515.
28. Corma, A.; García, H.; Llabrés i Xamena, F. X. Engineering Metal Organic Frameworks for Heterogeneous Catalysis. *Chemical Reviews* **2010**, *110* (8), 4606–4655. Available: https://doi.org/10.1021/cr9003924.
29. Lee, J.; Farha, O. K.; Roberts, J.; Scheidt, K. A.; Nguyen, S. T.; Hupp, J. T. Metal–Organic Framework Materials as Catalysts. *Chemical Society Reviews* **2009**, *38* (5), 1450. Available: https://doi.org/10.1039/b807080f.
30. Zhang, T.; Lin, W. Metal–Organic Frameworks for Artificial Photosynthesis and Photocatalysis. *Chem. Soc. Rev.* **2014**, *43* (16), 5982–5993. Available: https://doi.org/10.1039/c4cs00103f.
31. Wang, S.; Wang, X. Multifunctional Metal-Organic Frameworks for Photocatalysis. *Small* **2015**, *11* (26), 3097–3112. Available: https://doi.org/10.1002/smll.201500084.
32. Zhang, H.; Liu, G.; Shi, L.; Liu, H.; Wang, T.; Ye, J. Engineering Coordination Polymers for Photocatalysis. *Nano Energy* **2016**, *22*, 149–168. Available: https://doi.org/10.1016/j.nanoen.2016.01.029.
33. Dhakshinamoorthy, A.; Asiri, A. M.; García, H. Metal-Organic Framework (MOF) Compounds: Photocatalysts for Redox Reactions and Solar Fuel Production. *Angewandte Chemie International Edition* **2016**, *55* (18), 5414–5445. Available: https://doi.org/10.1002/anie.201505581.
34. Zeng, L.; Guo, X.; He, C.; Duan, C. Metal–Organic Frameworks: Versatile Materials for Heterogeneous Photocatalysis. *ACS Catalysis* **2016**, *6* (11), 7935–7947. Available: https://doi.org/10.1021/acscatal.6b02228.
35. Wang, H.; Lustig, W. P.; Li, J. Sensing and Capture of Toxic and Hazardous Gases and Vapors by Metal–Organic Frameworks. *Chemical Society Reviews* **2018**, *47* (13), 4729–4756. Available: https://doi.org/10.1039/c7cs00885f.
36. Gui, R.; Guo, L.; Bu, X.; Fu Yongxin; Wang, Z.; Liu, Q. Recent Advances in Dual-Emission Ratiometric Fluorescence Probes for Chemo/Biosensing and Bioimaging of Biomarkers. *Coordination Chemistry Reviews* **2019**, *383*, 82–103. Available: https://doi.org/10.1016/j.ccr.2019.01.004.
37. Rasheed, T.; Nabeel, F. Luminescent Metal-Organic Frameworks as Potential Sensory Materials for Various Environmental Toxic Agents. *Coordination Chemistry Reviews* **2019**, *401*, 213065. Available: https://doi.org/10.1016/j.ccr.2019.213065.
38. Li, Y.; Fu, Z.; Xu, G. Metal-Organic Framework Nanosheets: Preparation and Applications. *Coordination Chemistry Reviews* **2019**, *388*, 79–106. Available: https://doi.org/10.1016/j.ccr.2019.02.033.
39. Cai, H.; Huang, Y.-L.; Li, D. Biological Metal–Organic Frameworks: Structures, Host–Guest Chemistry and Bio-Applications. *Coordination Chemistry Reviews* **2019**, *378*, 207–221. Available: https://doi.org/10.1016/j.ccr.2017.12.003.
40. Zhang, Q.; Wang, C.-F.; Lv, Y.-K. Luminescent Switch Sensors for the Detection of Biomolecules Based on Metal–Organic Frameworks. *Analyst* **2018**, *143* (18), 4221–4229. Available: https://doi.org/10.1039/C8AN00816G.

41. Gu, C.; Huang, N.; Chen, Y.; Qin, L.; Xu, H.; Zhang, S.; Li, F.; Ma, Y.; Jiang, D. π-Conjugated Microporous Polymer Films: Designed Synthesis, Conducting Properties, and Photoenergy Conversions. *Angewandte Chemie* **2015**, *54* (46), 13594–13598. Available: https://doi.org/10.1002/anie.201506570.
42. Ahmad, S.; Liu, J.; Ji, W.; Sun, L. Metal–Organic Framework Thin Film-Based Dye Sensitized Solar Cells with Enhanced Photocurrent. *Materials* **2018**, *11* (10), 1868. Available: https://doi.org/10.3390/ma11101868.
43. Yildirim, O.; Bonomo, M.; Barbero, N.; Atzori, C.; Civalleri, B.; Bonino, F.; Viscardi, G.; Barolo, C. Application of Metal-Organic Frameworks and Covalent Organic Frameworks as (Photo)Active Material in Hybrid Photovoltaic Technologies. *Energies* **2020**, *13* (21), 5602. Available: https://doi.org/10.3390/en13215602.
44. Kitagawa, S.; Kitaura, R.; Noro, S. Functional Porous Coordination Polymers. *Angewandte Chemie International Edition* **2004**, *43* (18), 2334–2375. https://doi.org/10.1002/anie.200300610.
45. Tao, Y.; Kanoh, H.; Abrams, L.; Kaneko, K. Mesopore-Modified Zeolites: Preparation, Characterization, and Applications. *Chemical Reviews* **2006**, *106* (3), 896–910. Available: https://doi.org/10.1021/cr040204o.
46. Sherman, J. D. Synthetic Zeolites and Other Microporous Oxide Molecular Sieves. *Proceedings of the National Academy of Sciences* **1999**, *96* (7), 3471–3478. Available: https://doi.org/10.1073/pnas.96.7.3471.
47. Chen, H.; Wydra, J.; Zhang, X.; Lee, P.-S.; Wang, Z.; Fan, W.; Tsapatsis, M. Hydrothermal Synthesis of Zeolites with Three-Dimensionally Ordered Mesoporous-Imprinted Structure. *Journal of the American Chemical Society* **2011**, *133* (32), 12390–12393. Available: https://doi.org/10.1021/ja2046815.
48. Meininghaus, C. K. W.; Prins, R. Sorption of Volatile Organic Compounds on Hydrophobic Zeolites. *Microporous and Mesoporous Materials* **2000**, *35-36*, 349–365. Available: https://doi.org/10.1016/s1387-1811(99)00233-4.
49. Chew, T.-L.; Ahmad, A. L.; Bhatia, S. Ordered Mesoporous Silica (OMS) as an Adsorbent and Membrane for Separation of Carbon Dioxide (CO2). *Advances in Colloid and Interface Science* **2010**, *153* (1), 43–57. Available: https://doi.org/10.1016/j.cis.2009.12.001.
50. Tao, W.-H.; Yang, T. C.-K.; Chang, Y.-N.; Chang, L.-K.; Chung, T.-W. Effect of Moisture on the Adsorption of Volatile Organic Compounds by Zeolite 13×. *Journal of Environmental Engineering* **2004**, *130* (10), 1210–1216. Available: https://doi.org/10.1061/(asce)0733-9372(2004)130:10(1210).
51. Perot, G.; Guisnet, M. Advantages and Disadvantages of Zeolites as Catalysts in Organic Chemistry. *Journal of Molecular Catalysis* **1990**, *61* (2), 173–196. Available: https://doi.org/10.1016/0304-5102(90)85154-a.
52. Verdoliva, V.; Saviano, M.; De Luca, S. Zeolites as Acid/Basic Solid Catalysts: Recent Synthetic Developments. *Catalysts* **2019**, *9* (3), 248. Available: https://doi.org/10.3390/catal9030248.
53. Lozano-Castelló, D.; Lillo-Ródenas, M. A.; Cazorla-Amorós, D.; Linares-Solano, A. Preparation of Activated Carbons from Spanish Anthracite: I. Activation by KOH. *Carbon* **2001**, *39* (5), 741–749. Available: https://doi.org/10.1016/S0008-6223(00)00185-8.

54. Bansode, R. R.; Losso, J. N.; Marshall, W. E.; Rao, R. M.; Portier, R. J. Adsorption of Volatile Organic Compounds by Pecan Shell- and Almond Shell-Based Granular Activated Carbons. *Bioresource Technology* **2003**, *90* (2), 175–184. Available: https://doi.org/10.1016/s0960-8524(03)00117-2.
55. Siriwardane, R. V.; Shen, M.-S.; Fisher, E. P.; Poston, J. A. Adsorption of CO2on Molecular Sieves and Activated Carbon. *Energy & Fuels* **2001**, *15* (2), 279–284. Available: https://doi.org/10.1021/ef000241s.
56. Lillo-Ródenas, M. A.; Cazorla-Amorós, D.; Linares-Solano, A. Behaviour of Activated Carbons with Different Pore Size Distributions and Surface Oxygen Groups for Benzene and Toluene Adsorption at Low Concentrations. *Carbon* **2005**, *43* (8), 1758–1767. Available: https://doi.org/10.1016/j.carbon.2005.02.023.
57. Lu, W.; Chung. Mesoporous Activated Carbon Filaments. *MRS Proceedings* **1996**, *454*. Available: https://doi.org/10.1557/proc-454-9.
58. Srivastava, V.C., Mall, I.D. and Mishra, I.M. (2008) Adsorption of Toxic Metal Ions onto Activated Carbon Study of Sorption Behaviour through Characterization and Kinetics. Chemical Engineering and Processing Process Intensification, 47, 1269-1280. - References - Scientific Research Publishing. www.scirp.org. Available: https://www.scirp.org/reference/referencespapers?referenceid=2909678.
59. Tan, Y.; Li, Y.; Wang, W.; Ran, F. High Performance Electrode of Few-Layer-Carbon@Bulk-Carbon Synthesized via Controlling Diffusion Depth from Liquid Phase to Solid Phase for Supercapacitors. *Journal of Energy Storage* **2020**, *32*, 101672. Available: https://doi.org/10.1016/j.est.2020.101672.
60. Li, H.; Eddaoudi, M.; O'Keeffe, M.; Yaghi, O. M. Design and Synthesis of an Exceptionally Stable and Highly Porous Metal-Organic Framework. *Nature* **1999**, *402* (6759), 276–279. Available: https://doi.org/10.1038/46248.
61. Furukawa, H.; Cordova, K. E.; O'Keeffe, M.; Yaghi, O. M. The Chemistry and Applications of Metal-Organic Frameworks. *Science (New York, N.Y.)* **2013**, *341* (6149), 1230444. Available: https://doi.org/10.1126/science.1230444.
62. Eddaoudi, M.; Moler, D. B.; Li, H.; Chen, B.; Reineke, T. M.; O'Keeffe, M.; Yaghi, O. M. Modular Chemistry: Secondary Building Units as a Basis for the Design of Highly Porous and Robust Metal−Organic Carboxylate Frameworks. *Accounts of Chemical Research* **2001**, *34* (4), 319–330. Available: https://doi.org/10.1021/ar000034b.
63. Hoskins, B. F.; Robson, R. Design and Construction of a New Class of Scaffolding-like Materials Comprising Infinite Polymeric Frameworks of 3D-Linked Molecular Rods. A Reappraisal of the Zinc Cyanide and Cadmium Cyanide Structures and the Synthesis and Structure of the Diamond-Related Frameworks $[N(CH_3)_4][CuIZnII(CN)_4]$ and CuI[4,4',4',4'''-Tetracyanotetraphenylmethane]BF4.$XC_6H_5NO_2$. *Journal of the American Chemical Society* **1990**, *112* (4), 1546–1554. Available: https://doi.org/10.1021/ja00160a038.
64. Abrahams, B. F.; Hoskins, B. F.; Robson, R. A New Type of Infinite 3D Polymeric Network Containing 4-Connected, Peripherally-Linked Metalloporphyrin Building Blocks. *Journal of the American Chemical Society* **1991**, *113* (9), 3606–3607. Available: https://doi.org/10.1021/ja00009a065.
65. Gedrich, K.; Senkovska, I.; Klein, N.; Stoeck, U.; Henschel, A.; Lohe, M. R.; Baburin, I. A.; Mueller, U.; Kaskel, S. A Highly Porous Metal-Organic Framework with Open Nickel

Sites. *Angewandte Chemie (International Ed. in English)* **2010**, *49* (45), 8489–8492. Available: https://doi.org/10.1002/anie.201001735.
66. Furukawa, H.; Cordova, K. E.; O'Keeffe, M.; Yaghi, O. M. The Chemistry and Applications of Metal-Organic Frameworks. *Science (New York, N.Y.)* **2013**, *341* (6149), 1230444. Available: https://doi.org/10.1126/science.1230444.
67. Lincke, J.; Lässig, D.; Merten Kobalz; Bergmann, J.; Handke, M.; Jens Möllmer; Lange, M.; Roth, C.; Möller, A.; Staudt, R.; Harald Krautscheid. An Isomorphous Series of Cubic, Copper-Based Triazolyl Isophthalate MOFs: Linker Substitution and Adsorption Properties. *Inorganic Chemistry* **2012**, *51* (14), 7579–7586. Available: https://doi.org/10.1021/ic3003228.
68. Sánchez-Sánchez, M.; Getachew, N.; Díaz, K.; Díaz-García, M.; Chebude, Y.; Díaz, I. Synthesis of Metal–Organic Frameworks in Water at Room Temperature: Salts as Linker Sources. *Green Chemistry* **2015**, *17* (3), 1500–1509. Available: https://doi.org/10.1039/c4gc01861c.
69. Mehlana, G.; Ramon, G.; Bourne, S. A. The Role of C–H···π Interactions in Modulating the Breathing Amplitude of a 2D Square Lattice Net: Alcohol Sorption Studies. *CrystEngComm* **2014**, *16* (35), 8160–8168. Available: https://doi.org/10.1039/c4ce00496e.
70. Yaghi, O. M.; Li, H. Hydrothermal Synthesis of a Metal-Organic Framework Containing Large Rectangular Channels. *Journal of the American Chemical Society* **1995**, *117* (41), 10401–10402. Available: https://doi.org/10.1021/ja00146a033.
71. Noro, S.; Kitagawa, S.; Kondo, M.; Seki, K. A New, Methane Adsorbent, Porous Coordination Polymer [{CuSiF6(4,4′-Bipyridine)2}N]. *Angewandte Chemie International Edition* **2000**, *39* (12), 2081–2084. Available: https://doi.org/10.1002/1521-3773(20000616)39:12%3C2081::aid-anie2081%3E3.0.co;2-a.
72. Kitagawa, S.; Kitaura, R.; Noro, S. Functional Porous Coordination Polymers. *Angewandte Chemie International Edition* **2004**, *43* (18), 2334–2375. Available: https://doi.org/10.1002/anie.200300610.
73. Getzschmann, J.; Senkovska, I.; Wallacher, D.; Tovar, M.; Fairen-Jimenez, D.; Düren, T.; J.M. van Baten; Krishna, R.; Kaskel, S. Methane Storage Mechanism in the Metal-Organic Framework $Cu_3(Btc)_2$: An *in-Situ* Neutron Diffraction Study. *Microporous and Mesoporous Materials* **2010**, *136* (1-3), 50–58. Available: https://doi.org/10.1016/j.micromeso.2010.07.020.
74. Kesanli, B.; Cui, Y.; Smith, M. R.; Bittner, E. W.; Bockrath, B. C.; Lin, W. Highly Interpenetrated Metal-Organic Frameworks for Hydrogen Storage. *Angewandte Chemie International Edition* **2005**, *44* (1), 72–75. Available: https://doi.org/10.1002/anie.200461214.
75. Voorde, B. V. de; Bueken, B.; Denayer, J.; Vos, D. D. Adsorptive Separation on Metal–Organic Frameworks in the Liquid Phase. *Chemical Society Reviews* **2014**, *43* (16), 5766–5788. Available: https://doi.org/10.1039/C4CS00006D.
76. Li, J.-R.; Sculley, J.; Zhou, H.-C. Metal–Organic Frameworks for Separations. *Chemical Reviews* **2011**, *112* (2), 869–932. Available: https://doi.org/10.1021/cr200190s.
77. Yu, H.; Xiang, Q.; Fang, M.; Yang, Q.; Feron, P. Promoted CO2 Absorption in Aqueous Ammonia. *Greenhouse Gases: Science and Technology* **2012**, *2* (3), 200–208. Available: https://doi.org/10.1002/ghg.1280.

78. Jhung, S. H.; Lee, J.-H.; Yoon, J. W.; Serre, C.; Férey, G.; Chang, J.-S. Microwave Synthesis of Chromium Terephthalate MIL-101 and Its Benzene Sorption Ability. *Advanced Materials* **2007**, *19* (1), 121–124. Available: https://doi.org/10.1002/adma.200601604.
79. Choi, E.; Park, K.; Yang, C.; Kim, H.-J.; Son, J.; Lee, S. W.; Young Hee Lee; Min, D.; Kwon, Y. Benzene-Templated Hydrothermal Synthesis of Metal-Organic Frameworks with Selective Sorption Properties. *Chemistry: A European Journal* **2004**, *10* (21), 5535–5540. Available: https://doi.org/10.1002/chem.200400178.
80. Dhakshinamoorthy, A.; Alvaro, M.; Garcia, H. Commercial Metal–Organic Frameworks as Heterogeneous Catalysts. *Chemical Communications* **2012**, *48* (92), 11275. Available: https://doi.org/10.1039/c2cc34329k.
81. Liu, J.; Chen, L.; Cui, H.; Zhang, J.; Zhang, L.; Su, C.-Y. Applications of Metal–Organic Frameworks in Heterogeneous Supramolecular Catalysis. *Chem. Soc. Rev.* **2014**, *43* (16), 6011–6061. Available: https://doi.org/10.1039/c4cs00094c.
82. Ranocchiari, M.; Bokhoven, van. Catalysis by Metal–Organic Frameworks: Fundamentals and Opportunities. *Physical Chemistry Chemical Physics* **2011**, *13* (14), 6388–6388. Available: https://doi.org/10.1039/c0cp02394a.
83. Lee, J.-S.; Halligudi, S. B.; Jang, N.-H.; Hwang, D.-W.; Chang, J.-S.; Hwang, Y.-K. Microwave Synthesis of a Porous Metal-Organic Framework, Nickel(II) Dihydroxyterephthalate and Its Catalytic Properties in Oxidation of Cyclohexene. *Bulletin of the Korean Chemical Society* **2010**, *31* (6), 1489–1495. Available: https://doi.org/10.5012/bkcs.2010.31.6.1489.
84. Zhang, H.; Osgood, H.; Xie, X.; Shao, Y.; Wu, G. Engineering Nanostructures of PGM-Free Oxygen-Reduction Catalysts Using Metal-Organic Frameworks. *Nano Energy* **2017**, *31*, 331–350. Available: https://doi.org/10.1016/j.nanoen.2016.11.033.
85. Kholdeeva, O. A. Liquid-Phase Selective Oxidation Catalysis with Metal-Organic Frameworks. *Catalysis Today* **2016**, *278*, 22–29. Available: https://doi.org/10.1016/j.cattod.2016.06.010.
86. Rojas, S.; Colinet, I.; Cunha, D.; Hidalgo, T.; Salles, F.; Serre, C.; Guillou, N.; Horcajada, P. Toward Understanding Drug Incorporation and Delivery from Biocompatible Metal–Organic Frameworks in View of Cutaneous Administration. *ACS Omega* **2018**, *3* (3), 2994–3003. Available: https://doi.org/10.1021/acsomega.8b00185.
87. BünzliJ.-C. G. Lanthanide Luminescence for Biomedical Analyses and Imaging. *Chemical Reviews* **2010**, *110* (5), 2729–2755. Available: https://doi.org/10.1021/cr900362e.
88. Horcajada, P.; Chalati, T.; Serre, C.; Gillet, B.; Sebrie, C.; Baati, T.; Eubank, J. F.; Heurtaux, D.; Clayette, P.; Kreuz, C.; Chang, J.-S.; Hwang, Y. K.; Marsaud, V.; Bories, P.-N.; Cynober, L.; Gil, S.; Férey, G.; Couvreur, P.; Gref, R. Porous Metal–Organic-Framework Nanoscale Carriers as a Potential Platform for Drug Delivery and Imaging. *Nature Materials* **2009**, *9* (2), 172–178. Available: https://doi.org/10.1038/nmat2608.
89. Della Rocca, J.; Liu, D.; Lin, W. Nanoscale Metal–Organic Frameworks for Biomedical Imaging and Drug Delivery. *Accounts of Chemical Research* **2011**, *44* (10), 957–968. Available: https://doi.org/10.1021/ar200028a.
90. Robson, R. Design and Its Limitations in the Construction of Bi- and Poly-Nuclear Coordination Complexes and Coordination Polymers (Aka MOFs): A Personal View. *Dalton Transactions* **2008**, No. 38, 5113. Available: https://doi.org/10.1039/b805617j.

91. Öhrström, L. Let's Talk about MOFs—Topology and Terminology of Metal-Organic Frameworks and Why We Need Them. *Crystals* **2015**, *5* (1), 154–162. Available: https://doi.org/10.3390/cryst5010154.
92. Batten, S. R.; Champness, N. R.; Chen, X.-M.; Garcia-Martinez, J.; Kitagawa, S.; Öhrström, L.; O'Keeffe, M.; Paik Suh, M.; Reedijk, J. Terminology of Metal–Organic Frameworks and Coordination Polymers (IUPAC Recommendations 2013). *Pure and Applied Chemistry* **2013**, *85* (8), 1715–1724. Available: https://doi.org/10.1351/pac-rec-12-11-20.
93. Zhang, J.; Li, Z.; Qi, X.-L.; Wang, D.-Y. Recent Progress on Metal–Organic Framework and Its Derivatives as Novel Fire Retardants to Polymeric Materials. *Nano-Micro Letters* **2020**, *12* (1). Available: https://doi.org/10.1007/s40820-020-00497-z.
94. Mendes, R. F.; Almeida Paz, F. A. Transforming Metal–Organic Frameworks into Functional Materials. *Inorganic Chemistry Frontiers* **2015**, *2* (6), 495–509. Available: https://doi.org/10.1039/c4qi00222a.
95. Laing M., The Packing of Molecules in Crystals, *South African Journal of Science,* 1975, **71** 171-175. Available: https://journals.co.za/doi/pdf/10.10520/AJA00382353_7287.
96. Batten, S. R.; Champness, N. R.; Chen, X.-M.; Garcia-Martinez, J.; Kitagawa, S.; Öhrström, L.; O'Keeffe, M.; Suh, M. P.; Reedijk, J. Coordination Polymers, Metal–Organic Frameworks and the Need for Terminology Guidelines. *CrystEngComm* **2012**, *14* (9), 3001. Available: https://doi.org/10.1039/c2ce06488j.
97. James, S. L. Metal-Organic Frameworks. *Chemical Society Reviews* **2003**, *32* (5), 276. Available: https://doi.org/10.1039/b200393g.
98. Öhrström, L. Let's Talk about MOFs—Topology and Terminology of Metal-Organic Frameworks and Why We Need Them. *Crystals* **2015**, *5* (1), 154–162. Available: https://doi.org/10.3390/cryst5010154.
99. Rosi, N.L.; Eckert, J.; Eddaoudi, M.; Vodka, T.D.; Kim, J.; O'Keefe, M.; Yashi, M.O. *Hydrogen Storage in Microporous Metal-Organic Frameworks. Science **2003**, 300 (5622), 1127–1129*. Available: https://doi.org/10.1126/science.1083440.
100. Brown, I. D. Topology and Chemistry. *Structural Chemistry* **2002**, *13* (3/4), 339–355. Available: https://doi.org/10.1023/a:1015872125545.
101. Blatov, V. A.; Carlucci, L.; Ciani, G.; Proserpio, D. M. Interpenetrating Metal–Organic and Inorganic 3D Networks: A Computer-Aided Systematic Investigation. Part I. Analysis of the Cambridge Structural Database. **2004**, *6* (65), 377–395. Available: https://doi.org/10.1039/b409722j.
102. O'Keeffe, M.; Peskov, M. A.; Ramsden, S. J.; Yaghi, O. M. The Reticular Chemistry Structure Resource (RCSR) Database Of, and Symbols For, Crystal Nets. *Accounts of Chemical Research* **2008**, *41* (12), 1782–1789. Available: https://doi.org/10.1021/ar800124u.
103. Vladislav, B. A. Topological Relations between Three-Dimensional Periodic Nets. I. Uninodal Nets. *Acta Crystallographica Section A: Foundations and Advances* **2007**, *63* (4), 329–343. Available: https://doi.org/10.1107/s0108767307022088.
104. Blatov, V. A.; Shevchenko, A. P.; Proserpio, D. M. Applied Topological Analysis of Crystal Structures with the Program Package ToposPro. *Crystal Growth & Design* **2014**, *14* (7), 3576–3586. Available: https://doi.org/10.1021/cg500498k.

105. Carlucci, L.; Ciani, G.; Proserpio, D. M.; Mitina, T. G.; Blatov, V. A. Entangled Two-Dimensional Coordination Networks: A General Survey. *Chemical Reviews* **2014**, *114* (15), 7557–7580. Available: https://doi.org/10.1021/cr500150m.
106. Moulton, B.; Zaworotko, M. J. From Molecules to Crystal Engineering: Supramolecular Isomerism and Polymorphism in Network Solids. *Chemical Reviews* **2001**, *101* (6), 1629–1658. Available: https://doi.org/10.1021/cr9900432.
107. Batten, S. R.; Neville, S. M.; Turner, D. R. *Coordination Polymers: Design, Analysis and Application*; Uk: Cambridge, 2009.
Available:
https://books.google.co.za/books?id=iuixgwRs2eQC&printsec=frontcover#v=onepage&q&f=false
108. Robin, A. Y.; Fromm, K. M. Coordination Polymer Networks with O- and N-Donors: What They Are, Why and How They Are Made. *Coordination Chemistry Reviews* **2006**, *250* (15-16), 2127–2157.
Available: https://doi.org/10.1016/j.ccr.2006.02.013.
109. Leong, W. L.; Vittal, J. J. One-Dimensional Coordination Polymers: Complexity and Diversity in Structures, Properties, and Applications. *Chemical Reviews* **2010**, *111* (2), 688–764. Available: https://doi.org/10.1021/cr100160e.
110. Delgado-Friedrichs, O.; O'Keeffe, M. Crystal Nets as Graphs: Terminology and Definitions. *Journal of Solid-State Chemistry* **2005**, *178* (8), 2480–2485.
Available: https://doi.org/10.1016/j.jssc.2005.06.011.
111. Vladislav, B. A. Topological Relations between Three-Dimensional Periodic Nets. I. Uninodal Nets. *Acta Crystallographica Section A: Foundations and Advances* **2007**, *63* (4), 329–343.Available: https://doi.org/10.1107/s0108767307022088.
112. Seetharaj, R.; Vandana, P. V.; Arya, P.; Mathew, S. Dependence of Solvents, PH, Molar Ratio and Temperature in Tuning Metal Organic Framework Architecture. *Arabian Journal of Chemistry* **2019**, *12* (3), 295–315.
Available: https://doi.org/10.1016/j.arabjc.2016.01.003.
113. AbdulHalim, R. G.; Shkurenko, A.; Alkordi, M. H.; Eddaoudi, M. Supramolecular Isomers of Metal–Organic Frameworks Derived from a Partially Flexible Ligand with Distinct Binding Motifs. *Crystal Growth & Design* **2016**, *16* (2), 722–727.
Available: https://doi.org/10.1021/acs.cgd.5b01307.
114. Stock, N.; Biswas, S. Synthesis of Metal-Organic Frameworks (MOFs): Routes to Various MOF Topologies, Morphologies, and Composites. *Chemical Reviews* **2011**, *112* (2), 933–969. Available: https://doi.org/10.1021/cr200304e.
115. Meek, S. T.; Greathouse, J. A.; Allendorf, M. D. Metal-Organic Frameworks: A Rapidly Growing Class of Versatile Nanoporous Materials. *Advanced Materials* **2010**, *23* (2), 249–267. Avaible: https://doi.org/10.1002/adma.201002854.
116. Užarević, K.; Wang, T. C.; Moon, S.-Y.; Fidelli, A. M.; Hupp, J. T.; Farha, O. K.; Friščić, T. Mechanochemical and Solvent-Free Assembly of Zirconium-Based Metal-Organic Frameworks. *Chemical communications (Cambridge, England)* **2016**, *52* (10), 2133–2136. Available: https://doi.org/10.1039/c5cc08972g.
117. Rabenau, A. The Role of Hydrothermal Synthesis in Preparative Chemistry. *Angewandte Chemie International Edition in English* **1985**, *24* (12), 1026–1040. Available: https://doi.org/10.1002/anie.198510261.

118. Tranchemontagne, D. J.; Mendoza-Cortés, J. L.; O'Keeffe, M.; Yaghi, O. M. Secondary Building Units, Nets and Bonding in the Chemistry of Metal–Organic Frameworks. *Chemical Society Reviews* **2009**, *38* (5), 1257. Available: https://doi.org/10.1039/b817735j.
119. Yaghi, O. M.; O'Keeffe, M.; Ockwig, N. W.; Chae, H. K.; Eddaoudi, M.; Kim, J. Reticular Synthesis and the Design of New Materials. *Nature* **2003**, *423* (6941), 705–714. Avaible: https://doi.org/10.1038/nature01650.
120. Eddaoudi, M. Systematic Design of Pore Size and Functionality in Isoreticular MOFs and Their Application in Methane Storage. *Science* **2002**, *295* (5554), 469–472. Available: https://doi.org/10.1126/science.1067208.
121. Rowsell, J. L. C.; Yaghi, O. M. Metal–Organic Frameworks: A New Class of Porous Materials. *Microporous and Mesoporous Materials* **2004**, *73* (1-2), 3–14. Available: https://doi.org/10.1016/j.micromeso.2004.03.034.
122. Haldar, R.; Sikdar, N.; Maji, T. K. Interpenetration in Coordination Polymers: Structural Diversities toward Porous Functional Materials. *Materials Today* **2015**, *18* (2), 97–116. Available: https://doi.org/10.1016/j.mattod.2014.10.038.
123. Mei, L.; Chai, Z.; Chai, Z. Ordered Entanglement in Actinide-Organic Coordination Polymers. *Bulletin of the Chemical Society of Japan* **2018**, *91* (4), 554–562. Available: https://doi.org/10.1246/bcsj.20170418.
124. Jiang, H.-L.; Makal, T. A.; Zhou, H.-C. Interpenetration Control in Metal–Organic Frameworks for Functional Applications. *Coordination Chemistry Reviews* **2013**, *257* (15-16), 2232–2249. Available: https://doi.org/10.1016/j.ccr.2013.03.017.
125. Gong, Y.-N.; Zhong, D.-C.; Lu, T.-B. Interpenetrating Metal–Organic Frameworks. *CrystEngComm* **2016**, *18* (15), 2596–2606. Available: https://doi.org/10.1039/c6ce00371k.
126. Aggarwal, H.; Das, R.; Bhatt, P. M.; Barbour, L. J. Isolation of a Structural Intermediate during Switching of Degree of Interpenetration in a Metal–Organic Framework. **2015**, *6* (8), 4986–4992. Available: https://doi.org/10.1039/c5sc01796c.
127. Zhang, J.; Wojtas, L.; Larsen, R. W.; Eddaoudi, M.; Zaworotko, M. J. Temperature and Concentration Control over Interpenetration in a Metal−Organic Material. *Journal of the American Chemical Society* **2009**, *131* (47), 17040–17041. Available: https://doi.org/10.1021/ja906911q.
128. Aggarwal, H.; Das, R.; Bhatt, P. M.; Barbour, L. J. Isolation of a Structural Intermediate during Switching of Degree of Interpenetration in a Metal–Organic Framework. **2015**, *6* (8), 4986–4992. Available: https://doi.org/10.1039/c5sc01796c.
129. Verma, G.; Butikofer, S.; Kumar, S.; Ma, S. Regulation of the Degree of Interpenetration in Metal–Organic Frameworks. *Topics in Current Chemistry* **2019**, *378* (1). Available: https://doi.org/10.1007/s41061-019-0268-x.
130. Elsaidi, S. K.; Mohamed, M. H.; Wojtas, Ł.; Anjana Chanthapally; Pham, T.; Space, B.; Vittal, J. J.; Zaworotko, M. J. Putting the Squeeze on $CH_4$ and $CO_2$ through Control over Interpenetration in Diamondoid Nets. *Journal of the American Chemical Society* **2014**, *136* (13), 5072–5077. Available: https://doi.org/10.1021/ja500005k.
131. Ferguson, A.; Liu, L.; Tapperwijn, S. J.; Perl, D.; Coudert, F.-X.; Van Cleuvenbergen, S.; Verbiest, T.; van der Veen, M. A.; Telfer, S. G. Controlled Partial Interpenetration in Metal-Organic Frameworks. *Nature Chemistry* **2016**, *8* (3), 250–257. Available: https://doi.org/10.1038/nchem.2430.

132. Yang, G.-P.; Hou, L.; Ma, L.-F.; Wang, Y.-Y. Investigation on the Prime Factors Influencing the Formation of Entangled Metal–Organic Frameworks. *CrystEngComm* **2013**, *15* (14), 2561. Available: https://doi.org/10.1039/c3ce26435a.
133. Barbour, L. J. Crystal Porosity and the Burden of Proof. **2006**, No. 11, 1163–1163. Available: https://doi.org/10.1039/b515612m.
134. Prasad, T. K.; Suh, M. P. Control of Interpenetration and Gas-Sorption Properties of Metal-Organic Frameworks by a Simple Change in Ligand Design. *Chemistry - A European Journal* **2012**, *18* (28), 8673–8680. Available: https://doi.org/10.1002/chem.201200456.
135. Lun, D. J.; Geoffrey; Telfer, S. G. A General Thermolabile Protecting Group Strategy for Organocatalytic Metal−Organic Frameworks. *Journal of the American Chemical Society* **2011**, *133* (15), 5806–5809. Available: https://doi.org/10.1021/ja202223d.
136. Sing, K. S. W. Adsorption Methods for the Characterization of Porous Materials. *Advances in Colloid and Interface Science* **1998**, *76-77*, 3–11. Available: https://doi.org/10.1016/s0001-8686(98)00038-4.
137. Dai, Z.; Deng, J.; Aboukeila, H.; Yan, J.; Ansaloni, L.; Mineart, K. P.; Giacinti Baschetti, M.; Spontak, R. J.; Deng, L. Highly $CO_2$-Permeable Membranes Derived from a Midblock-Sulfonated Multiblock Polymer after Submersion in Water. *NPG Asia Materials* **2019**, *11* (1), 1–7. Available: https://doi.org/10.1038/s41427-019-0155-5.
138. MacGillivray, L. R.; Papaefstathiou, G. S.; Friščić, T.; Hamilton, T. D.; Bučar, D.-K.; Chu, Q.; Varshney, D. B.; Georgiev, I. G. Supramolecular Control of Reactivity in the Solid State: From Templates to Ladderanes to Metal−Organic Frameworks. *Accounts of Chemical Research* **2008**, *41* (2), 280–291. Available: https://doi.org/10.1021/ar700145r.
139. Vittal, J. J. Supramolecular Structural Transformations Involving Coordination Polymers in the Solid State. *Coordination Chemistry Reviews* **2007**, *251* (13-14), 1781–1795. https://doi.org/10.1016/j.ccr.2007.02.002.
140. Halder, G. J. Guest-Dependent Spin Crossover in a Nanoporous Molecular Framework Material. *Science* **2002**, *298* (5599), 1762–1765. Available: https://doi.org/10.1126/science.1075948.
141. Matsuda, R.; Kitaura, R.; Kitagawa, S.; Kubota, Y.; Kobayashi, T. C.; Horike, S.; Takata, M. Guest Shape-Responsive Fitting of Porous Coordination Polymer with Shrinkable Framework. *Journal of the American Chemical Society* **2004**, *126* (43), 14063–14070. Available: https://doi.org/10.1021/ja046925m.
142. Bradshaw, D.; Warren, J. E.; Rosseinsky, M. J. Reversible Concerted Ligand Substitution at Alternating Metal Sites in an Extended Solid. *Science* **2007**, *315* (5814), 977–980. https://doi.org/10.1126/science.1135445.
143. Lee, E.B.; Jang, S.-Y.; Myunghyun Paik Suh. Multifunctionality and Crystal Dynamics of a Highly Stable, Porous Metal−Organic Framework $[Zn_4O(NTB)_2]$. **2005**, *127* (17), 6374–6381. Available: https://doi.org/10.1021/ja043756x.
144. Horike, S.; Matsuda, R.; Tanaka, D.; Matsubara, S.; Mizuno, M.; Endo, K.; Kitagawa, S. Dynamic Motion of Building Blocks in Porous Coordination Polymers. *Angewandte Chemie International Edition* **2006**, *45* (43), 7226–7230. Available: https://doi.org/10.1002/anie.200603196.

145. Zhang, J.-P.; Liao, P.-Q.; Zhou, H.-L.; Lin, R.-B.; Chen, X.-M. Single-Crystal X-Ray Diffraction Studies on Structural Transformations of Porous Coordination Polymers. *Chem. Soc. Rev.* **2014**, *43* (16), 5789–5814. Available: https://doi.org/10.1039/c4cs00129j.
146. Allan, P. K.; Xiao, B.; Teat, S. J.; Knight, J. W.; Morris, R. E. In Situ Single-Crystal Diffraction Studies of the Structural Transition of Metal−Organic Framework Copper 5-Sulfoisophthalate, Cu-SIP-3. *Journal of the American Chemical Society* **2010**, *132* (10), 3605–3611. Available: https://doi.org/10.1021/ja910600b.
147. Gómez-Gualdrón, D. A.; Colón, Y. J.; Zhang, X.; Wang, T. C.; Chen, Y.-S.; Hupp, J. T.; Yildirim, T.; Farha, O. K.; Zhang, J.; Snurr, R. Q. Evaluating Topologically Diverse Metal–Organic Frameworks for Cryo-Adsorbed Hydrogen Storage. *Energy & Environmental Science* **2016**, *9* (10), 3279–3289. Available: https://doi.org/10.1039/c6ee02104b.
148. Kitagawa, S.; Uemura, K. Dynamic Porous Properties of Coordination Polymers Inspired by Hydrogen Bonds. *Chemical Society Reviews* **2005**, *34* (2), 109–109. Available: https://doi.org/10.1039/b313997m.
149. Satoshi Horike; Nagarkar, S. S.; Ogawa, T.; Kitagawa, S. A New Dimension for Coordination Polymers and Metal–Organic Frameworks: Towards Functional Glasses and Liquids. *Angewandte Chemie* **2020**, *59* (17), 6652–6664. Available: https://doi.org/10.1002/anie.201911384.
150. Carrington, E. J.; McAnally, C. A.; Fletcher, A. J.; Thompson, S. P.; Warren, M.; Brammer, L. Solvent-Switchable Continuous-Breathing Behaviour in a Diamondoid Metal–Organic Framework and Its Influence on CO2 versus CH4 Selectivity. *Nature Chemistry* **2017**, *9* (9), 882–889. Available: https://doi.org/10.1038/nchem.2747.
151. Férey, G. Giant Flexibility of Crystallized Organic–Inorganic Porous Solids: Facts, Reasons, Effects and Applications. *New Journal of Chemistry* **2016**, *40* (5), 3950–3967. Available: https://doi.org/10.1039/c5nj02747k.
152. Zhang, S.-Y.; Jensen, S.; Tan, K.; Wojtas, L.; Roveto, M.; Cure, J.; Thonhauser, T.; Chabal, Y. J.; Zaworotko, M. J. Modulation of Water Vapor Sorption by a Fourth-Generation Metal-Organic Material with a Rigid Framework and Self-Switching Pores. *Journal of the American Chemical Society* **2018**, *140* (39), 12545–12552. Available: https://doi.org/10.1021/jacs.8b07290.
153. Foo, M.L.; Matsuda, R.; Yuh Hijikata; Krishna, R.; Sato, H.; Satoshi Horike; Hori, A.; Duan, J.; Sato, Y.; Kubota, Y.; Takata, M.; Kitagawa, S. An Adsorbate Discriminatory Gate Effect in a Flexible Porous Coordination Polymer for Selective Adsorption of $CO_2$ over $c_2H_2$. **2016**, *138* (9), 3022–3030. Available: https://doi.org/10.1021/jacs.5b10491.
154. Uemura, K.; Kitagawa, S.; Kondo, M.; Fukui, K.; Kitaura, R.; Chang, H.-C.; Mizutani, T. Novel Flexible Frameworks of Porous Cobalt(II) Coordination Polymers That Show Selective Guest Adsorption Based on the Switching of Hydrogen-Bond Pairs of Amide Groups. *Chemistry - A European Journal* **2002**, *8* (16), 3586. Available: https://doi.org/10.1002/1521-3765(20020816)8:16%3C3586::aid-chem3586%3E3.0.co;2-k.
155. Sakata, Y.; Furukawa, S.; Kondo, M.; Hirai, K.; Horike, N.; Takashima, Y.; Uehara, H.; Louvain, N.; Meilikhov, M.; Tsuruoka, T.; Isoda, S.; Kosaka, W.; Sakata, O.; Kitagawa, S. Shape-Memory Nanopores Induced in Coordination Frameworks by Crystal Downsizing. *Science* **2013**, *339* (6116), 193–196. Available: https://doi.org/10.1126/science.1231451.

156. Yang, Q.; Lama, P.; Sen, S.; Matteo Lusi; Chen, K.; Gao, W.; Mohana Shivanna; Pham, T.; Nobuhiko Hosono; Kusaka, S.; Perry, J. J.; Ma, S.; Space, B.; Barbour, L. J.; Kitagawa, S.; Zaworotko, M. J. Reversible Switching between Highly Porous and Nonporous Phases of an Interpenetrated Diamondoid Coordination Network That Exhibits Gate-Opening at Methane Storage Pressures. *Angewandte Chemie* **2018**, *57* (20), 5684–5689. Available: https://doi.org/10.1002/anie.201800820.
157. F. H. Allen, S. Bellard, M. D. Brice, B. A. Cartwright, A. Doubleday, H. Higgs, T. Hummelink, B. G. Hummelink-Peters, O. Kennard, W. D. S. Motherwell, J. R. Rodgers, D. G. Watson, Acta Crystallogr. Sect. B 1979, 35, 2332 – 2339.
158. Ewald, P.P.; Hermann, C.; Strukturbericht 1913 – 1928, Akademische Verlagsgesellschaft, Leipzig, 1929.
159. Bruno, I. J.; Cole, J. C.; Edgington, P. R.; Kessler, M.; Macrae, C. F.; McCabe, P.; Pearson, J.; Taylor, R. New Software for Searching the Cambridge Structural Database and Visualizing Crystal Structures. *Acta Crystallographica Section B Structural Science* **2002**, *58* (3), 389–397. Available: https://doi.org/10.1107/s0108768102003324.
160. Pauling, L. The Principles Determining the Structure of Complex Ionic Crystals. *Journal of the American Chemical Society* **1929**, *51* (4), 1010–1026. Available: https://doi.org/10.1021/ja01379a006.
161. Allen, F. H.; Bellard, S.; Brice, M. D.; Cartwright, B. A.; Doubleday, A.; Higgs, H.; Hummelink, T.; Hummelink-Peters, B. G.; Kennard, O.; Motherwell, W. D. S.; Rodgers, J. R.; Watson, D. G. The Cambridge Crystallographic Data Centre: Computer-Based Search, Retrieval, Analysis and Display of Information. *Acta Crystallographica Section B Structural Crystallography and Crystal Chemistry* **1979**, *35* (10), 2331–2339. Available: https://doi.org/10.1107/s0567740879009249.
162. Groom, C. R.; Bruno, I. J.; Lightfoot, M. P.; Ward, S. C. The Cambridge Structural Database. *Acta Crystallographica Section B: Structural Science, Crystal Engineering and Materials* **2016**, *72* (2), 171–179. Available: https://doi.org/10.1107/S2052520616003954.
163. Li, A.; Bueno-Perez, R.; Wiggin, S.; Fairen-Jimenez, D. Enabling Efficient Exploration of Metal–Organic Frameworks in the Cambridge Structural Database. *CrystEngComm* **2020**, *22* (43), 7152–7161. Available: https://doi.org/10.1039/d0ce00299b.
164. Li, A.; Bueno-Perez, R.; Wiggin, S.; Fairen-Jimenez, D. Enabling Efficient Exploration of Metal–Organic Frameworks in the Cambridge Structural Database. *CrystEngComm* **2020**, *22* (43), 7152–7161. Available: https://doi.org/10.1039/d0ce00299b.
165. Hartshorn, R.M.; Hellwich, K.-H.; Yerin, A.; Damhus, T.; Hutton, A.T. *Brief Guide to the Nomenclature of Inorganic Chemistry. Chemistry International* ***2015***, 37 (5-6). Available: https://doi.org/10.1515/ci-2015-0524.
166. Wilmer, C. E.; Leaf, M.; Lee, C. Y.; Farha, O. K.; Hauser, B. G.; Hupp, J. T.; Snurr, R. Q. Large-Scale Screening of Hypothetical Metal–Organic Frameworks. *Nature Chemistry* **2011**, *4* (2), 83–89. Available: https://doi.org/10.1038/nchem.1192.
167. Watanabe, T.; Sholl, D. S. Accelerating Applications of Metal–Organic Frameworks for Gas Adsorption and Separation by Computational Screening of Materials. *Langmuir* **2012**, *28* (40), 14114–14128. Available: https://doi.org/10.1021/la301915s.

168. Goldsmith, J.; Wong-Foy, A. G.; Cafarella, M. J.; Siegel, D. J. Theoretical Limits of Hydrogen Storage in Metal–Organic Frameworks: Opportunities and Trade-Offs. *Chemistry of Materials* **2013**, *25* (16), 3373–3382.
Available: https://doi.org/10.1021/cm401978e.

169. Chung, Y. G.; Camp, J.; Haranczyk, M.; Sikora, B. J.; Bury, W.; Krungleviciute, V.; Yildirim, T.; Farha, O. K.; Sholl, D. S.; Snurr, R. Q. Computation-Ready, Experimental Metal–Organic Frameworks: A Tool to Enable High-Throughput Screening of Nanoporous Crystals. *Chemistry of Materials* **2014**, *26* (21), 6185–6192.
Available: https://doi.org/10.1021/cm502594j.

170. Moghadam, P. Z.; Li, A.; Wiggin, S. B.; Tao, A.; Maloney, A. G. P.; Wood, P. A.; Ward, S. C.; Fairen-Jimenez, D. Development of a Cambridge Structural Database Subset: A Collection of Metal–Organic Frameworks for Past, Present, and Future. *Chemistry of Materials* **2017**, *29* (7), 2618–2625.
Available: https://doi.org/10.1021/acs.chemmater.7b00441.

# CHAPTER 2

# Experimental and Computational Methods

This chapter lists the metal salt, organic ligand and solvents that were utilized in the synthesis of metal-organic frameworks in this project. Synthetic protocol and analytical methods used to characterize MOFs, included X-ray diffraction, hot stage microscopy, differential scanning calorimetry, thermogravimetric analysis, and gas sorption The programs used to solve, refine and analyze the crystal structures, as well as those used to mine the Cambridge Structural Database and analyze the mined structures, are also described.

## 2.1. MATERIALS

The organic ligand (**Figure 2.1**) 4,4'-(hexaflouroisopropylidene)bis(benzoic acid) (purity 98%.), Copper(II) nitrate hemi(pentahydrate) ($Cu(NO_3)_2 \cdot 2.5\ H_2O$) (purity 98%), *N,N'*-dimethylformamide (purity 99.8%), *N,N'*-diethylformamide (purity 99.8%), *N,N'*-dimethylacetamide (purity 99.8%), *N,N'*-diethylacetamide (purity 99.8%), were all purchased from Sigma Aldrich. These starting materials were used without any further purification. Deionised water was obtained from a Milli-Q water purification system.[1]

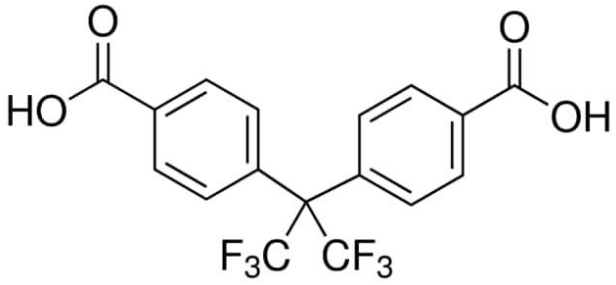


**Figure 2.1.** The structure of 4,4′-(hexafluoroisopropylidene)bis(benzoic acid).

## 2.2. GENERAL SYNTHESIS

**General Synthetic Methodology: Solvothermal synthesis**

Metal-organic frameworks were synthesized using one method:

solvothermal synthesis using vials. Copper(II) nitrate hemi(pentahydrate) ($Cu(NO_3)_2 \cdot 2.5\ H_2O$) amounts were carefully weighed out and dissolved in water separately. 4,4′-(hexafluoroisopropylidene)bis(benzoic acid) was dissolved in *N,N'*-dimethylformamide for vial 1 and *N,N'*-diethylformamide for vail 2, respectively. Each solution of ($Cu(NO_3)_2 \cdot 2.5\ H_2O$) was added to each vail of ligand dissolved in specific solvent.

The solvent containing reagents were sealed under high pressure (above 1 atm) and temperature 90 °C in a glass vail and heated for different hours/days in an oven before being slowly cooled to promote crystallization.

## 2.3. STRUCTURAL ANALYSIS

### 2.3.1. Single Crystal X-ray Diffraction (SCXRD)

The analysis method of single crystal X-ray diffraction (SCD) is effective for revealing the crystalline material's structure. A crystal's molecular packing and arrangement can be seen, allowing for the evaluation of atomic coordination, bond lengths, bond distances, and intermolecular interactions.

Single crystals of suitable quality were selected and mounted using a cryoloop and Paratone N oil. Data collections were carried out on Bruker D8 Venture diffractometer using Mo-*Kα* ($\lambda$ = 0.71073 Å) radiation, produced at 50 kV and 1.4 mA, with the crystal temperature controlled using an Oxford Cryostream- 800. Data reduction and unit cell parameter refinement were performed using SAINT-Plus.[2] All intensity data were scaled and corrected for Lorentz-polarisation and absorption effects using the programme SADABS.[3] Structure solution and refinement were implemented using the crystallographic suite OLEX2.[4] The crystal structures were solved by SHELXT,[5] with subsequent refinement using the full-matrix least square method, based on $F^2$ values against all reflections, including anisotropic displacement parameters for all non-H atoms, as employed in SHELXL-2018/9.[6] X-Seed and MERCURY were used for generating high- quality crystal structure images.[7,9] Both programs use the POV-RAY program to generate the images.[9]

### 2.3.2. Powder X-Ray Diffraction (PXRD)

Powder X-ray diffraction (PXRD) involves the X-ray irradiation of a polycrystalline sample. PXRD produces 'fingerprint' patterns which are unique to the analysed materials. The Bruker D2 Phaser 2$^{nd}$ Gen X-ray diffractometer with a CuKα radiation (λ= 1.5406) and X-ray generator fixed with X-rays generated at a current flow of 10 mA and a voltage of 30kV, was used to collect the PXRD data. The PXRD patterns were collected over a range of $4 - 40^o$ using a step size rate of $0.016^o s^{-1}$ resulting in a run time of 15 minutes.

Variable-Temperature Powder X-ray diffraction (VT-PXRD) measurements were performed on a Bruker D8 Advance X-ray diffractometer in the $4 - 40^{\circ}$ $2\theta$ range using a step size rate $0.015\ ^{\circ}.s^{-1}$ and X-rays generated at 30 kV and 40 mA. Experimentally obtained PXRD patterns were compared to the simulated PXRD patterns calculated from the single crystal data by using MERCURY. A Bruker wide-temperature Bruker MTC stage which was used to heat the samples in situ under vacuum and thus record changes in the PXRD patterns upon activation of the MOFs.

## 2.4. THERMAL ANALYSIS

The physical properties of the crystals were evaluated using three thermal analysis techniques, namely, hot stage microscopy (HSM), thermogravimetric analysis (TGA), and differential scanning calorimetry (DSC).

### 2.4.1 Hot Stage Microscopy (HSM)

This technique permits for the visualization of thermal events such as desolvation or decomposition. It was moreover utilized to observe visual changes (such as colour changes) which may not be observable using TGA or DSC. This type of examination is qualitative and may exhibit temperature differences with respect to the onset of thermal events when compared to DSC and TGA due to differences in experimental setups.

The samples were placed on a coverslip under silicon oil (bubble formation in the oil indicate release of solvent or decomposition) and viewed with a Nikon SMZ-10 stereoscopic microscope fitted with a Linkam THMS600 hot stage and a Linkam TP92 temperature control unit. A real-time Sony Digital Hyper HAD colour video camera was used to capture thermal events and images were viewed with the Soft Imaging System program called analySIS. A heating rate of 10 °C $min^{-1}$ was used to study the thermal behaviour of the sample. Samples were heated over a temperature range of room temperature to 450 °C.

### 2.4.2. Thermogravimetric Analysis (TGA)

TGA measures the percentage mass loss of a sample as a function of temperature. This was used to determine MOF:solvent ratios and the thermal stabilities of the desolvated frameworks in terms of their coordination bonds, i.e., when the MOFs start to decompose. Surface-dried samples of 2-3 mg were placed in open aluminium pans. A heating rate of 10 °C $min^{-1}$ was used, whilst temperatures ranges varied according to the initial results obtained by HSM. TGA was performed on a TA-Q500 analyser (**Figure 2.2**) from TA instruments with the Universal Analysis 2000 software to analyse the results obtained from TGA experiments. Dry nitrogen gas flowed over the samples at 60 $cm^3$ $min^{-1}$.

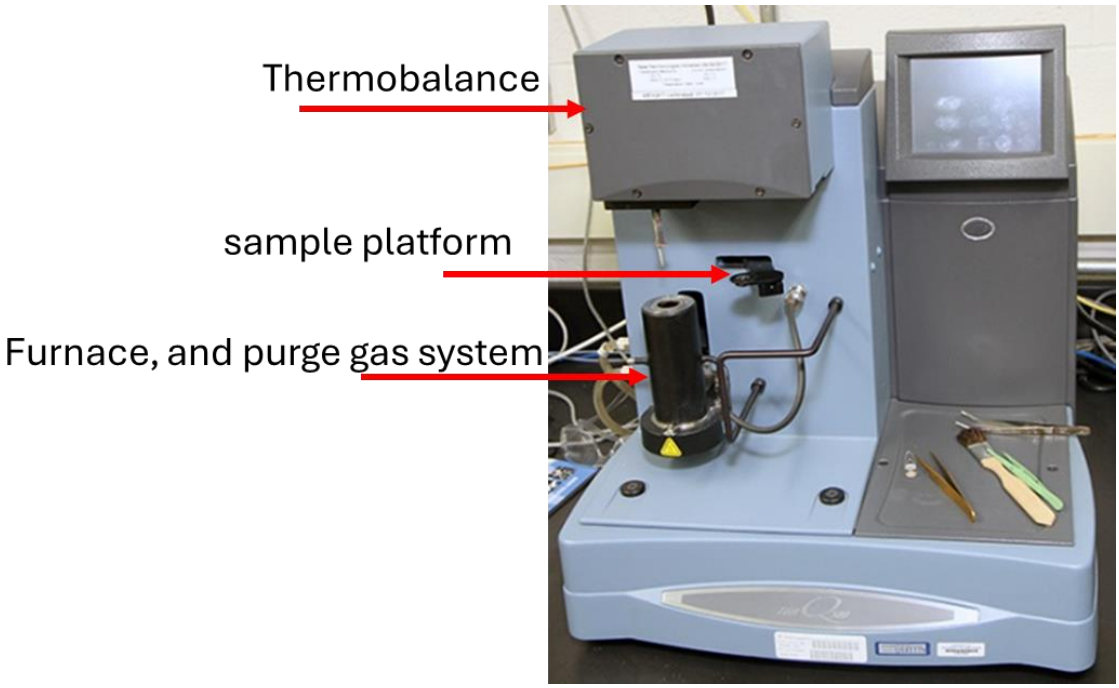


**Figure 2.2.** TGA Q500 used for TGA analyses.

### 2.4.3. Differential Scanning Calorimetry

DSC was used to measure the difference in the heat flow between the sample and reference pans, with this difference plotted as a function of temperature (**Figure 2.3**). The temperature range over which the endo- or exotherms occur of different thermal events, such as desolvation and decomposition, were measured. Surface-dried samples of 1-2 mg were used for all runs. Samples were placed in aluminium pans with holes in the lid to allow for ventilation and heated at 10 °C $min^{-1}$. Exothermic and endothermic reactions are presented on the DSC thermograms by peaks and troughs, respectively. The temperature range used was determined by prior HSM and TG analysis as samples were not taken to decomposition in order to avoid spillage and instrument damage.

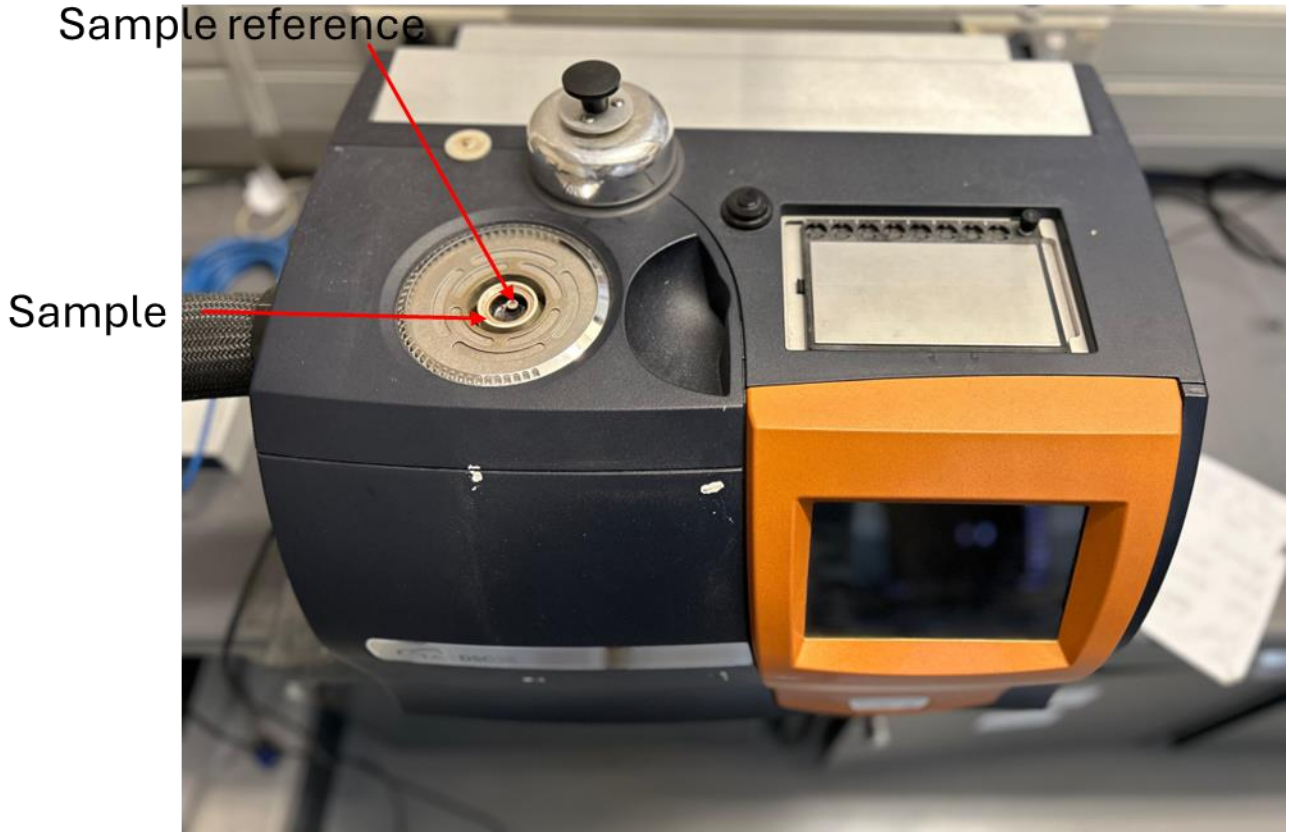


**Figure 2.3.** DSC25 used for DSC analyses.

## 2.5. ADDITIONAL STRUCTURE ANALYSIS PROGRAMS

### 2.5.1. Cambridge Structural Database (CSD)

The Cambridge Crystallographic Data Centre (CCDC) manages and provides the Cambridge Structural Database (CSD).[10] Given that it has comprehensive records, including the chemical formula, structure, unit cell, defined geometry, intermolecular interactions, authors, etc., it is an effective tool for searching published single-crystal structures. More than 50 years have passed since the database was created.[10]

### 2.5.2. Mercury

Exploring and visualizing structures is possible with Mercury,[11-13] a component of the CSD software suite. In addition to morphology calculations, the program includes capabilities such as simulations of powder diffractograms, multiple structure overlay, computation and visualization of volume accessible to probes, and probe-accessible volume.[14]

### 2.5.3. PoreBlazer

PoreBlazer, developed as simulation package for computational characterization of crystalline and amorphous materials. It is mainly used to calculate the pore volume, accessible surface area, largest pore diameter, pore limiting diameter, pore size distribution, and other properties.[15,16]

### 2.5.4. ToposPro

An extensive investigation of the geometrical and topological characteristics of periodic structures (crystals, networks, and tilings) can be performed using the software package known as ToposPro. ToposPro was developed with the specific purpose of processing huge crystallographic data sets and identifying correlations between structural parameters. ToposPro is capable of completing crystallochemical tasks such as (i) topological classification and identification of periodic and molecular structures, (ii) search for occurrence of topological motifs in crystal structures, (iii) analysis of molecular packings, these are a few.[17-22]

## 2.6. GAS AND WATER VAPOUR SORPTION

Studies on gas sorption were conducted to find out whether the MOFs could take up gases like nitrogen and carbon dioxide. In addition, studies on the sorption of water vapor was also carried out on the substances. Using a Micromeritics 3Flex Surface Area Analyzer, these tests were conducted. The samples were heated up to 200 °C under vacuum before beginning the examination. This made sure that any solvent that was still in the sample was evacuated because the analysis needed an empty framework.

A Micromeritics Flowprep was used to process 150–200 mg of the sample, which was heated to 60 °C and exposed to a continuous flow of nitrogen gas for at least 24 hours in order to completely remove any solvent from the sample's structure. During tests carried out at 273 - 298 K a Micromeritics water bath was utilized, whereas liquid nitrogen was used for experiments carried out at 77 K. Acetone and dry ice were combined to provide a low temperature slurry at 195 K, which was employed for gas sorption tests. Surface areas were determined using the Brunauer-Emmett-Teller (BET) model.

## 2.7. Appendices

Supplementary data obtained from single crystal X-ray studies are provided as electronic supplementary information.

**Table 1.1.** Crystallographic data files that can be found in the Appendices.

| File Extensions | Contents |
|---|---|
| .hkl | Reflection data |
| .res | SHELX coordinate data |
| .lis | PLATON output file |
| .cif | Crystallographic information data |
| .pdf | CheckCif Report |
| .fcf | Observed and calculated intensities |

## 2.8. References


1. Milli-Q Water, Millipore Corporation, Billerica, Massachusetts, USA.

2. Bruker D8 VENTURE, v20193; Bruker AXS Inc., Madison, WI, USA. Apex3, 2019.

3. G.M. Sheldrick. SADABS; Bruker AXS Inc.: Madison, Wisconsin, USA, 2001

4. O.V. Dolomanov, L.J. Bourhis, R.J. Gildea, J.A.K. Howard, H. Puschmann, OLEX2: A complete structure solution, refinement and analysis program. J. Appl. Crystallogr. 2009, 42, 339−341.

5. G.M. Sheldrick, SHELXT - Integrated space-group and crystalstructure determination. Acta Crystallogr., Sect. A: Found. Adv. 2015,71, 3−8

6. G.M. Sheldrick, Crystal structure refinement with SHELXL. Acta Crystallogr., Sect. C: Struct. Chem. 2015, 71, 3−8.

7. L.J. Barbour, X-Seed 4: updates to a program for smallmolecule supramolecular crystallography. J. Appl. Crystallogr. 2020, 53, 1141−1146

8. C.F. Macrae, I.J. Bruno, J.A. Chisholm, P.R. Edgington, P. McCabe, E. Pidcock, L Rodriguez-Monge, R. Taylor, J. van de Streek, P.A. Wood, Mercury CSD 2.0 - new features for the visualization and investigation of crystal structures. J. Appl. Crystallogr. 2008, 41, 466−470

9. POV-Ray for Windows, ver. 3.6; Persistence of Vision Raytracer Pty. Ltd.: 2004

10. C. R. Groom, I. J. Bruno, M. P. Lightfoot and S. C. Ward, Acta Crystallogr.

Sect. B Struct. Sci. Cryst. Eng. Mater., 2016, B72, 171–179.

11. C. F. Macrae, P. R. Edgington, P. McCabe, E. Pidcock, G. P. Shields, R. Taylor, M. Towler and J. Van De Streek, J. Appl. Crystallogr., 2006, 39, 453–457.

12. C. F. Macrae, I. J. Bruno, J. A. Chisholm, P. R. Edgington, P. McCabe, E. Pidcock, L. Rodriguez-Monge, R. Taylor, J. Van De Streek and P. A. Wood, J. Appl. Crystallogr., 2008, 41, 466–47.

13. Macrae, C. F.; Sovago, I.; Cottrell, S. J.; Galek, P. T. A.; McCabe, P.; Pidcock, E.; Platings, M.; Shields, G. P.; Stevens, J. S.; Towler, M.; Wood, P. A. Mercury 4.0: From Visualization to Analysis, Design and Prediction. *Journal of Applied Crystallography* **2020**, *53* (1), 226–235. https://doi.org/10.1107/S1600576719014092.

14. van Heerden, D. P.; Barbour, L. J. Guest-Occupiable Space in the Crystalline Solid State: A Simple Rule-of-Thumb for Predicting Occupancy. *Chemical Society Reviews* **2021**, *50* (2), 735–749. Available: https://doi.org/10.1039/d0cs01040e.

15. Sarkisov, L.; Harrison, A. Computational Structure Characterisation Tools in Application to Ordered and Disordered Porous Materials. *Molecular Simulation* **2011**, *37* (15), 1248–1257. Available: https://doi.org/10.1080/08927022.2011.592832.

16. Sarkisov, L.; Kim, J. Computational Structure Characterization Tools for the Era of Material Informatics. *Chemical Engineering Science* **2015**, *121*, 322–330. Available: https://doi.org/10.1016/j.ces.2014.07.022.

17. Blatov, V. A. Voronoi–Dirichlet Polyhedra in Crystal Chemistry: Theory and Applications. *Crystallography Reviews* **2004**, *10* (4), 249–318. Available: https://doi.org/10.1080/08893110412331323170.

18 Blatov, B. A.; Olaf Delgado-Friedrichs; O'Keeffe, M.; Proserpio, D. M. Three-Periodic Nets and Tilings: Natural Tilings for Nets. *Acta Crystallographica Section A: Foundations and Advances* **2007**, *63* (5), 418–425. Available: https://doi.org/10.1107/s0108767307038287.

19. Blatov, V. A. *Multipurpose crystallochemical analysis with the program package TOPOS*. www.iucr.org. https://www.iucr.org/resources/commissions/crystallographic-computing/newsletters/7/topos (accessed 2024-02-05).

20. Blatov, V. A. Nanocluster Analysis of Intermetallic Structures with the Program Package TOPOS. *Structural Chemistry* **2012**, *23* (4), 955–963. Available: https://doi.org/10.1007/s11224-012-0013-3.

21. Blatov, V. A.; O'Keeffe, M.; Proserpio, D. M. Vertex-, Face-, Point-, Schläfli-, and Delaney-Symbols in Nets, Polyhedra and Tilings: Recommended Terminology. *CrystEngComm* **2010**, *12* (1), 44–48. https://doi.org/10.1039/b910671e.

22. Blatov, V. A.; Carlucci, L.; Ciani, G.; Proserpio, D. M. Interpenetrating Metal–Organic and Inorganic 3D Networks: A Computer-Aided Systematic Investigation. Part I. Analysis of the Cambridge Structural Database. **2004**, *6* (65), 377–395. https://doi.org/10.1039/b409722j.

# CHAPTER 3

The search for entangled (this is the 'umbrella' term which includes interpenetration and polycatenation) metal-organic frameworks structures is covered in this section. The searches are conducted using the Cambridge Structural Database (CSD) program Conquest on the CSD MOF subset (**Figure 3.1**).

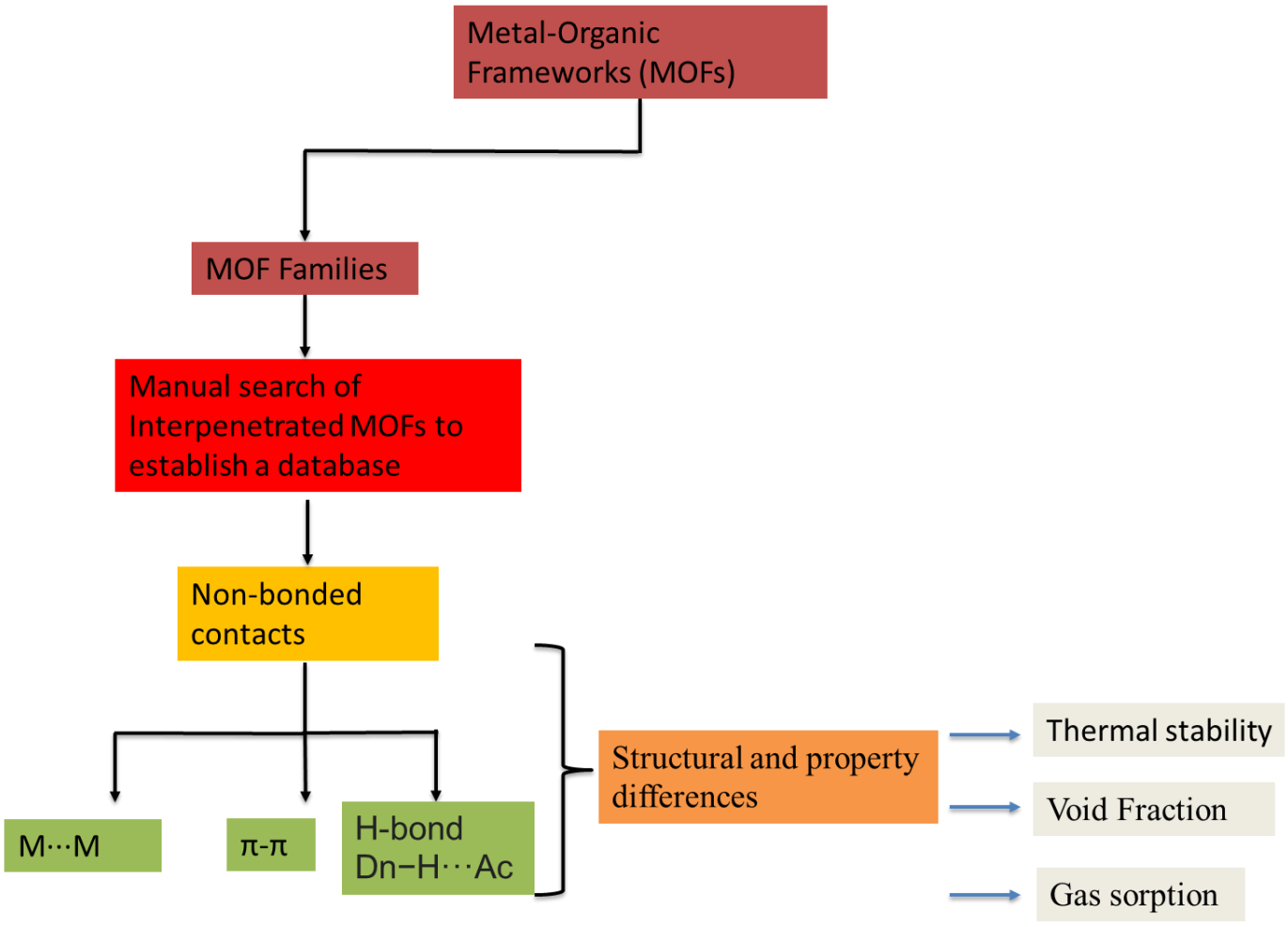


**Figure 3.1.** Diagram displaying how the CSD's MOF subset database was processed and analyzed.

In this chapter the first section is based on the work published in 2020 by Moghadam and Fairen-Jimenez *et al.* in which they utilized the CSD to construct search criteria for specific MOF families based on the characteristic SBUs found in these MOF families.[1] These criteria are discussed below with examples given for each type of MOF family.

Moghadam and Fairen-Jimenez *et al.* based their searches on the 2016 (May update) 5.37 version of the CSD, whereas these families are updated in this thesis according to the 2021 5.43 version of the CSD (01 April 2021), using the MOF subset.

## 3.1. Queries: Search Motifs and Update For The Seven Families Of MOF

Conquest is an interface which can be used to search and retrieve structures according to certain search methods. These include searching according to compound name, elemental composition, formula, literature reference, unit cell parameters, space group, experimental details, and other structure information details.

One of the most popular search methods is to use a chemical substructure motif with or without chemical constraints. It also allows one to perform 2D and 3D geometric searching. as well as searches for non-bonded contacts, which may be intramolecular or intermolecular. There are over 121 093 structures in the MOF subset which includes 1D, 2D and 3D MOF structures which are 1-periodic, 2-periodic and 3-periodic according to definition adopted in this thesis.[1] In order to reduce the number of MOFs investigated to a manageable size for manual inspection, seven MOF families, as identified by Moghadam and Fairen-Jimenez *et al.*, but updated according to 2021 5.43 version of CSD (01 April 2021), were chosen. This reduced the number of structures to 11 395 (herein after referred to as the MOF subset subgroup in this thesis).

The rationale for the selection of search motifs will be explained using the zirconium-oxide (Zr-oxide) based MOF family. Zr-oxide based MOFs have the metal ion linked to the oxygen atoms of carboxylate functional groups in a bridging, bidentate fashion (**Figures 3.1a** and **3.1d**). The first hitlist is created by combining the first “must have” criterion and the “must not have” criterion (**Figures 3.1a** and **3.1c**), which produces 655 structures. The second hitlist is created by combining the second “must have” criterion and the “must not have” criterion (**Figures 3.1b** and **3.1c**), which produces 3 structures. When combining the two hitlists, the unique number of hits, using the “in either List A or List B” option in Conquest, is 656.

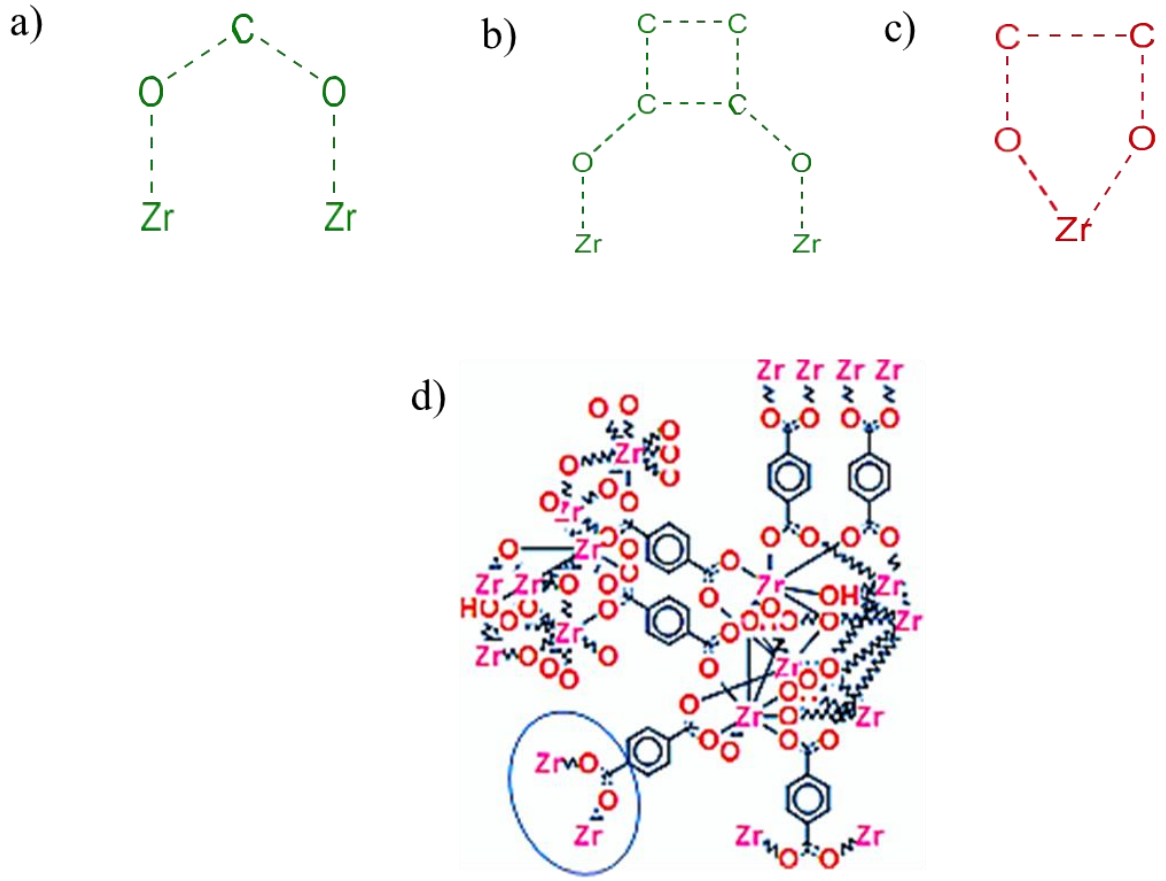

**Figure 3.1.** The criteria utilized for searching Zr-oxide based MOFs. The first ‘‘must have’’ criterion is (a) a bridging, bidentate carboxylate and (b) the second ‘‘must have’’ criterion is a square motif. (c) This motif, where vicinal oxygen atoms bond to the same Zr ion, eliminates structures not considered as part of the Zr-oxide based MOFs. (d) Illustration of the first ‘‘must have’’ criterion in UiO-66 (CSD refcode RUBTAK02). *Figure reprinted (adapted) with P. Z. Moghadam, A. Li, X-W. Liu, R. Bueno-Perez, S.-D Wang, S.B. Wiggin, P.A. Wood, D. Fairen-Jimenez, Chem. Sci., 2020,11, 8373-8387. Copyright (2020) Royal Society of Chemistry.*[1]

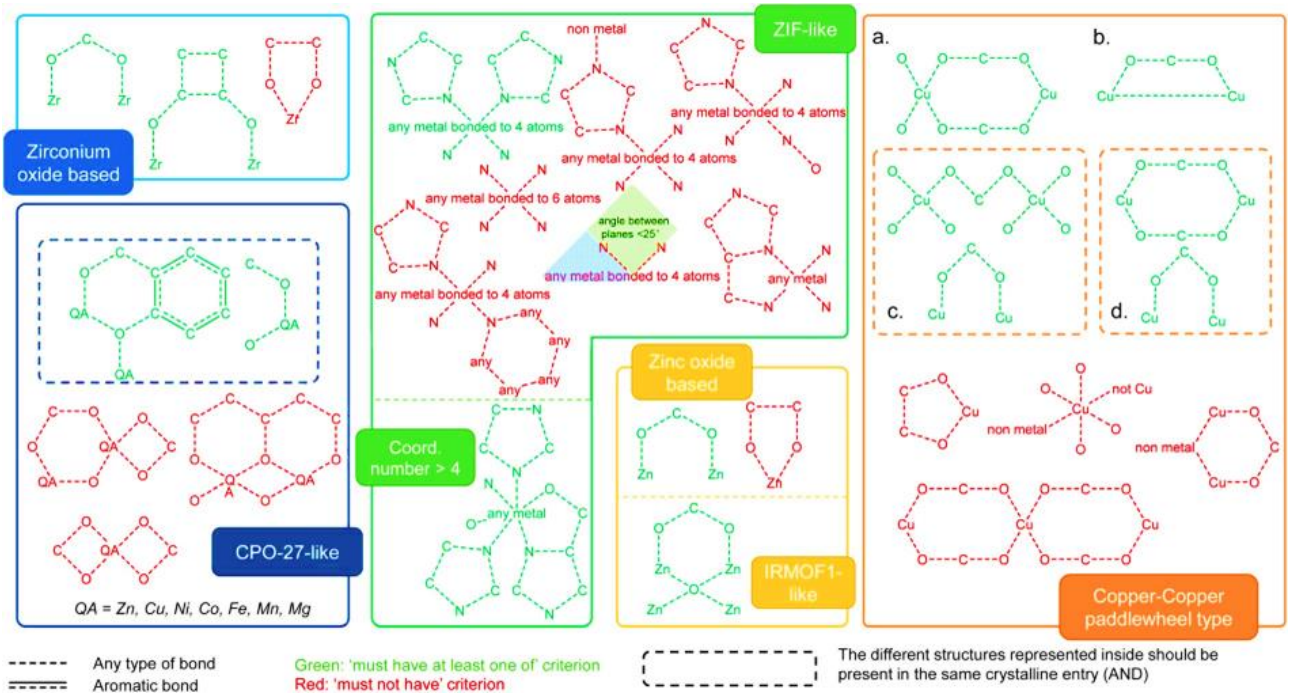


**Figure 3.2.** The CSD MOF subset subgroup was identified using criteria based on certain secondary building components and their relationship to the organic linkers. The seven families are the Zr-oxide, MOF-74/CPO-27-like, ZIF-like (including with coordination > 4), zinc oxide, IRMOF-1-like MOF, and Cu-Cu paddle-wheeled MOFs. Each green and red motif represents "must have" and 'must not have" criteria, respectively. Each green motif must be present in a separate search, combined with all the red motifs. [Green motifs in dotted boxes are treated as a single query]. The hitlists are then combined, producing a list comprising only of unique hits (or reference codes). *Figure reprinted (adapted) with P. Z. Moghadam, A. Li, X-W. Liu, R. Bueno-Perez, S.-D Wang, S.B. Wiggin, P.A. Wood, D. Fairen-Jimenez, Chem. Sci., 2020,11, 8373-8387. Copyright (2020) Royal Society of Chemistry*. [1]

The criteria for searching all seven families are illustrated **Figure 3.2**, with MOFs belonging to the other six families identified using the same methodology as outlined for the zirconium family, stated above as an example. A few families having search criteria that require certain search queries with structures inside the dotted boxes should be treated as a single search query, e.g., Coordination Polymer of Oslo-27(CPO-27) and Copper-Copper paddlewheel type c and d "must have" criteria.

The numbers of structures for the seven families, i.e., Zr-oxide, Cu–Cu paddlewheel, Zeolitic imidazolate frameworks (ZIF-like), Zinc-oxide (Zn-oxide), Isoreticular MOF-1-like (IRMOF-1-like), Coordination Polymer of Oslo-27/(CPO-27-like/MOF-74) and ZIF-like with coordination number > 4 MOF families, were updated using the 2021(01 April) version 5.43 of the CSD (**Table 3.1**). The total number that was found when updating the families is 11 395 structures. Implied that "must not have" criteria structures have been removed.

The total of 656 structures for the Zr-oxide family resulted from the two "must have" and one "must not have" criterion. The "must have" criteria yielded a total of 670 structures and the "must not have" eliminated 14 structures. In the case of the Zn-oxide family, a total of 6115 structures resulted from "must have" criterion, whilst the "must not have" criterion eliminated a total of 319 structures leaving the number at 5796 unique structures.

Isoreticular MOF-1-like structures is the third family listed in **Table 3.1** with a total number of 574 structures, whilst MOF-74/CPO-27-like structures total 2114 structures with the "must have" criterion. The three "must not have" criterion remove 298, 69, 581 structures, respectively, resulting in a family with 2087 MOF structures. It should be noted that all of the "must not have" results are not unique thus the number when subtracted from the total does not give a total of 2087 when considered individually.

The Cu–Cu paddlewheel family has four "must have" criteria, (the most of any family) each contributing a certain number to the total. The first criterion returns 1523 structures, the second returns 1099 structures but only adds 447 unique structures to the list, the third returns 1285 structures adding 463 unique structures to the list, whilst the last "must have" criterion finds 1071 structures, adding 21 unique structures. This totals to 2454 structures, with the four "must not have" criteria removing a total of 541 undesired structures, leaving a total of 1913 MOF structures for the family.

The last two families are related in that they are zeolitic imidazolate frameworks (ZIF-like). The first family has a metal center that is tetrahedrally coordinated with four imidazolates ligated to it and the second includes ZIFs with a metal coordination number of 6 or 8. The "must have" criterion for the first family returned a total of 512 structures. When applying the six "must not have" criteria, the first criterion eliminated 188 structures, the second criterion eliminated 67 structures, the third eliminated 1 structure, the fourth criterion removed 25 structures, the fifth 4 structures and the last one 8 structures. This resulted in 359 unique structures, the second family does not have any "must not have" criteria except "must have" that results in 10 unique structures.

The total number of structures across all the families increased by 6 374 structures, as compared to the number reported in the initial paper by Moghadam and Fairen-Jimenez *et al*.[1,2] This is not surprising considering the unique properties of MOFs and the resulting extensive research on these materials, causing an exponential growth in their number. The highest increase in terms of absolute numbers was seen in the Zn-oxide and CPO-27 MOF groups. This demonstrates how the variety of MOFs has exponentially increased thanks to the modularity of their synthesis. Graphical comparison of the numbers for each of the seven MOF families found in the 2016 and 2021 versions of the CSD is illustrated in **Figure 3.3** whilst **Figure 3.4** illustrates an increase in these numbers. The 2023 version of the CSD will likely show an increase in these numbers due to the extensive research into MOFs, however study presented in this thesis is limited to the 2021 version due to the time taken to manually search the subset groups for entangled MOFs.

**Table 3.1.** Comparison of the number of structures in the selected MOF families found in the 2016 (May update) 5.37 and 2021 (01 April 2021) 5.43 versions of the CSD. The last column reports the difference in numbers found between the two CSD versions.

| Family | 2016 | 2021 | Difference | Grownth (%) |
|---|---|---|---|---|
| **Zr-Oxide** | 77 | 656 | 579 | 852 |
| **Zn-Oxide** | 3187 | 5796 | 2609 | 182 |
| **IRMOF 1-like** | 354 | 574 | 220 | 162 |
| **Coord. Number >4** | 6 | 10 | 4 | 167 |
| **CPO-27-like/MOF-74-like** | 108 | 2087 | 1979 | 1932 |
| **ZIF-Type** | 274 | 359 | 85 | 191 |
| **Cu–Cu paddlewheel** | 1015 | 1913 | 898 | 188 |
| **TOTAL** | 5021 | 11395 | 6374 | 227 |

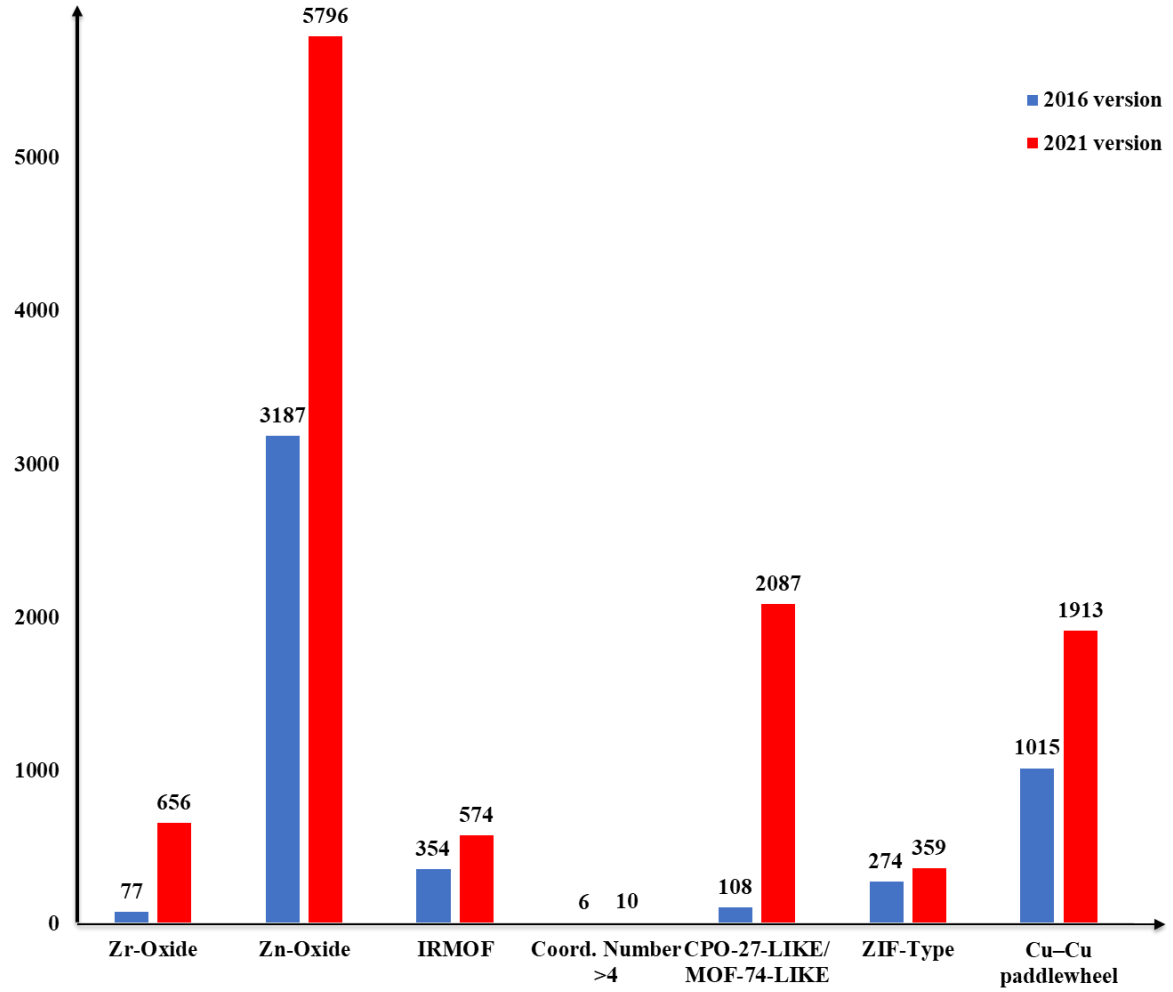


**Figure 3.3.** Comparison of the number of structures found for the seven selected MOF families in the 2016 (May) 5.37 and 2021 (April) 5.43 versions of the CSD.

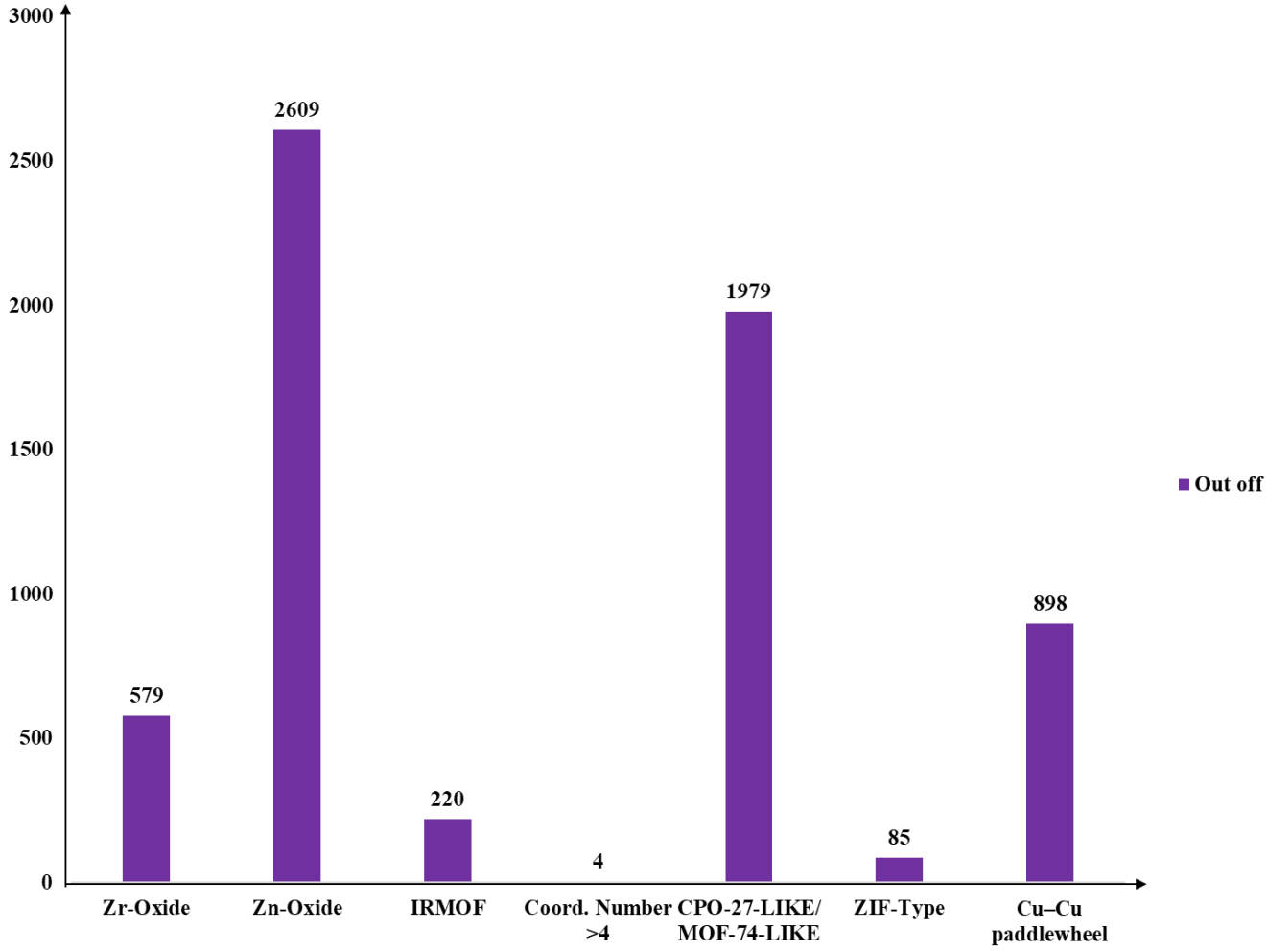


**Figure 3.4.** The increase in MOF structures for the seven selected MOF families in the 2021 (April) version 5.43 version of the CSD.

## 3.2. Search for Entangled MOFs In The Seven MOF Families.

### 3.2.1. Manual Search

Currently, there is no MOF subset database that specifically lists entangled MOF structures. The seven families of MOFs were manually searched for entangled structures, by inspection in Mercury. This was to establish a reference list of entangled structures for each MOF family in order to evaluate the degree of success of the search criteria. Hitlists produced from the search criteria developed to find entangled MOFs can then be compared to the reference list (**Table 3.2.**).

The manual search indicated that the Zn-Oxide family, which has the largest number of MOF structures (5796), has a total of 238 structures (4.1%) that are entangled, as revealed by manual inspection. This is followed by the third largest family, the Cu–Cu paddle-wheeled family with a total number of 1913 MOF structures, that has a total of 77 structures (3.7%) that are entangled.

The fourth largest family is the Zr-Oxide family, that has a total of 34 structures (5.2%) that are entangled. Isoreticular Metal Organic Framework (IRMOF 1-like) family which is the fifth largest family, has a total of 41 crystal structures (7.1%) that are entangled. The remaining families, namely the Coord. Number > 4, CPO-27 and ZIF-Type families had entangled MOFs, despite the CPO-27-like/MOF-74 being the second largest MOF family.

**Table 3.2.** The number and percentage of entangled structures found by manual inspection for the seven selected MOF families (CSD version 5.43 01 April).

| MOF Family | Total number of structures in family | Total number of entangled Entangled structures | Percentage entangled structures (%) |
|---|---|---|---|
| **Zr-Oxide** | 656 | 34 | 5.2 |
| **Zn-Oxide** | 5796 | 238 | 4.1 |
| **IRMOF-1-like** | 574 | 41 | 7.1 |
| **Coord. Number >4** | 10 | 0 | 0 |
| **CPO-27-like/MOF-74-like** | 2087 | 0 | 0 |
| **ZIF-Type** | 359 | 0 | 0 |
| **Cu–Cu paddle-wheeled** | 1913 | 71 | 3.7 |

Two reasons can be offered as to why certain families in the database showed no presence of interpenetrated MOFs. These are based on the (i) linker length, and (ii) the secondary building units (SBUs) and topology of the framework.

(i) Linker length

The zeolitic imidazolate framework-like (ZIF-like) family structures, including those with a metal coordination number > 4, yielded no entangled structures. There are two likely reasons based on linker length, i.e., (i) steric hindrance around the metal site together with the relative short imidazole linkers employed in these structures, form structures with small pore apertures that do not allow a second framework to 'thread' through the first and (ii) introducing bulky functional groups in the organic units to create steric hindrance (**Figure 3.5**).[2] These two reasons prevent this family from forming entangled MOF structures. Some of the structures in the circled structure contain coordinated carboxylate groups which results in limited specific orientations, thus there is little rotation of the ligands for flexibility thus less chance of producing interpenetrated MOFs.

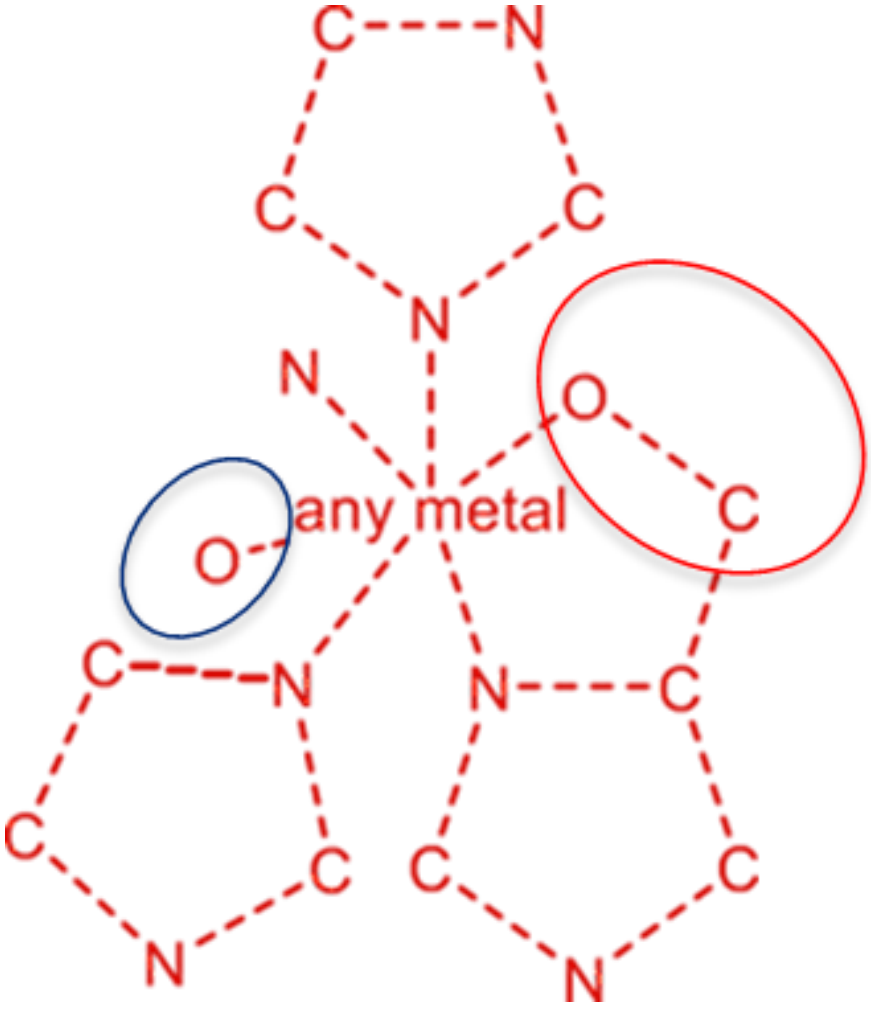


**Figure 3.5** The Coord. Number >4 ZIF-like structures, illustrating the) steric hindrance around the metal site, contributing to small pockets and blue indicating hindrance for rotation and bridging. *Figure reprinted (adapted) with P. Z. Moghadam, A. Li, X-W. Liu, R. Bueno-Perez, S.-D Wang, S.B. Wiggin, P.A. Wood, D. Fairen-Jimenez, Chem. Sci., 2020,11, 8373-8387. Copyright (2020) Royal Society of Chemistry*. [1]

(ii) the secondary building units (SBUs) and topology of the framework.

When searching through some of the families the CPO-27 family sticks out from the rest as having honeycomb-like structures, with hexagonal channels. Most of the structures in the CPO-27 family are adopting the same topology and SBUs, whilst there are a few structures that are not following this topology and SBU (**Figure 3.6**). There is a link between these rod-like geometries, and its associated nets in terms of the lack of interpenetrated structures and this due to their short periodicity of the SBU thus it is said to be "forbidden catenation".[3,4] Other reasons include (i) robust and rigid in nature (based on supramolecular interactions preventing the framework from collapsing even if the void space is large), (ii) some topologies are innately non-interpenetrating, (iii) the application of various reaction conditions, i.e., different solvents, conditions, and template effects affect the product and (iv) adding bulky functional groups to produce steric hindrance in organic units.[2-4] It so happens that sometimes neither the above mentioned play a role, i.e., a non-interpenetrated framework can be created out of an interpenetrated one. This entails the rearrangement that produces a new SBU and proceeds in a single crystal to single crystal (SCSC) manner.

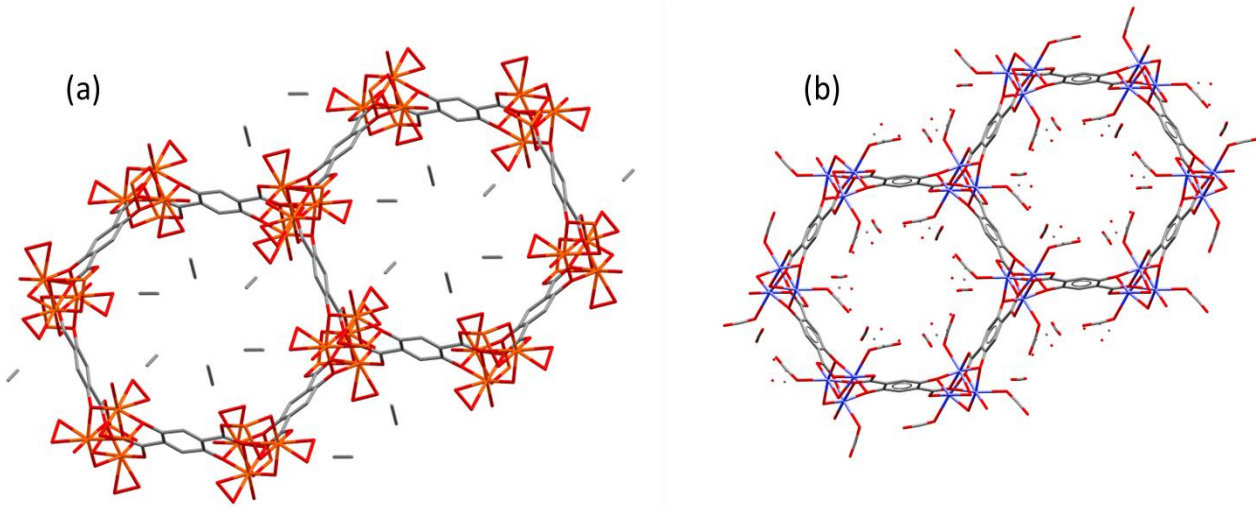


**Figure 3.6.** Illustration of the MOF-74/CPO-27-like structures. (a) and (b) are examples that can be found in this family that does not have a single example of an entangled MOF.

## 3.3. Search For Entangled MOF (using selected ConQuest search criteria).

The next step was to search each MOF family for entangled structures using ConQuest search criteria and then comparing the resulting hitlists to these obtained from the manual searches. ConQuest provides an option to search for structures based on defined distances between one point (atom or centroid) and another (atom or centroid). Furthermore, the distances may be defined as intramolecular, intermolecular or both (both may be present in one structure). In fact, searches for non-bonded intermolecular interaction between any two types of atoms

should also yield entangled MOFs, if ConQuest recognizes a framework, which is a coordination polymer, as a single molecular entity. Unfortunately, it was found that the search program does not recognize a single framework as a single molecular entity because the intermolecular search option identified non-bonded contacts within the same coordination polymer, i.e., intramolecular distances, and as a result also yielded non-entangled structures in the resulting list. Note that "contacts" has a relaxed definition in that an interaction is not necessarily implied; rather, it merely finds atoms/centroids within a certain distance or distance range.

Searching by metal···metal distances for entangled structures was not very successful in terms of discriminating between entangled and non-entangled structures. This could be due to the intraframework distances also being identified. It was then decided to use hydrogen bonding, C-H···π and π···π interactions as search criteria since these interactions may occur to a greater degree between frameworks as compared to within the same framework. The donor···acceptor, donor···$\pi_{centroid}$ and $\pi_{centroid}$···$\pi_{centroid}$ distance ranges for the hydrogen bonding, C-H···π and π···π interactions, respectively, were guided by the criteria used by the program PLATON in identifying these interactions.

### 3.3.1. Hydrogen Nonbonding "D−H···A" Interactions

Hydrogen bonds are electrostatic in nature, and their strengths range from 1-30 kcal/mol depending on the electronegativity of the donor and acceptor atoms and the geometry of the hydrogen bond i.e., the donor···acceptor distance and donor−H···acceptor angle. There are a number of different hydrogen bond motifs that may be present in crystal structures (**Figure 3.7**). Using the simple motif as a search criterion may identify structures containing the other or more complex motifs as well.

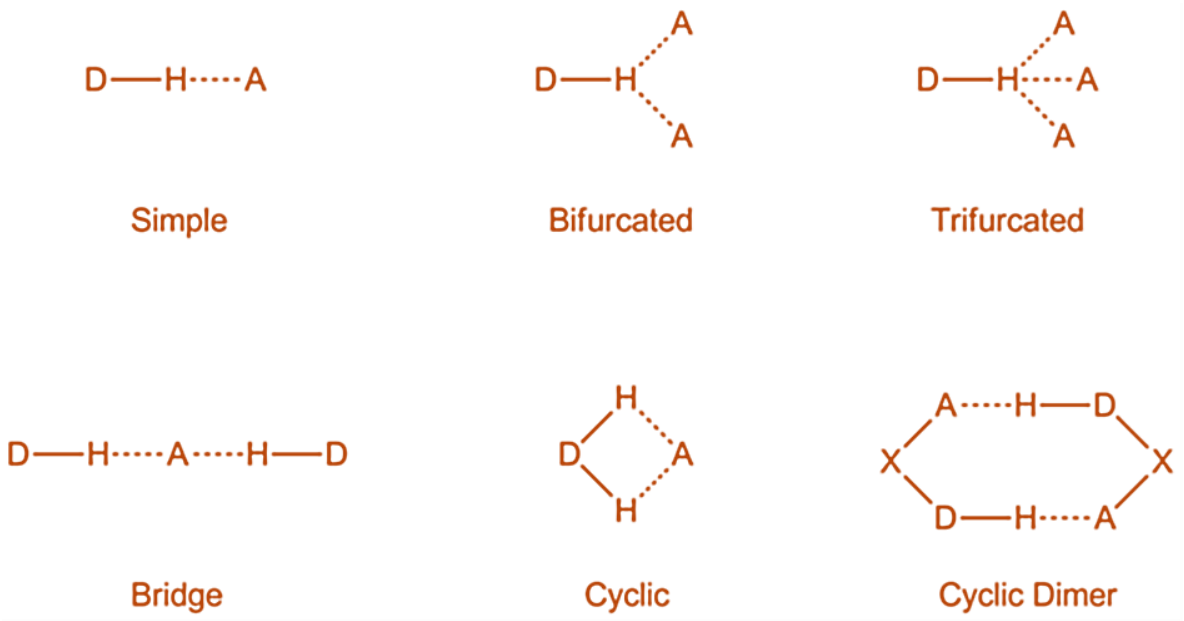


**Figure 3.7.** Schematic illustration of a range of different hydrogen bond motifs that may be present in crystal structures.

PLATON uses the van der Waals radii (also referred to as the contact radii) of the atoms, where these are involved in the non-bonded interactions (**Table 3.3**). For example, one of the criteria for identifying a hydrogen bond is that the donor atom (D) to acceptor atom (A) distance is within $d(D\cdots A) < R(D) + R(A) + 0.50$ Å, where $R$ is the van der Waals radius of the atom. In this search the donor atoms considered were C, N and O and the acceptor atoms were N, O, S, F, Cl and Br (**Table 3.4**). Based on the van der Waals radii of these donor and acceptor atoms the maximum distances for each unique combination of donor and acceptor atoms range from 3.54 Å (O···O) to 4.05 Å (C···Br). These are maximum distances for the identification of hydrogen bonding interactions, the most prevalent distances for each contribution being significantly shorter. For example, the most prevalent donor-to-acceptor distances for O-H···O hydrogen bonding interactions fall in the range 2.7-2.8 Å when analyzing the CSD full MOF subset.[8] PLATON does not specify a minimum distance for D···A interactions, but for this search it was set to be 2.3 Å (~0.5 Å less than the most prevalent distance range for O···O interactions), whilst the maximum distance was relaxed to 5 Å in order to include entangled structures which may not have these interactions between frameworks. The second and third hydrogen bonding criteria that must also be present for PLATON to identify these interactions, relate to the hydrogen atom to acceptor atom distance ($d(H\cdots A) < R(H) + R(A) - 0.12$ Å) and the hydrogen bond angle (D-H···A > 100°). However, these criteria were not included in the searches in order for the latter to be less restrictive.

**Table 3.3.** van der Waals or contact radii used by PLATON.[5-8]

| Elements | C | H | F | N | O | S | Cl | Br |
|---|---|---|---|---|---|---|---|---|
| **Radius (Å)** | 1.70 | 1.20 | 1.47 | 1.55 | 1.52 | 1.80 | 1.75 | 1.85 |

**Table 3.4.** Donor to acceptor distances (in Å) based on d(D···A) < R(D) + R(A) + 0.50 Å.

***Donor***

| ***Acceptor*** | C | N | O |
|---|---|---|---|
| *F* | 3.67 | 3.52 | 3.49 |
| *N* | 3.75 | 3.6 | 3.57 |
| *O* | 3.72 | 3.57 | 3.54 |
| *S* | 4 | 3.85 | 3.82 |
| *Cl* | 3.95 | 3.8 | 3.77 |
| *Br* | 4.05 | 3.9 | 3.87 |

Each MOF family subset was searched using the D···A distance criterion (2.3 – 5Å), the results of which were compared with the reduced lists containing the entangled MOFs established by the manual inspection (**Table 3.5**).The Zn-Oxide family has the largest number of entangled MOF structures of the seven families with 174 structures that were found from the search criterion followed by the Cu–Cu paddle-wheeled family with 35 structures, the Zr-Oxide family with 15 structures and finally the IRMOF-1-like family with a total number of 9 crystal structures that are entangled and (**column 4 in Table 3.5**).

The success of the search criteria was defined in two ways. Firstly, expressing the number of entangled structures found in the search results as a percentage of the total number of MOF structures in this list, gives the degree of success of the search criteria in terms of discriminating between entangled and non-entangled structures (**column 5 in Table 3.5**). Secondly, the number of entangled structures found in the search results expressed a percentage of the number of entangled structures found by manual inspection, i.e., the true number of entangled structures (**column 6 in Table 3.5**).

Using the first success rate indicator, the Zr-oxide MOF family had the highest percentage of entangled structures (16%) and the Cu–Cu paddle-wheeled MOF the family had the lowest (3.0%), showing that the search criterion had the most and least success to discriminate behaviour entangled and non-entangled structures for these two families, respectively (**column**

**5 in Table 3.5**). The second success rate indicator (**column 6 in Table 3.5**) shows the distance criterion was most successful in finding the entangled structures in the Zn-oxide MOF family (73%) and least successful in the findings of the IRMOF-1-like family (22%).

**Table 3.5.** Comparison of entangled structures found using hydrogen bonding search criteria with those found by manual inspection.

| MOF Family | Entangled structures from manual inspection reference list. | Percentage of entangled structures found by manual inspection. | No. of structures in list generated from search. (2.3 – 5Å) | No. of entangled structures in search list. (2.3 – 5Å) | Percentage Entangled in search list. | Percentage of search list entangled structures with respect to those found by manual inspection. | Average percentage. |
|---|---|---|---|---|---|---|---|
| Zr-Oxide | 34 | 5.2 | 93 | 15 | 16 | 44 | 30 |
| Zn-Oxide | 238 | 4.1 | 4237 | 174 | 4.1 | 73 | 38.6 |
| IRMOF-1-like | 41 | 7.1 | 174 | 9 | 5.2 | 22 | 13.6 |
| Cu-Cu Paddlewheel | 71 | 3.7 | 1166 | 35 | 3.0 | 49 | 26 |

### 3.3.2. Pi−Pi (π–π) Interactions

Aromatic pi–pi interactions are important interactions to consider since many MOFs have linkers with aromatic rings. Pi–pi interactions can be classified as sandwich, T-shaped or parallel-displaced depending on the relative orientation and displacement of the two aromatic rings. PLATON identifies aromatic pi-pi ring interactions when $C_g \cdots C_g$ 6.0 Å, where $C_g$ refers to the center of gravity of the aromatic ring.[9-11] In this search only "center of gravity···center of gravity" ($C_g \cdots C_g$) distances in the range 0−6 Å were considered and not the relative orientations of the aromatic rings (**Figure 3.8**), even though PLATON has additional criteria for the latter in its identification of aromatic pi–pi interactions.

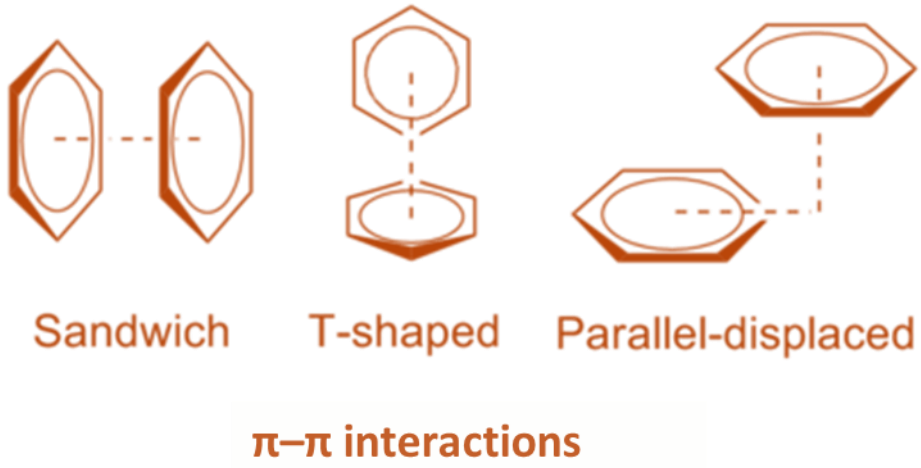


**Figure 3.8.** Schematic illustration of the different types of non-contact π–π interactions that may be found in MOF crystal structures.

The MOF family subset subgroups were searched using $C_g \cdots C_g$ distance criterion (0-6Å), the findings of which were compared to the reduced lists containing the entangled MOFs established by the manual inspection. The Zn-Oxide family has the largest number of entangled MOF structures of the seven families with 79 structures that were found from the search criterion followed by the Cu–Cu paddle-wheeled family with 32 structures, the Zr-Oxide family with 14 structures and finally the IRMOF-1-like family with a total number of 7 crystal structures that are entangled and (**column 4 in Table 3.6**).

The success of the search criteria was defined in two ways. Firstly, expressing the number of entangled structures found in the search results as a percentage of the total number of MOF structures in this list, gives the degree of success of the search criteria in terms of discriminating between entangled and non-entangled structures (**column 5 in Table 3.6**). Secondly, the number of entangled structures found in the search results expressed a percentage of the number of entangled structures found by manual inspection, i.e., the true number of entangled structures (**column 6 in Table 3.6**).

Using the first success rate indicator, the Zr-oxide MOF family had the highest percentage of entangled structures (35%) and the Zn-oxide MOF the family had the lowest (3.8%), showing that the search criterion had the most and least success to discriminate behaviour entangled and non-entangled structures for these two families, respectively (**column 5 in Table 3.5**). The second success rate indicator (**column 6 in Table 3.5**) shows the distance criterion was most successful in finding the entangled structures in the Cu-Cu Paddlewheel MOF family (45%) and least successful in the of the IRMOF-1-like family (17%).

**Table 3.6.** Comparison of entangled structures found using π···π interactions search criteria with those found by manual inspection.

| MOF Family | Entangled structures from manual inspection reference list. | Percentage of entangled structures found by manual inspection. | No. of structures in list generated from search. (0 - 6 Å) | No. of entangled structures in search list. (0-6Å) | Percentage entangled in search list. | Percentage of search list entangled structures with respect to those found by manual inspection. | Average percentage. |
|---|---|---|---|---|---|---|---|
| Zr-Oxide | 34 | 5.2 | 40 | 14 | 35 | 41 | 38 |
| Zn-Oxide | 238 | 4.1 | 2065 | 79 | 3.8 | 33 | 18.4 |
| IRMOF-1-like | 41 | 7.1 | 108 | 7 | 6.5 | 17 | 11.8 |
| Cu-Cu Paddlewheel | 71 | 3.7 | 528 | 32 | 6.1 | 45 | 25.6 |

### 3.3.3. C–H···π Weak Interactions

The third set of criteria for intermolecular interactions was created, C–H···π interactions. The search was conducted on a range of distances from 1.8 Å -3 Å between hydrogen atom and the aromatic ring's centroid, this distance was adopted from Kumar and Balaji 2014 paper on C-H…pi interactions.[8]

**Table 3.7.** Comparison of entangled structures found using C–H···π interactions search criteria with those found by manual inspection.

| MOF Family | Entangled structures from manual inspection reference list. | Percentage of entangled structures found by manual inspection. | No. of structures in list generated from search. (1.8-3Å) | No. of entangled structures in search list. (1.8-3Å) | Percentage entangled in search list. | Percentage of search list entangled structures with respect to those found by manual inspection. | Average percentage. |
|---|---|---|---|---|---|---|---|
| Zr-Oxide | 34 | 5.2 | 12 | 6 | 50 | 18 | 34 |
| Zn-Oxide | 238 | 4.1 | 890 | 31 | 3.5 | 13 | 8.3 |
| IRMOF-1-like | 41 | 7.1 | 53 | 2 | 3.8 | 4.9 | 4.4 |
| Cu-Cu Paddlewheel | 71 | 3.7 | 204 | 12 | 5.9 | 17 | 11.5 |

Each MOF family subset subgroups was searched using the C–H···π distance criterion (1.8 -3 Å), these findings were compared with the reduced lists containing the entangled MOFs established by the manual inspection (**Table 3.5**). The Zn-Oxide family has the largest number of entangled MOF structures of the seven families with 31 structures that were found from the search criterion followed by the Cu–Cu paddle-wheeled family with 12 structures, the Zr-Oxide family with 6 structures and finally the IRMOF-1-like family with a total number of 2 crystal structures that are entangled and (**column 4 in Table 3.7**).

The success of the search criteria was judged based on two ways. Firstly, expressing the number of entangled structures found in the search results as a percentage of the total number of MOF structures in this list, gives the degree of success of the search criteria in terms of discriminating between entangled and non-entangled structures (**column 5 in Table 3.7**). Secondly, the number of entangled structures found in the search results expressed a percentage of the number of entangled structures found by manual inspection, i.e., the true number of entangled structures (**column 6 in Table 3.7**).

Using the first success rate indicator, the Zr-oxide MOF family had the highest percentage of entangled structures (50%) and the Zn-oxide MOF the family had the lowest (3.5%), showing that the search criterion had the most and least success to discriminate behaviour entangled and non-entangled structures for these two families, respectively (**column 5 in Table 3.7**). The second success rate indicator (**column 6 in Table 3.7**) shows the distance criterion was most successful in finding the entangled structures in the Zr-oxide MOF family (18 %) and least successful in the of the IRMOF-1-like family (4.9%).

## 3.4. Selected examples of structural and property differences between entangled MOFs and their isostructural counterparts for each of the four MOF families.

Entanglement in MOFs results in an increase in pore surfaces, potential flexibility of the frameworks, and may come with improved properties. The significant differences in properties of entangled and non-entangled structures warrants a need to be able to search the CSD for entangled MOF structures due their porous nature, thermal stabilities, liquid, and gas sorption capacity. **Figure 3.9** and **Table 3.8** show examples of entangled and their non-entangled counterparts belonging to four of the seven families, investigated in this chapter, which showed any entanglement.

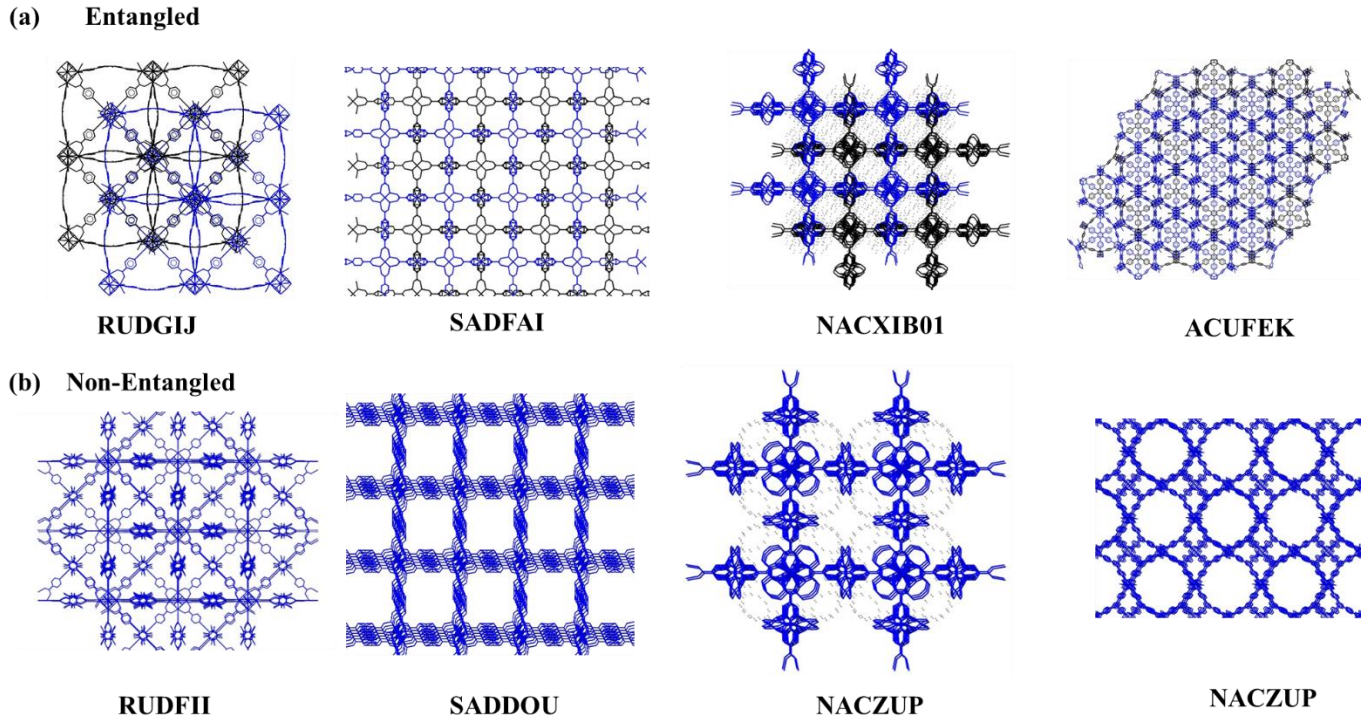


**Figure 3.9.** Examples of (a) entangled MOFs and their isoreticular (b) non-entangled counterparts, from left to right, are examples of Zr-Oxide, Zn-Oxide, IRMOF-1-like and Cu-Cu Paddlewheel family, respectively.

### 3.4.1. Thermal Stability (Decomposition, Crystallinity With Temperature)

For many MOF structures, thermogravimetric analysis (TGA) data are available. TGA experiments measure mass loss in a sample as it is heated at a constant rate in a specific atmosphere. For MOFs, this typically occurs in several distinct steps, beginning with desolvation at relatively low temperatures and progressing to extensive mass loss at the temperature of decomposition. Assuring the thermal stability of MOFs after desolvation is important for guiding their activation protocols for sorption studies, thus without variable-temperature powder X-ray diffraction (VT-PXRD) one is limited in formulating the activation protocols of these MOFs.

For the Zirconium-oxide family isoreticular structures RUDFII (non-entangled) and RUDGIJ (entangled) there was no TGA information available. The Zinc oxide family shows that SADDOU and SADFAI showed decomposition temperatures of 400 °C and 450 °C respectively. The IRMOF family shows 440 °C and 365 °C for non-entangled NACZUP and entangled NACXIB01 structures, respectively. And the last family Cu–Cu paddle-wheeled the decomposition temperatures for non-entangled NIBHOW is 350 °C and entangled ACUFEK 250 °C (**Table 3.8**). Looking also at their nature, the entangled MOFs based on the TGAs

provided they are more thermally stable than the other group. It should be highlighted that determining a material's thermal stability requires more information than just TGA data. That is, structural changes that take place in the absence of mass loss are not picked up by the method. Amorphization or framework collapse, phase transitions, or melting are examples of these processes thus the need for VT-PXRD. In all of these selected MOF structures in each of the four MOF families, such a study was not carried out thus one can not only conclude based on TGA alone that the entangled structures are more stable than their counterparts.

**Table 3.8.** Summary of TGA data for the selected structurers in each family.

| ***Family*** | **Structure** | **Type** | **Decomposition temperatures (°C)** |
|---|---|---|---|
| *Zirconium Oxide* | RUDGIJ | Entangled | -[a] |
| | RUDFII | non-entangled | -[a] |
| *Zinc Oxide* | SADFAI | Entangled | 450[b] |
| | SADDOU | non-entangled | 400[b] |
| *IRMOF-1-like* | NACXIB01 | Entangled | 365[b] |
| | NACZUP | non-entangled | 440[b] |
| *Cu–Cu paddle-wheeled* | ACUFEK | Entangled | 250[b] |
| | NIBHOW | non-entangled | 350[b] |

[a] data not available [b] Values were read off from thermograms provided original article authors by the author of this thesis.

### 3.4.2. Structural Void Fraction

When researchers find a novel structure or material, they often initially look for fundamental descriptors, which are the traditional characteristics. For MOFs, this would be the void fraction, largest cavity diameter (LCD), and pore limiting diameter (PLD), and of each structure. One of the first structural characteristics to predict the sorption properties of a MOF is to assess its void fraction.

In the Zircoium-oxide family isoreticular structures RUDFII (non-entangled) and RUDGIJ (entangled) showed calculated void fractions of 75.9% and 64.7% respectively. The Zinc oxide family shows that SADDOU and SADFAI showed calculated void fractions of 83.8% and 68.8% respectively. The IRMOF-1-like family shows 83.8% and 19.3% for non-entangled NACZUP and entangled NACXIB01 structures, respectively. And the last family Cu–Cu paddle-wheeled the calculated void fraction for non-entangled NIBHOW is 87.1% and entangled ACUFEK 71.8% (**Table 3.9**). Looking also at their nature, the entangled MOFs based on the TGAs provided they are more thermally stable than the other group.

Although these this data points out that non-entangled calculated void fractions are greater than that of the entangled structures, it is to be expected since the void space decreases with entanglement. However, the experimental data for gas and liquid sorption is different due to

the entangled structures being flexible to accommodate more gas than the calculated void space.

**Table 3.9.** Summary of the calculated void fractions for the selected structurers in each family.

| *Family* | Structure | Type | Void Fraction |
|---|---|---|---|
| *Zirconium Oxide* | RUDGIJ | Entangled | 64,7 |
| | RUDFII | non-entangled | 75,9 |
| *Zinc Oxide* | SADFAI | Entangled | 68,8 |
| | SADDOU | non-entangled | 83,8 |
| *IRMOF* | NACXIB01 | Entangled | 19,3 |
| | NACZUP | non-entangled | 46,1 |
| *Cu–Cu paddle-wheeled* | ACUFEK | Entangled | 71,8 |
| | NIBHOW | non-entangled | 87,1 |

### 3.4.3. Difference In Sorption Properties

The most crucially important role in the use of energy resources is played by gas storage. Both toxic gases (CO and $NH_3$) and the aforementioned energy-related gases ($CO_2$, $H_2$, and $CH_4$) are covered. The nature of the MOF itself also plays a role in the efficient storage of such materials. Based on **Table 3.9**, the examples given suggests that entangled MOFs decreases gas sorption as due to decreased void space.

**Table 3.10.** Summary of liquid and gas sorption.

| *Family* | Structure | $N_2$ sorption ($cm^3\ g^{-1}$) | BET (Langmuir) surface area ($m^2/g$) | $H_2$ sorption ($cm^3\ g^{-1}$) | $CO_2$ sorption ($cm^3\ g^{-1}$) | $CH_4$ sorption ($cm^3\ g^{-1}$) |
|---|---|---|---|---|---|---|
| ***Zirconium Oxide*** | RUDGIJ Entangled | 490 | 1973 (2191) | – | – | – |
| | RUDFII Non-Entangled | 590 | 2256 (2585) | – | – | – |
| ***Zinc Oxide*** | SADFAI Entangled | 435 | 1610 | 199 | 45 | 11 |
| | SADDOU Non-Entangled | 1103 | 3200 (3970) | 154 | 21 | 12 |
| ***IRMOF-1-like*** | NACXIB01 Entangled | – | – | – | – | – |
| | NACZUP Non-Entangled | – | – | – | – | – |
| ***Cu–Cu paddle-wheeled*** | ACUFEK Entangled | – | 2700 | 394 | – | – |
| | NIBHOW Non-Entangled | – | 3800 | 919 | – | – |

– Not available

## 3.5. Discussion and Conclusion

The purpose of this study was to evaluate the created criteria to effectively locate entangled structure and comparing the manual searches conducted on all the families. The results demonstrate that only 30% of structures on average for the Zr-oxide family that were identified were discovered to be entangled as a measure of success. A total of 38% of these structures for the Zn-oxide family were recovered. The IRMOF-1-like family showed an average of 13.6% and Cu-Cu paddlewheel family 26% using the developed criteria for hydrogen non-bonding interactions "D−H···A" (**column 7 in Table 3.5**).

The predominant family in the search for entangled structures for hydrogen non-bonding interactions is the Zn-oxide family, followed by Zr-oxide family. The third family is the Cu-Cu paddlewheel family, and the last one is IRMOF-1-like family.

Using the developed criteria for π···π nonbonding interactions, an average of 38% structures for the Zr-oxide family was recovered. The other families such as Zn-oxide family showed an average of 18.4 %, the IRMOF-1-like family showed an average of 11.8 %. And this search criterion Cu-Cu paddlewheel family was the runner up with 25.6 % structures on average were found (**column 7 in Table 3.6**).

The last search criterion C–H···π weak contacts interactions produced 34% of the expected structures for Zr-oxide family, and 8.3 % for the Zn-oxide family. The search criterion demonstrated a search potential of 4.4 for the IRMOF-1-like family and 11.5 % for the Cu-Cu paddlewheel family (**column 7 in Table 3.7**). Although efficacy of each search criterion form can be observed.

In the case of the π···π nonbonding interactions and C–H···π weak contacts interactions the predominant family in the search for entangled structures is the Zr-oxide family, followed by Cu-Cu paddlewheel family. The third family is the Zn-oxide family, and the last one is IRMOF-1-like family.

## 3.6. References


1. P. Z. Moghadam, A. Li, X-W. Liu, R. Bueno-Perez, S.-D Wang, S.B. Wiggin, P.A. Wood, D. Fairen-Jimenez, Chem. Sci., 2020,11, 8373-8387
2. R. Haldar, N. Sikdar, T. K. Maji, Materials today, 2015, 18 (2), 97-116
3. N.L. Rosi, M. Eddaoudi, J. Kim, M. O'Keeffe, O.M. Yaghi
4. A. Schoedel, M. Li, D. Li, M. O'Keeffe, O.M. Yaghi
5. G.A.Jeffrey & W.Saenger, Hydrogen Bonding in Biological Structures Springer-Verlag, Berlin, 1991, pp 20.
6. C. E. MacBeth, B.S. Hammes, V. G. Young, Jr., and A. S. Borovik, Inorg. Chem. 2001, 40, 18, 4733–4741.
7. A.L.Spek, Acta Cryst. 2009, D65, 148-155.
8. G.A.Jeffrey, H.Maluszynska & J.Mitra., Int.J.Biol.Macromol.(1985),7,336-348
9. C. R. Groom, I. J. Bruno, M. P. Lightfoot and S. C. Ward, *Acta Cryst.* (2016). B72, 171-179.
10. B.H Lessard, A.J Lough, T.P. Bender, *Acta Crystallogr E Crystallogr Commun*. 2016 72,988-94.
11. D.B Ninković, G.V Janjić, D. Veljković, D.N. Sredojević, S.D. Zarić (2011) *ChemPhysChem*,2011, 12: 3511-3514
12. E.C Lee, D. Kim, P. Jurečka, P. Tarakeshwar, P. Hobza, K.S. Kim, *J Phys Chem A* 2007, 111(18), 3446–3457
13. Kumar, M., Balaji, P.V., J Mol Model 2014, 20, 2136.

# CHAPTER 4

The synthesis, characterisation and application of novel Cu-based 2-periodic, isoreticular metal-organic frameworks are presented in this chapter. The solvents employed were *N,N'*-dimethylformamide, *N,N'*-diethylformamide, and water. Thermal analysis (HSM, DSC and TGA) and X-ray diffraction (SCXRD, PXRD, and VT-PXRD) were used to comprehensively characterize the MOFs. The analytical findings for each MOF are discussed in sections of the chapter that are split according to each characterisation approach. The porosities of the MOFs were investigated by assessing their ability to sorb various gases and water vapour.

## 4.1. Synthesis

### 4.1.1. $[Cu_2(hfipbb)_2(DMF)_2]_n \cdot n(DMF)_4$ (1)

The ligand 4,4'-(hexafluoroisopropylidene)bis(benzoic acid) ($H_2$hfipbb) (38 mg, 0.10 mmol) was dissolved in 3 mL *N,N*'-dimethylformamide (DMF). In a separate vial, copper(II) nitrate hemi(pentahydrate) (29 mg, 0.12 mmol) was dissolved in 1.5 mL methanol. Both solutions were warmed with stirring and the resulting clear solutions were mixed together in glass vials, capped and sealed with Parafilm. The solution was heated under autogenous pressure to 90 °C for 12-14 hours. These were then allowed to cool slowly to room temperature, producing turquoise single crystals of **1** (also referred to as **MOFDMF(NIP)**).

### 4.1.2. $[Cu(hfipbb)(DEF)]_n \cdot n(DEF)_2$ (2)

The ligand 4,4′-(hexafluoroisopropylidene)bis(benzoic acid) (38 mg, 0.10 mmol) was dissolved in 3 mL of *N,N*'-diethylformamide (DEF). In a separate vial, copper(II) nitrate hemi(pentahydrate) (29 mg, 0.12 mmol) was dissolved in 1 mL of water and added to the ligand solution. The solution was capped and heated to 90 °C for 6-7 hours, after which it was allowed to cool slowly to room temperature, yielding block-shaped blue single crystals of **2** (also referred to as **MOFDEF(NIP)**).

### 4.1.3. $[Cu_2(hfipbb)_2(H_2O)_2]_n$ (3)

**MOF$H_2$O(NIP)** was synthesised by submerging newly synthesized crystals of **MOFDMF (NIP)** in water for 7 days at room temperature. However, there was too much crystal fracturing for single crystal X-ray data collection. Instead, the PXRD patterns of the material was recorded and compared with the PXRD pattern of the original crystals of **MOFDMF(NIP)**.

The synthetic protocols of the three MOF are summarised in **scheme 4.1**.

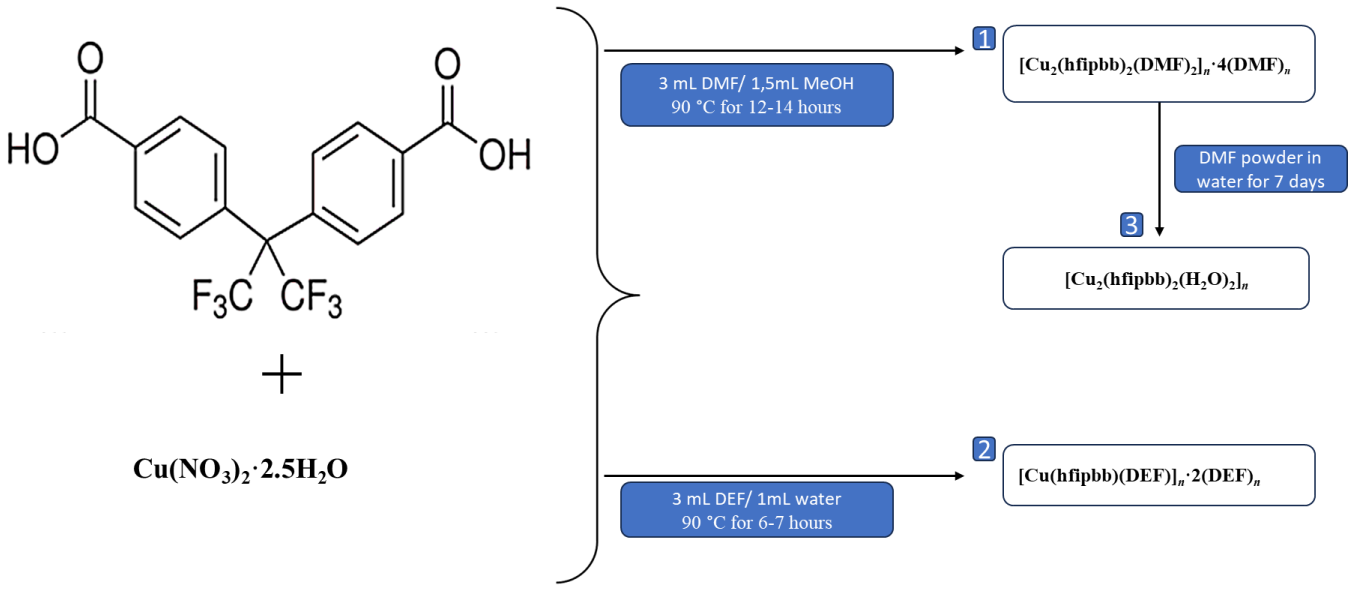


**Scheme 4.1.** Schematic diagram for synthesis of **[Cu$_2$(hfipbb)$_2$(DMF)$_2$]$_n$·*n*(DMF)$_4$ (1)**, **[Cu(hfipbb)(DEF)]$_n$· *n*(DEF)$_2$ (2)** and **[Cu$_2$(hfipbb)$_2$(H$_2$O)$_2$]$_n$ (3)**.

## 4.2. Single Crystal X-ray Diffraction

The synthesized novel 2-periodic, copper-based non-interpenetrated MOF, with the formula $[Cu_2(hfipbb)_2(DMF)_2]_n \cdot n(DMF)_4$ **(1)** named in this thesis **MOFDMF(NIP**), is isoreticular to Chatterjee *et al.*[1] copper-based interpenetrated $[Cu(hfipbb)(DMF)]_n \cdot n(DMF)_{0.5}$ MOF named in this thesis **MOFDMF(IP)**

### 4.2.1 Structure Solution and Refinement

A single crystal of each MOF compound, crystal **MOFDMF(NIP)** was selected from the mother liquor and mounted using a cryoloop and Paratone N oil. Data collection was carried out on a Bruker D8 Venture diffractometer using Mo Kα (λ = 0.71073 Å) radiation (the single crystal X-ray data collection procedure is outlined in **section 2.3.1** check details given in chapter 2). The crystal and refinement data are presented in **Table 4.1**.

**Table 4.1.** Crystal and refinement data for MOFs **MOFDMF(NIP)**.

| | **MOFDMF(NIP)** |
|---|---|
| ASU formula | $C_{26}H_{29}CuF_6N_3O_7$ |
| Formula weight | 673.06 |
| Temperature / K | 100(2) |
| Crystal system | monoclinic |
| Space group | $P2_1/c$ |
| a / Å | 25.9078(12) |
| b /Å | 10.5945(4) |
| c / Å | 24.3823(10) |
| α / ° | 90 |
| β / ° | 116.3230(10) |
| γ / ° | 90 |
| Volume / $Å^3$ | 5998.5(4) |
| Z | 8 |
| ρcalc / g $cm^{-3}$ | 1.491 |
| $\mu$ / $mm^{-1}$ | 0.813 |
| F(000) | 2760.0 |
| Crystal size/ $mm^3$ | 0.40 × 0.16 × 0.02 |
| Radiation | MoKα (λ = 0.71073) |
| 2θ range for data collection / ° | 3.342 to 55.174 |
| Index ranges | $-33 \leq h \leq 33$, $-13 \leq k \leq 13$, $-31 \leq l \leq 31$ |
| Reflections collected | 398663 |
| Independent reflections | 13871 [$R_{int}$ = 0.0911, $R_{sigma}$ = 0.0275] |
| Data/ restraints/ parameters | 13871/210/787 |
| Goodness-of-fit on $F^2$ | 1.209 |
| Final R indexes [I>=2σ(I)] | $R1$ = 0.0845, $wR2$ =0.1733 |
| Final R indexes [all data] | $R_1$ = 0.0940, $wR_2$ = 0.1778 |
| Largest diff. peak/hole / e $Å^{-3}$ | 2.32/-0.90 |

### 4.2.2. Structure Analysis of:

### $[Cu_2(hfipbb)_2(DMF)_2]_n \cdot n(DMF)_4$ (1)

Single crystal X-ray diffraction analysis reveals that compound **MOFDMF(NIP)** crystallizes in the monoclinic crystal system, in the space group of $P2_1/c$ (**Table 4.1**). The asymmetric unit (ASU) (**Figure 4.1**) consists of two crystallographically independent $Cu^{2+}$ metal ions, two coordinated DMF molecules, four uncoordinated DMF molecules and, two fully deprotonated 4,4'-(hexafluoroisopropylidene)bis(benzoic acid) (hfipbb) ligands.

Each $Cu^{2+}$ metal ion center adopts a square pyramidal geometry resulting from four different carboxylate oxygen atoms (O1, O2, O3 and O4) from one unique ligand and one oxygen atom (O1S) from the ligated solvent DMF molecule occupying the axial position. The metal ions form Cu···Cu paddlewheels (2.6115(11) Å) secondary building units (SBUs) involving two $Cu^{2+}$ ions and eight oxygen atoms of the hfipbb ligands in a bridging, bidentate fashion. The coordination extends into a 2-periodic framework, which is non-interpenetrated, and forms diamond-shaped channels down the b-axis. Each 2-periodic framework contains one of the $Cu^{2+}$ ions, hfipbb ligands and coordinated DMF molecules, resulting in adjacent frameworks being crystallographically unique.

A list of the unique C–O and Cu–O bond lengths are given in **Table 4.2**, which are in the expected range.[2] The equal length of C1A–O1A, C1A–O2A are 1.266(5) and 1.255(5) Å, respectively, whereas a C=O and C–O bond distance would be closer to 1.2 Å and 1.3 Å, respectively, in a carboxylic acid group that is not deprotonated.[2] The near C–O bond length, indicating that the carboxylic acid group are deprotonated, are as a result of the delocalization of the negative charge.

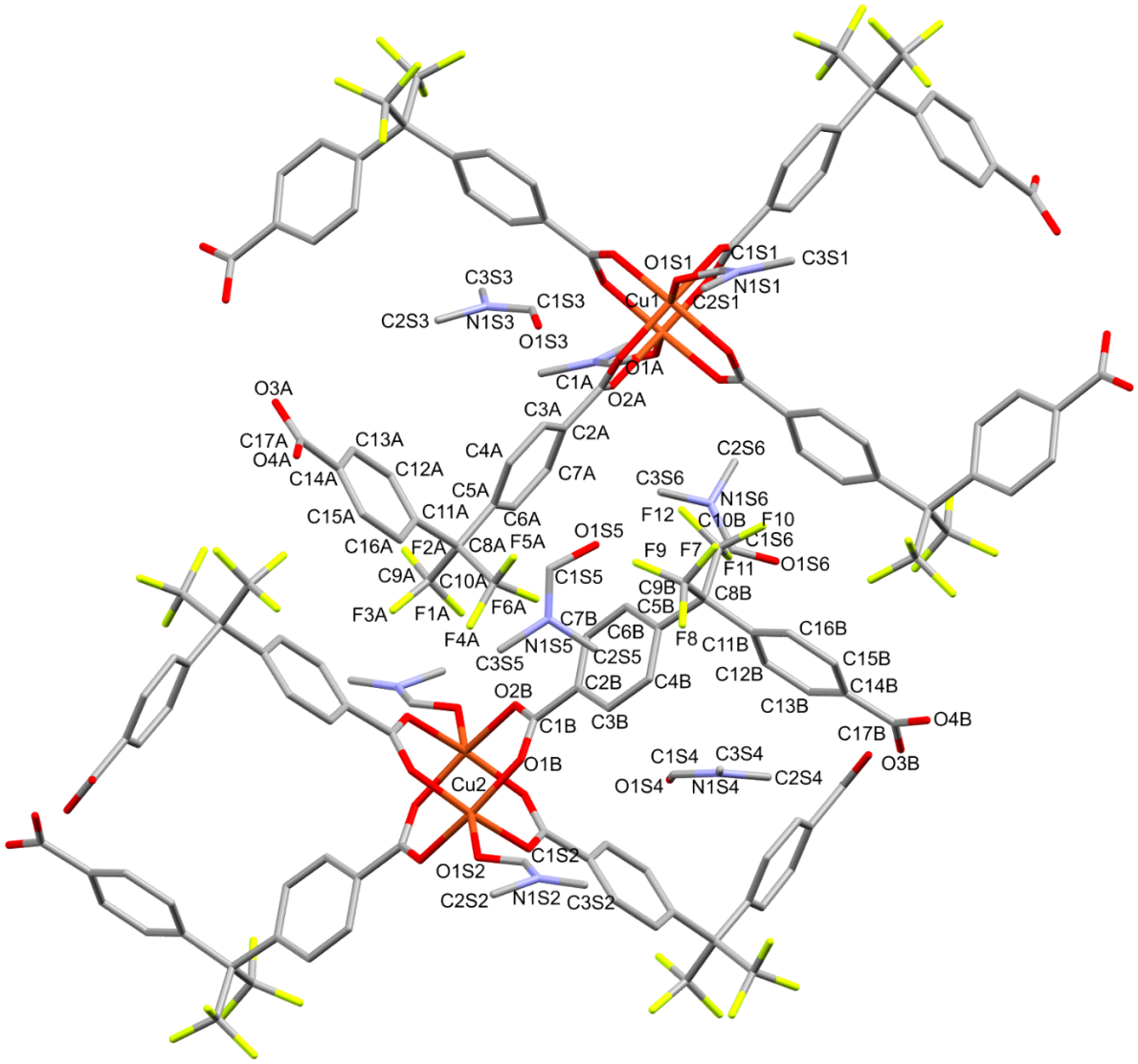


**Figure 4.1.** Labelled ASU and full coordination sphere around the $Cu^{2+}$ ion of **MOFDMF(NIP)**. Hydrogen atoms have been omitted for clarity.

**Table 4.2.** List of bond lengths and Cu···Cu distances involving $Cu^{2+}$ metal cations of **MOFDMF(NIP)**.

| Bond | Length (Å) |
|---|---|
| Cu1···Cu1 | 2.6115(11) |
| Cu2···Cu2 | 2.6204(11) |
| Cu1–O1A | 1.950(3) |
| Cu1–O2A | 1.970(3) |
| Cu1–O3A | 1.969(3) |
| Cu1–O4A | 1.949(3) |
| Cu1–O1S1 | 2.121(4) |
| Cu2–O1B | 1.965(3) |
| Cu2–O2B | 1.964(3) |
| Cu2–O3B | 1.965(3) |
| Cu2–O4B | 1.962(3) |
| Cu2–O1S2 | 2.130(3) |
| C1A–O1A | 1.266(5) |
| C1A–O2A | 1.255(5) |
| C1B–O1B | 1.268(6) |
| C1B–O2B | 1.247(6) |

### 4.2.3. Crystal Packing and Void Space Analysis of MOFDMF(NIP)

The extended structure of **MOFDMF(NIP)** reveals that the oxygen atoms of the ligand carboxylate groups, join the nearby SBUs to create a 2-periodic layer in the bc plane (**Figure 4.2**). When viewed perpendicular to the c-axis, the layer appears as a zigzag chain (**Figure 4.3**), whereas when viewed along the b-axis, it appears as a ladder with 1D channels. Two of the unique uncoordinated DMF molecules fill the diamondoid voids created by 1D channels. Along the a-axis, these layers are neatly layered one on top of the other.

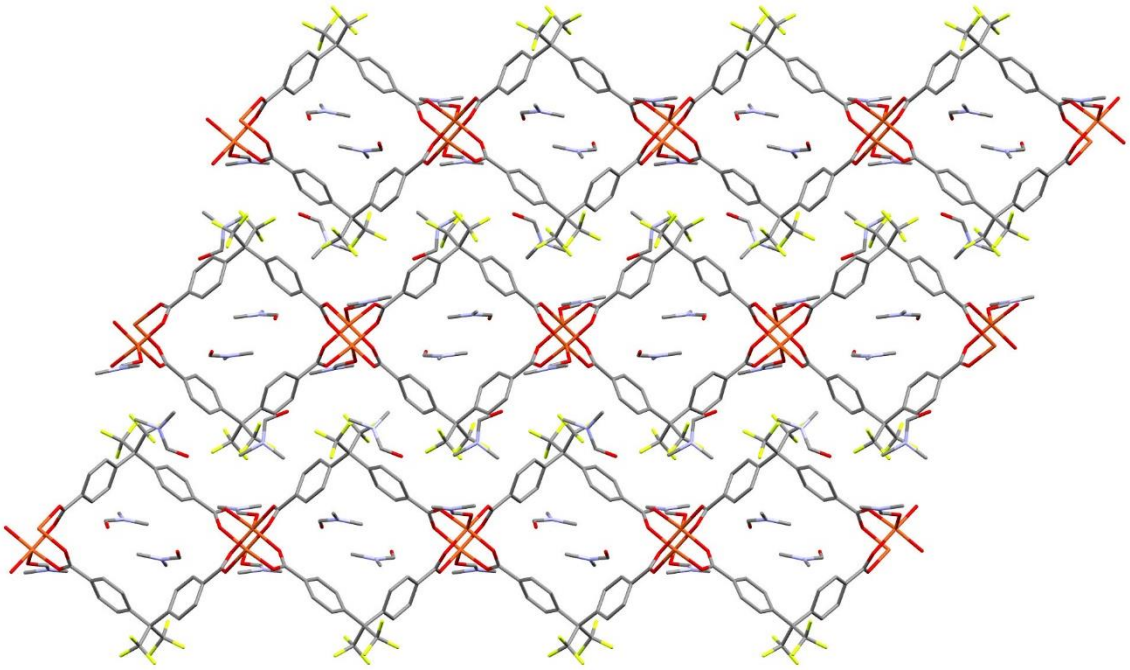

**Figure 4.2.** Packing diagram of **MOFDMF(NIP)** along the crystallographic b-axis showing an edge-on view of the 2-periodic frameworks. Diamondoid channels contain DMF solvent molecules.

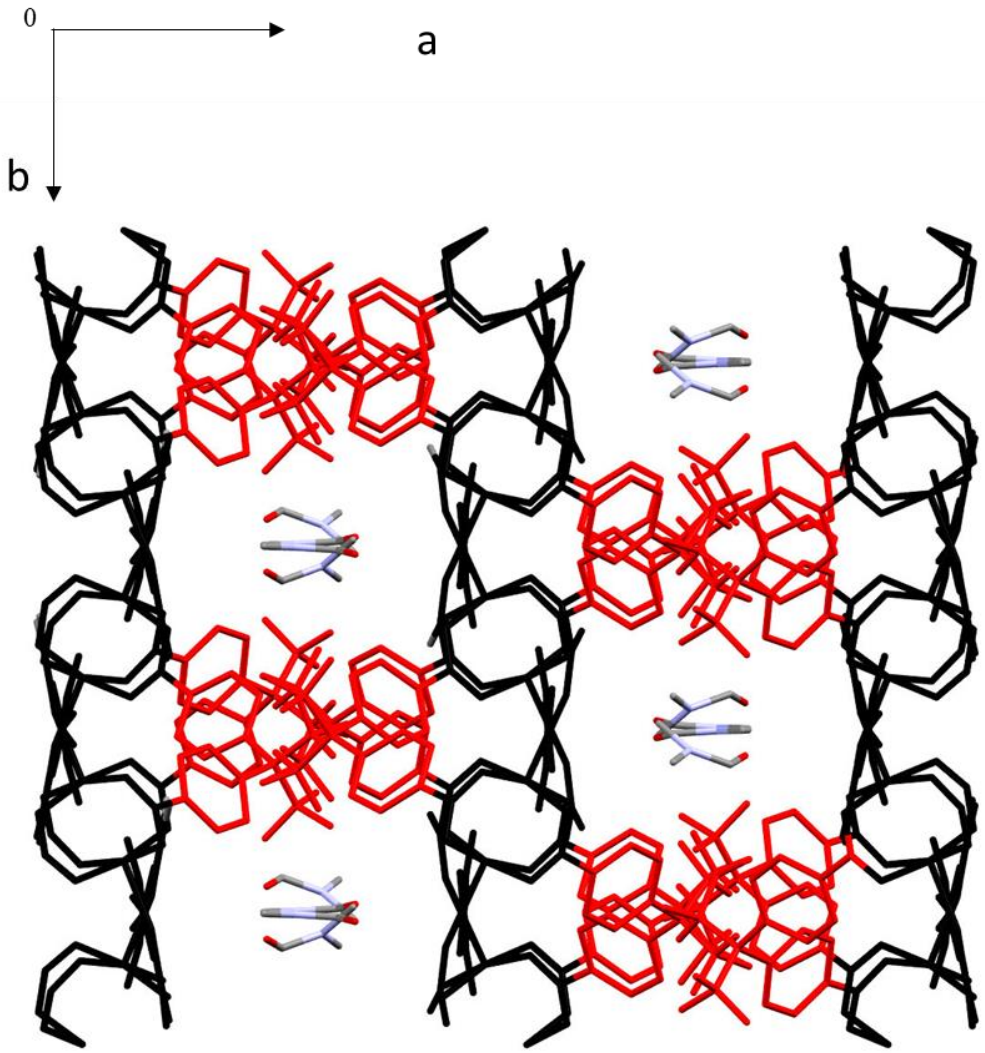


**Figure 4.3.:** Side (c-axis) view of 2D network layer appears as a ladder chain.

The other two unique uncoordinated DMF solvents molecules are found between stacked 2D frameworks (**Figure 4.4**). Deletion of the uncoordinated solvent molecules' coordinates reveals a contact surface potential void space of 39 % of the unit cell and total potential solvent volume. This void space also includes the space between adjacent 2-periodic frameworks that was occupied by two unique uncoordinated DMF molecules. Thus, it is likely that the 2-periodic frameworks will move closer to each other once this solvent is removed (**Figure 4.4**). This is consistent with what was observed by Chatterjee *et al*. for **MOFDMF(IP)** where relative movements of the 2D frameworks were deduced by using a set of planes as a reference point with respect to the location of the trifluoromethyl groups of the 2D layers.[1]

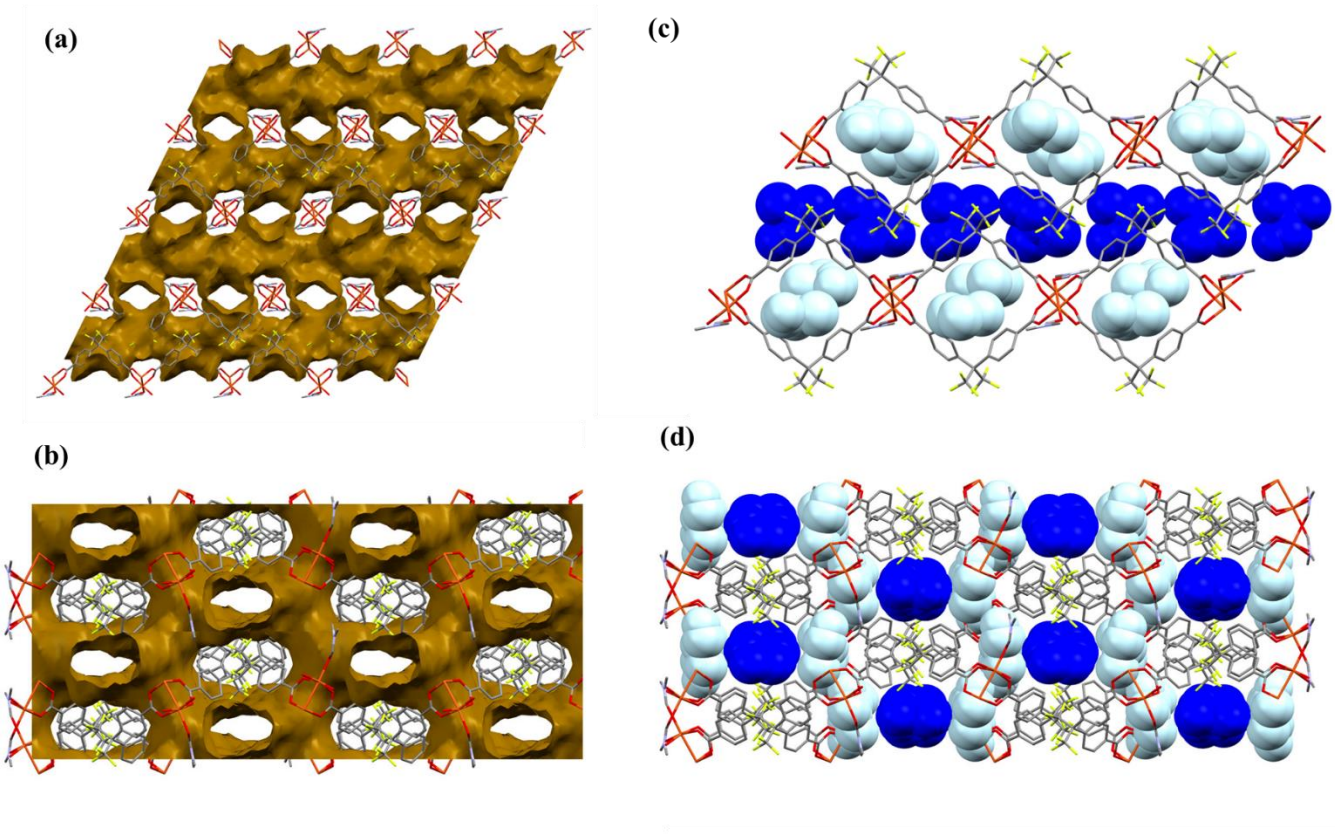


**Figure 4.4.** View of the contact surface potential void space along the (a) b- and (b) c-axes indicating 1D channels down each of these directions. The blue molecules indicate solvents in between the 2-periodic layers and the light blue molecules indicate solvents inside diamond-shaped channels along the (c) b- and (d) c-axis.

The 2-periodic frameworks are non-interpenetrated as revealed by colour-coding of individual frameworks in **Figure 4.5**. The independent nets then stack on top of one another via supramolecular interactions to create a layered structure. The interlayer stacking distance is approximately half of a-axis, 12.954 Å 2D layer lying in the (200) hkl-planes. The intralayer metal---metal distance is half of c axis, 12.191 Å, arranged in the (002) hkl-planes (**Figure 4.6**).

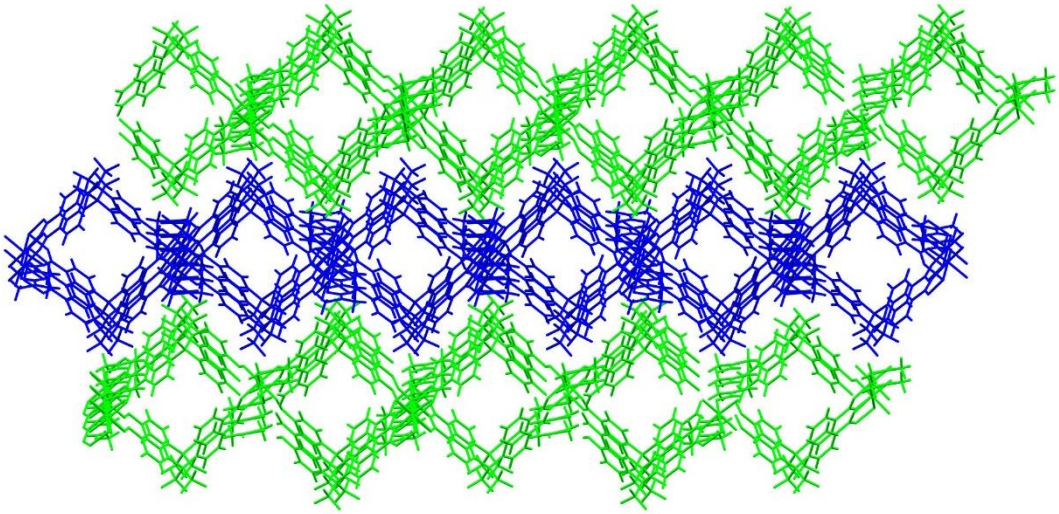

**Figure 4.5.** Packing diagram of **MOFDMF(NIP),** colour-coding of individual frameworks show that the structure is non-interpenetrated.

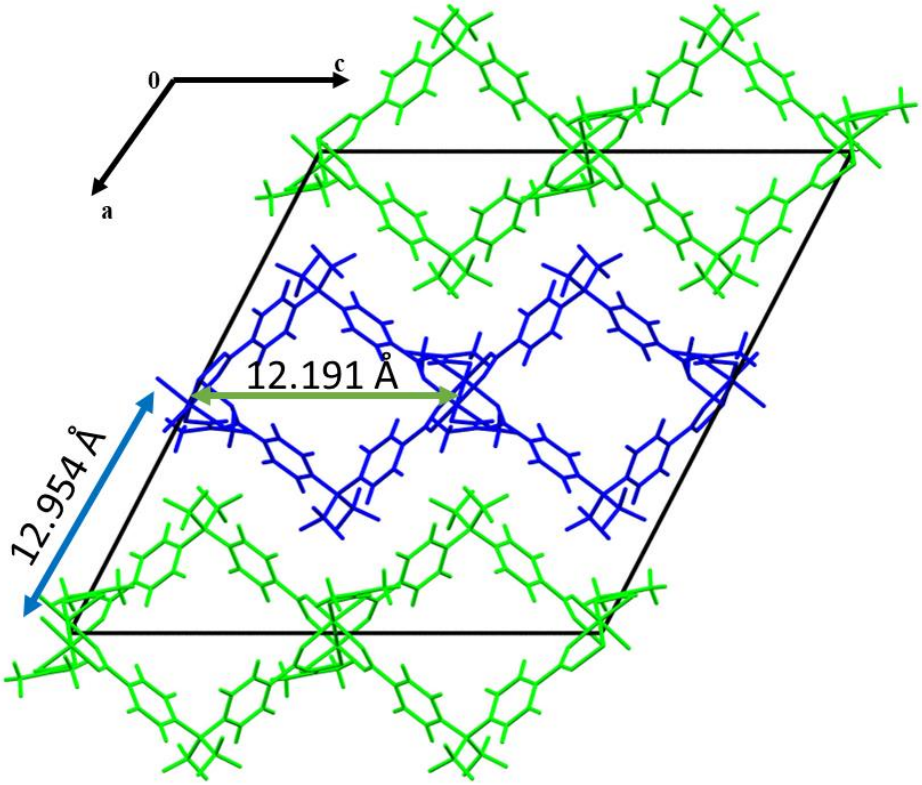


**Figure 4.6.** Crystal structure of **MOFDMF(NIP)** stacking layers viewed down b-axis, (a) the **blue line** shows the interlayer stacking distances of approximately12.954 Å and intralayer space metal---metal distance is 12.191 Å **green line**.

## 4.3. Hydrogen Bonding

Intermolecular hydrogen bonding consists of solvent···framework, framework···solvent interactions (no interframework hydrogen bonding is present) in hydrogen bonding. The first set of hydrogen bonding is C3S1–H3SC···F9 and C3S2–H3SE···F4A which are from ligated solvent···framework interactions. The second set of hydrogen bonds C7A–H7A···O1S5 and C2S6–H2SR···F7, which are two set of interactions are from framework and solvent between layers···framework interactions, respectively. The last interaction is C4B–H4B···O1S4, which is a framework···solvents interactions, and all of these are shown in **Figure 4.7** and only shows intermolecular hydrogen bonding although intramolecular hydrogen bonding are also present as shown in Table 3.

Notably, the majority of intra- and intermolecular interactions are C-H···Ac interactions, where Ac = F ad O (**Table 4.7**). Based on the data provided, solvent with the suffix "S3" (solvent inside the channel) shows no interaction of hydrogen bonding.

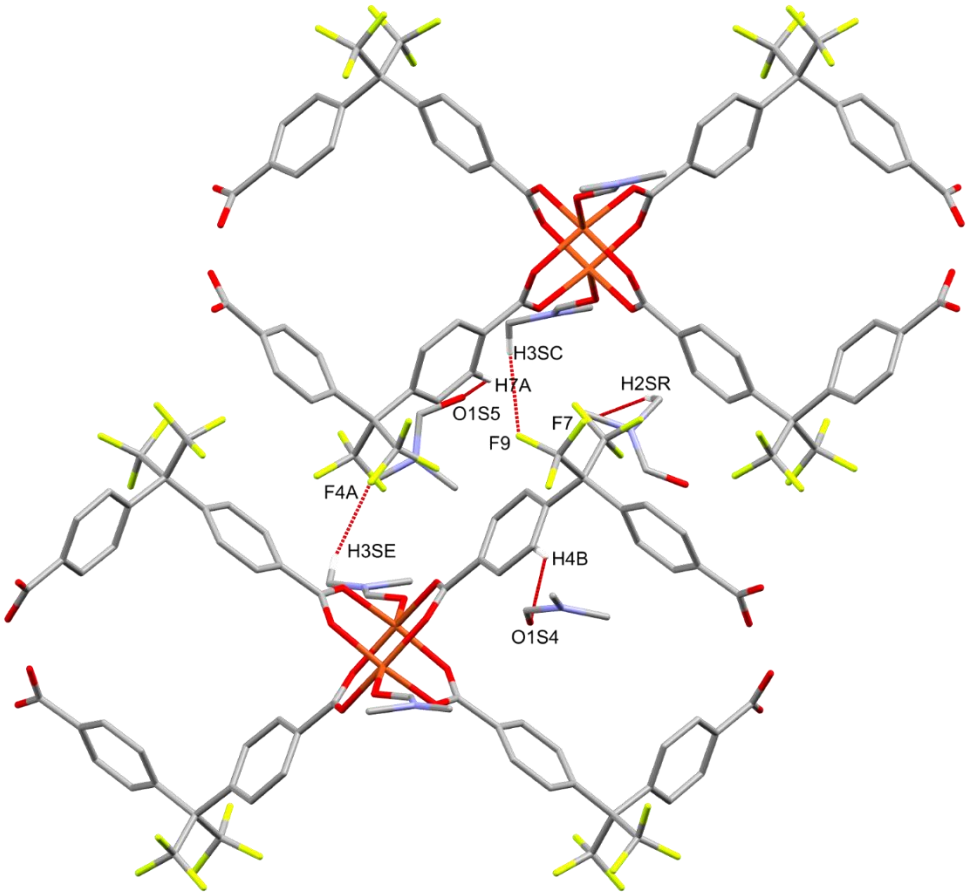


**Figure 4.7.** Hydrogen bonding in the structure of **MOFDMF(NIP)** showing uncoordinated DMF molecules interacting with the framework.

**Table 4.3.** Summary of hydrogen bond parameters in the crystal structure of **MOFDMF(NIP)**. The intramolecular hydrogen bonds are indicated, and the important intermolecular hydrogen bonds are indicated by an asterisk.

| **Donor–H⋯Acceptor** | **H⋯A(Å)** | **D⋯A (Å)** | **D – H⋯A (°)** | **Symmetry operators** |
|---|---|---|---|---|
| C1S1–H1S1⋯O2A (intra) | 2.55 | 3.144(7) | 120 | -x, 2-y, 1-z |
| C2S1–H2SC⋯O1S1 (intra) | 2.40 | 2.781(10) | 103 | |
| C4B–H4B⋯F8 (intra) | 2.54 | 2.960(6) | 107 | |
| *C4B–H4B⋯O1S4 | 2.53 | 3.256(9) | 134 | |
| C6A–H6A⋯F1A (intra) | 2.39 | 3.023(7) | 124 | |
| C6B–H6B⋯F11 (intra) | 2.49 | 2.920(6) | 107 | |
| C6B–H6B⋯F12 (intra) | 2.38 | 3.001(6) | 123 | |
| *C3S1–H3SC⋯F9 | 2.47 | 3.369(15) | 152 | -x,1-y,1-z |
| *C7A–H7A⋯O1S5 | 2.58 | 3.294(9) | 132 | x, 1+y, z |
| *C2S2–H2SE⋯O1B | 2.42 | 3.345(11) | 156 | 1-x, 1-y, 1-z |
| *C3S2–H3SE⋯F4A | 2.44 | 3.258(13) | 141 | 1-x, 1-y, 1-z |
| C16A–H16A⋯F4A (intra) | 2.29 | 2.946(6) | 126 | |
| C16B–H16B⋯F7 (intra) | 2.40 | 3.032(6) | 124 | |
| C2S3–H2SI⋯O1S3 (intra) | 2.40 | 2.792(16) | 104 | |
| C2S4–H2SJ⋯O1S4 (intra) | 2.38 | 2.784(13) | 104 | |
| C2S6–H2SP⋯O1S6 (intra) | 2.34 | 2.757(11) | 105 | |
| *C2S6–H2SR⋯F7 | 2.46 | 3.292(8) | 142 | x, 1+y, z |

*These marked interactions are intermolecular interactions, specifically framework⋯framework or to solvent and solvent⋯solvent.

## 4.4. Powder X-Ray Diffraction

The crystals of **MOFDMF(NIP)**, prepared under solvothermal conditions, were ground to a fine powder then subjected to PXRD analysis. The PXRD pattern of as-synthesized non-interpenetrated crystals of **MOFDMF(NIP)** obtained from this sample was then compared to its calculated PXRD pattern, Mercury based on the single crystal structure of **MOFDMF(NIP)**. The two PXRD patterns were a match to each other, confirming the bulk purity of the material. A high degree of crystallinity is indicated by distinct high peaks (relative to the background). MOF **1** will be referred to as MOFDMF non-interpenetrated (NIP) from here onward (**Figure 4.8**).

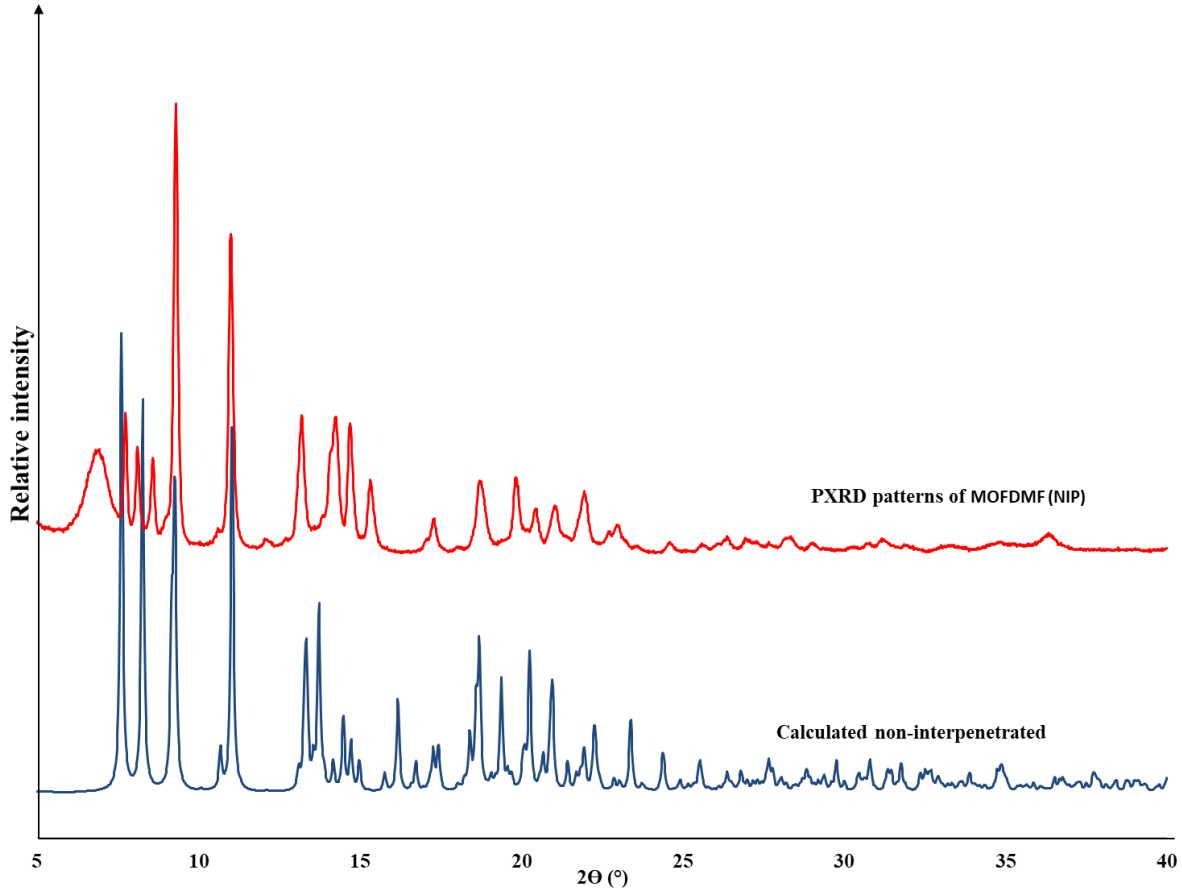


**Figure 4.8.** Calculated PXRD trace patterns of non-interpenetrated and the experimental PXRD patterns of **MOFDMF(NIP)** confirming bulk purity.

### 4.4.1. Variable-Temperature Powder X-Ray Diffraction Studies

The crystals of **MOFDMF(NIP)** were ground, put on a sample holder and the temperature was then raised from 25 °C to 350 °C. The experiment was carried out at temperatures ranging from 25 to 240 °C and results obtained between 100 °C and 275 °C demonstrate that the compound's crystallinity is maintained as the temperature rises (**Figure 4.9**).

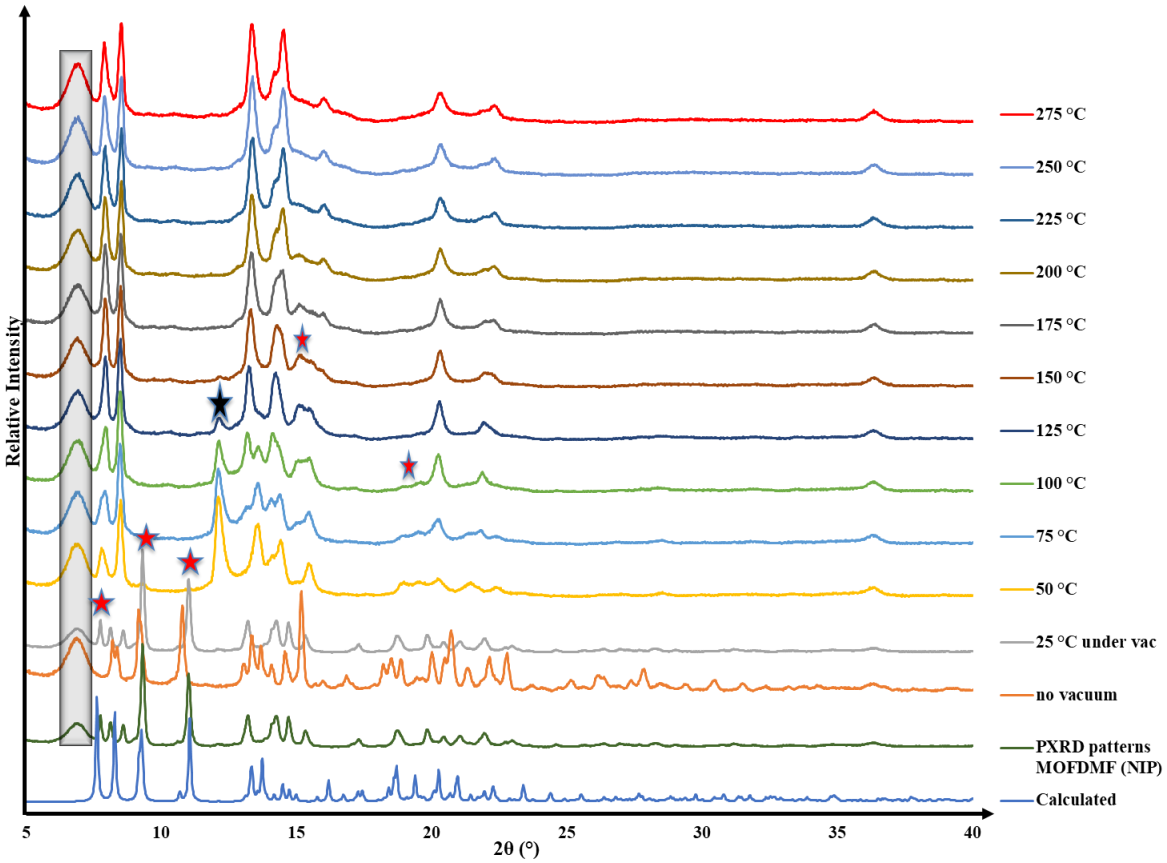


**Figure 4.9.** The PXRD patterns of as-synthesized crystal **MOFDMF(NIP)** and, non-interpenetrated DMF in blue (calculated) are compared to the variable-temperature PXRDs. VT-PXRD is also plotted (from orange to red colour).

The crystallinity of **MOFDMF(NIP)** was evaluated using VT-PXRD under high vacuum and heating conditions, which are required for its activation in gas sorption studies. The calculated pattern was close to the PXRD pattern of **MOFDMF(NIP)** at 25 °C and ambient pressure. The broad peak at 7° 2θ (indicated by the shaded bar) is a sample-stage artifact (background scattering) that appears in all PXRD diffractograms (**Figure 4.9**). When subjected to vacuum at 25 °C in the calculated pattern, three peaks at 7.6, 9.24° and 11.04° 2θ peaks at 50 °C, shown by red-star symbol disappear suggesting structural changes.

The appearance of a new peak at 12.2° 2θ peak at 50° to 125°C is shown by a black star, which indicates structural changes have occurred. Chatterjee *et al.* observed the same structural changes and concluded that this change was due to the layers shifting after the removal of solvent between the layers.[1]

Another change is indicated by the fourth red star, at 15.2° 2θ, at 200°C in the VT-PXRD pattern the intensity of this peak at 15.2° 2θ decreased as compared to other VT-PXRD patterns at lower temperatures and this suggests further structural changes such as the 2D layers shifting, moving closer to each other upon heating. Chatterjee *et al.* observed the same structural changes and concluded that this change was due to the layers shifting after the removal of solvent between the layers.[1]

The 2-periodic layers shift, when the uncoordinated DMF molecules are removed. However, the loss of the metal coordinated DMF molecules does not drastically affect the relative positions of the 2-periodic layers, thus no major changes occur at higher temperatures in the PXRD patterns, and when the desolvated sample is exposed to air at room temperature, which will involve the readsorption of water molecules onto the unsaturated metal sites. The VT-PXRD experiments attest to the thermal stability of the desolvated MOF crystals, with regards to crystallinity, at high temperatures and upon exposure to air (no vacuum) at room temperature.

The sample kept its crystallinity even after being desolvated up to 350°C. The single crystal is an excellent representation of the bulk material because the calculated PXRD pattern of **MOFDMF(NIP)** and the observed pattern at 25 °C were a good match. **MOFDMF(NIP)** maintained its crystallinity up to 350°C after desolvation. The pattern shift at high temperatures suggests a structural alteration when the sample goes through desolvation **MOFDMF(NIP)**.

## 4.5. Thermal Analysis

### 4.5.1. Hot Stage Microscopy (HSM)

The thermal events that were observed in HSM experiments occurred at slightly different temperatures than those in the TG and DSC analyses due to differences in experimental set ups, nonetheless they correspond to those observed in the latter two techniques. Crystals of **MOFDMF(NIP)** were heated from 22 $^{o}$C – 370 $^{o}$C under silicone oil. Silicone oil was used so that the loss of solvent can be indicated by the formation of bubbles.

The crystals began to change colour at 56$^{o}$C to a lighter green colour, which is indicative start of desolvation (**Figure 4.10.b**). At about 159$^{o}$C another colour change is observed, where the colour becomes distinctively opaque as the crystal loses solvent (supported by TGA), indicated by bubble (red circle in **Figure 4.10.c**).

The crystal experiences another colour change, from a blue crystal to purple crystal, this indicates the loss of coordinated solvent (**Figure 4.10.d**). There after bubbles emerge, with the colour change suggesting the beginning of decomposition (**Figure 4.10. e**). The crystals disintegrate at 362$^{o}$C, to a brown colour in combination with bubbles, indicate decomposition of the crystal.

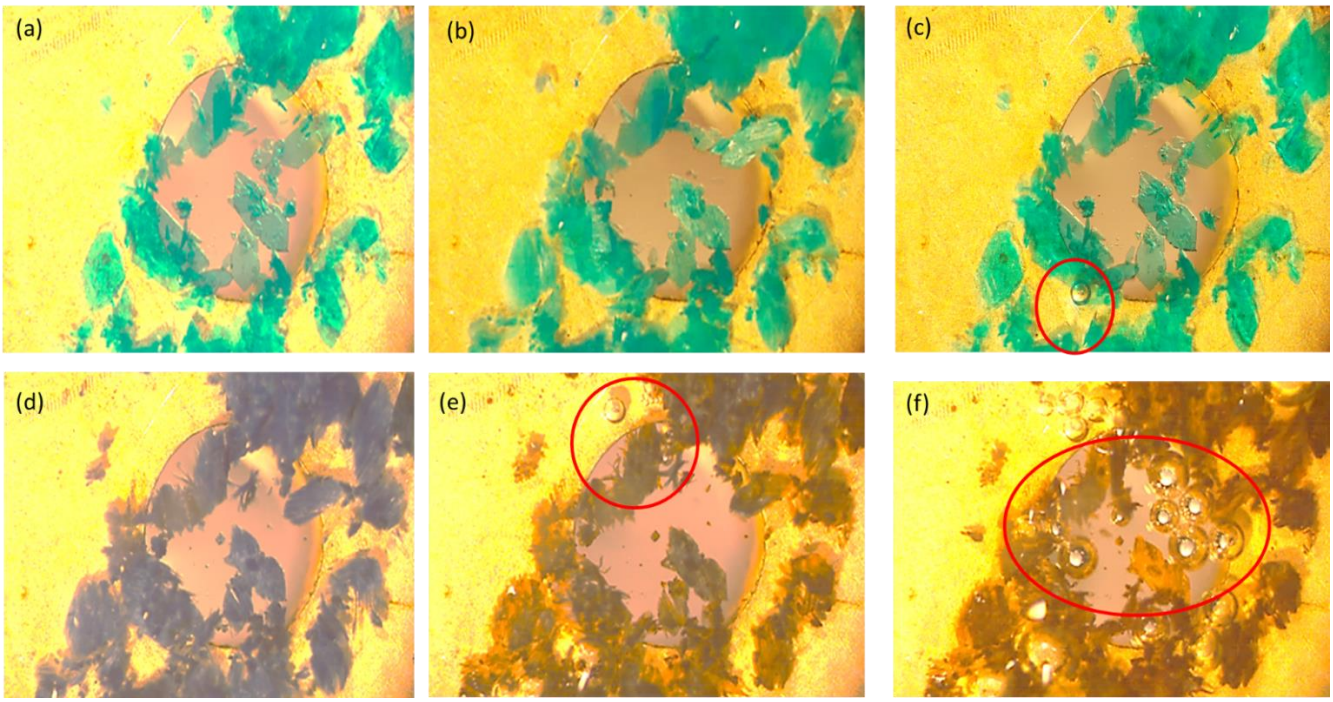


**Figure 4.10.** HSM images of **MOFDMF(NIP)** at (a) 22ºC, (b) 56ºC, (c) 159ºC, (d) 225ºC, (e) 325ºC, (f) 362ºC.

### 4.5.2. Thermogravimetric and Differential Scanning Calorimetry Analysis

Thermogravimetric analysis (TGA) and differential scanning calorimetry (DSC) were used to investigate the thermal stability of **MOFDMF(NIP)**. The TGA thermogram of MOFDMF (NIP) shows a mass loss with distinct three mass losses (**Figure 4.11.**). The first mass loss is 20.6% (calc. 21.7%) of uncoordinated solvent, between 100 ºC – 150 ºC, shortly it was followed by second mass loss of 10.4% (calc. 10.8%) ligated solvent, also between 200 ºC – 275 ºC with a total mass loss of up to 31.0%. Structural decomposition is indicated by the remainder of the TGA thermogram 350 ºC unequivocal proof of the inclusion of the solvent molecules in the bulk sample. This findings alongside the crystal structure suggests that all the non-ligated solvents evacuate first then followed by the ligated.

DSC analysis corroborates the mass losses observed in TGA as indicated by the endotherms in the range 20 °C – 400 °C. The DSC thermogram for **MOFDMF(NIP)** shows three different endotherms (**Figure 4.11.**). The first endotherm corresponds to uncoordinated solvent (DMF), with an onset temperature of 100ºC and a peak temperature at 125ºC. The second endotherm has an onset temperature of 200ºC and a peak temperature of 225ºC which corresponds to coordinated DMF. The third endotherm has an onset temperature of about 300ºC and a peak temperature of 350ºC, which corresponds with the onset of decomposition, as also indicated in the TG analysis.

**Table 4.4.** Summary of calculated and experimental mass losses and their associated temperature ranges for **1.**

| | **Calculated Mass loss (%)** | **Experimental mass loss (%)** | **Temperature range (°C)** |
|---|---|---|---|
| MOFDMF (NIP) | Total = 32.6<br>$1^{st}$ =21.7<br>$2^{nd}$ =10.8 | Total = 31.0<br>$1^{st}$ =20.6<br>$2^{nd}$ =10.4 | <br>$1^{st}$ = 35 – 87<br>$2^{nd}$ =87 – 300 |

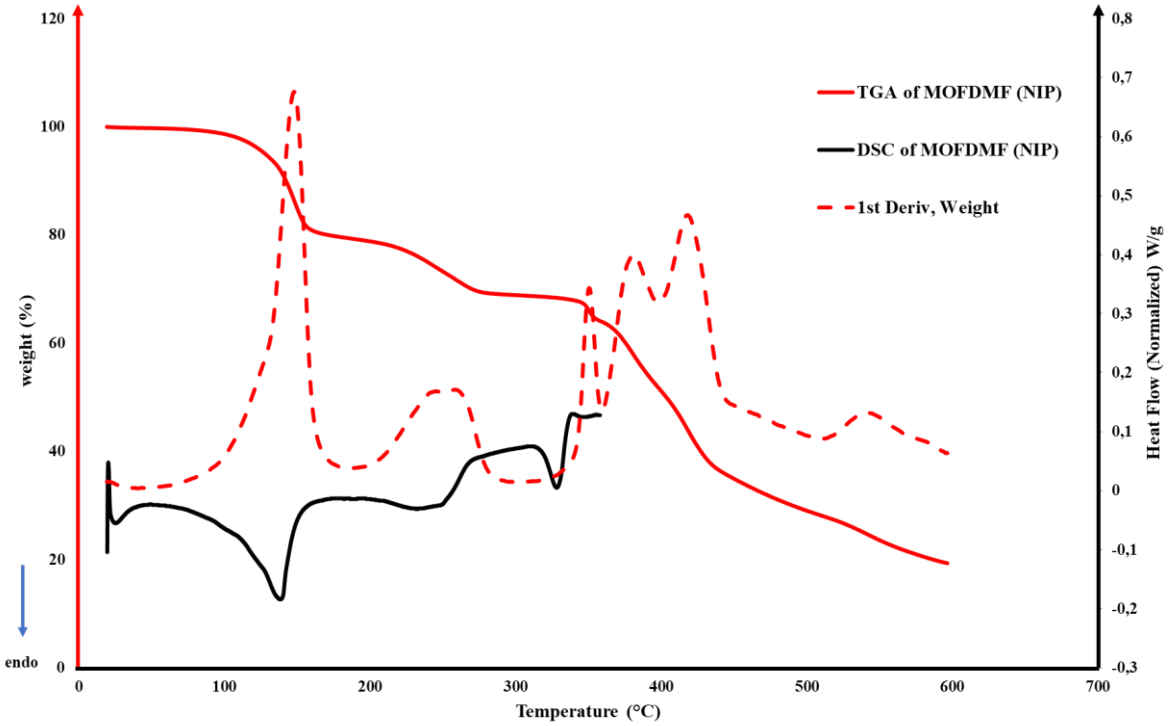


**Figure 4.11.** Overlay of the TGA (red), TGA derivative (red) and DSC (black) thermograms for **MOFDMF(NIP)**.

## 4.6. Single Crystal X-ray Diffraction

The synthesized novel 2-periodic, copper-based non-interpenetrated MOF, of the formula $[Cu(hfipbb)(DEF)]_n \cdot n(DEF)_2$ **(2)** named in this thesis **MOFDEF(NIP)**, is isoreticular to Chatterjee *et al.*[1] copper-based interpenetrated $[Cu(hfipbb)(DEF)]_n$ named in this thesis **MOFDEF(IP)**.

### 4.6.1 Structure Solution and Refinement

A single crystal of each MOF compound was selected, crystal **MOFDEF(NIP)** was selected from the mother liquor and mounted using a cryoloop and Paratone N oil. Data collections was carried out on a Bruker D8 Venture diffractometer using Mo Kα (λ = 0.71073 Å) radiation (the single crystal X-ray data collection procedure is outlined in **section 2.3.1**. check details given in chapter 2). The crystal and refinement data are displayed in **Table 4.5**.

**Table 4.5.** Crystal and refinement data for MOFs **MOFDEF(NIP)**.

| | **MOFDEF (NIP)** |
|---|---|
| ASU formula | $C_{32}H_{41}CuF_6N_3O_7$ |
| Formula weight | 757.22 |
| Temperature / K | 100(2) |
| Crystal system | monoclinic |
| Space group | $P2_1/c$ |
| a / Å | 13.3756(7) |
| b /Å | 10.6889(6) |
| c / Å | 24.1185(12) |
| α / ° | 90 |
| β / ° | 100.543(2) |
| γ / ° | 90 |
| Volume / $Å^3$ | 3390.0(3) |
| Z | 4 |
| ρcalc / g $cm^{-3}$ | 1.484 |
| $\mu$ / $mm^{-1}$ | 0.728 |
| F(000) | 1572.0 |
| Crystal size/ $mm^3$ | 0.46 × 0.25 × 0.04 |
| Radiation | MoKα (λ = 0.71073) |
| 2θ range for data collection / ° | 4.18 to 54.388 |
| Index ranges | $-17 \leq h \leq 17$, $-13 \leq k \leq 13$, $-30 \leq l \leq 30$ |
| Reflections collected | 190658 |
| Independent reflections | 7513 [$R_{int}$ = 0.0624, $R_{sigma}$ = 0.0183] |
| Data/ restraints/ parameters | 7513/252/446 |
| Goodness-of-fit on $F^2$ | 1.034 |
| Final R indexes [I>=2σ(I)] | $R_1$ = 0.0824, $wR_2$ = 0.2332 |
| Final R indexes [all data] | $R_1$ = 0.0958, $wR_2$ = 0.2490 |
| Largest diff. peak/hole / e $Å^{-3}$ | 1.18/-1.13 |

### 4.6.2. Structure Analysis of:

### **[Cu(hfipbb)(DEF)]$_n$·2(DEF)$_n$ (2)**

Single crystal X-ray diffraction analysis of MOF **MOFDEF (NIP)** revealed that the coordination polymer crystalized in the monoclinic crystal system, in the space group $P2_1/c$ (**Table 4.5.)**. The asymmetric unit (ASU) (**Figure 4.12.**) consists of one crystallographically independent $Cu^{2+}$ metal ion, two uncoordinated DEF molecules and two coordinated DEF molecules, one completely deprotonated 4,4'-(hexafluoroisopropylidene)bis(benzoic acid) (hfipbb) ligand.

The geometry of the $Cu^{2+}$ metal ion is distorted square pyramidal, resulting from four different carboxylate oxygen atoms (O1, O2, O3 and O4) from the ligand and one oxygen atom (O1B) from the ligated solvent DEF molecule occupying the axial position. The Cu–Cu (Cu···Cu distance of 2.6115(11) Å) paddlewheel secondary building unit (SBU) involving two $Cu^{2+}$ ions and eight oxygen atoms of the hfipbb ligands in a bridging, bidentate fashion. The coordination polymer extends into a 2-periodic framework, which is non-interpenetrated, and forms diamond-shaped channels down the b-axis. The 2-periodic framework contains one $Cu^{2+}$ metal ion, hfipbb ligand and coordinated DMF molecules.

A list of the unique C–O and Cu–O bond lengths are given in **Table 4.6**, which are in the expected range.[2-4] The near equal C–O bond lengths, indicating that the carboxylic acid groups are deprotonated, are as a result of the delocalization of the negative charge. For example, the bond distance of C1L–O1L and C1L–O2L are (1.261(5) Å) and (1.259(5) Å), respectively, whereas a C=O and C–O bond distance would be closer to 1.2 Å and 1.3 Å, respectively, in a carboxylic acid group that is not deprotonated.[2]

The unique Cu – O bonds have bond lengths ranging from 1.962(3) Ǻ to 2.121(3) Ǻ. The paddlewheel motif secondary building block (SBU), with a Cu1···Cu1$^1$ interatomic distance of 2.6335(10) Ǻ and is made up of the neighboring tetragonal pyramids. Bond lengths and the spacing between Cu atoms in the complex are similar to those in the published literature.[2,3]

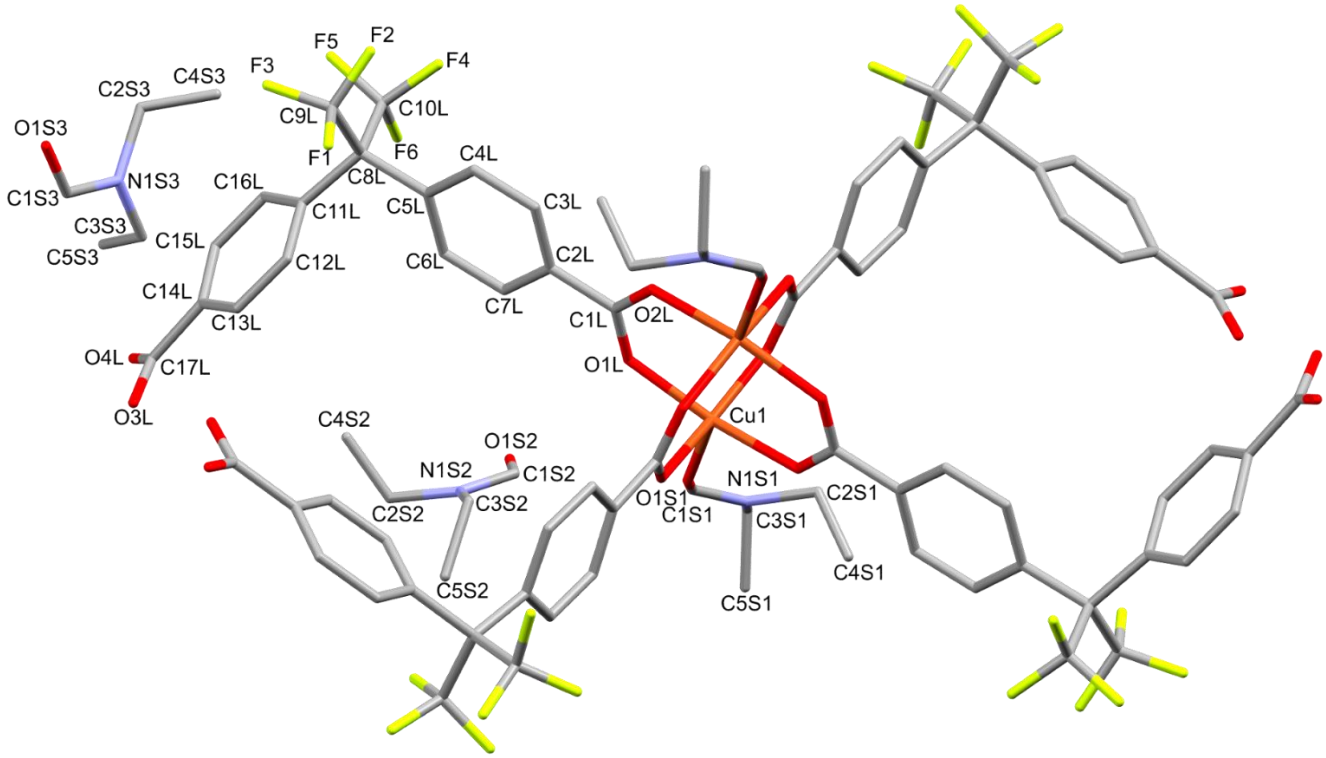


**Figure 4.12.** Labelled ASU and full coordination sphere around the $Cu^{2+}$ ion of **MOFDEF (NIP)**. Hydrogen atoms have been omitted for clarity.

**Table 4.6.** List of bond lengths and Cu···Cu distances involving $Cu^{2+}$ metal cations of **MOFDEF (NIP)**.

| Bond | Length (Å) |
|---|---|
| Cu1···Cu1 | 2.6335(10) |
| Cu1–O1L | 1.969(3) |
| Cu1–O2L | 1.964(3) |
| Cu1–O3L | 1.970(3) |
| Cu1–O4L | 1.962(3) |
| Cu1–O1S1 | 2.121(3) |
| C1L–O1L | 1.261(5) |
| C1L–O2L | 1.259(5) |
| C17L–O3L | 1.257(6) |
| C17L–O4L | 1.255(6) |
| C1S3–O1S3 | 1.290(15) |

### 4.6.3. Crystal Packing and Void Space Comparison:

The extended structure of **MOFDEF(NIP)** reveals that the oxygen atoms of the ligand carboxylate group join the nearby SBUs to create a 2-periodic layer in the bc plane (**Figure 4.13.**). When viewed perpendicular to the c-axis, the layer appears as zigzag (**Figure 4.14.**), whereas when viewed along the c-axis, it appears as diamodoid with 1D channels, with two symmetrically equivalent uncoordinated DEF molecules fill the diamondoid voids and, two symmetrically equivalent uncoordinated DEF molecules in between the layers.

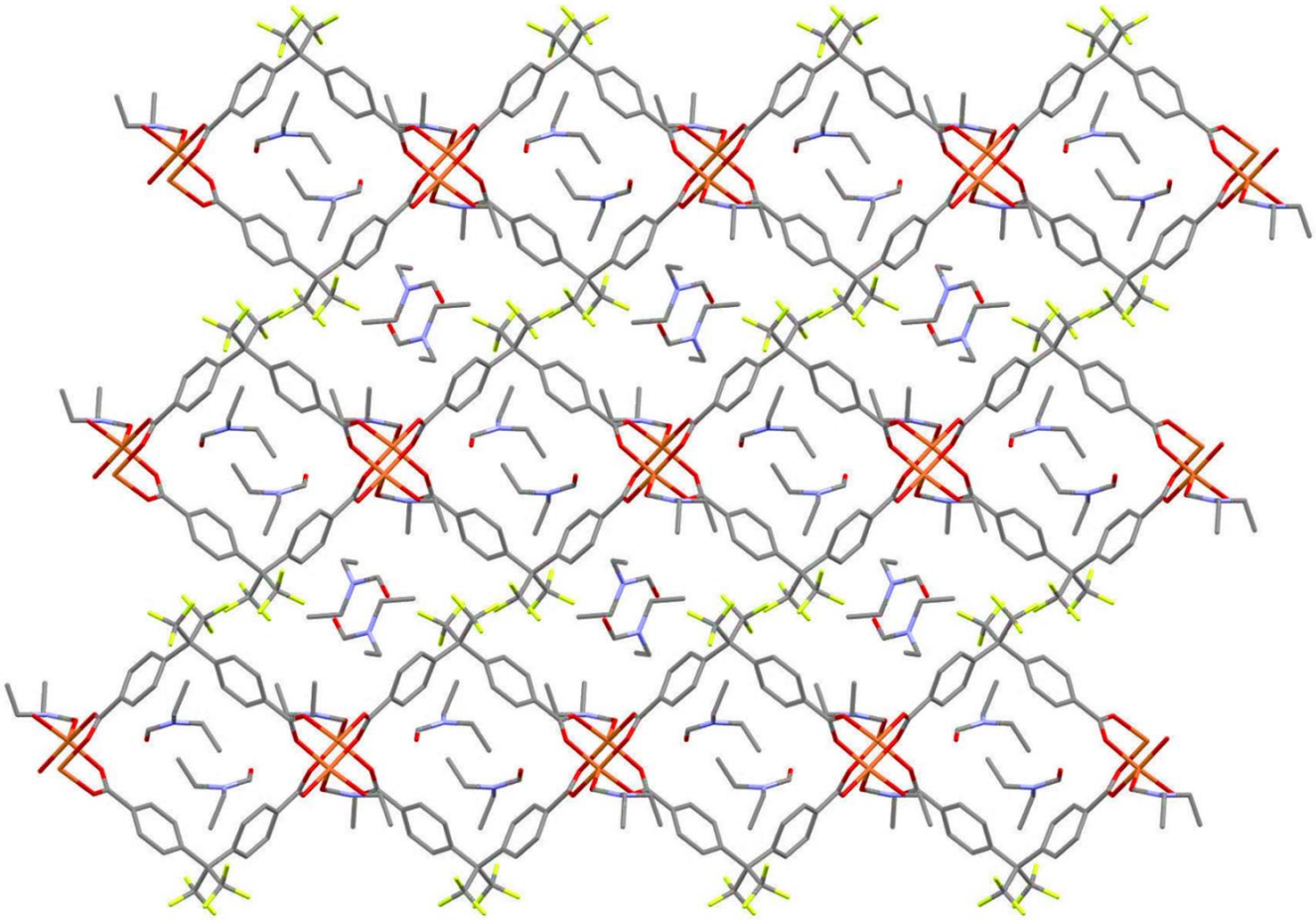

**Figure 4.13.** Packing diagram of **MOFDEF(NIP)** along the crystallographic b-axis showing an edge-on view of 2-periodic frameworks with diagonally aligned, diamondoid channels containing DEF solvent molecules.

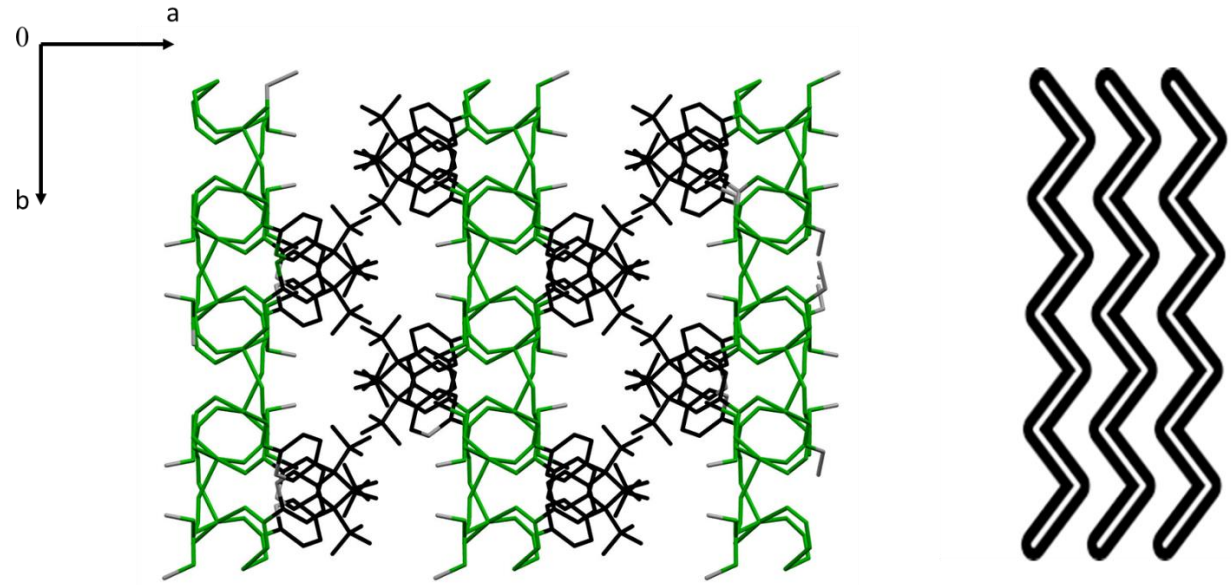


**Figure 4.14.** Crystal packing diagram of **MOFDEF (NIP)** side c-axis view of 2D network layer appears as a zigzag chain.

The other unique uncoordinated DEF solvents molecules are found between stacked 2D frameworks (**Figure 4.13**). Deletion of the uncoordinated solvent molecules' coordinates reveal a contact surface potential void space of 40.4 % of the unit cell, this void space also includes the space between adjacent 2-periodic frameworks that was occupied by two unique DEF molecules. Thus, it is likely that the 2-periodic frameworks will move closer to each other once this solvent is removed (**Figure 4.14**), this has been made evident by the work of Chatterjee *et al*.[1]

Unlike **MOFDMF(NIP)** when viewing down c-axis, where there is solvent in between the layers and forming additional 1D channels there are no such channels in **MOFDEF (NIP)** (**Figure 4.15**) either in the a-axis or c-axis (these axes are at 100° to each other). However, when viewing the structure at 45°, relative to the ac-axis point of origin the contact space potential void space it is forming 2D channels.

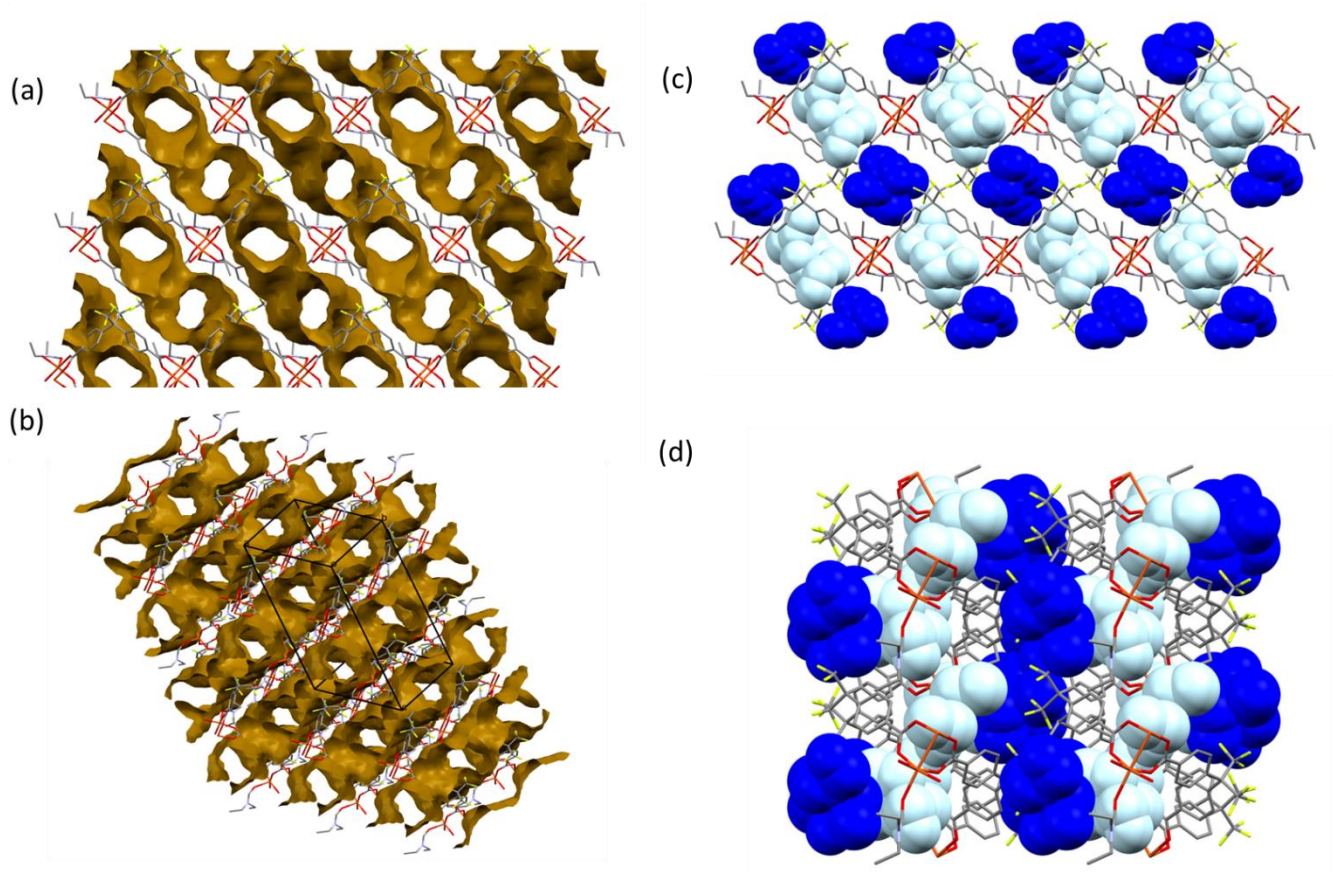


**Figure 4.15.** View of the contact surface potential void space down the (a) b- and (b) 45°, relative to the ac-axis indicating 1D channels down each of these directions. The blue molecules indicate solvents in between the 2-periodic layers and the light blue molecules indicate solvents inside diamond-shaped channels. Mercury using a probe radius of 1.2 Å and grid spacing of 0.7 Å.

The 2 periodic frameworks are non-interpenetrated as revealed by colour-coding of individual frameworks (**Figure 4.16**). The independent nets then stack on top of one another via supramolecular interactions to create a layered structure. The interlayer stacking distance is equal to a-axis, 13.376 Å 2D layer lying in the (200) hkl-planes. The intralayer metal---metal distance is half of c axis, 12.059 Å, arranged in the (002) hkl-planes (**Figure 4.17**).

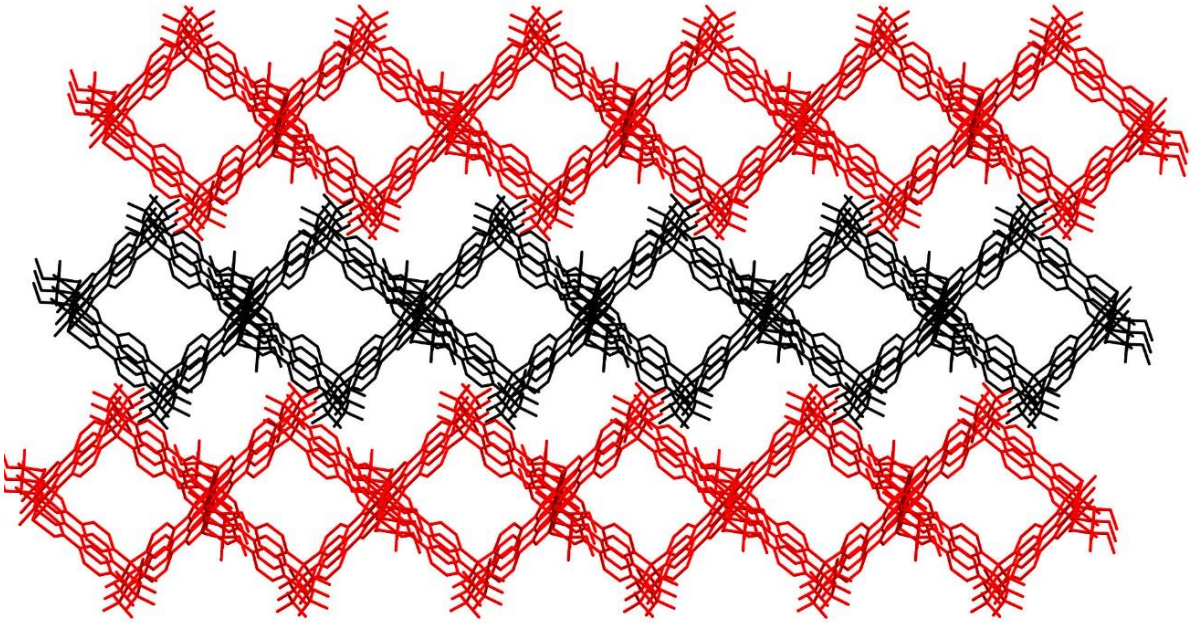

**Figure 4.16.** Packing diagram of **MOFDEF(NIP),** colour-coding of individual frameworks show that the structure is non-interpenetrated.

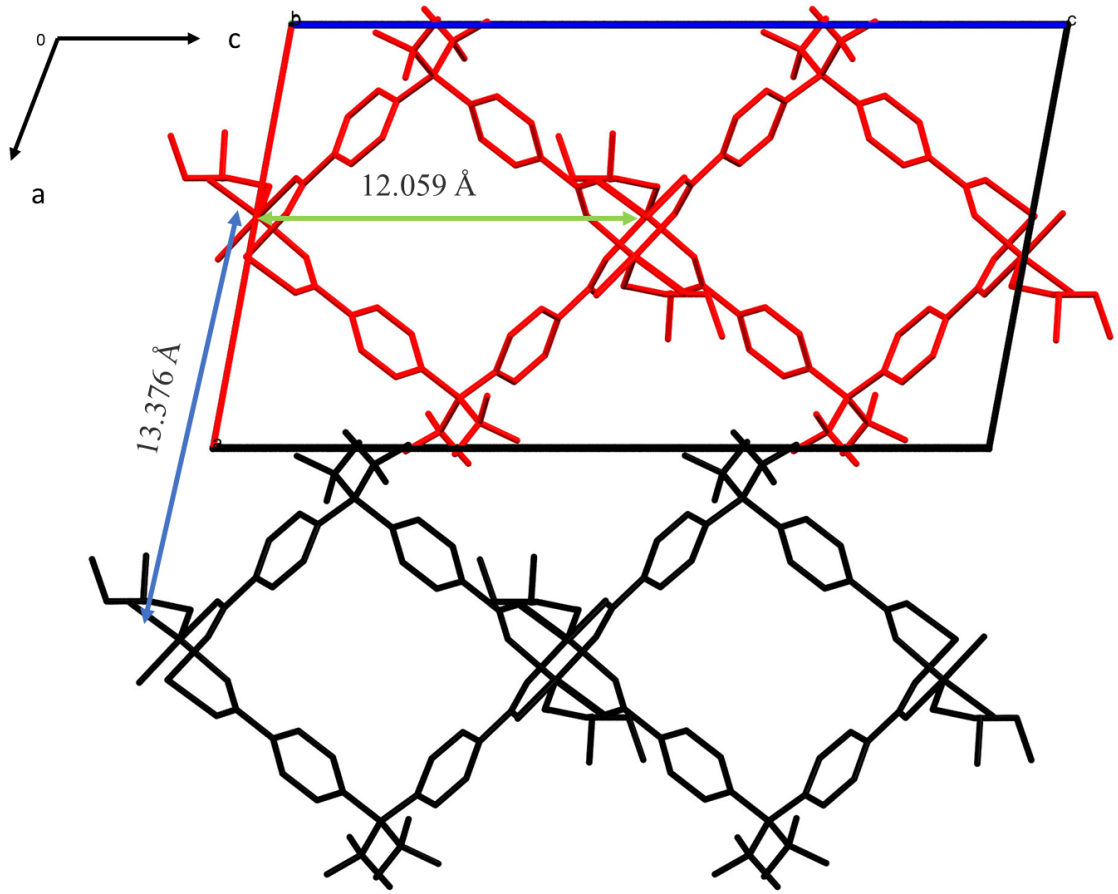


**Figure 4.17.** Crystal structure of **MOFDEF(NIP)** viewed down b-axis, (a) the blue line shows the interlayer stacking distances of 13.376 Å and an intralayer space metal---metal distance of 12.059 Å **green line**.

## 4.7. Hydrogen Bonding

Intermolecular hydrogen bonding consists of solvent···framework and framework···solvent interactions (there is no interframework hydrogen bonding present). The hydrogen bonds are C2S1–H2SA···O1S2 and C1S2–H1S2···O1S1 are ligated solvent–channel solvent interactions. Another intermolecular hydrogen bond is the C2S3–H2SF···O1S3 framework···solvent interactions. The last pair of interactions is C2S3– H3SE··· O1S1 and C4S3– H4SH··· O1S3 between ligated solvent and channel solvent. All of these interactions are shown in **Figure 4.18** which shows intermolecular hydrogen bonding although intramolecular hydrogen bonding is also present as shown in **Table 4.7.**

Notably, the majority of intra- and intermolecular interactions are C-H···Ac interactions, where Ac = F and O (**Table 4.7**). Contrary to **1**, all solvents are involved and, as in the case if **1** there seems to be no framework···framework interactions.

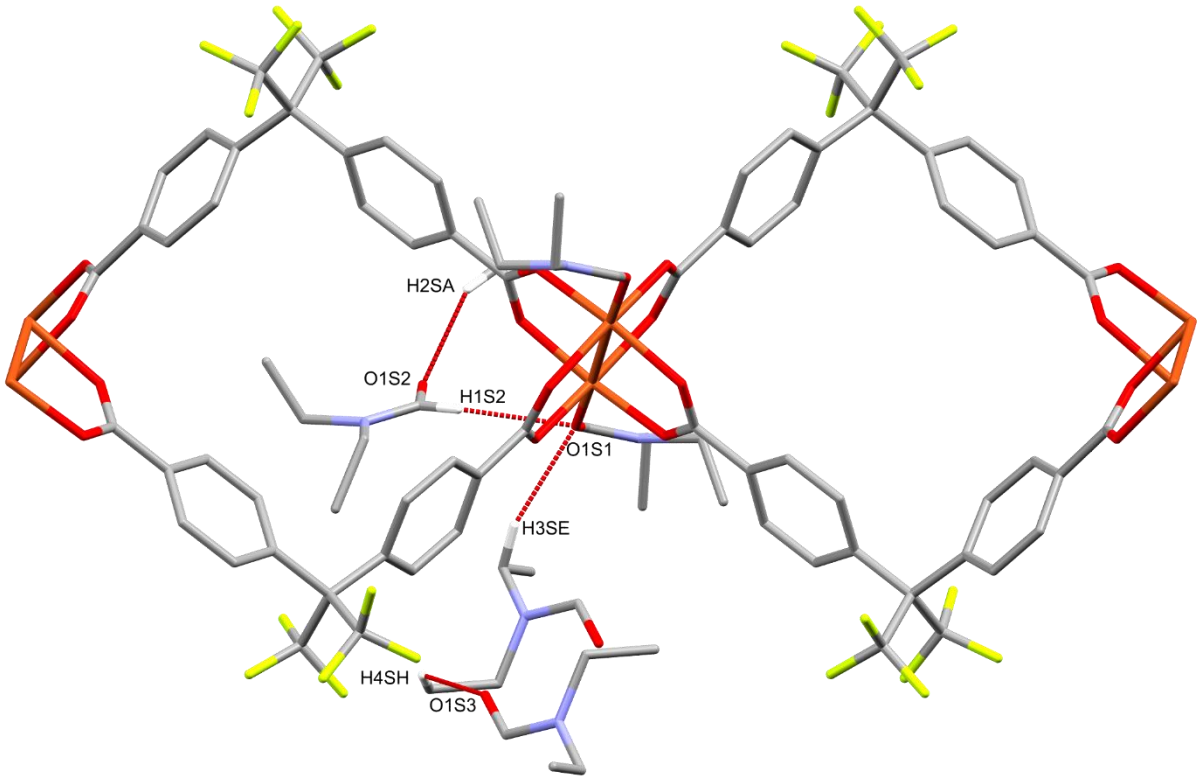


**Figure 4.18.** Hydrogen bonding in the structure of **MOFDEF(NIP)** showing uncoordinated DEF molecules interacting with each other and with the framework.

**Table 4.7.** Summary of hydrogen bond parameters in the crystal structure of **MOFDEF (NIP)**. The intramolecular hydrogen bonds are indicated, and the important intermolecular hydrogen bonds are indicated by an asterisk.

| **Donor–H⋯Acceptor** | **H⋯A (Å)** | **D⋯A (Å)** | **D – H⋯A (°)** | **Symmetry operators** |
|---|---|---|---|---|
| *C2S1–H2SA⋯O1S2 | 2.50 | 3.421(18) | 154 | 1-x,1-y,1-z |
| C2S1–H2SB⋯O1S1 (intra) | 2.50 | 2.842(13) | 100 | |
| C4L–H4L⋯F2 (intra) | 2.37 | 3.021(6) | 126 | |
| C3S1–H3SB⋯O3L (intra) | 2.59 | 3.444(11) | 144 | 1-x, $\frac{1}{2}$+y, $\frac{1}{2}$-z |
| *C1S2–H1S2⋯O1S1 | 2.47 | 3.332(8) | 151 | |
| C12L–H12L⋯F1 (intra) | 2.50 | 2.960(6) | 110 | |
| C2S2–H2SC⋯O1S2 (intra) | 2.40 | 2.761(11) | 101 | |
| C16L–H16L⋯F5 (intra) | 2.35 | 2.971(6) | 123 | |
| C16L–H16L⋯F6 (intra) | 2.42 | 2.857(6) | 108 | |
| C2S3–H2SF⋯O1S3 (intra) | 2.44 | 2.87(3) | 106 | -x,1-y, -z |
| *C2S3–H2SF⋯O1S3 | 2.18 | 2.62(4) | 105 | 1-x, $\frac{1}{2}$ +y, $\frac{1}{2}$-z |
| *C2S3– H3SE⋯ O1S1 | 2.47 | 3.311(17) | 142 | 1-x, $\frac{1}{2}$+y, $\frac{1}{2}$-z |
| *C4S3– H4SH⋯ O1S3 | 1.91 | 2.54(4) | 120 | -x,1-y, -z |

*These marked interactions are intermolecular interactions, specifically framework⋯framework or to solvent and solvent⋯solvent.

## 4.8. Powder X-Ray Diffraction

The crystals of **MOFDEF (NIP)**, prepared under solvothermal conditions, were ground to a fine powder then subjected to PXRD analysis. The PXRD pattern of the as-synthesized non-interpenetrated crystals of **MOFDEF (NIP)** obtained from this sample was then compared to its calculated PXRD pattern, as determined by Mercury based on the single crystal structure of **MOFDEF (NIP)**. The two PXRD patterns match each other, confirming the bulk purity of the material. A high degree of crystallinity is indicated by distinct high peaks (relative to the background (**Figure 4.19**).

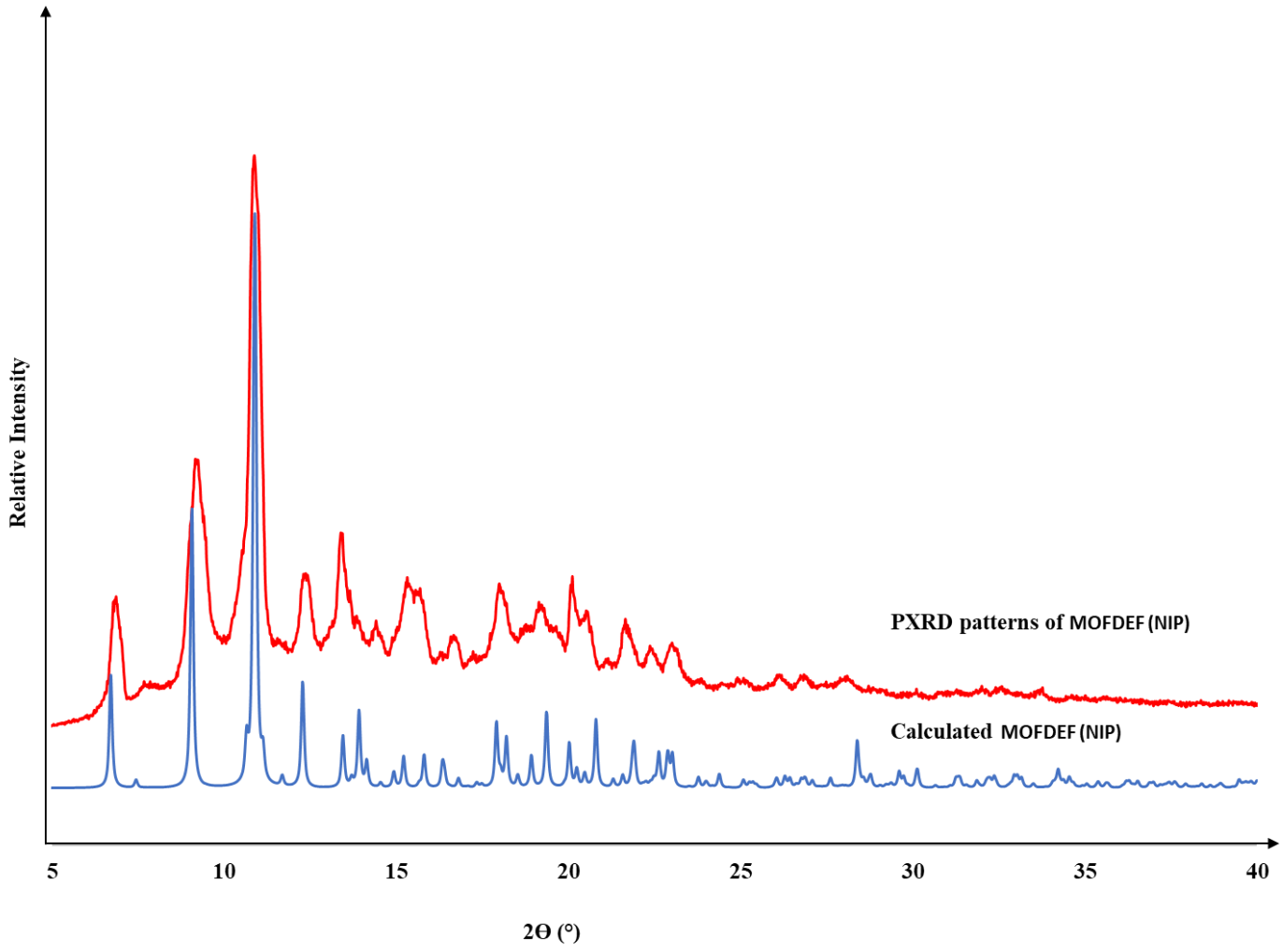


**Figure 4.19.** PXRD trace of calculated non-interpenetrated DEF (blue), and PXRD pattern of **MOFDEF(NIP)** (red) confirming bulk purity.

### 4.8.1. Variable-Temperature Powder X-Ray Diffraction Studies

The crystals of MOFDEF (NIP) were ground, put on a sample holder and the temperature was then raised from 25 °C to 300 °C. The experiment was carried out at temperatures ranging from 25 to 240 °C and results obtained between 100 °C and 275 °C demonstrate that the compound's crystallinity is maintained as the temperature is increased (**Figure 4.20**).

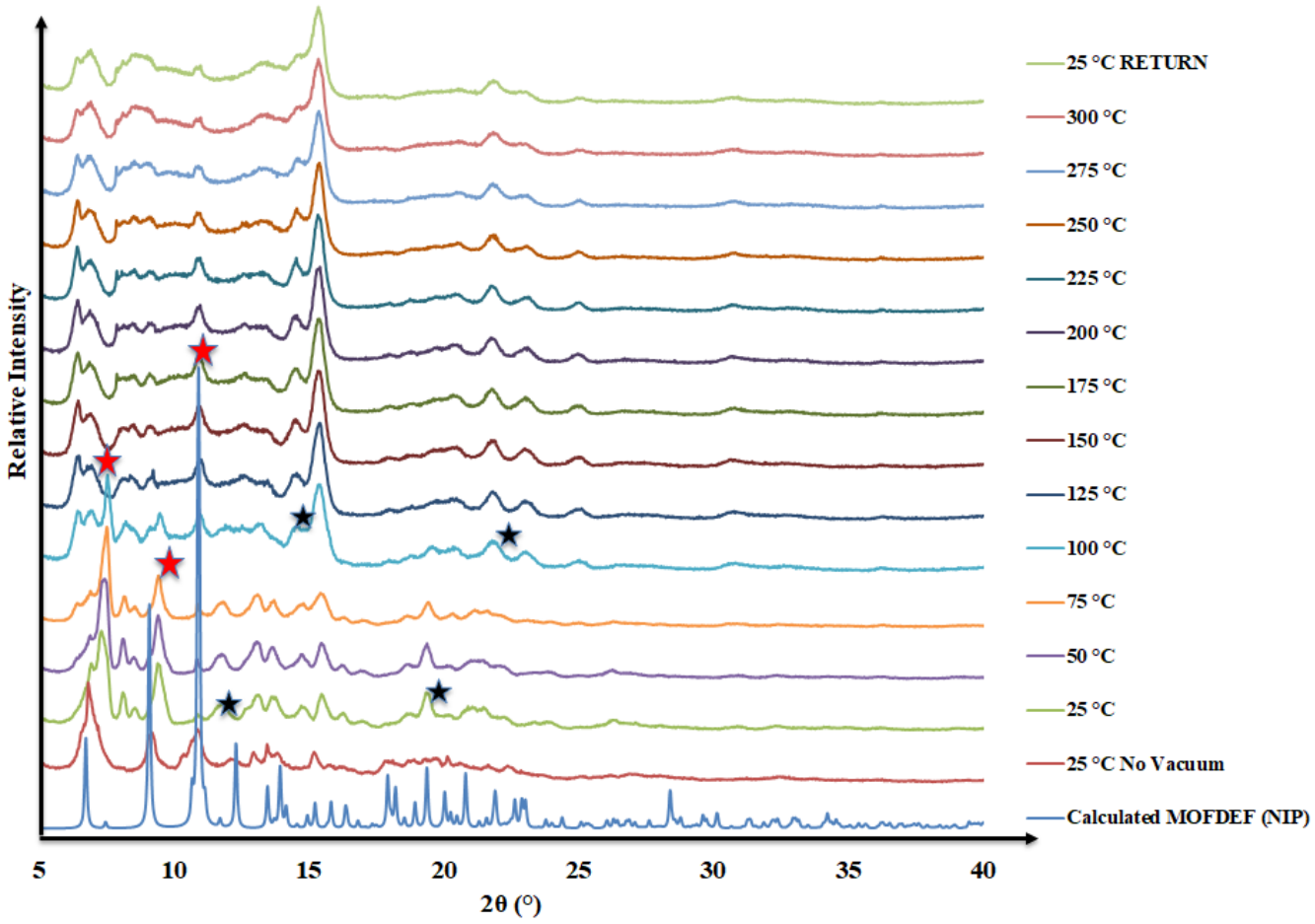


**Figure 4.20.** The PXRD patterns of as-synthesized **MOFDEF(NIP)** and, **MOFDEF(NIP)** in blue (calculated) are compared to the variable-temperature PXRDs. VT-PXRD is also plotted (from red to green colour).

The crystallinity of **MOFDEF(NIP)** was evaluated using VT-PXRD under high vacuum and heating conditions, which are required for their activation in gas sorption studies. The calculated pattern matched the PXRD pattern of MOFDEF (NIP) at 25 °C and ambient pressure. When subjected to vacuum at 25 °C in the calculated pattern, three peaks at 6.7°, 9.1°, 10.9° 2θ peaks at 50 °C, shown by red-star symbol in **Figure 4.20**.

The most intense peak at 10.9 are decreasing in the VT-PXRD diffractograms, in particular the intensity of this peak at 10.9° 2θ has decreased shift of 2D layers nearby upon heating, this suggests that the loss of solvent occurs with some structural change in their individual PXRD

traces, Chatterjee *et al.* observed the similar structural changes and concluded that this change was due to the layers shifting after the removal of solvent between the layers.[1]

The appearance of a new peaks (indicated by black star) at 12.62°, 21.70 2θ peaks at 50°C to 75°C and is shown by a black star, which indicates structural changes have occurred. The second appearance of new peaks at 14.68°, 19.59° 2θ peaks at 100°C to 275°C. The 2-periodic layers shift, this occurs once the uncoordinated DEF molecules are removed. However, the loss of the metal coordinated DEF molecules does not drastically affect the relative positions of the 2-periodic layers, thus no major changes occur at higher temperatures in the PXRD, and when the desolvated sample is exposed to air at room temperature, which will involve the readsorption of water molecules to the unsaturated metal sites. The VT PXRD experiments attest to the stability of the desolvated lattice, with regards to crystallinity, at high temperatures and upon exposure to air (open chamber or no vacuum) at room temperature.

The sample kept its crystallinity even after being desolved up to 350°C. The single crystal is an excellent representation of the bulk material because the calculated PXRD pattern of **MOFDEF(NIP)** and the observed pattern at 25°C were a good match. **MOFDEF(NIP)** maintained its crystallinity up to 350°C of desolvation. The pattern shift at high temperatures suggests a structural alteration when the sample goes through desolvation **MOFDEF(NIP)**.

## 4.9. Thermal Analysis

### 4.9.1. Hot Stage Microscopy (HSM)

Selected crystals of MOFDMF (NIP) were heated from 23$^{o}$C – 324$^{o}$C under silicone oil. Silicone oil was used so that the loss of solvent can be indicated by the formation of bubbles.

The crystals began to show bubble formation at 103$^{o}$C, which is indicative of the start of desolvation and can be supported by TGA (**Figure 4.21.b**). The bubbling at continues and at 255$^{o}$C the crystal experiences another colour change, from a blue crystal to purple crystal, this indicates the loss of coordinated solvent as supported by TGA. The disintergration of crystals can be limited to the loss of uncoordinated solvent between the layers, resulting in the layers moving closer together (**Figure 4.24.d**). The crystals disintegrate at 324$^{o}$C, to a brown colour in combination with bubbles, indicating decomposition of the crystal.

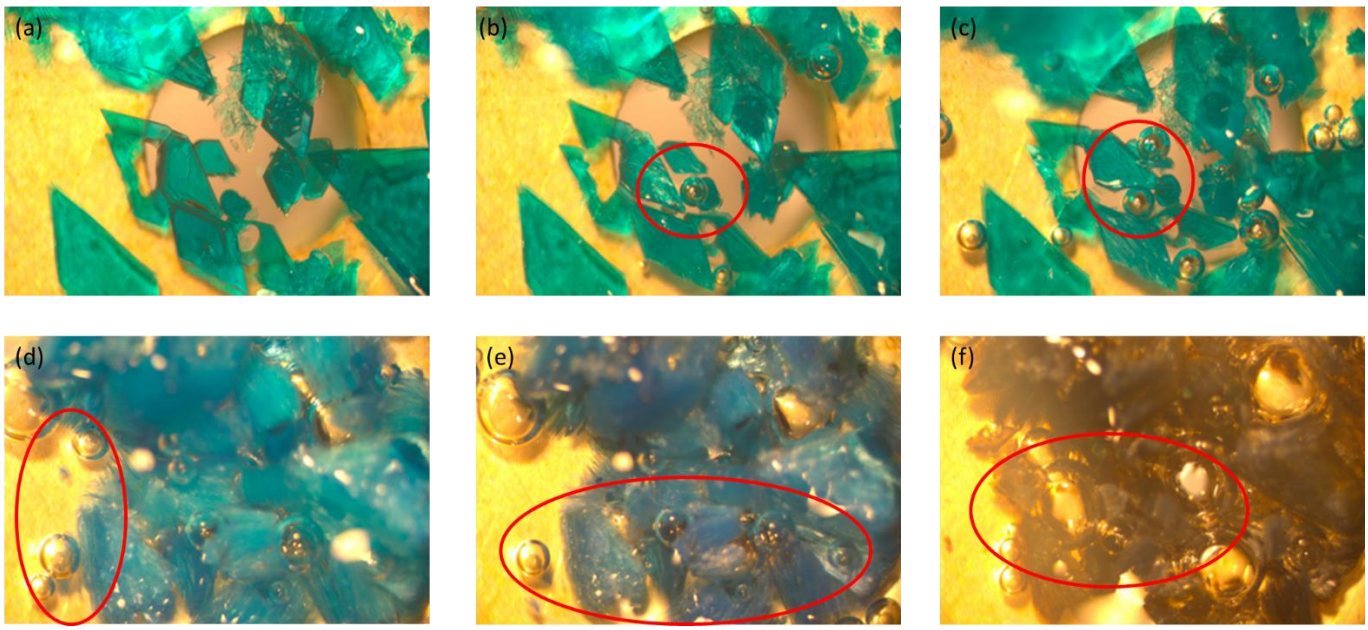


**Figure 4.21.** HSM images of **MOFDMF (NIP)** at (a) 23.9ºC, (b) 103ºC, (c) 125ºC, (d) 255ºC, (e) 293ºC and (f) 324ºC. Red circles same for **2** indicate points of bubble formation.

### 4.9.2. Thermogravimetric and Differential Scanning Calorimetry Analysis

The thermal stability of **MOFDEF(NIP)** was investigated using thermogravimetric analysis (TGA) and differential scanning calorimetry (DSC). **MOFDEF(NIP)** TGA thermogram shows a mass loss with three distinct mass losses (**Figure 4.22.**). The first mass loss is 11.5% (calc. 13.3%) of uncoordinated solvent between 100 ºC and 175 ºC, followed by a second mass loss of 13.0% (calc. 13.3%) of ligated solvent between 200 ºC and 275 ºC, for a total mass loss of 24.5% (calc. 26.6%). The remainder of the TGA thermogram at 350 ºC indicates structural decomposition.

DSC analysis confirms the mass losses observed in TGA, as indicated by endotherms ranging from 20°C – 400°C. **MOFDEF(NIP)** DSC thermogram shows four different endotherms (Figure 4.22.). The first endotherm corresponds to an uncoordinated solvent (DEF) for which an onset temperature of 100 ºC and a peak temperature of 125 ºC were observed using the TRIOS software. The second endotherm has a 125 ºC onset temperature and a 275 ºC peak temperature, both of which correspond to uncoordinated DEF.

The third endotherm has an onset temperature of about 275°C and a peak temperature of 300°C, which corresponds to the start of ligated solvent evacuation, as shown by the TG analysis. The final endotherm has an onset temperature of around 300°C and a peak temperature of 325°C, which corresponds to the start of decomposition, as indicated by the TG analysis.

**Table 4.8.** Summary of TGA values indicating total mass loss for **MOFDEF(NIP).**

| | **Calculated Mass loss (%)** | **Experimental mass loss (%)** | **Temperature range (°C)** |
|---|---|---|---|
| MOFDEF (NIP) | Total = 26.6<br>$1^{st}$ = 13.3<br>$2^{nd}$ = 13.3 | Total = 24.5<br>$1^{st}$ =11.5<br>$2^{nd}$ =13.0 | <br>$1^{st}$ = 30 – 125<br>$2^{nd}$ =175 – 300 |

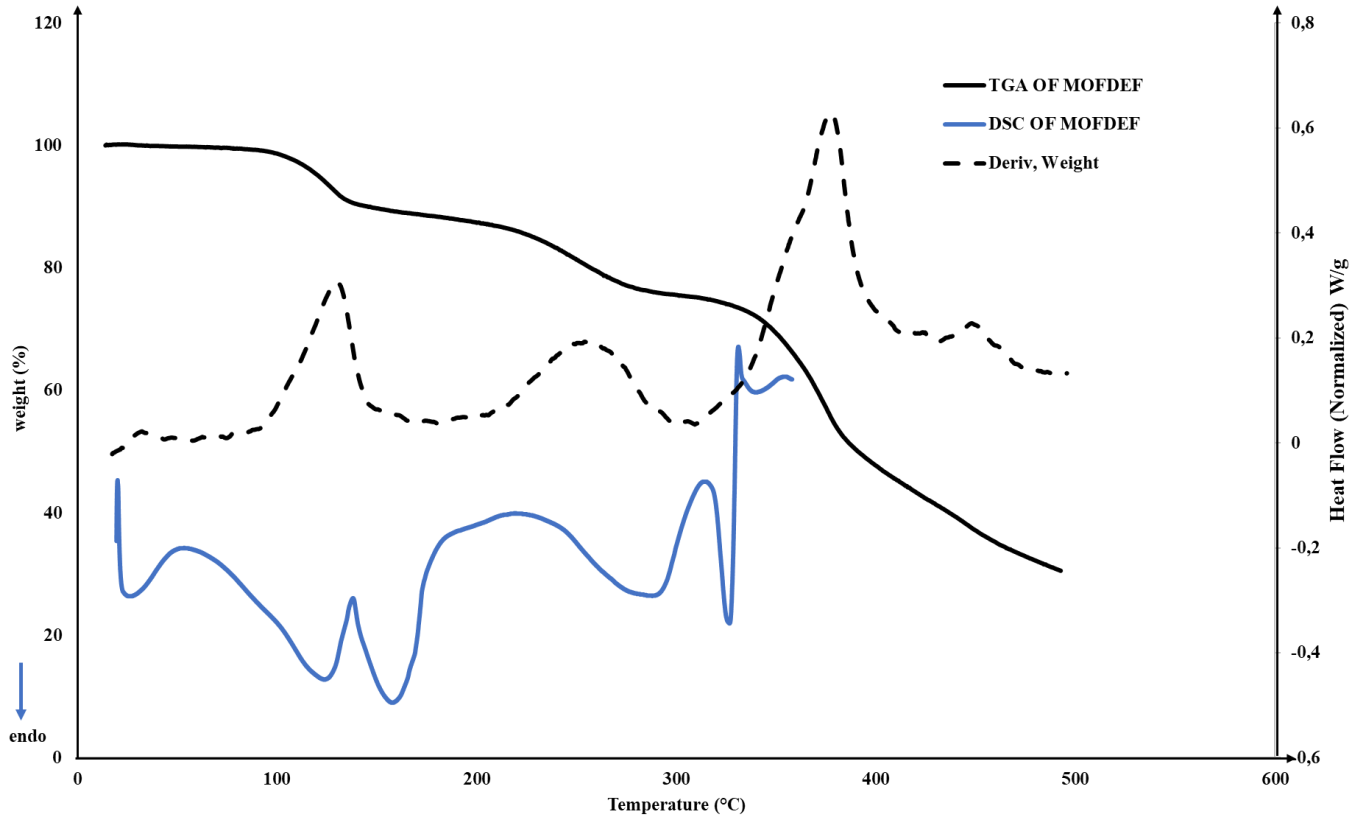


**Figure 4.22.** Overlay of the TGA (black), TGA derivative (black) and DSC (blue) thermograms for crystal **MOFDEF(NIP)**.

## $[Cu_2(hfipbb)_2(H_2O)_2]_n$ (3)

Crystals of the synthesized novel 2-periodic, copper-based non-interpenetrated MOF, of the formula $[Cu_2(hfipbb)_2(DMF)_2]_n \cdot n(DMF)_4$ **(1)** named in this thesis **MOFH₂O(NIP)**, was submerged in water for 7 days at room temperature to create of $[Cu_2(hfipbb)_2(H_2O)_2]_n$ **(3)** or **MOFH₂O(NIP)**. However, there was significant crystal fracturing, precluding single crystal data collection instead, PXRD and VT PXRD patterns of the material were compared to those of the original **MOFDMF(NIP)** to confirm that the material was different. The formula was established using TGA and DSC.

## 4.10. Powder X-Ray Diffraction

The water exchanged crystals of **MOFH₂O (NIP)**, were ground to a fine powder then subjected to PXRD analysis. The PXRD pattern of as-synthesized solvent exchanged non-interpenetrated crystals of **MOFH₂O(NIP)** obtained from this sample was then compared to the calculated PXRD pattern of the original **MOFDMF (NIP)** crystals. The two PXRD patterns did not match each other, confirming the bulk sample was different from the original material. A high degree of crystallinity is indicated by distinct high peaks (relative to the background) (**Figure 4.23.)**.

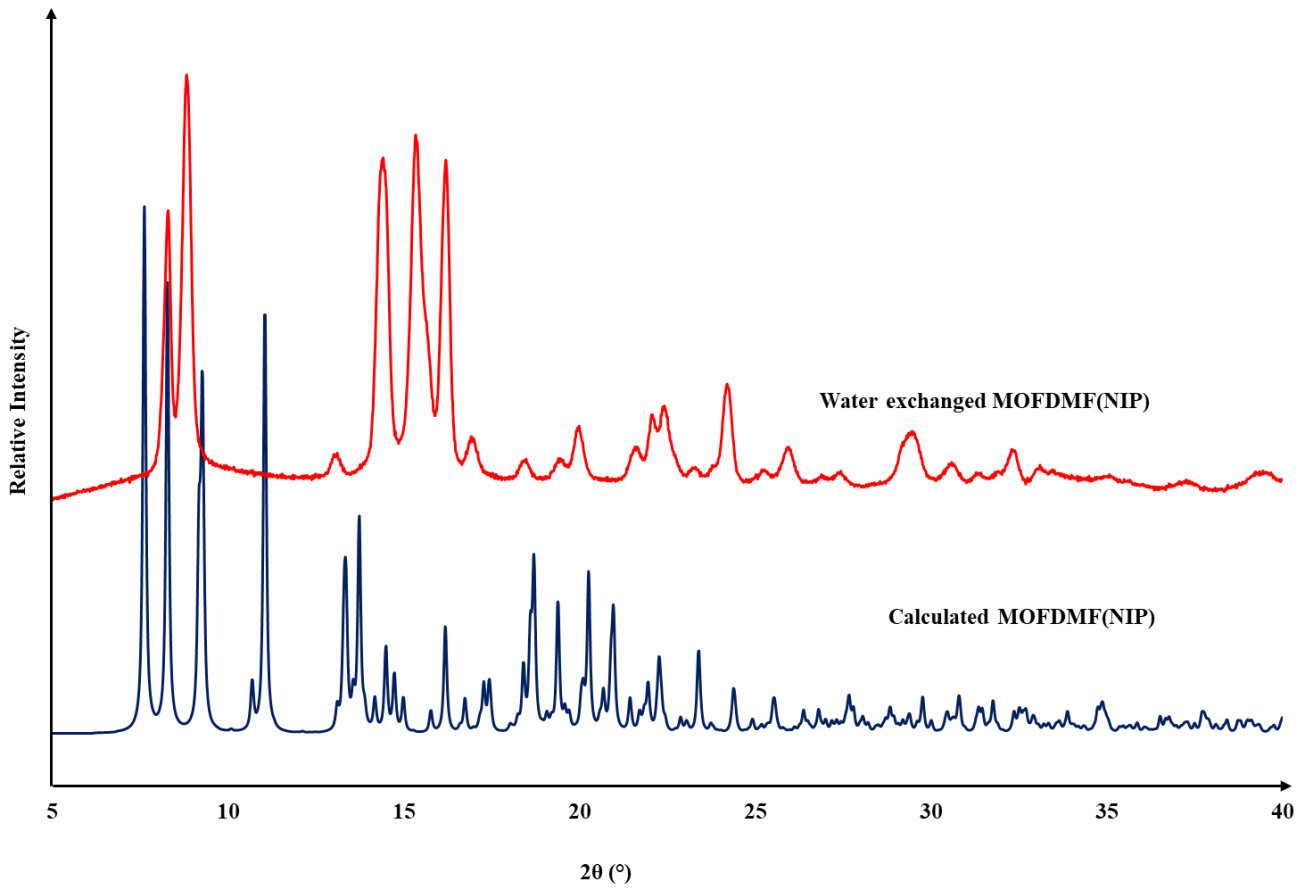


**Figure 4.23.** PXRD traces of calculated **MOFDMF(NIP)**, and the 7-day water exchanged crystals of **MOFDMF(NIP)** or **MOFH₂O(NIP).**

### 4.10.1. Variable-Temperature Powder X-Ray Diffraction Studies

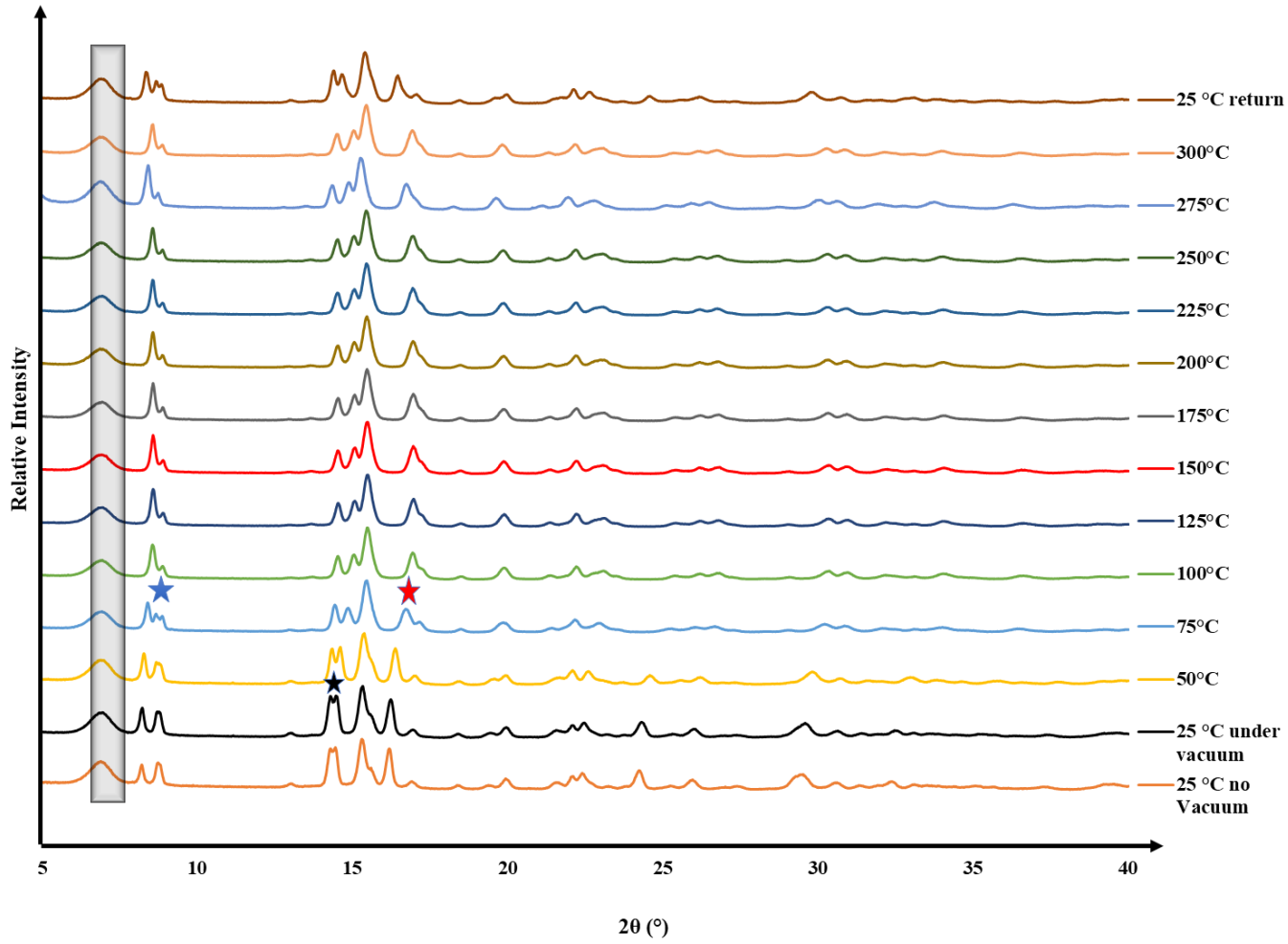


**Figure 4.24.** The Variable-temperature PXRDs diffractograms of **MOFH$_2$O(NIP)**.

The crystallinity of **MOFH$_2$O(NIP)** upon desolvation was evaluated using VT-PXRD under high vacuum and heating conditions, which are required for their activation in gas sorption studies. The calculated pattern was close to the PXRD pattern of the water exchanged **MOFDMF(NIP)** at 25 °C and ambient pressure (**Figure 4.24**). When subjected to vacuum at 25 °C the five peaks observed in the calculated pattern still appear at 8.3°, 8.9°,14.5°, 15.4°, and 16.26° 2θ peaks at 50°C (**Figure 4.24**).

The peak at 14.5° 2θ in the 25°C -under vacuum PXRD pattern begins to split into two in the PXRD patterns continuing up to 300°C (shown by a black star in **Figure 4.24**). Another similar change is observed at 75°C, when the peak at 8.8° 2θ splits (blue star) but this is not evidence in the PXRD patterns higher temperatures. (The last change occurs, when a new peak emerges at 75°C and present up to 300°C). During the experiment the sample retained its crystallinity even after desolvation and throughout the temperatures range up to 300°C.

Unlike the other crystals, one cannot mention layers moving inwards as by assumption based on the Chatterjee *et al*., they made water interpenetrated version of the sample and there were no signs of 2-periodic layers shifting.

## 4.11. Thermal Analysis

### 4.11.1. Thermogravimetric and Differential Scanning Calorimetry Analysis

Thermogravimetric analysis (TGA) and differential scanning calorimetry (DSC) were used to investigate the thermal stability of $MOFH_2O$ (NIP). The TGA thermogram of $MOFH_2O$ (NIP) shows a mass loss with distinct two mass losses (**Figure 4.25.**). The first mass loss is 3.6% (calc. 3.8%) of coordinated solvent, between 125 $^oC$ – 250 $^oC$, corresponding to one water molecule per $Cu^{2+}$ ion, effectively replacing the coordinated DMF molecules of **MOFDMF(NIP)**. The second is structural decomposition is indicated by the remainder of the TGA thermogram at 350 $^oC$. There is no ndication of another solvent either than water in the channels of the MOF.

DSC analysis corroborates the mass losses observed in TGA as indicated by the endotherms in the range 20 °C – 400 °C. The DSC thermogram for **$MOFH_2O$(NIP)** shows three different endotherms (**Figure 4.25.**). The endotherm, corresponding to uncoordinated $H_2O$, has an onset temperature of 100$^oC$ and a peak temperature at 125$^oC$, which corresponds to the loss of ligated solvent, as also indicated in the TG analysis.

**Table 4.8.** Summary of TGA values indicating total mass loss for **$MOFH_2O$(NIP).**

| | **Calculated Mass loss (%)** | **Experimental mass loss (%)** | **Temperature range (°C)** |
|---|---|---|---|
| $MOFH_2O$ (NIP) | 3.8 | 3.6 | 125 – 250 |

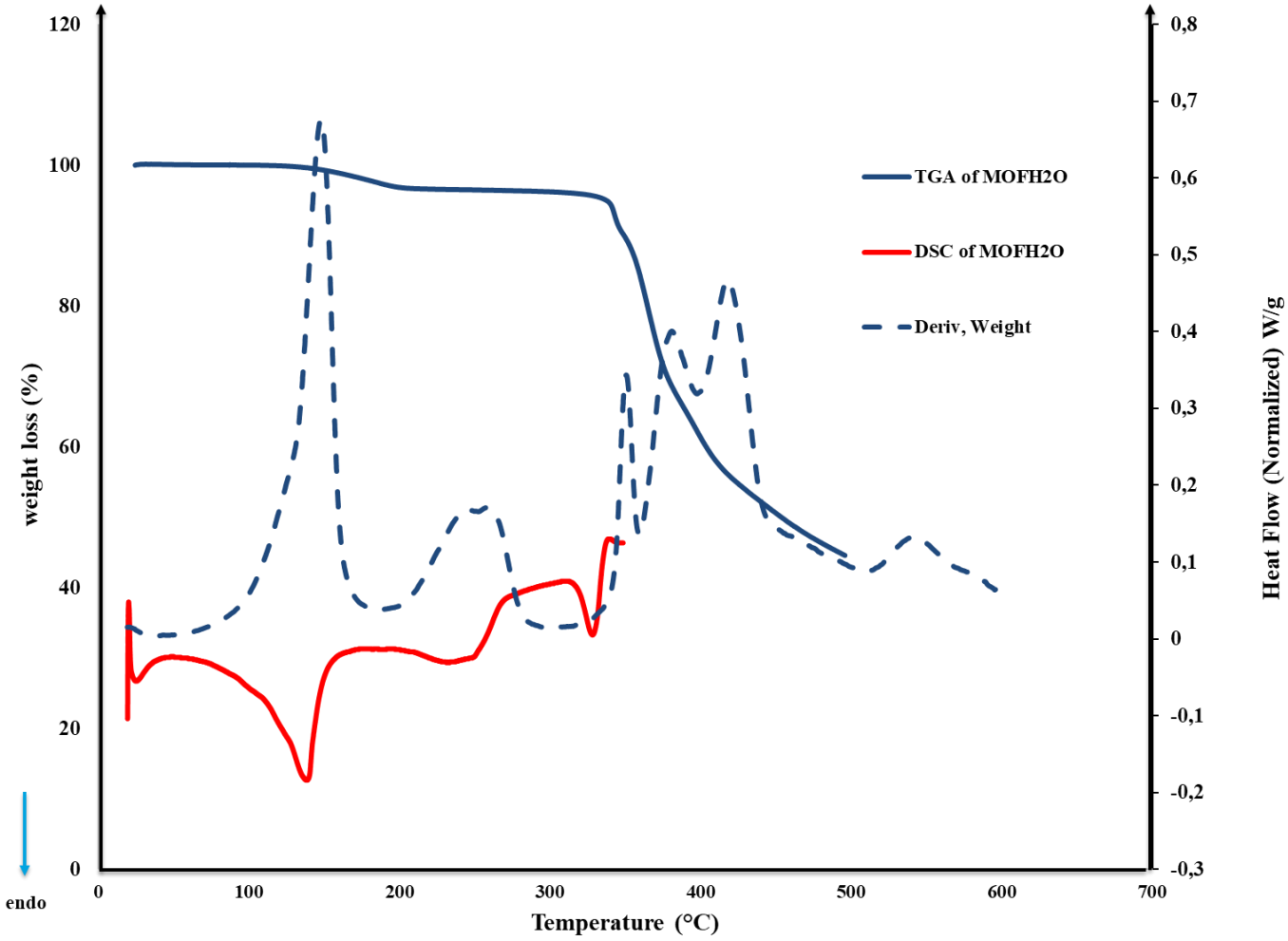


**Figure 4.25.** Overlay of the TGA (blue), TGA derivative (dashed blue) and DSC (red) thermograms for **MOFH$_2$O (NIP)**.

## 4.12. Gas Sorption Studies

To ascertain the capacity of **MOFDMF(NIP), MOFDEF(NIP)** and **MOF$H_2O$(NIP)** to adsorb various gases and water vapour, sorption experiments were performed. For each MOF, the BET surface area and isosteric heats of adsorption were calculated using nitrogen sorption at 77 K and carbon dioxide sorption between 273 – 298K, respectively. MOFs **MOFDMF (NIP), MOFDEF (NIP)** and **MOF$H_2O$ (NIP)** were heated to 200 K to activate the MOFs for subsequent sorption of water vapor (298 K), carbon dioxide (195, 273, 283 and 298 K), hydrogen and nitrogen gases at (77 K).

### 4.12.1. Carbon Dioxide Sorption

At 298 K, **MOFDMF (NIP)**, had a sorption maximum value of 19.6 $cm^3$ (STP) $g^{-1}$ (0.39 molecules of $CO_2$ per Cu-L unit) at an absolute pressure of 801 mmHg. As expected, the $CO_2$ sorption is higher at lower temperatures (sorption is an exothermic process). At 283K the carbon dioxide sorption of 22.3 $cm^3$ (STP) $g^{-1}$ (0.90 molecules of $CO_2$ per Cu-L unit) at an absolute pressure of 810 mmHg, whilst at 273 K being 23.9 $cm^3$ (STP) $g^{-1}$ (0.97 molecules of $CO_2$ per Cu-L unit) at an absolute pressure of 783 mmHg (**Figure 4.26.a**).

**MOFDEF(NIP)** adsorbed a maximum value of 17.9 $cm^3$ (STP) $g^{-1}$ (0.36 molecules of $CO_2$ per Cu-L unit) at an absolute pressure of 801 mmHg, at 298K. This increased at 283 K and 273 K with maximum values of 21.1 $cm^3$ (STP) $g^{-1}$ (0.43 molecules of $CO_2$ per Cu-L unit) at an absolute pressure of 810 mmHg, and 23.4 $cm^3$ (STP) $g^{-1}$ (0.47 molecules of $CO_2$ per Cu-L) at an absolute pressure of 783 mmHg.

The $CO_2$ sorption for **MOFDMF(NIP)** is marginally higher than for MOFDEF(NIP) at these temperatures. Given that the potential void space of MOFDEF(NIP) is only slightly higher than that of MOFDMF(NIP) (40 % vs 39 %) and that the layers move closer together upon desolvation, as established from VT-PXRD experiments, it is not surprising that their sorption values are closer to each other with those for MOFDMF(NIP) being slightly higher. (**Figure 4.26.b**).

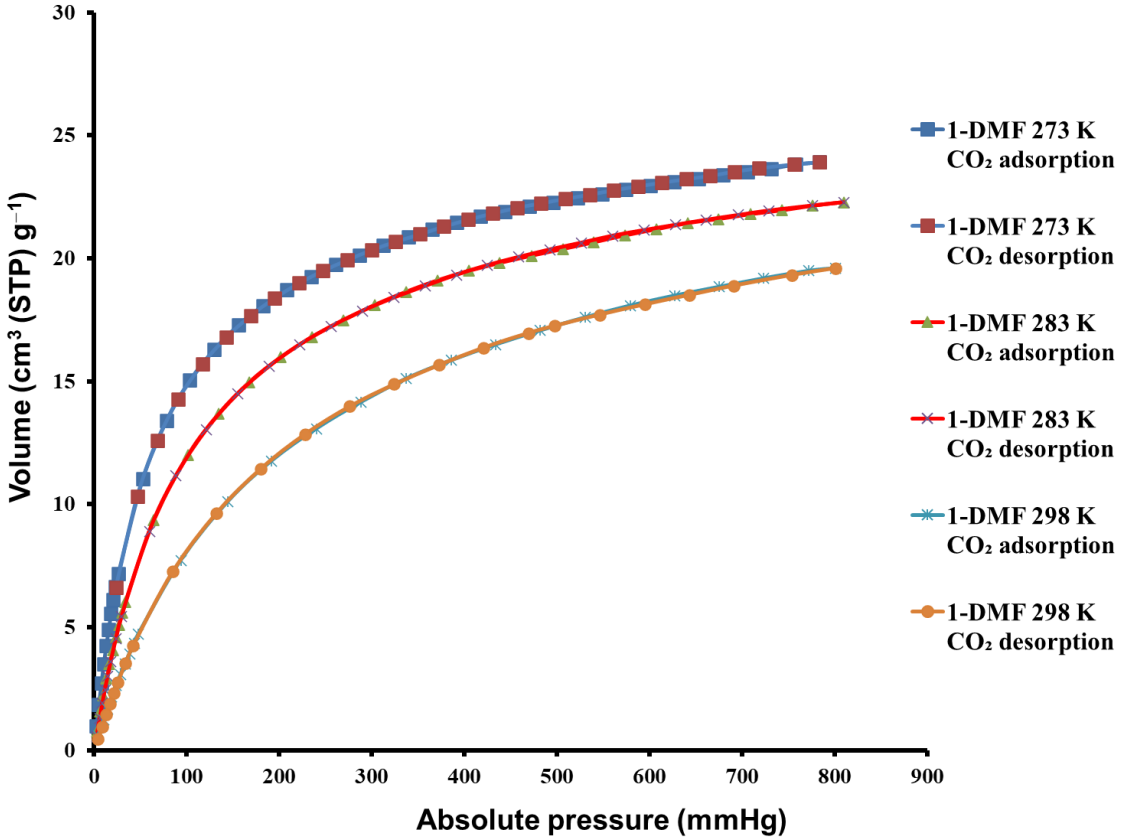


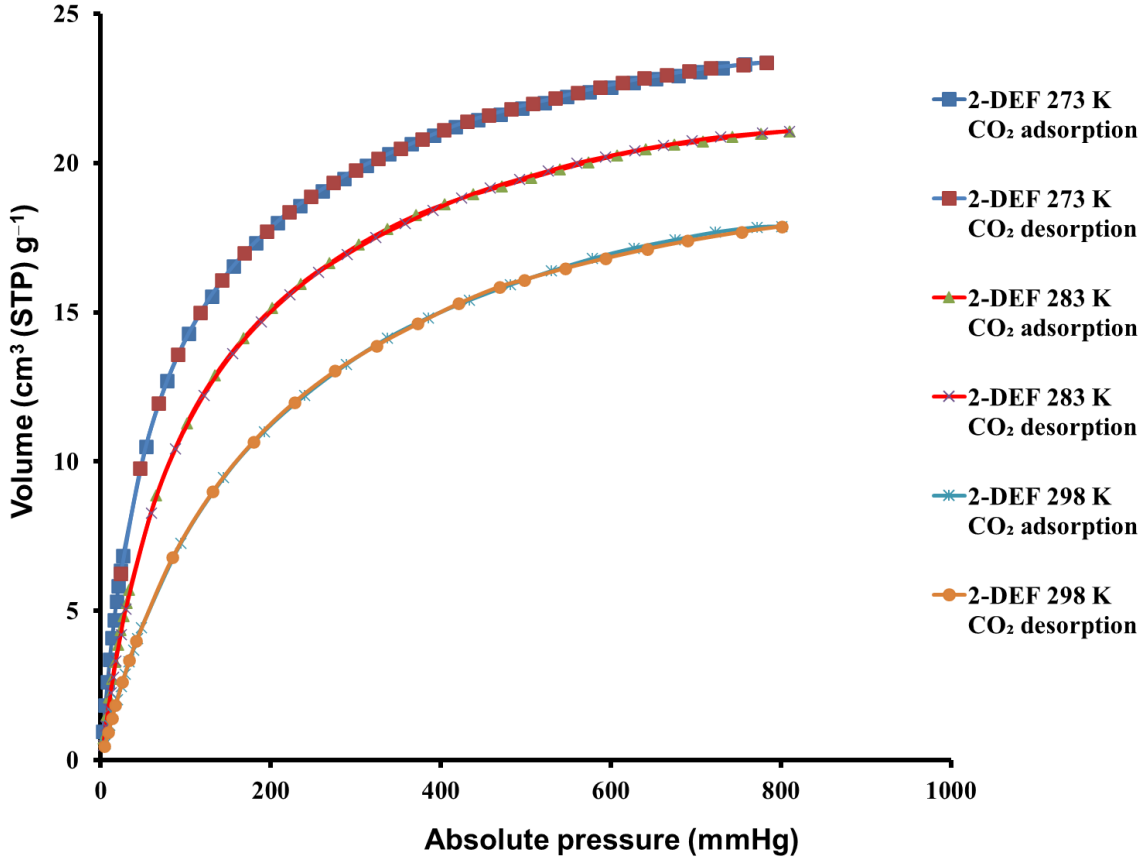


**Figure 4.26.** The adsorption and desorption isotherms for $CO_2$ sorption for (a) **MOFDMF(NIP)** and (b) **MOFDEF(NIP)** at 273 K, 283 K and 298 K.

On the contrary at 195 K, $CO_2$ the sorption order follows the potential void space order, with **MOFDEF(NIP)** showing higher $CO_2$ sorption than **MOFDMF(NIP)** (**Figure 4.27.**). An initial type-I isotherm for carbon dioxide sorption for **MOFDMF(NIP)** is observed up to an absolute pressure of 622 mmHg, sorption of 40.8 $cm^3$ (STP) $g^{-1}$ corresponding to 0.82 molecules of $CO_2$ per Cu-L unit) and for **MOFDEF(NIP)** up to absolute pressure of 583 mmHg (sorption of 44.2 $cm^3$ (STP) $g^{-1}$ corresponding to 0.90 molecules of $CO_2$ per Cu-L unit) is observed. Both isotherms show inflection points after these respective pressures that are characterised by a second steep increase in sorption to 770 mmHg for **MOFDMF(NIP)** and **MOFDEF(NIP)**. The maximum sorption values are 71.6 $cm^3$ (STP) $g^{-1}$ (1.45 molecules of $CO_2$ per Cu-L unit) for **MOFDMF(NIP)** and with maximum values of 78.7 $cm^3$ (STP) $g^{-1}$ (1.59 molecules of $CO_2$ per Cu-L unit) for **MOFDEF(NIP)**.

Both isotherms show a 3-step decrease upon desorption. The first desorption inflection points are at 275 mmHg, and 62.5 $cm^3$ (STP) $g^{-1}$ and 276 mmHg, and 67.7 $cm^3$ (STP) $g^{-1}$ for **MOFDMF (NIP)** and **MOFDEF (NIP)**, respectively. The lower inflection points are at 64.6 mmHg, and 41.2 $cm^3$ (STP) $g^{-1}$ and 82.3 mmHg, and 44.2 $cm^3$ (STP) $g^{-1}$, for **MOFDMF (NIP)** and **MOFDEF (NIP)**, respectively.

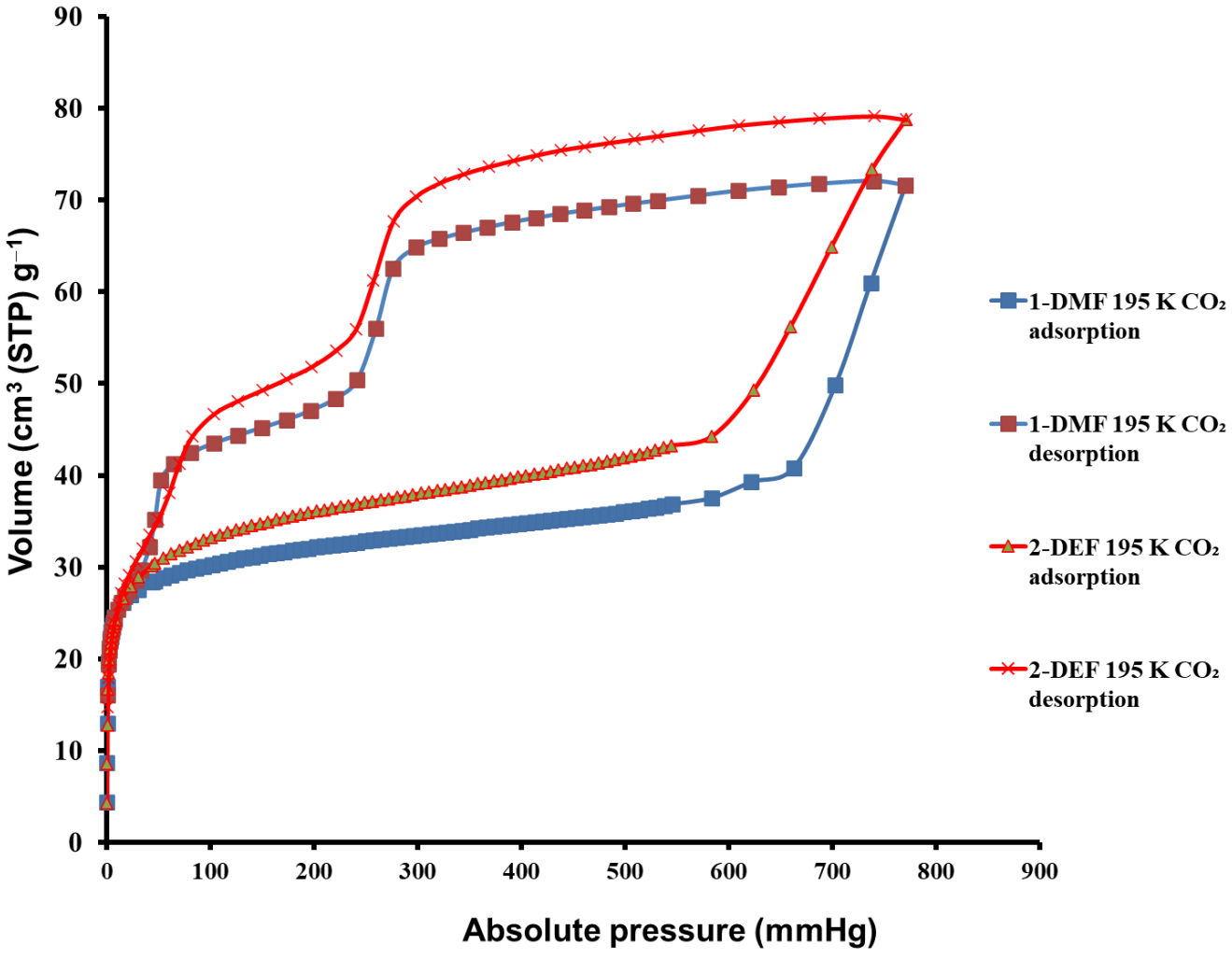


**Figure 4.27.** Carbon dioxide sorption isotherms at 195 K for **MOFDMF(NIP)** and **MOFDEF(NIP)**.

The order of extent of hysteresis is **MOFDMF(NIP)** > **MOFDEF(NIP)**, with values of 39% for **MOFDMF(NIP)** and 35%, respectively when using the Barbour *et al.* hysteresis formula.[6] Both **MOFDMF(NIP)** and **MOFDEF(NIP)** isotherms indicate significant extents of hysteresis, i.e. when at low pressures upon desorption, **MOFDMF(NIP)** and **MOFDEF(NIP)** "hold on" to the $CO_2$ molecules or have higher sorption than at the same pressure upon adsortion.

Looking at other gases that were also absorbed they show small hysteretic behaviour which is relatively low. The degree of hysteresis in the hydrogen sorption isotherms was lower but still significant, in the order **MOFDEF(NIP)** > **MOFDMF(NIP)**, 12% for **MOFDEF(NIP)** and 7.9% for **MOFDMF (NIP)**. It was also relatively low for water vapor sorption hysteresis also 8,2[a] and 7.5[a] for **MOFDEF(NIP)** and **MOFDEF(NIP)**, respectively (**Table 4.9**). The water sorption isotherms show that the channels of the framework are relatively hydrophobic as most of water sorption is accounted for by water coordinated to the metal ions.

**Table 4.9.** Extent of Hysteresis (%) for $CO_2$, $H_2$, and Water Vapour Sorption Isotherms in **MOFDMF(NIP)**, **MOFDEF(NIP)**.

| **Extent of hysteresis gas/vapour** | **MOFDMF(NIP)** (%) | **MOFDEF(NIP)** (%) |
|---|---|---|
| $CO_2$ sorption at 195 K | 39[a] | 35 |
| $H_2$ sorption at 77 K | 7.9 | 12 |
| water vapor sorption at 298 K | 7.5 | 8.2 |

[a]Hysteresis extent calculated using the Barbour *et al*. formula.

The values for the isosteric heat of adsorption, $Q_{st}$, sorption isotherms were calculated based on the 283-298 K sorption isotherms. In their respective loading ranges, the isosteric heats of adsorption, $Q_{st}$, for **MOFDMF(NIP)** and **MOFDEF(NIP)** are comparable, with average values of 31.7 (0.2) and 32.7 (0.1) kJ $mol^{-1}$, respectively (Table 4.10.). Despite exhibiting reduced $CO_2$ sorption, the $Q_{st}$ values of **MOFDEF(NIP)** are predominantly higher than those of **MOFDMF(NIP)** the respective loading ranges.

**Table 4.10.** Summary $Q_{st}$ Values Determined from $CO_2$ Isotherms in the Temperature Range 273 – 298 K

| | **MOFDMF (NIP)** | **MOFDEF (NIP)** |
|---|---|---|
| Load range ($cm^3$ (STP) $g^{-1}$) | 0.9 – 18.0 | 0.9 – 18.0 |
| $Q_{st}$ range (kJ $mol^{-1}$) | 30.9 – 32.0 | 31.5 – 34.3 |
| average $Q_{st}$ (kJ $mol^{-1}$) | 31.7 (0.2) * | 32.7 (0.1) * |

*Number in brackets refer to the average of the uncertainties determined for each $Q_{st}$ value in the loading range as determined by the Micromeritics software. That is, it is not the standard deviation calculated from the $Q_{st}$ values that contribute to the average $Q_{st}$ value.

In contrast at 195 K **MOFH$_2$O(NIP)** exhibits less $CO_2$ sorption than **MOFDMF(NIP)** and **MOFDEF(NIP)** (**Figure 4.28**). Interestingly, there is no inflection point that signify a second steep to increase in sorption, however a subtle change in slope occurs at 583 mmHg (**Figure 4.28**). Due to the inability to obtain a structure, the $CO_2$ molecules per Cu-L unit for a type-I isothermal carbon dioxide sorption for **MOFH$_2$O(NIP)** at an absolute pressure of 771 mmHg, at a value of 42.8 $cm^3$ (STP) $g^{-1}$ (molecules of $CO_2$ per Cu-L unit).

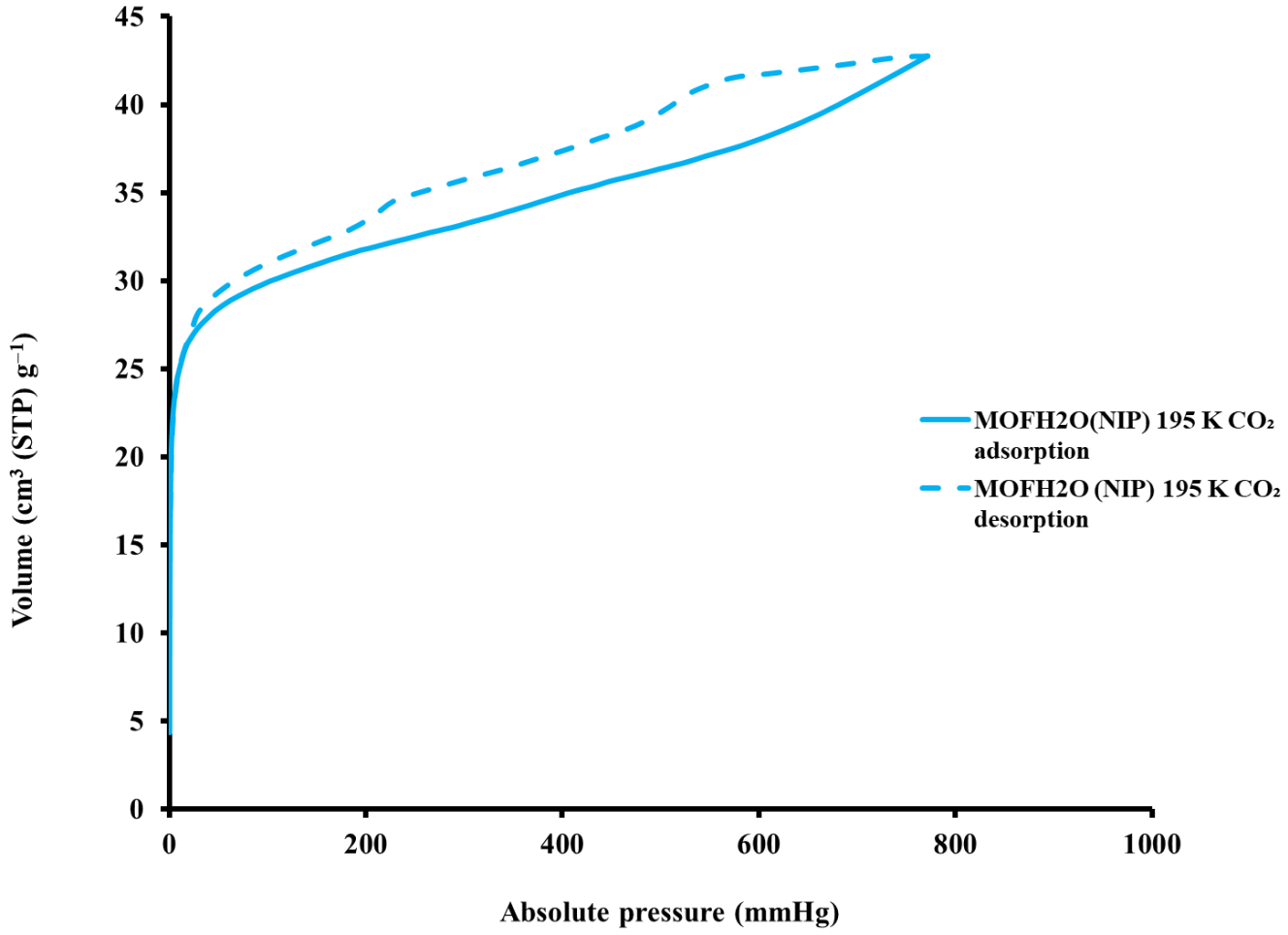


**Figure 4.28.** Carbon dioxide adsorption and desorption isotherm for **MOFH$_2$O(NIP)** at 195 K.

### 4.12.2. Hydrogen Sorption

The order of hydrogen sorption maxima at 77 K and P ~ 800 mmHg is **MOFDMF(NIP)** > **MOFDEF(NIP)** with values of 60.7 and 50.6 $cm^3$ (STP) $g^{-1}$ which correspond to 1.23 and 1.02 $H_2$ atoms per Cu-L unit, respectively (**Figure 4.29**).

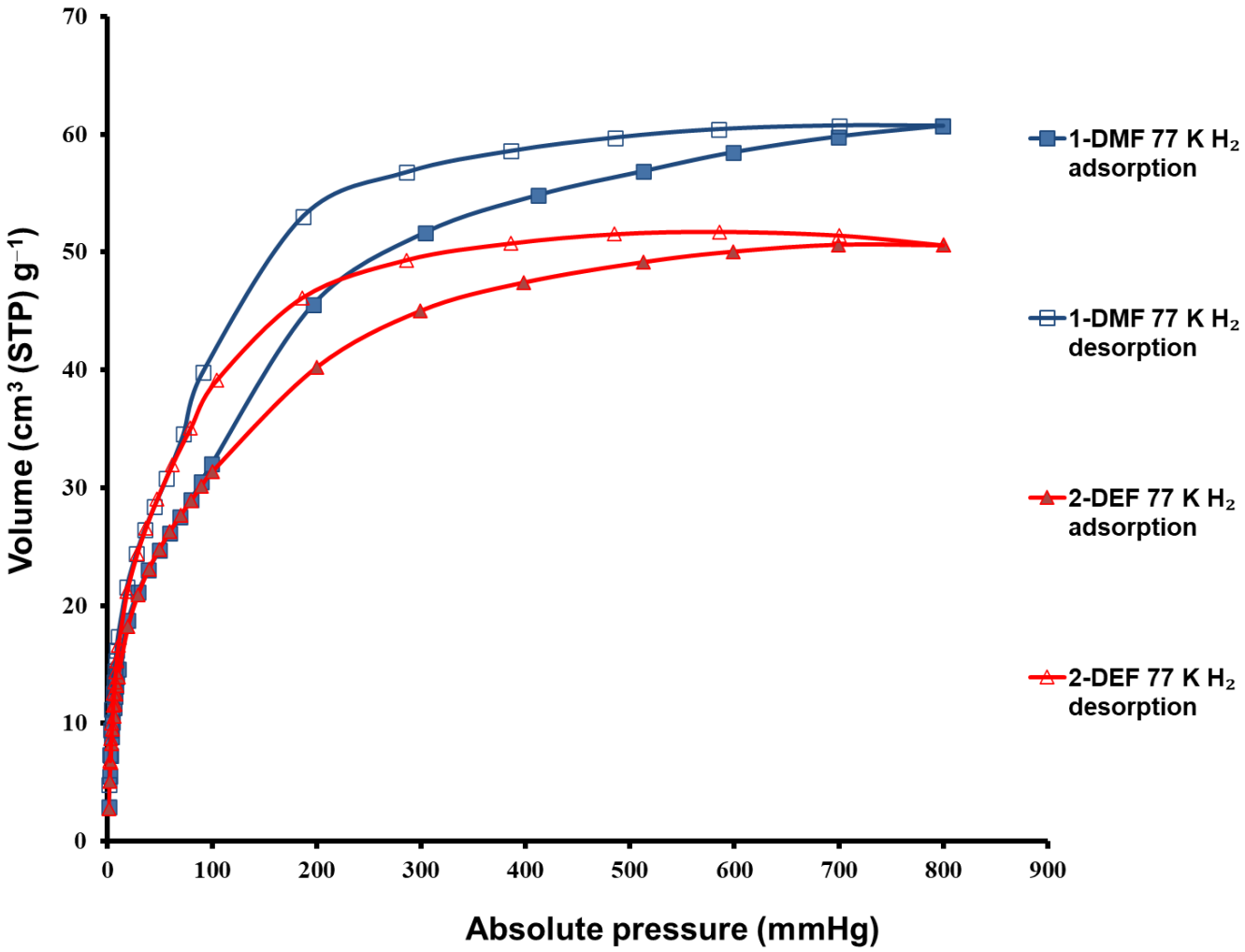


**Figure 4.29**. Adsorption and desorption isotherms for Hydrogen sorption for **MOFDMF(NIP)** and is **MOFDEF(NIP)** at 77 K.

### 4.5.3. Water Vapour Sorption

Water sorption studies were performed at 298K for **MOFDMF(NIP)** and is **MOFDEF(NIP)**. Both MOFs show high affinity for water vapour as both isotherms display steep uptakes (**Figure 4.30**). With maximum water sorption of 55.3 $cm^3$ (STP) $g^{-1}$ at $P/P_o$ = 0.76 (1.12 water molecules per Cu-L) and 55.3 $cm^3$ (STP) $g^{-1}$ at $P/P_o$ = 0.76 (1.12 water molecules per Cu-L) for **MOFDMF(NIP)** and **MOFDEF(NIP)**, respectively. The steep curve for both suggests that unsaturated metal sites are filled first i.e. the water molecules are coordinated. For **MOFDMF (NIP)** these would correspond to 1 water molecule per $Cu^{2+}$ ion, as well as for **MOFDEF(NIP)**, which effectively replaces the original ligated DMF or DEF molecule. This means that essentially no water molecules are taken up in the MOF cavities, establishing them as hydrophobic.

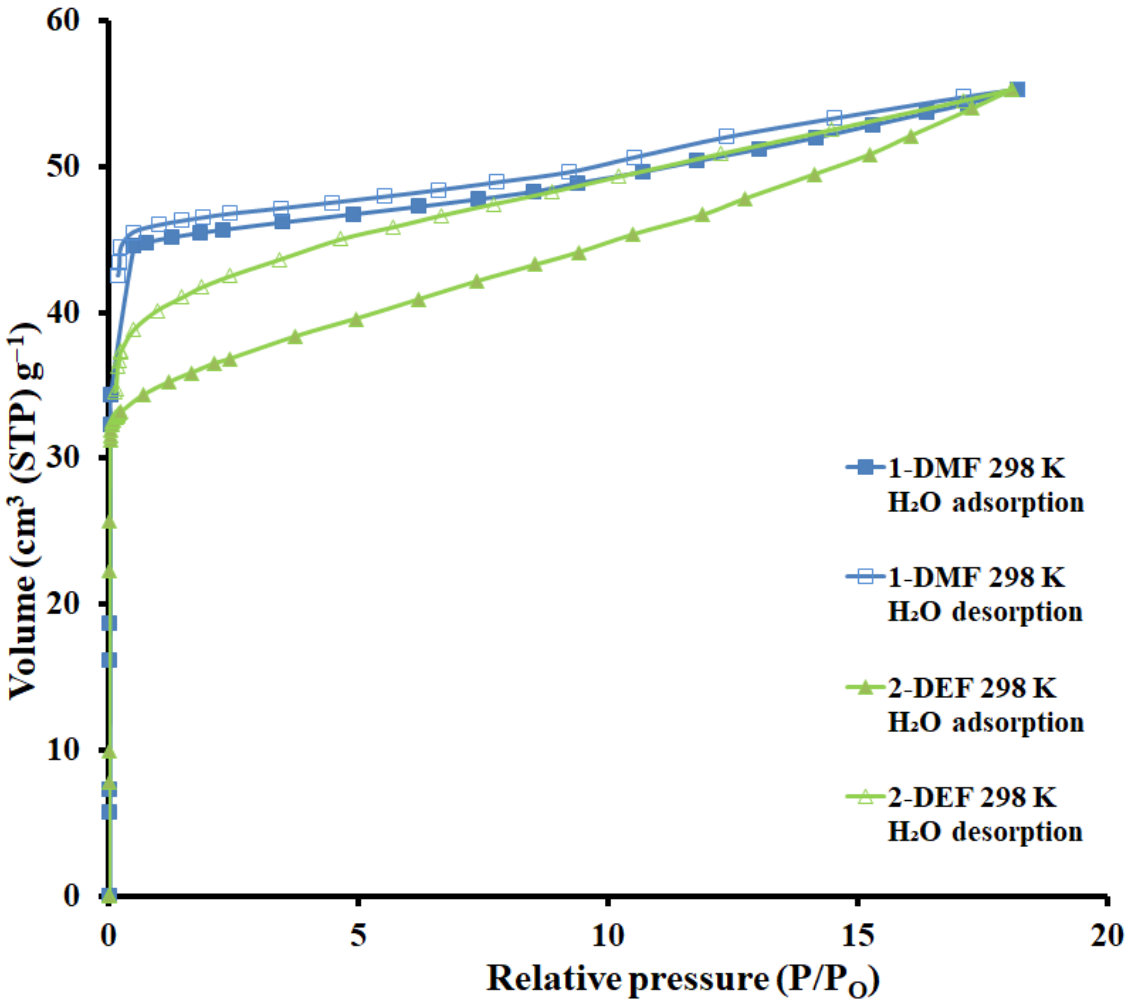


**Figure 4.30.** Adsorption and desorption isotherms for water vapour sorption for **MOFDMF(NIP)** and **MOFDEF(NIP)** at 298 K.

## 4.13. Conclusions

### 4.13.1. Introduction to previous work

In 2022 Chatterjee *et al*.[1] published the synthesis and characterization of two 2-periodic metal-organic frameworks and one water exchange MOF, with the formulae $[Cu(hfipbb)(DMF)]_n \cdot 0.5(DMF)_n$, $[Cu(hfipbb)(DEF)]_n$, $[Cu(hfipbb)(H_2O)]_n.0.5(DMF)_n$. These are all isoreticular (having the same network of connections) with the MOFs presented in this thesis. However, the Chatterjee *et al*. structures are all doubly interpenetrated, whilst the ones presented in this thesis are non-interpenetrated. The Chatterjee *et al* structures are renamed as MOFDMF (IP), MOFDMF (IP) and $MOFH_2O$ (IP) for $[Cu(hfipbb)(DMF)]_n \cdot 0.5(DMF)_n$, $[Cu(hfipbb)(DEF)]_n$, and $[Cu(hfipbb)(H2O)]_n.0.5(DMF)_n$, respectively.

The three pairs will be named based on their degrees of interpenetration and type of solvent included. The structures will be given names for convenience in this thesis:

### 4.13.2. Thermal stability

VT-PXRD experiments revealed that the bulk samples of all the structures were crystalline as those of the previously published structures. They further show that all the structures exhibited structural changes, these were also quoted by Chatterjee *et al*. (i) layers moving close to each other after solvent removal, this is supported by the disappearance of peaks for both interpenetrated and non-interpenetrated MOF structures. (ii) the interpenetrated MOF structures were significantly more stable. Although the interpenetrated structures showed higher stability than their counter parts. The entangled **MOFDMF(IP)** (125°C) and **MOFDEF(IP)** (125°C**)** show higher temperatures for removal of uncoordinated solvent and layers shifting whereas non-entangled structures show **MOFDMF(NIP)** (87°C) and **MOFDEF(NIP)** (125°C), for the doubly interpenetrated structures the layers only moved once the ligated solvent molecules were removed, whereas the non-interpenetrated structures showed movement after the solvent in between the layers was removed. The TGA data is provided in **Table 4.12** and **Figure 4.31**. correlates the VT-PXRD experimental findings.

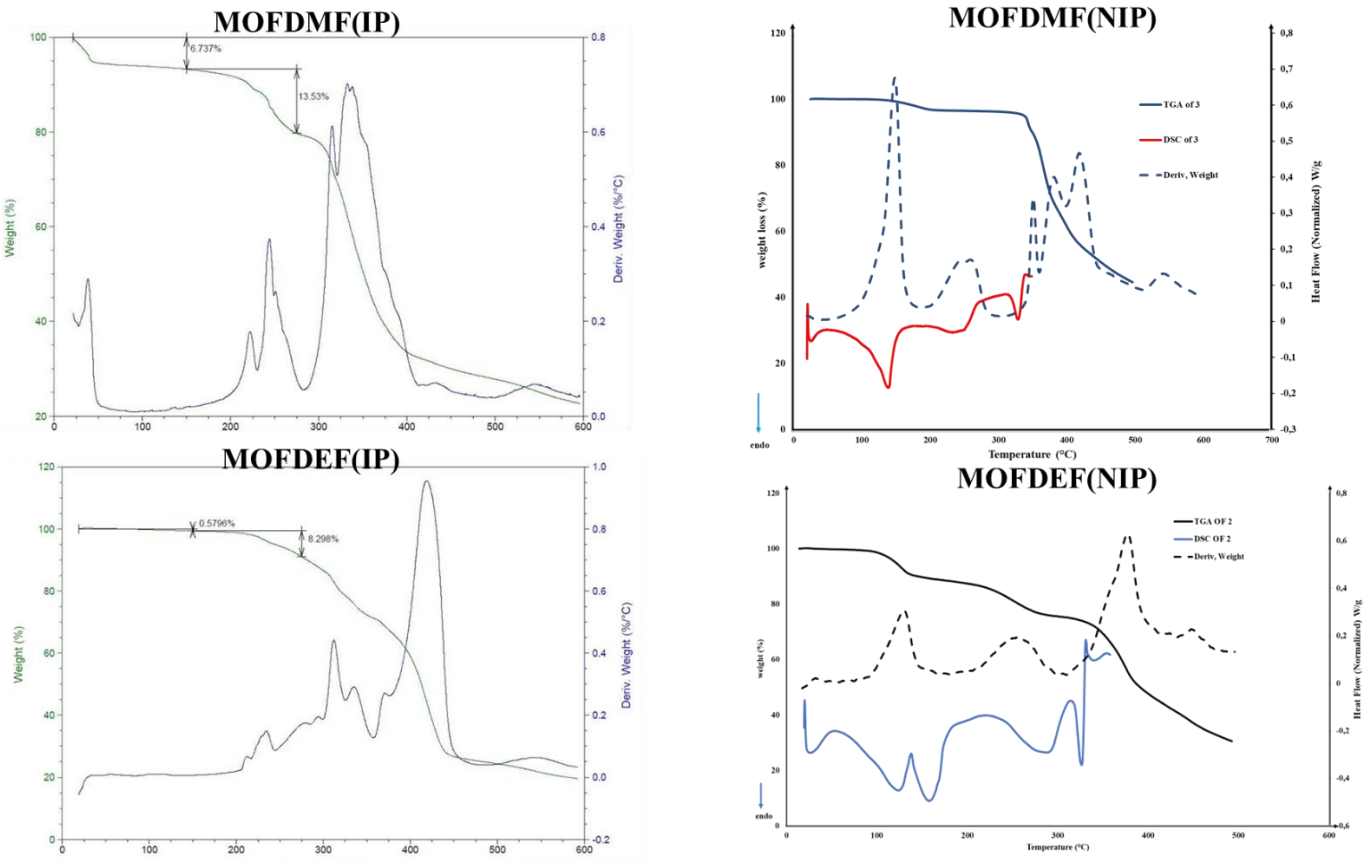


**Figure 4.31.** TGA graphs of weight % vs temperature and the first derivative of weight % with respect to temperature for interpenetrated and non-interpenetrated.

**Table 4.12.** Summary of selected isoreticular copper paddlewheel-based 2-periodic MOF structures TGA values.

| | **Experimental mass loss (%)** | **Temperature range (°C)** |
|---|---|---|
| MOFDMF (IP) | Total = 24.5<br>$1^{st}$ =6.7<br>$2^{nd}$ =13.5 | <br>$1^{st}$ = 50 – 125<br>$2^{nd}$ =125 – 270 |
| MOFDMF (NIP) | Total = 31.0<br>$1^{st}$ =20.6<br>$2^{nd}$ =10.4 | <br>$1^{st}$ = 30 – 87<br>$2^{nd}$ =87 – 300 |
| MOFDEF (IP) | Total = 24.5<br>$1^{st}$ =0.58<br>$2^{nd}$ =8.29 | <br>$1^{st}$ = 25 – 125<br>$2^{nd}$ =125 – 250 |
| MOFDEF (NIP) | Total = 24.5<br>$1^{st}$ =11.5<br>$2^{nd}$ =13.0 | <br>$1^{st}$ = 30 – 125<br>$2^{nd}$ =175 – 300 |
| MOF$H_2O$ (IP) | - | - |
| MOF$H_2O$ (NIP) | $1^{st}$ =3.6 | $1^{st}$ = 125 – 250 |

### 4.13.3. Void Space Analyses and Gas sorption

Comparing the void space of each pair, **MOFDMF(NIP)** > **MOFDMF(IP)**, with values 39% and 10.7% respectively. Looking at the second set of MOFs also follows the same order, where **MOFDEF(NIP)** > **MOFDEF(IP)** with values 40.4% > 8.2% respectively. Although these calculated values are different, one thing that can be taken into consideration is the fact that layers will move closer together. Although the third set of structures one was not able to get a crystal structure based on the observed thread, all of the interpenetrated structures have lower void spaces than the non-interpenetrated. The potential void space of **MOFDMF(NIP)** and **MOFDEF(IP)** includes the detection of solvent molecules between the layers, which ultimately will move closer together. The difference in void spaces of activated MOFs is not what is expected.

**Table 4.11.** Percentage (%) of void space of all the isoreticular copper paddlewheel-based 2-periodic MOF structures.

| MOF | Degree of Entanglement | Percent void space per unit cell volume without solvent present (%) | 'Channel-Only' void space |
|---|---|---|---|
| MOFDMF (IP)[1] | Interpenetrated 2-fold | 10.7 | 10.7 |
| MOFDMF (NIP) | Non-Interpenetrated | 39 | 22.6 |
| MOFDEF (IP)[1] | Interpenetrated 2-fold | 8.2 | 8.2 |
| MOFDEF (NIP) | Non-Interpenetrated | 40.4 | 19.4 |
| MOF$H_2O$ (IP)[1] | Interpenetrated 2-fold | 12.5 | 12.5 |
| MOF$H_2O$ (NIP) | Non-Interpenetrated | - | - |

1.As published by Chatterjee et al.[1]

- This material was powder, there is no crystal structure to determine void space.

All sorption studies of $N_2$ at 77 K were negligible for Chatterjee *et al*. and the structures in this thesis, thus one could not determine the BET surface areas of all the forementioned structures. whilst $H_2$ sorption revealed sorption isotherms which displayed some hysteresis observed upon desorption, **MOFDMF(NIP) > MOFDMF(IP) and MOFDMF(IP) >MOFDEF(NIP)**. The 195 K $CO_2$ and $H_2O$ sorption isotherms also showed hysteresis upon desorption which indicated the retention of gas/vapour at lower pressures. For $CO_2$ 195K, the hysteresis in the carbon dioxide sorption for **MOFDMF(IP)** and **MOFDEF(IP)** showed greater sorption with values 176.7 $cm^3$ (STP) $g^{-1}$ and 98.8 $cm^3$ (STP) $g^{-1}$, respectively and when compared to the non-interpenetrated versions they are superior in this case because their values are 71.6 and 78.7 $cm^3$ (STP) $g^{-1}$, for **MOFDMF(NIP)** and **MOFDEF(NIP)** respectively. The water structures are different, the non-interpenetrated version have 42.8 $cm^3$ (STP) $g^{-1}$ **MOF$H_2O$(NIP)** > whereas **MOF$H_2O$(IP)** is 31.0 $cm^3$ (STP) $g^{-1}$, this suggest that in the case of the water solvent these structures hold more gas than their counter parts. Nevertheless, the degrees of hysteresis are small despite one structure is either interpenetrated (IP) or the other non-interpenetrated (NIP). A summary is given in **Table 4.12**.

**Table 4.12.** Gas sorption of all the isoreticular copper paddlewheel-based 2-periodic MOF structures.

| MOFs | $H_2$ | $CO_2$ at 195 K | $CO_2$ at 298 K | Water vapor sorption |
|---|---|---|---|---|
| MOFDMF (IP)[1] | 51.9 | 176.7 | 34.8 | 45.3 |
| MOFDMF (NIP) | 60.7 | 71.6 | 19.6 | 55.3 |
| MOFDEF (IP)[1] | 55.9 | 98.8 | 20.4 | 37.8 |
| MOFDEF (NIP) | 50.6 | 78.7 | 22.3 | 55.3 |
| $MOFH_2O$ (IP)[1] | - | 31.0 | - | - |
| $MOFH_2O$ (NIP) | - | 42.8 | - | 42.8 |
| | | | | |

- Sorption studies were not performed.

## 4.14. Reference


1. N. Chatterjee, C.L. Oliver, *Inorganic Chemistry*, 2022, **61**, 3516-3526.
2. C.R. Groom, I.J. Bruno, M.P. Lightfoot, S.C. Ward, *Acta Crystallogr. Sect. B,* 2016, **72**, 171-179
3. L. Pan, D.H. Olson, L.R. Ciemnolonski, R. Heddy, J. Li, *Angew. Chem. Int. Ed.*, 2006, **45**, 616.
4. R. Kitaura, F. Iwahori, R. Matsuda, S. Kitagawa, Y. Kubota, M. Takata, T.C. Kobayashi*, Inorg. Chem.,* 2004, **43**, 6522-6524.
5. A. W. Addison, T. N. Rao, J. Reedijk, J. V. Rijn, G. C. Verschoor, *J. Chem. Soc., Dalton Trans.* 1984, 7, 1349 -1356.
6. P. Lama, H. Aggarwal, C.X. Bezuidenhout, L.J. Barbour, *Angewandte Chemie-International Edition* 2016, **55**, 13271-13275.
7. S.A. Sapchenko, M.O. Barsukova, R.V. Belosludov, K.A. Kovalenko, D.G. Samsonenko, A.S. Poryvaev, A.M. Sheveleva, M.V. Fedin, A.S. Bogomyakov, D.N. Dybtsev, M. Schröder, V. Fedin, *Inorg. Chem.* 2019, **58**, 6811-6820.

# CHAPTER 5

## 5.1. Summary

### 5.1.1. Computer-based section:

Evaluating the created criteria to effectively locate entangled structures and comparing the manual searches conducted on all the families included in this study. The success of the search criteria was defined in two ways. Firstly, expressing the number of entangled structures found in the search results as a percentage of the total number of MOF structures in this list, gives the degree of success of the search criteria in terms of discriminating between entangled and non-entangled structures. Secondly, the number of entangled structures found in the search results expressed a percentage of the number of entangled structures found by manual inspection, i.e., the true number of entangled structures.

The results of the two ways of demonstrated success of the search criteria defined for the hydrogen non-bonding interactions "D−H···A" illustrates that the success rate of finding these structures on average percentage of the two Zn-oxide > Zr-oxide > Cu-Cu paddlewheel > IRMOF-1-like. Whereas for π···π nonbonding success rate is Zr-oxide > Cu-Cu paddlewheel > Zn-oxide > IRMOF-1-like. And the last search criterion shows that the average success rate is Zr-oxide > Cu-Cu paddlewheel > Zn-oxide > IRMOF-1-like.

### 5.1.2. Experimental section:

Three Cu-based 2D, 2-periodic novel isoreticular MOFs have been synthesized solvothermally using the flourinated, 4,4'-(Hexaflouroisopropylidene)bis(benzoic acid) based ligand, with **3** synthesised via water exchange. VT-PXRD experiments showed that the bulk samples of **MOFDMF(NIP)**, **MOFDEF(NIP)** and **MOF$H_2O$(NIP)** retained good crystallinity up to high temperatures of 300 °C, even though the degree of crystallinity of **MOFDEF(NIP)** and **MOF$H_2O$(NIP)** appeared to be higher than that of **MOFDMF(NIP)**. The VT-PXRD studies further showed that the 2D, 2-periodic frameworks of **MOFDMF(NIP)** and **MOFDEF(NIP)** shift upon desolvation, whereas those of **MOFDMF(NIP)**.

The BET surface areas of all the MOF structures could not be found due to the structures not performing well in the sorption studies of $N_2$. Other sorption studies revealed the $H_2$, $CO_2$ and water vapour sorption values of **MOFDMF(NIP)** were higher than those of **MOFDEF(NIP)** at 298 K to 273 K for $CO_2$, but lower 195 K and both structures demonstrated large hysteresis upon desorption which indicated the retention of gas/vapour at lower pressures. The sorption isotherms for $H_2$ were also higher for **MOFDMF(NIP)** than those of **MOFDEF(NIP)**. For water vapour sorption studies, the two MOF structures' sorption isotherms were the same in terms of maximum value. These differences in sorption can largely be attributed to the poorer crystallinity of **MOFDEF(NIP)**.

The conducted $CO_2$ sorption for **MOF$H_2O$(NIP)** did not show any hysteresis upon desorption, the sorption isotherm. Furthermore, **MOFDMF(NIP)** and **MOFDEF(NIP)** compared well with their isoreticular counterparts in terms of their sorption properties.

## 5.2. Future work

### 5.2.1. Computer-based section:

This experiment still leaves some questions unanswered, such as what would happen if the ligand did not contain a π-stacking group but was still interpenetrated? Is it possible to create a computer algorithm that analyzes the structure, topology, and interpenetration in these families? Would it be possible to search for non-contact interactions, in Conquest to recognize that a framework is a coordination polymer.

### 5.2.2. Experimental section

Future work could include the crystal structure of **MOF$H_2O$(NIP)** and of the activated phases of **MOFDMF(NIP)**, **MOFDEF(NIP)** and **MOF$H_2O$(NIP)** would be very informative in terms of determining the actual void spaces before sorption experiments commence. This is because heating the crystals destroyed the monocrystallinity of the crystals. The need for additional research to obtain crystal structures of the activated phases of these isoreticular structures may provide additional insight into the subtle features of these MOFs in their sorption properties.